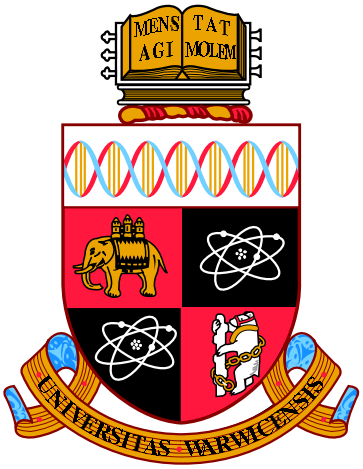

Convective overshoot in the atmosphere of white dwarf stars

by

Timothy Jack Cunningham

Thesis

Submitted to the University of Warwick

for the degree of

Doctor of Philosophy

Astronomy and Astrophysics

June 2020

Contents

Acknowledgments

Personal Acknowledgements

The work presented in this thesis would not have been possible without the support of some very important people who are mentioned below.

Firstly, I would like to thank my supervisor, Pier-Emmanuel Tremblay, for giving me the opportunity, resources and training to develop as a scientist. I could not have hoped for a better mentor on this journey and am grateful for his guidance and friendship along the way. I am also grateful for the opportunities I have received from the Warwick Astronomy & Astrophysics Group to train on telescopes around the world. Thanks go to Lars Bildsten and Hans-Günter Ludwig for kindly hosting me for collaborative visits in Santa Barbara and Heidelberg which helped inform my research directions.

I would also like to extend my thanks to all of those within the Warwick Astronomy & Astrophysics group who have made my time here so memorable. Particular thanks go to my PhD sister, Elena, and Chris, Nicola, Matt, Matthew, James, Mark, Ashley, Ry, and Jack for your support with science and life. I am also thankful to those in the Pub Wednesday collective for reminding me that a PhD should be fun. And for introducing me to my wonderful housemate Sam. I would also like to thank all my friends who have supported me on this journey. Particular mentions go to Fox, John, Thor, Atti, Aisling, Adam, Oli and Aaron.

Special thanks go to Odette for her patience, love and support. And to my family – my mum, dad and sister, my aunts, uncles and cousins – for their constant love and support throughout this journey.

Institutional Acknowledgements

The research leading to these results has received funding from the European Research Council under the European Union's Horizon 2020 research and innovation programme n. 677706 (WD3D).

This research was supported in part by the National Science Foundation under Grant No. NSF PHY-1748958.

This thesis has made use of observations from the following observatories and institutions:

This work has made use of data from the European Space Agency (ESA) mission *Gaia* (https://www.cosmos.esa.int/gaia), processed by the *Gaia* Data Processing and Analysis Consortium
(DPAC, https://www.cosmos.esa.int/web/gaia/dpac/consortium). Funding for the DPAC has been provided by national institutions, in particular the institutions participating in the *Gaia* Multilateral Agreement.

SDSS-III, funding for which has been provided by the Alfred P. Sloan Foundation, the Participating Institutions, the National Science Foundation, and the U.S. Department of Energy Office of Science. The SDSS-III web site is http://www.sdss3.org/.

SDSS-III is managed by the Astrophysical Research Consortium for the Participating Institutions of the SDSS-III Collaboration including the University of Arizona, the Brazilian Participation Group, Brookhaven National Laboratory, Carnegie Mellon University, University of Florida, the French Participation Group, the German Participation Group, Harvard University, the Instituto de Astrofisica de Canarias, the Michigan State/Notre Dame/JINA Participation Group, Johns Hopkins University, Lawrence Berkeley National Laboratory, Max Planck Institute for Astrophysics, Max Planck Institute for Extraterrestrial Physics, New Mexico State University, New York University, Ohio State University, Pennsylvania State University, University of Portsmouth, Princeton University, the Spanish Participation Group, University of Tokyo, University of Utah, Vanderbilt University, University of Virginia, University of Washington, and Yale University.

Declarations

I submit this thesis to the University of Warwick graduate school for the degree of Doctor of Philosophy. This thesis has been composed by myself and has not been submitted for a degree at another University.

An appreciable quantity of thesis includes material from published/submitted papers written by myself which are detailed below:

- Cunningham et al. (2019), *Convective overshoot and macroscopic diffusion in pure-hydrogen-atmosphere white dwarfs*. Chapter 3 makes use of material from this work.
- Cunningham et al. (2020) *From hydrogen to helium: the spectral evolution of white dwarfs as evidence for convective mixing*. Chapter 5 makes use of material from this work.

In addition, the conclusions make use of material from both of these papers and Chapter 4 is based on work that will be submitted as a paper soon. The general discussion throughout this thesis benefited greatly from the input of co-authors on these published and soon to be submitted papers.

The analysis and work presented in this thesis was carried out by the author, with the following exceptions: 1D structures of microscopic diffusion were kindly provided by Detlev Koester, the extended grid of hydrodynamic simulations presented in Chapter 3 for the indirect diffusion experiments were calculated by Pier-Emmanuel Tremblay, data for the sample of metal-polluted white dwarfs used in Chapters 3 & 4 were provided by Jay Farihi, in Chapter 4 the 3D results characterising cool DA convection zones were provided by Pier-Emmanuel Tremblay, and those characterising DB convection zones were provided by Elena Cukanovaite. In Chapter 5 the DA and DB spectral models shown in Fig. 5.1

were computed by Odette Toloza, the determination of atmospheric parameters (effective temperature and surface gravity) was made by Pier-Emmanuel Tremblay, and the white dwarf spectral types were determined largely by Nicola Gentile Fusillo. The discussion in Sections 4.4.4–4.4.5 were mostly written by Pier-Emmanuel Tremblay and is included in this thesis as this forms part of a paper that is soon to be submitted for publication.

★★★

What though Dreams be wandering fancies, by some lawless force entwined,
Empty bubbles, floating upwards through the current of the mind?
There are powers and thoughts within us, that we know not, till they rise
Through the stream of conscious action from where Self in secret lies.
But when Will and Sense are silent, by the thoughts that come and go,
We may trace the rocks and eddies in the hidden depths below.

JAMES CLERK MAXWELL

Abstract

At least a quarter of white dwarf stars have heavy elements in their atmosphere. The source of these metals is predominantly accretion of the evolved planetary systems they hosted as main sequence stars. Precise spectroscopic abundance measurements provide the only method by which to determine the bulk composition of exoplanetary material. As white dwarfs cool they develop surface convection zones and the mass mixed in these regions is a critical input into models of debris-accretion at white dwarfs. But so far all studies have relied upon a century old prescription of convection called the mixing length theory.

In this thesis I employed 3D radiation hydrodynamics (RHD) with the CO^{5}BOLD code to study the properties of convection zones in the surface layers of hydrogen-atmosphere (DA) white dwarfs. I used passive scalars to derive the effective diffusion coefficient due to convective overshoot for white dwarfs in the effective temperature range 11 400–18 000 K. I found that when compared to the mixing length theory the mixed mass is expected to increase by up to 2.5 orders of magnitude. This directly impacts the inferred accreted masses and leads to an order of magnitude increase in inferred accretion rates.

I also present the first transport coefficients in white dwarf atmospheres which describe the advection-diffusion of a passive scalar across the surface. These results cover most of the parameter space of convective white dwarfs and lead to an investigation into whether convection zones are effective at spreading material across the surface. I find that warm ($\gtrsim$ 14 000 K) DA white dwarfs are unable to efficiently homogenize material at the surface, challenging the often-held assumption that observed metals are homogeneously mixed. For cooler DAs and helium-atmosphere (DB) white dwarfs I find evidence that supports a homogeneous distribution of metals across the surface.

Finally, I analysed a sample of white dwarfs observed with *Gaia*, SDSS, and *Galex* to test the hypothesis that DA white dwarfs will transform into DB-type objects when their hydrogen convection zone reaches the deeper helium layer. I found that 22% of white dwarfs will undergo such a spectral change in the temperature range 20 000 K to 9000 K, with no spectral evolution ruled out at 5σ. The rate of spectral change was combined with the previous determination of convection zone mass to derive a distribution of hydrogen mass in white dwarfs. These results can serve as an input to asteroseismological models and a constraint on stellar evolution models.

Chapter 1

Introduction

1.1 White dwarfs

White dwarfs are the compact stellar tombstones left behind by the majority of stars. Their high density and slow cooling have made them a powerful lens through which to study fundamental constants, atomic physics, evolved exoplanetary systems, Galactic dynamics and, as is the concern of this thesis, convection. With over a century of prolonged research effort the known white dwarfs are numerous and remarkably well understood, but with increasingly precise observational facilities and sophisticated atmosphere simulations it is clear that we still have much to learn about these fascinating objects and the Universe they inhabit.

1.1.1 Discovery

In order of discovery, the first four *classical white dwarfs* are 40 Eridani B, Sirius B, Procyon B, and van Maanen 2. The first, 40 Eridani B, was discovered as a companion to the F-type star 40 Eridani A (Herschel, 1785) though it was at least a century before it was classified as a white dwarf. In 1910 Williamina Fleming classified its appearance as type A (Bond et al., 2017) and in the same year Henry N. Russell and Edward C. Pickering noted it to be significantly fainter (five magnitudes) than its companion (Russell, 1944). Fleming's spectral classification was confirmed shortly after by Adams (1914) who concluded from its faintness that the star had a smaller radius but significantly higher temperature than its companion.

The discovery of Sirius B was preceded by observations of Bessel (1844) who, on finding that the proper motions of Sirius and Procyon were being "very sensibly altered", hypothesised that these nearby stars may be gravitationally associated with an undetected companion. This was confirmed in 1862 by Alven G. Clarke who made the first observation of Sirius' companion (Flammarion, 1877) which at the time was separated from Sirius by 10 arcsecs on the sky. At $\approx$ 8 light years from Earth, Sirius B is our closest white dwarf. The companion to Procyon was discovered a few decades later (Schaeberle, 1896) but its identification was preceded by the discovery of the first isolated white dwarf; van Maanen's star (vMa2).

van Maanen (1917) initially classified this as an F-type star due to the presence of strong metal absorption lines but due to its low luminosity it was soon after reclassified as a white dwarf (Luyten, 1922) although it was many decades before the significance of these metal lines was understood (this is discussed in more detail in Section 1.2). Luyten is credited with coining the term *white dwarf* upon realising that these sub-luminous objects belonged in a class of their own. Since then over 30,000 white dwarfs have been spectroscopically classified using the Sloan Digital Sky Survey (SDSS) (Kleinman et al., 2013a; Kepler et al.,

2015) and the recent data release of *Gaia* revealed it is likely there are ten times as many white dwarfs in the solar neighbourhood (Gaia Collaboration et al., 2018b; Gentile Fusillo et al., 2019a).

Upon their discovery the existence of these sub-luminous compact white dwarfs was incompatible with the understanding of possible star configurations. Fortunately the development of quantum mechanics was already underway and as we will see in Section 1.1.3 proved to be essential for explaining the high internal density of these objects. In the absence of an established theory of stellar structure and evolution the origin of these stars was also unknown. We now know that white dwarfs are the degenerate end stage of life for most stars and we will consider this journey of stellar evolution in the following.

1.1.2 Formation

The interstellar medium (ISM) is a sparse collection of matter and radiation which predominantly comprises hydrogen in its atomic (H) and molecular (H_2) form. These atoms and molecules are distributed in clumps, and it is in these higher density regions that stars are born. When these so-called *molecular clouds* experience gravitational instabilities (due to e.g. bubbles and shocks) the local material density can fluctuate. If the density is sufficiently high the local volume will exceed a critical mass above which the material will commence a gravitational collapse, overcoming the local force of pressure. Named after its proponent, this critical mass limit is called the Jeans Mass (Jeans, 1902). If the mass of material undergoing this gravitational collapse is less than $\approx 0.08\ M_\odot$ the result will be the formation of a brown dwarf; a sub-stellar object capable of fusing deuterium in its core, but not hydrogen. If however the collapsing material exceeds $0.08\ M_\odot$ the temperature and pressure in the core will be sufficient to fuse hydrogen into helium. At this point the star is formed and its journey of stellar evolution begins as it enters the main-sequence (MS).

The main-sequence refers to the most prominent distribution of stars when one plots their effective temperature against their luminosity. The luminosity, L, of a star is defined (Tayler, 1994) as

$$L = 4\pi R^2 \sigma T_{\rm eff}^4 \,, \tag{1.1}$$

where R is the stellar radius, σ is the Stefan-Boltzmann constant and $T_{\rm eff}$ is the effective temperature. This $T_{\rm eff}$–L plane is referred to as the Hertzsprung-Russell (HR) diagram and serves as a vital tool for estimating the age and evolutionary stage of a star. A schematic HR diagram is plotted in Fig. 1.1. When a star enters the main-sequence it is at "zero-age-main-sequence" or ZAMS and stars spend the majority of their lives in this region. During this phase they are undergoing stable hydrogen fusion in the core and the pressure produced through this process provides the outward force opposing gravitational collapse. The balance

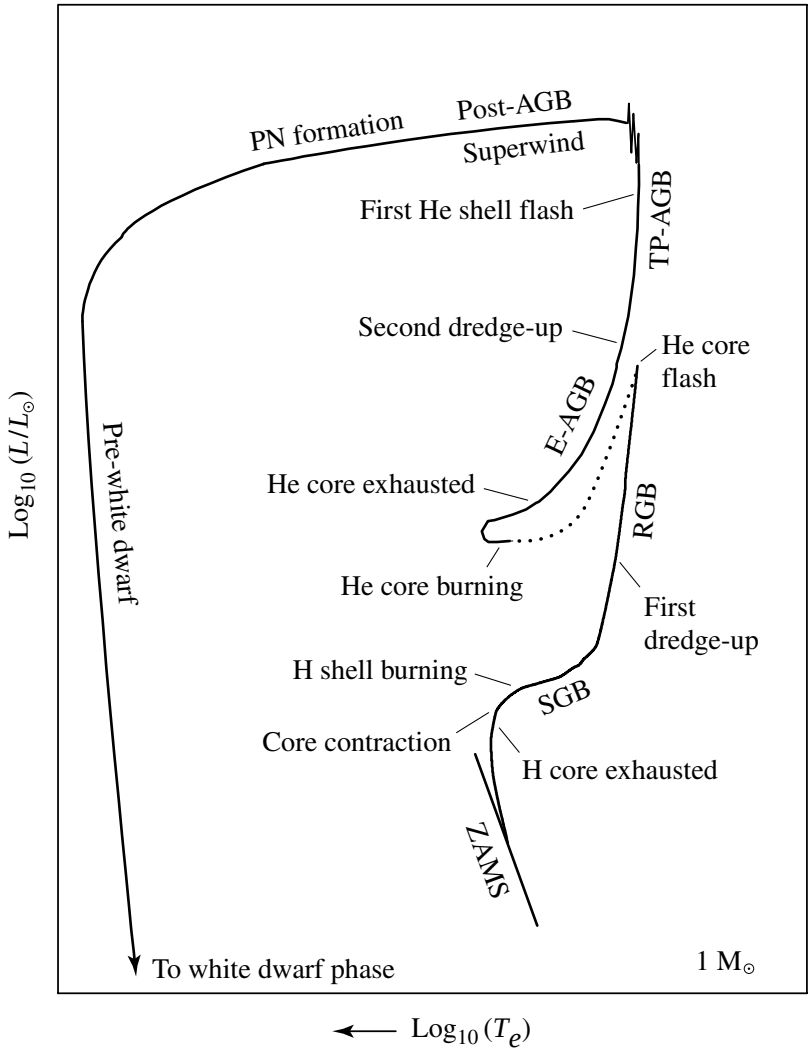

Figure 1.1: A schematic diagram of the evolution of a low-mass star of 1 $M_\odot$ from the zero-age main sequence to the formation of a white dwarf star. The dotted phase of evolution represents rapid evolution following the helium core flash. The various phases of evolution are labeled as follows: Zero-Age-Main-Sequence (ZAMS), Sub-Giant Branch (SGB), Red Giant Branch (RGB), Early Asymptotic Giant Branch (E-AGB), Thermal Pulse Asymptotic Giant Branch (TP-AGB), Post- Asymptotic Giant Branch (Post-AGB), Planetary Nebula formation (PN formation), and Pre-white dwarf phase leading to white dwarf phase. Figure and caption reproduced from Carroll & Ostlie (2006).

in any given layer between the outward pressure force and gravitational contraction is called the hydrostatic equilibrium and the ability of a star to maintain this balance depends on the stellar properties; primarily mass and metallicity.

A star with mass equivalent to that of the Sun ($M_\odot$) will spend approximately 10 Gyr on the main-sequence and the length of time a star spends in this phase is strongly dependent on (inversely proportional to) its mass. The following expression (Hansen & Kawaler, 1994) provides an estimate for the relation between main-sequence lifetime and stellar mass

$$\tau_{\rm MS} \approx 10^{10} \left(\frac{M}{M_\odot} \right)^{-2.5} \text{ years} \,, \tag{1.2}$$

where M is the stellar mass. This assumes a mass-luminosity relation such that

$$L \propto M^{3.5} \,. \tag{1.3}$$

This mass-luminosity relation is derived empirically for main-sequence stars in the mass range 2–55 $M_\odot$ (Harwit, 1988). The implication of Equation (1.2) is that, compared to the Sun, a star ten times more massive will exist on the main-sequence for a thousandth of the time. The initial mass of the star also has implications for the post-main-sequence evolutionary pathway of the stellar object and its ultimate fate.

Once a star has finished fusing the available hydrogen in the core the pressure opposing gravitational collapse is no longer present and a gravitational contraction of the helium core occurs. What happens next is mostly determined by the stellar mass. If the star is of extremely low mass ($\lesssim 0.23\ M_\odot$) it may evolve directly to a white dwarf (Adams & Laughlin, 1997). This is theoretical as this evolutionary pathway is predicted to take far longer than the current age of the universe. For stars with larger masses ($\gtrsim 0.23\ M_\odot$) the core contraction at the cessation of hydrogen fusion can provide sufficiently high temperature and pressure to trigger hydrogen-burning in the shell surrounding the helium core. In response to the core contraction the outer layers expand, in part to maintain thermal equilibrium, via the so-called *mirror principle* (Kippenhahn & Weigert, 1990). As the luminosity scales with surface area (Eq. 1.1) this expansion causes a large increase in brightness and thus the star quickly evolves off the main-sequence into the sub-giant branch (SGB).

As the outer layers expand they cool and eventually become fully convective at around 5000 K. At this point they have traversed the sub-giant branch (SGB) to reach the bottom of the red-giant branch (RGB). Stars ascend the RGB as a result of continued fusion of hydrogen in the shell. This increases the mass of helium in the core, which facilitates more efficient fusion of hydrogen. This feedback increases the core temperature and the outer layers expand and cool in response. This increase in size drives the increasing luminosity

characteristic of the RGB. Eventually temperatures in the helium core exceed the minimum required ($\sim 10^8$ K) to drive the fusion of helium via the triple-alpha process. For low-mass stars ($< 2\,M_\odot$) the helium cores are already degenerate at this point and the fusion is rapid producing a *helium flash*. For intermediate-mass ($\approx 2M_\odot$-$8M_\odot$) and massive stars ($> 8\,M_\odot$) the triple-alpha process starts before the core becomes degenerate resulting in a more gradual build up of carbon and oxygen in the core.

All low-mass, intermediate-mass and massive stars will enter the asymptotic giant branch (AGB) when the central helium reserves have been depleted. Evolution during the early AGB (E-AGB) is analogous to the RGB with now helium shell burning on top of a carbon/oxygen core. Via the mirror principle the outer layers of E-AGB stars expand in response to the shell burning observed as a luminosity increase. At the cessation of helium shell burning the thermal pulsing AGB (TP-AGB) stage begins. This brings additional hydrogen shell burning in the outer layers. Driven by stellar winds, mass-loss during the AGB phase may liberate up to $\approx$ 80% of the stellar mass into the ISM (Marigo et al., 2020), an effect which can be enhanced with thermal pulses (Wood et al., 2004). We will see in Chapter 5 that white dwarfs can provide a constraint on the mass-loss and hydrogen depletion during these late AGB thermal pulses.

Once the wind-driven mass-loss has depleted most of the stellar envelope the degenerate core is left surrounded by a *planetary nebula* (PN) comprising the stripped material. During this phase the core contracts and is subjected to gravitational heating. Once the core reaches $\sim 10^5$ K the star begins to cool as it enters the white dwarf phase. Low-mass and intermediate mass stars will evolve into white dwarfs with C/O cores. The fate of most massive stars is to continue burning increasingly heavy elements resulting in an iron core and evolving into a neutron star or black hole via a supernova explosion. However, the massive stars with the lowest mass ($\approx$ 8–10 $M_\odot$) may evolve into massive or ultra-massive white dwarfs with O/Ne/Mg cores (Camisassa et al., 2019).

1.1.3 Mass

Studies of the earliest classical white dwarfs in the 1910s revealed them to have densities 3–4 orders of magnitude larger than the Sun which was at the time not considered possible (Öpik, 1916; Eddington, 1927). Whilst this conundrum captivated astronomers, in 1925 Wolfgang Pauli discovered that multiple identical fermions cannot occupy the same quantum state (Pauli, 1925). The *Pauli Exclusion Principle* became one of the central tenets of quantum mechanics and implied that fermions (particles with half-integer spin) in the same space must occupy different energy levels or spin directions. Due to the discretization of available energy levels and the finite energy of a closed system this gives fermions at high densities an effective volume. In the following year Fermi and Dirac independently incorporated this

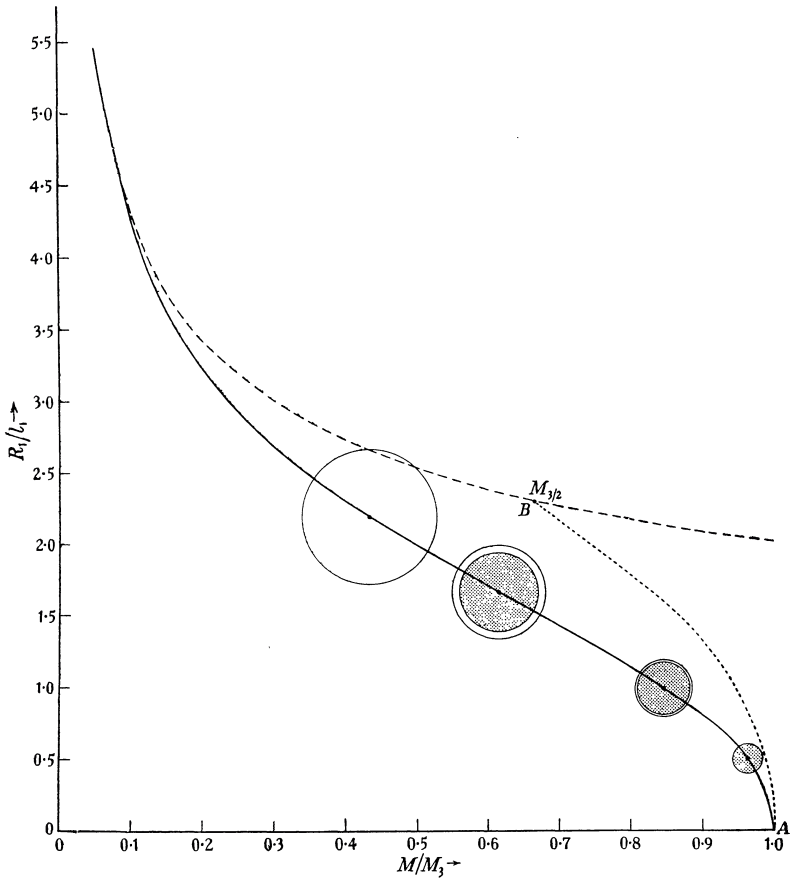

Figure 1.2: The solid curve represents the exact mass-radius-relation for the highly collapsed configurations. This curve tends asymptotically to the dashed curve as $M \rightarrow 0$. Figure reproduced from Chandrasekhar (1935).

physics into a statistical model describing a distribution of many identical fermions in the same system (Fermi, 1926; Dirac, 1926). White dwarf densities imply an extremely high density of electrons, one of the elementary fermions, and this lead Fowler (1926) to realise that the Fermi-Dirac statistics were required to describe the existence of such objects. It was then understood that white dwarfs must be supported by *electron degeneracy pressure*. This was a critical advancement in our understanding of white dwarfs and was swiftly followed by the discovery of another remarkable property of these compact objects.

Theoretical mass limit

The existence of an upper limit on the mass of a white dwarf was a conceptual breakthrough made by Anderson (1929) and Stoner (1930). It was already accepted that Fermi-Dirac statistics were required to explain the stability of an object with a typical white dwarf density of $\sim 10^5 \mathrm{g\,cm^{-3}}$, but they realised that in a sufficiently massive white dwarf the (predominantly unbound) electrons could have velocities approaching the speed of light. This motivated the incorporation of special relativity into the model of an electron degenerate gas, the key result of which was the existence of an upper limit on the mass of a white dwarf. The reason this upper limit is not typically attributed to Stoner or Anderson is that their models assumed the white dwarf to be a homogeneous sphere of uniform density. This led to predicted mass limits of 1.1 $M_\odot$ and 0.7 $M_\odot$, respectively, which we now know to be an underestimate. Relaxing this assumption, Chandrasekhar instead modelled the white dwarf as a polytrope which was known at the time to better represent stellar density profiles.

A polytrope is an expression, or equation of state, relating the pressure and density of a sphere such that

$$P \propto \rho^{(n+1)/n}\,, \tag{1.4}$$

where P is the pressure, ρ is the density and n is called the polytropic index. Thanks to the ubiquity of spherical objects in space this equation finds much utility in astrophysics with different polytropic-indexes fitting well the properties of different stellar objects. For example; neutron stars are often modelled with $0.25 < n < 1$ (Lattimer & Prakash, 2001; Raithel et al., 2016), red-giants with $n = 1.5$ and solar-type stars with $n = 3$ (Hansen & Kawaler, 1994). Chandrasekhar proposed a hybrid polytropic model combining polytropes of index $n = 3$ and $n = 1.5$ for the relativistic (high-mass) and non-relativistic (low-mass) regimes, respectively. In the relativistic regime this displayed the desired asymptotic behaviour with the radius tending to 0 as the mass approached some limit M_3. The mass-radius relations arising from this model are shown in Fig. 1.2 as presented by Chandrasekhar

(1935). The mass limit in this instance is defined by the author's Eq. 63 as

$$M_3 = 5.728 M_\odot / \mu^2 \,, \tag{1.5}$$

where μ is the nucleon–electron ratio in the interior. Assuming a core composition of C/O one can substitute $\mu = 2$ into this equation to find $M_3 = 1.432\,M_\odot$. This has essentially remained the canonical upper limit of white dwarf mass still used today which is why the *Chandrasekhar mass* is synonymous with this mass limit and this important result earned Chandrasekhar half of the 1983 Nobel Prize in Physics. A surprising consequence of employing an equation of state based on Fermi-Dirac statistics is that the radius of a white dwarf is inversely proportional to its mass. As such, if the mass of a white dwarf increases above the Chandrasekhar mass (M_3) the compact object will contract significantly and explode into a supernova, evolving into either a neutron star or a black hole. Whether or not this happens is largely determined by the progenitor mass on the main-sequence, the distribution of which we will consider now.

Initial masses

The mass of a white dwarf is largely determined by its initial mass on the main-sequence and thus its evolutionary pathway (see Section 1.1.2). Quantifying the distribution of masses in main-sequence stars is an active field of research borne from the work of Salpeter (1955) who developed the first initial mass function (IMF). Salpeter made an empirical fit to the cumulative distribution of those stars in the solar neighbourhood more massive than the Sun. This led to the conclusion that the distribution of masses in main-seequence stars was well described by

$$\phi(M) \propto M^{-\alpha} \tag{1.6}$$

where the constant exponent $\alpha = 2.35$ and the number of stars born in the mass range M to $M + dM$ is defined as $\phi(M)dM$. Shown in Fig. 1.3, Salpeter's model implies that the number of stars formed per mass interval drops away sharply with increasing mass. Coupled with the prediction that all stars less massive than $\approx 9\,M_\odot$ are expected to evolve into white dwarfs (Iben et al., 1997), it has been inferred that this is the expected end state for 97% of all stars. Refining the IMF has been the focus of many studies in the last half-century, particularly focused on low-mass stars with masses $< 1\,M_\odot$ (e.g., Miller & Scalo 1979; Kroupa 2001; Chabrier 2003 also shown in the figure) following the observation that the Salpeter IMF generally provides an over-prediction in this regime. Nonetheless the Salpeter IMF is considered an appropriate choice for white dwarf population studies (e.g., Tremblay et al. 2019b; Fontaine et al. 2001) as only those stars with masses $\gtrapprox 0.8\,M_\odot$ are likely to have formed into white dwarfs within a Hubble time.

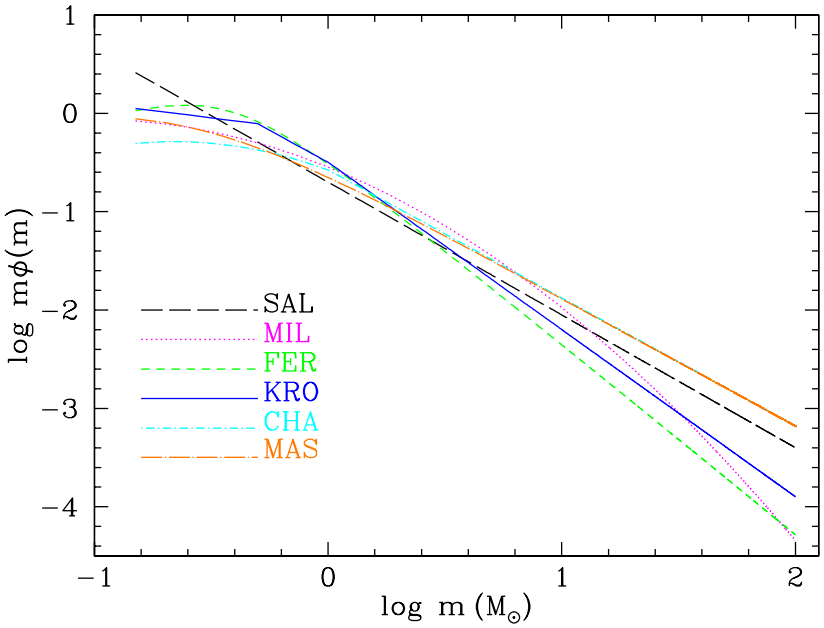

Figure 1.3: The initial mass functions defined via the classical functional forms employed in the literature, including those of Salpeter (1955); Miller & Scalo (1979); Ferrini et al. (1990); Kroupa (2001); Chabrier (2003); Maschberger (2013) labelled as SAL, MIL, FER, KRO, CHA, and MAS, respectively). Figure reproduced from Mollá et al. (2015).

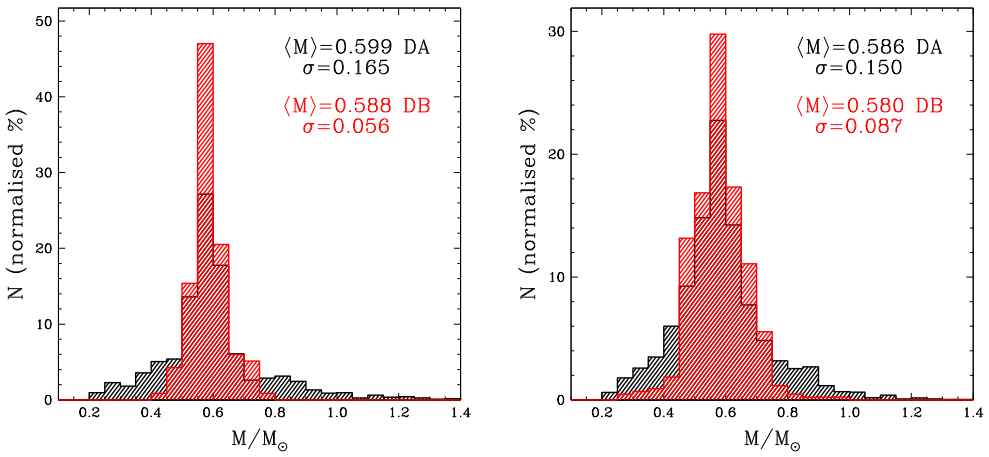

Figure 1.4: *Left:* *Gaia* photometric mass distributions for the (1145) DA white dwarfs in Gianninas et al. (2011) and the (116) DB and DBA stars in Rolland et al. (2018). All distributions have been renormalized to unity for an easier comparison of the different samples. *Right:* Similar to the left-hand panel but for the (2726) DA white dwarfs in SDSS DR7 and the (405) DB/DBA stars from SDSS DR12 (Koester & Kepler, 2015). Figure and caption reproduced from Tremblay et al. (2019a).

Final masses

For a given star, the evolutionary stages between the main-sequence and white dwarf phase typically liberate about 60% of the initial stellar mass into the ISM (Cummings et al., 2018). But despite the large range of initial masses expected to yield a white dwarf, when one considers the white dwarfs which have formed in the Milky Way there is a significant preference for the mass to be close to $0.6\,M_{\odot}$. This is illustrated by Fig. 1.4 where four distributions of white dwarfs with either hydrogen atmospheres (DA) or helium atmospheres (DB) are reproduced from Tremblay et al. (2019a). All four samples depict the sharply peaked distribution around $0.6\,M_{\odot}$. Given that the progenitors to these objects were once 0.8–10 $M_{\odot}$ main-sequence stars, the tendency for the white dwarf population to evolve to around $0.6\,M_{\odot}$ is quite a remarkable fact of nature. It has been shown that this sharp peak can be recovered with a combination of the Salpeter IMF, a constant star formation rate (SFR) and a suitable choice of initial-final mass relation (Tremblay et al., 2016b; Kilic et al., 2020).

Tremblay et al. (2019a) point out that the standard deviation of the DB mass distribution is significantly smaller than the analogous DA distribution, so whilst the mean masses of the two spectral classes are in agreement, the range of progenitor masses may be much narrower in the case of DBs. It was claimed by Kleinman et al. (2013b) that the large standard deviation in the DAs from the SDSS DR7 catalogue is partly due to a *high-*

mass bump at around 0.8 $M_{\odot}$, which the authors attributed to the result of stellar mergers. However, binary population synthesis models have recently shown that mergers cannot fully explain this feature and that crystallisation is a more likely explanation (Kilic et al., 2020).

Although white dwarfs exhibit a strong mass preference of $\approx 0.6\ M_{\odot}$ the existence of massive ($> 0.8\ M_{\odot}$) and ultra-massive ($> 1.1\ M_{\odot}$) white dwarfs is now well established: Limoges et al. (2015) found 8% of objects in the SUPERBLINK northern hemisphere 40 pc sample to have masses in excess of 1 $M_{\odot}$ and in the SDSS DR12 sample Kepler et al. (2016) found 94 white dwarfs above 1 $M_{\odot}$. The formation of such objects via isolated, single degenerate evolution is predicted for main-sequence stars of 6–9 $M_{\odot}$ (Camisassa et al., 2019), in which case it is expected that during the AGB carbon ignition can be triggered, leaving behind a predominantly O/Ne core with traces of Mg (Siess, 2006). If, however, an equally massive white dwarf is formed via a merger it is more likely to have a predominantly C/O core (Weidemann, 2003), meaning the white dwarf mass in this regime does not have a one-to-one correspondence with interior composition. The product of merging white dwarfs is of great interest to studies of Type 1a Supernovae but lies beyond the scope of this thesis.

The existence of O/Ne/Mg white dwarfs has been confirmed in classical novae systems based on the spectroscopic abundances of the outbursting material (Livio & Truran, 1994). However, determining the interior composition of an isolated, non-accreting white dwarf presents a greater challenge. One approach is to study the pulsating ultra-massive white dwarfs (e.g., Castanheira et al. 2010; Hermes et al. 2013) where asteroseismological models can predict pulsational properties; the periods of which are rather sensitive to the assumed composition of the interior (Camisassa et al., 2019). However, asteroseismological models are also highly sensitive to parameters such as hydrogen layer thickness and convective boundary treatment (Althaus et al., 2010a). We will now go on to consider the internal structure of a canonical white dwarf at 0.6 $M_{\odot}$ in more detail.

1.1.4 Structure

The stellar evolution of most stars ends at the white dwarf phase and, as we saw in the previous section, this typically results in a white dwarf of $\approx$0.6 $M_{\odot}$. In this case the progenitor was sufficiently massive to fuse helium into carbon and oxygen during the RGB. As the white dwarf forms the core is supported only by electron degeneracy pressure and the whole star is in a high density regime. The surface gravity of such an object is approximately 100,000 times that on the surface of the Earth and this leads to a discrete separation of material based on its atomic mass; the heavy elements sink to the core and in opposition those lighter float to the surface. Within 1–10 million years the white dwarf establishes a stable, onion-like structure with a degenerate core of C/O, a shell of He on top and a shell of H on top of that. By adopting a suitable equation of state the white dwarf structure can be modelled from

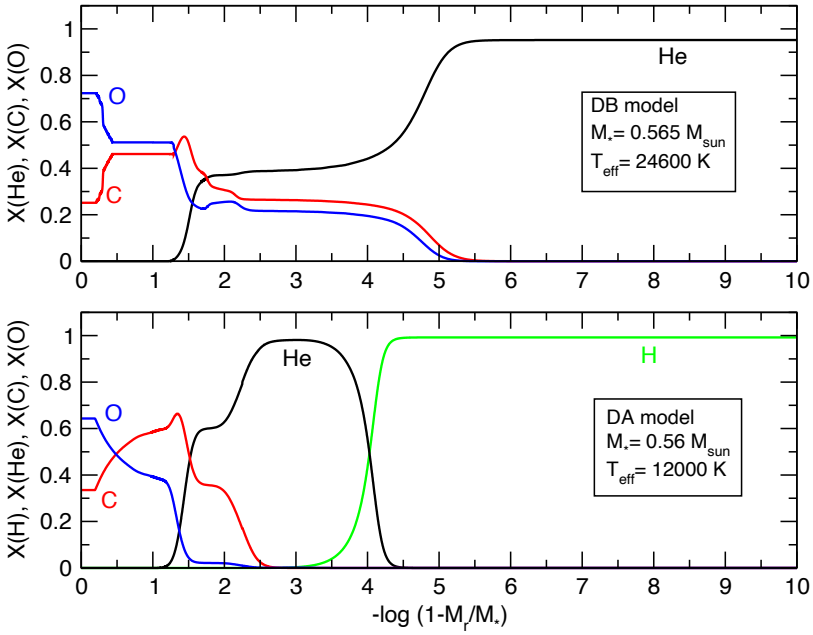

Figure 1.5: The internal chemical structure of a DA white dwarf at 12,000 K and a DB white dwarf at 24,600 K on bottom and top, respectively. Figure reproduced from Althaus et al. (2010a).

static calculations or evolutionary models. The result of the latter is shown in Fig. 1.5 for a hydrogen atmosphere (DA) the bottom panel.

If the star undergoes significant thermal pulses towards the end of the AGB (Herwig et al., 1999) up to all the hydrogen can be ignited before the white dwarf fully forms. Following the last thermal pulse, any remaining hydrogen envelope is expected to be removed by mass loss during the quiescent He-burning phase (Iben & Renzini, 1983). This can leave the white dwarf without its outer H shell, instead exposing the He shell underneath. After their formation and with temperatures of ~200 000 – 75 000 K, these stars are likely to be classified as the H-deficient PG 1159 stars (Hügelmeyer et al., 2007). As they cool it is likely these objects become spectral type DO (Unglaub & Bues, 2000; Althaus et al., 2005), where such stars are typically observed to have effective temperatures in the range ≈120 000 K–45 000 K (Hügelmeyer et al., 2007; Eisenstein et al., 2006). Once they reach temperatures ≲30 000 K, where the He I absorption lines dominate the spectrum, they become spectral type DB (Bergeron et al., 2011). The chemical blueprint of these relatively cool He-atmosphere white dwarfs (DB) is shown in the top panel of the figure. The structure of a white dwarf is sensitive to its mass which, as was discussed earlier, is typically around 60% less than that of its progenitor (Cummings et al., 2018) due to mass loss. This is true if the initial mass was between ≈0.5–8.0$M_{\odot}$. For very low mass progenitors ($\lesssim 0.5M_{\odot}$), mass

loss may play a role in creating low-mass helium white dwarfs through interactions with a large planetary companion (Nelemans & Tauris, 1998) or with a neutron star in a close binary system (Benvenuto & De Vito, 2005). Once a white dwarf has formed its structure will slowly evolve as a result of important physical processes which occur at different stages of its evolution.

1.1.5 Evolution and cooling

White dwarfs have proven to be excellent cosmochronometers (Fontaine et al., 2001) for two reasons; their cooling process is remarkably slow and their effective temperature is a monotonic function of age. We will explore these two concepts in the following.

The cessation of nuclear fusion on the AGB leaves behind a hot white dwarf with no stable mechanism for heat production. Its evolution then becomes dominated by cooling processes as the large thermal reservoir attempts to thermalise with the surrounding space. The dominant cooling mechanism throughout the white dwarf lifetime is radiation, whereby photons escape the star from the outer non-degenerate surface layers. Because of their intrinsically small surface area white dwarfs are very poor radiators meaning their cooling takes many times the current age of the universe. The cooling age $t_{\rm cool}$ is the white dwarf age from the AGB and for a given mass this can be inferred from the luminosity with the aid of an appropriate cooling model.

The first white dwarf cooling model was developed by Mestel (1952) who assumed a mostly isothermal white dwarf releasing its thermal energy by radiation. The isothermal assumption is well justified given the highly conductive nature of degenerate matter. In his model the age and luminosity are predicted to obey

$$t_{\rm cool} \propto L^{-5/7}\,, \tag{1.7}$$

where L is the stellar luminosity. Later work revealed that additional sources of luminosity were necessary for a complete description of the cooling process. We will briefly highlight three significant additions made to the physics of white dwarf cooling.

Neutrino cooling: First proposed by Chin et al. (1966) and Savedoff et al. (1969), it is now well-known that in young (hot) white dwarfs neutrino cooling provides a significant source of luminosity. Formed in the central region where the density is highest, neutrinos escape the white dwarf with minimal interaction (Althaus et al., 2010a) carrying with them a significant amount of energy. Strictly this effect breaks the isothermal assumption, producing a temperature a factor 2 lower in the centre (Hansen et al., 2015). As the white dwarf ages neutrino cooling ceases to provide a significant source of luminosity but may be important down to $T_{\rm eff} \sim 25,000\,{\rm K}$ (Winget et al., 2004). Direct detection of the neutrino

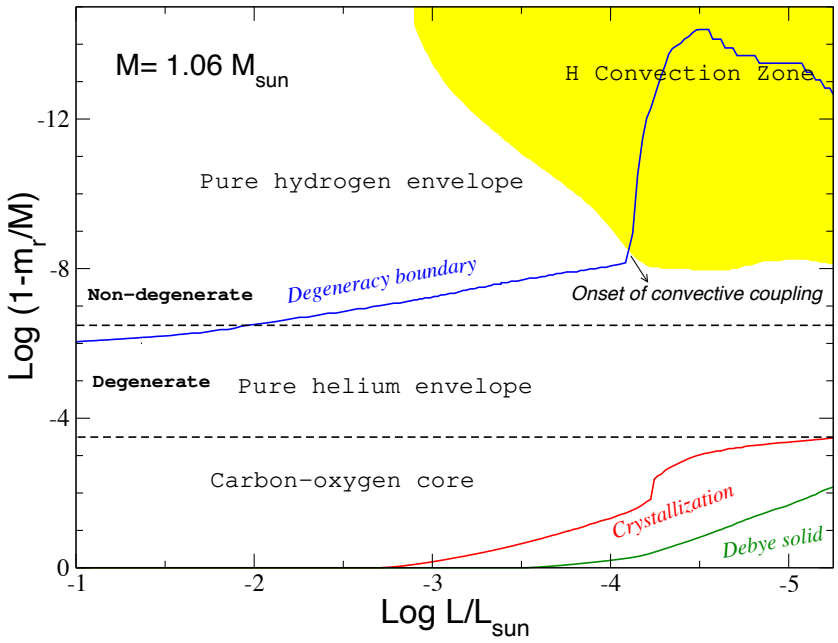

Figure 1.6: The logarithm of the outer mass fraction of an evolving massive white dwarf as a function of the surface luminosity. The location of the different chemical regions and the domain of the physical processes relevant for the white dwarf evolution are indicated. Figure and caption reproduced from Althaus et al. (2010a).

emission during white dwarf cooling is not currently feasible, but observational confirmation is provided by comparing observed and predicted luminosity functions (e.g., Hansen et al. 2015).

Gravitational contraction: Whilst the radius of a white dwarf is relatively stable, it may decrease by a half over the course of its lifetime (D'Antona & Mazzitelli, 1990; Althaus et al., 2010a). This gravitational contraction provides a non-neligible source of luminosity in young white dwarfs and becomes significant again at the onset of the Debye cooling phase (D'Antona & Mazzitelli, 1989). With the density increasing the central region of degeneracy encroaches on the non-degenerate surface layers. The predicted radial extent of the degenerate region is depicted in Fig. 1.6 at different evolutionary stages.

Crystallisation: At the beginning of the 1960s Abrikosov & Gor'kov (1960); Kirzhnitz (1960) and Salpeter (1961) independently concluded that materials with sufficiently high density to produce degenerate electrons can undergo a phase transition where the ions form a periodic lattice structure at cool temperatures. It was predicted that this would occur in the centre of old (∼1–10 Gyr) white dwarfs where the non-degenerate carbon and oxygen ions would gradually crystallise from inside-out, forming a body-centred cubic lattice structure and releasing latent heat in the process (van Horn, 1968; Salaris et al., 1997; Fontaine

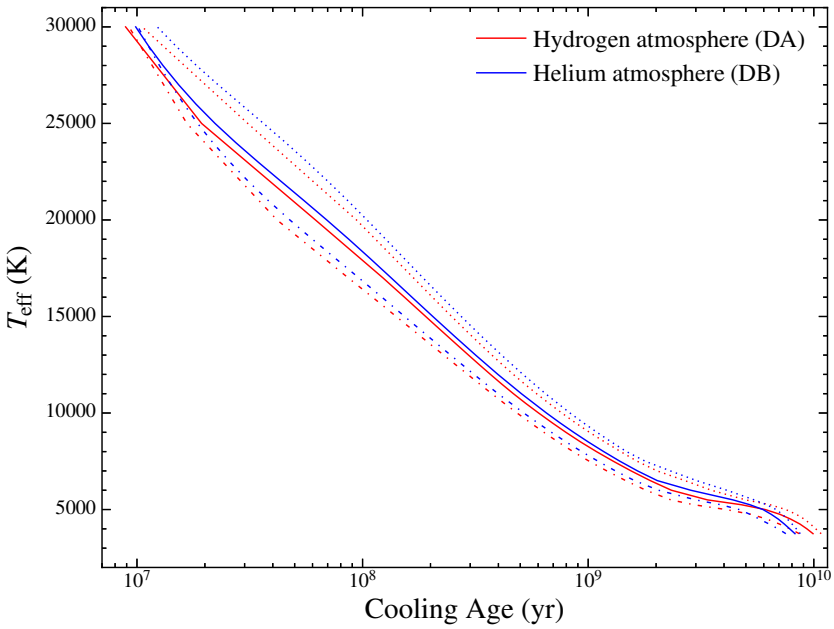

Figure 1.7: Cooling tracks for white dwarfs of mass (from bottom to top) 0.6 $M_\odot$, 0.7 $M_\odot$and 0.8 $M_\odot$ (Fontaine et al., 2001). Figure reproduced from Wilson (2017).

et al., 2001). Definitive observational evidence of this delay in cooling was seen for the first time following the second data release of the *Gaia* mission (Tremblay et al., 2019b). The crystallisation front is also shown in Fig. 1.6.

Incorporating these physical processes, sophisticated cooling models today allow relatively precise determinations of white dwarf ages for a given mass. Some of these models are shown in Fig. 1.7. Such models have been exploited in numerous studies to determine galactic kinematics (e.g., Pauli et al. 2006; Anguiano et al. 2017) and the age of the Galactic disk (Leggett et al., 1998; Winget et al., 1987; D'Antona & Mazzitelli, 1978). We will now consider in more detail the transport of heat within the white dwarf envelope.

1.1.6 Atmospheric energy transport

The degenerate core of a white dwarf is able to transport energy with negligible impedance but surrounding this core is a non-degenerate, optically thick layer which can be 2–3 orders of magnitude cooler than the degenerate core. (Fontaine et al., 2001). The drop in temperature occurs mostly in the non-degenerate envelope creating a very large radiative temperature gradient with respect to radius. It is thus crucial to have an accurate model describing the physical processes responsible for energy transport through these layers. This is either dominated by *radiative* or *convective* processes at early or late stages, respectively. In the following we consider the physics of these two regimes.

Radiative atmospheres

In young white dwarfs energy is transferred through these surface layers – from the core to the surface – by radiation. The path of a given photon is greatly hindered by absorption and scattering processes, the physics of which is encapsulated in an *opacity*; dependent on the intrinsic photon energy (frequency) and the nature of the interactions with the constituents of the atmosphere. This cascade of absorption and re-emission is formalised in the radiative transfer equation, providing one knows the opacity of the stellar atmosphere.

The work of Eddington (1926) on the radiative equilibrium of stellar interiors led to the understanding that white dwarf stars have opacities dominated by *bound-free*, *bound-bound*, *free-free*, and *scattering* interactions. Absorbed by a H or He atom, in *bound-free absorption* a photon liberates an electron orbiting the atomic nucleus. This process is reversed if an electron is later reabsorbed by an ion (e.g., H^+) causing it to lose energy via the emission of a photon. If the photon is less energetic *bound-bound* absorption may occur, whereby the electron is elevated to a higher energy level whilst remaining bound to the nucleus. In *free-free absorption* an unbound electron absorbs a photon during a collision with an ion, gaining energy in the process. Finally, *scattering* occurs when a photon interacts with a charged particle effectively altering its trajectory and intrinsic energy. A photon of given frequency may be absorbed or scattered via any of these processes if its trajectory comes within the absorption cross-sectional area of an individual atom or electron. The higher the local density, the more likely this is to occur, further impeding the journey of a given photon. The combination of absorption cross-sections and atmospheric density is expressed by an *opacity* which implicitly determines the mean time it takes for a photon to escape the white dwarf.

In the regime where bound-free and free-free absorption dominate it was shown by Kramers in 1923 (Carson et al., 1968) that the mean opacity contribution for a given process can be written as

$$\kappa \propto \rho T^{-7/2} \tag{1.8}$$

where κ is the opacity in units of $\mathrm{cm}^2\,\mathrm{g}^{-1}$ and ρ and T are the density and temperature, respectively. This is known as *Kramer's opacity law* and this was the treatment of opacity adopted in the cooling model of Mestel.

Generally when treating the atmospheric properties one considers as an independent variable the mean opacity over the full electromagnetic spectrum. Because the emergent flux is not uniform in frequency the mean is typically weighted by an appropriate choice of continuum spectrum. The white dwarf continuum is relatively well-described as a blackbody and thus a grey opacity (independent of frequency) can be derived using the Planck distribution. One such grey opacity is the *Rosseland mean opacity* which is defined

as

$$\bar{\kappa} = \frac{\int_0^\infty u(\nu, T) d\nu}{\int_0^\infty \kappa^{-1} u(\nu, T) d\nu} \tag{1.9}$$

where ν is frequency and $u(\nu, T) = \partial B(\nu, T)/\partial T$ is the temperature derivative of the Planck function $B(\nu, T)$. The Rosseland mean opacity is appropriate when the radiative transport equation is treated in the *diffusion approximation*. This approximation assumes that the photon mean free path is sufficiently small that the local radiance is mostly isotropic.

Outside the core the density decreases dramatically as a function of radius and, depending on the cooling age, below $\rho \sim 1$ g cm^{-3} the degeneracy is lifted (Fontaine et al., 2001). At this point the envelope constituents are able to absorb photons and the opacity becomes very large, greatly reducing the mean free path. In the outermost layers – those containing only $\sim 10^{-14}$ of the total white dwarf mass – the density has decreased to $-5 \lesssim \log \rho/[\mathrm{g\,cm^{-3}}] \lesssim 0$ and here the mean free path increases enough to allow the majority of emitted photons to escape. The point from which $\approx 2/3$ of photons escape is usually used to define the *photosphere* and is equivalently defined as the radius at which the optical depth is of order unity ($\tau \approx 1$). The optical depth at distance, d, below the surface is the product of opacity, local density and depth from surface such that $\tau = \kappa \rho d$. Optically thick and thin media are defined by large (> 1) and small (< 1) optical depths, respectively. The Rosseland mean optical depth, τ_R, is used throughout this thesis to study the outermost layers.

Radiation prevails as the dominant process of atmospheric energy transport for the first ~10–100 Myr of white dwarf evolution. Over this time the white dwarf is gradually cooling via the processes discussed in the previous section until eventually a small convection zone forms in the outermost layers. In the following we will consider in more detail the evolution of this surface convection zone.

Convection

The criterion for convective stability was defined by Schwarzschild (1906) as

$$\nabla_{\mathrm{ad}} > \nabla_{\mathrm{rad}} \tag{1.10}$$

where ∇_{ad} and ∇_{rad} are the adiabatic and radiative temperature gradients, respectively. The intuition behind this expression arises by considering a radiative atmosphere where a parcel of fluid is perturbed adiabatically (i.e., without energy exchange) to a region of lower density – i.e., towards the surface. If the temperature of that parcel is lower (or equivalently that its density is higher) than its new surroundings the parcel will return towards its original position. This is the scenario if ∇_{ad} is larger than ∇_{rad} and the system can be described as

being *stable against convection*. If on the other hand ∇_{ad} is smaller than ∇_{rad} the parcel will be warmer (or less dense) than its new surroundings and continue to rise. This is the requirement for convective instabilities to arise.

As the white dwarf cools, previously ionized atoms and electrons in the surface layers begin to recombine. The once ionized gas thus becomes only *partially ionized* facilitating more photon scattering and absorption events which increases the heat capacity of the gas. This drastically reduces the adiabatic temperature gradient until at some point it is exceeded by the radiative temperature gradient. In this regime Eq. 1.10 is no longer satisfied and a superficial convection zone emerges. It is initially energetically inefficient because, despite the presence of advective flows, very little of the total flux is carried convectively. In DA white dwarfs a convection zone emerges around 18,000 K (Cunningham et al., 2019) and in DBs this occurs around 60,000 K (Bergeron et al., 2011). As the star cools the partial ionization front extends deeper into the star. The convection zone grows in mass and the fraction of the total flux carried by convection increases dramatically. In DAs and DBs convection becomes reasonably efficient at ≈12,000 K and 32,000 K, respectively (Cunningham et al., 2019; Cukanovaite et al., 2019b). We return to this in more detail in Section 3.4. The growing surface convection zone of a massive white dwarf is shown in Fig. 1.6, whilst Fig. 1.8 shows the evolution of the convection zone in DA and DB atmospheres. After the convection zone emerges it will grow monotonically in mass until the base of the convective region reaches the degenerate layers, a significant event in white dwarf evolution called *convective coupling* (Fontaine et al., 2001).

Convective coupling occurs in white dwarfs with effective temperatures of $\approx 6000 \pm 300$ K (see Fig. 6 of Fontaine et al. 2013). By this point in the evolution the convection zone is near-adiabatic meaning that most of the flux is being carried convectively and thus leads to a strong coupling of the surface layers and the internal thermal reservoir.

In main-sequence stars the strongest observational evidence for convection is that of solar granulation. The properties of this granulation has been well modelled with 3D hydrodynamic simulations (Stein & Nordlund, 1998). The primary evidence for the existence of white dwarf surface convection zones is the impact they have on evolutionary pathways when included in the modelling. van Horn (1970) states that the presence of a convective envelope lowers the temperature at the base of the non-degenerate region by a factor 4, directly impacting the luminosity and thus evolution of the white dwarf.

The convective turnover timescale for white dwarfs is on the order $t_{cv} \sim 1$ s. Given the long evolutionary timescale it is not feasible to include this process in detail within a white dwarf cooling model. This problem was tackled by Prandtl & Tietjens (1925) with the development of mixing length theory (MLT). In this model one of the free parameters, α, is used to define a characteristic length over which it is assumed that a displaced parcel

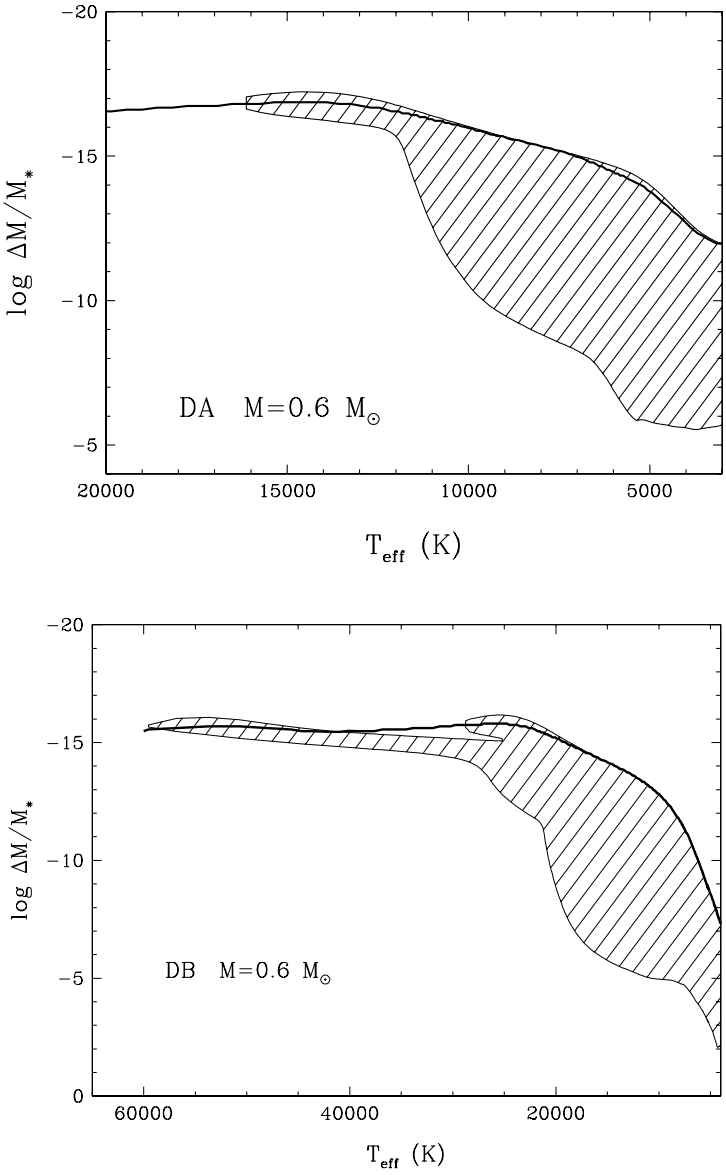

Figure 1.8: *Top*: Location of the hydrogen convection zone (hatched area) as a function of $T_{\rm eff}$ in a 0.6 $M_{\odot}$ DA white dwarf using the mixing length theory prescription of convection. The y-axis expresses on a logarithmic scale the mass fraction ΔM above a certain point with respect to the total mass of the star $M_{\star}$. The thick solid line indicates the location of the photosphere. *Bottom*: Similar to the top panel but for a 0.6 $M_{\odot}$ DB white dwarf using the ML2/α=0.6 version of the mixing length theory. Figures reproduced from Dufour et al. (2007) and Bergeron et al. (2011) on the top and bottom, respectively.

of fluid will preserve its properties before equalizing thermally with its new surroundings. This mixing length, l, is usually expressed in the form

$$l = \alpha H_P \,, \tag{1.11}$$

where H_P is the pressure scale height which is defined as the distance over which the pressure changes by a factor e, and α is a free parameter. This formalism provides an approximate 1D description of the transport of energy inside a convection zone and, despite being developed as a “rough approximation" by its designer, has been utilised almost ubiqitously in astrophysical models because of its computational simplicity. Convection is prevalent throughout stellar evolution – in particular during the CNO cycle in massive stars (Böhm-Vitense, 1992; Salaris & Cassisi, 2005) and during nuclear burning on the AGB (Timmes et al., 1994; Siess, 2006; Lecoanet et al., 2016) – and so evolution codes have relied upon this model of convection (e.g. Kovetz et al. 2009; Paxton et al. 2015). These powerful stellar evolution codes have facilitated many astonishing results but there is significant evidence to suggest that mixing length theory is not appropriate in some contexts (Stancliffe et al., 2015; Aerts, 2019). A solution to this problem is considered in detail in Chapter 3 but I will introduce the conundrum briefly in the following.

An alternative expression of the Schwarzschild criterion (Eq. 1.10) is based on the gradient of entropy such that a medium can be considered convectively unstable if

$$\frac{ds}{dr} < 0 \,, \tag{1.12}$$

where s is the entropy and r is the radius (increasing outwards). In this manner a convection zone is defined by a region with negative entropy gradient and one of the shortcomings of mixing length theory is that it does not predict convective velocities outside of this region, a scenario that we know to be unphysical.

Evidence to suggest that the structure of a convective region cannot be so neatly defined first came first from meteorology where observational (Priestley & Swinbank, 1947) and theoretical (Deardorff, 1961, 1966) studies suggested that the convective velocities do not immediately vanish outside of the formally unstable layers. This has also been confirmed in an astrophysical context (Spiegel, 1963; Roxburgh, 1978; Zahn, 1991) and, with the help of multi-dimensional simulations, in a white dwarf specific context (Freytag et al., 1996; Tremblay et al., 2015a; Kupka et al., 2018; Cunningham et al., 2019). The latter is the main focus of this thesis and will be considered in more detail in Chapters 2 & 3. We will now outline the various spectral appearances of white dwarfs detailed in the literature.

Table 1.1: Spectral types of white dwarfs reproduced from Table 1 of McCook & Sion (1999)

Spectral Type	Characteristics
DA	Only Balmer lines; no He I or metals present
DB	He I lines; no H or metals present
DC	Continuous spectrum, no lines deeper than 5% in any part of the electromagnetic spectrum
DO	He II strong; He I or H present
DZ	Metal lines only; no H or He lines
DQ	Carbon features, either atomic or molecular in any part of the electromagnetic spectrum
P	Magnetic white dwarfs with detectable polarization
H	Magnetic white dwarfs without detectable polarization
X	Peculiar or unclassifiable spectrum
E	Emission lines are present
?	Uncertain assigned classification; a colon (:) may also be used
V	Optional symbol to denote variability

1.1.7 Spectral types

Since their discovery over a century ago it has become resoundingly clear that white dwarfs possess pristine atmospheres of hydrogen or helium. Approximately 75–80% have an outer layer comprised almost entirely of hydrogen whilst the remainder instead possess a helium outer layer. This difference can be discerned with a spectroscopic observation which provides the frequency dependence of the emergent flux. In the case of single white dwarfs the continuum is expected to be relatively blackbody-like, but at certain wavelengths photons interact with the constituents of the envelope through absorption and scattering processes outlined previously.

If a white dwarf spectrum exhibits only absorption lines which can be attributed to hydrogen transitions (e.g., Lyman and Balmer lines) then the white dwarf is classified as a DA and if it shows only He I lines then it is classified as a DB. In some cases the spectral appearance does not reveal the atmospheric composition so clearly. For instance, below $\approx$ 12000 K the He absorption is significantly reduced and in this regime a pure He atmosphere white dwarf will appear to have no spectral absorption features. This also applies to H atmospheres below $\approx$ 6000 K and these featureless spectra are classified as DC, where the C indicates a continuous spectrum.

Table 1.1 shows the predominant spectral types used in the white dwarf literature.

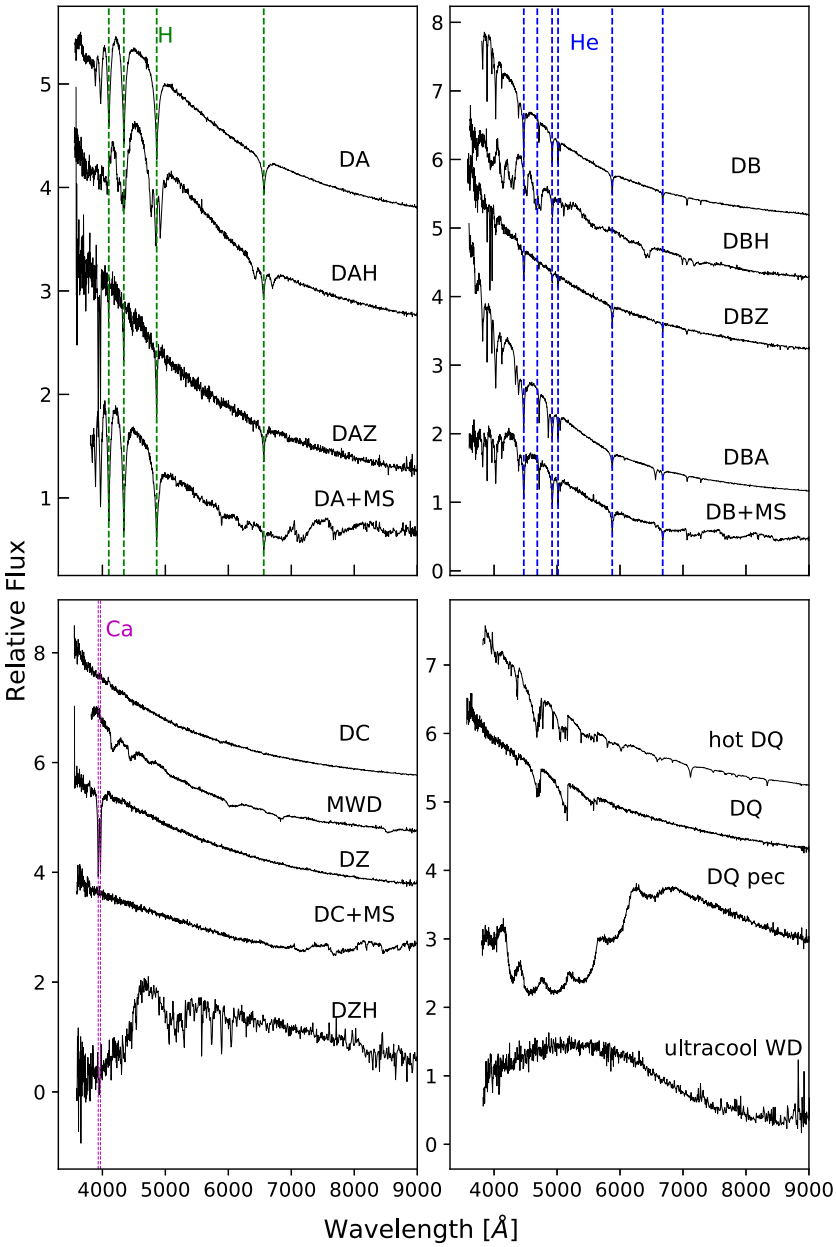

Figure 1.9: Representative SDSS spectra of the different white dwarf subclasses. The spectra have been offset vertically for visualization. Figure and caption reproduced from Gentile Fusillo et al. (2019a).

Each spectral type can be combined, such that a DBA white dwarf indicates a white dwarf with a predominantly He atmosphere with some H features in its spectra. White dwarfs with absorption lines of heavy metals are given a letter Z such that a DAZ is hydrogen-rich with photospheric metals, a DBZ is helium-rich with metals and a DZ is likely a cool He-rich white dwarf with metals. Fig 1.9 shows the characteristic spectra of eighteen spectral types taken with SDSS. These include carbon-rich white dwarfs: the DQs with absorption from either C I or molecular C_2, the hot-DQs with C II lines and the DQ peculiar stars with blue-shifted Swan bands from C_2. Also shown are magnetic (H) variations of the common spectral types and blended spectra of a white dwarf with a main-sequence companion. Of all these various white dwarf types those with metal-pollution (Z) are most pertinent to this thesis. We will consider these more closely in the following.

1.2 Metal-polluted white dwarfs

The paradigm that has been presented so far is that white dwarfs are the dense tombstones left behind at the end of stellar evolution and that this density leads to a marked chemical stratification ordered by atomic mass. The atmospheres of such objects are then a pristine shell of either H or He, but the third white dwarf to be discovered contradicts this picture somewhat. The third closest white dwarf to the Sun, van Maanen 2 was discovered by van Maanen (1917) and, although it was known to be a white dwarf, it was many decades before it received its current classification as a *metal-polluted* white dwarf. Farihi (2016) confirmed that the spectra taken in 1917 showed metal absorption lines corresponding to calcium (see Fig. 1.10) making that observation the first evidence of metal pollution in white dwarfs.

Approximately 25–50% of white dwarfs today show clear evidence of metal pollution in their atmospheres (Koester et al., 2014), a fact at odds with the idea that white dwarfs possess pristine atmospheres. By definition metals have a higher atomic mass ($Z > 2$) than the constituents of the white dwarf atmosphere and they should thus sink to the core on short timescales (Schatzman, 1945). Metals observed in warm white dwarfs ($\gtrsim 30\,000$ K) are likely to be supported by radiative levitation, and thus their origin could be primordial (left over from stellar evolution) or the result of accretion. However, below $\approx$30 000 K, the effects of radiative levitation are expected to become significantly less dominant. Indeed, from extensive spectroscopic studies over the last two decades it is now clear that the origin of metal pollution in white dwarfs below $\approx$30 000 K cannot be primordial, i.e., the metals must have arrived at the surface of the white dwarf after it was formed. It is now well-accepted that the source of the vast majority of this material is the rocky and gaseous remnants of evolved exoplanetary systems, a concept which will be considered in more detail in Chapter 3. In the following we will consider the evolution of planetary systems and how metal-polluted

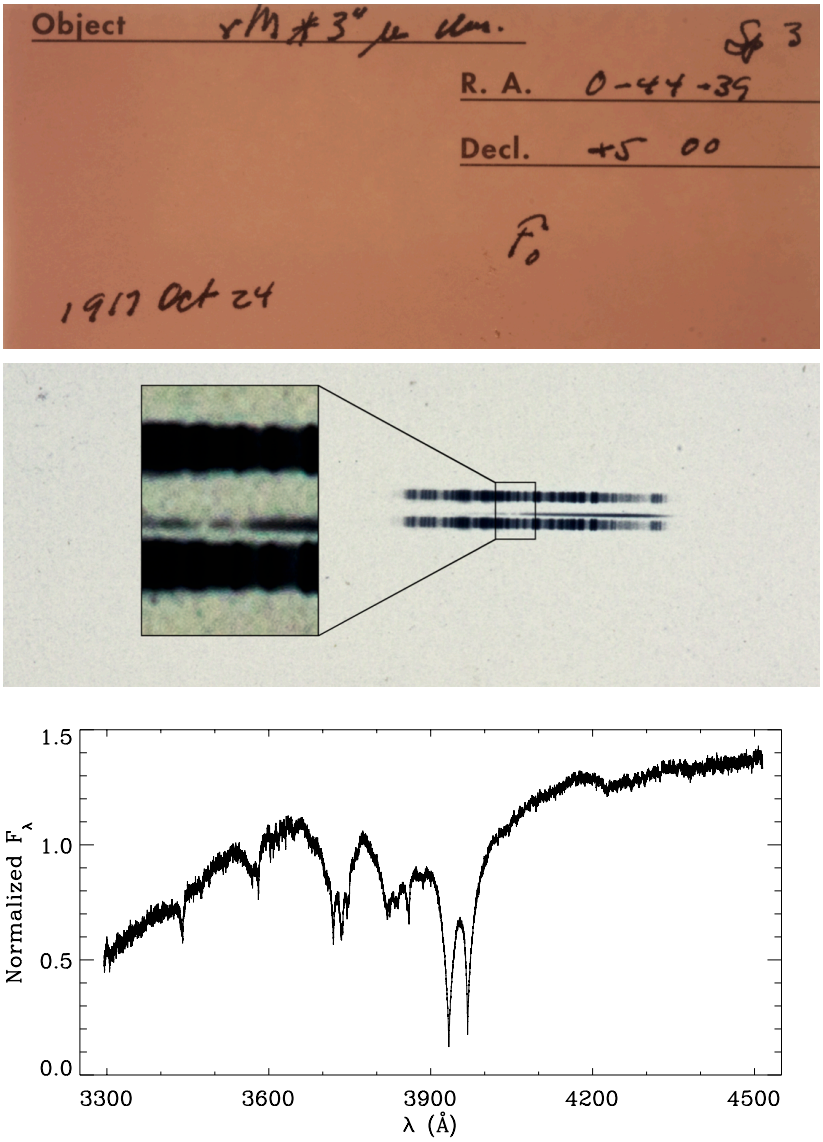

Figure 1.10: The prototype metal-enriched white dwarf vanMaanen 2 (vMa 2). Upper panels: The 1917 photographic plate spectrum of vMa 2, and plate sleeve with handwritten notes by observer W. S. Adams (van Maanen, 1917). Box highlighted are the strong Ca II H and K Fraunhofer lines, and are relatively easy to see in the century old spectrum. Lower panel: An optical spectrum of vMa 2 taken with UVES on the Very Large Telescope (VLT). All salient features are absorption due to Fe, Mg, or Ca. Figure and caption reproduced from Farihi (2016).

white dwarfs come to be.

1.2.1 Fate of planetary systems

When the Sun exhausts its central hydrogen reserves in about 10 Gyr it will begin its stellar evolution as detailed previously; evolving through the RGB, onto the AGB and eventually into a white dwarf. But what will be left of the Solar System at this end stage of life and will Earth survive?

By the end of the RGB the radius of the Sun is likely to increase by two orders of magnitude (Pols et al., 1998). It currently stands at 7×10^5 km and one astonomical unit (AU) – the orbital radius of the Earth around the Sun – is equivalent to 1.5×10^8 km. The Sun should thus expand to a radius of 0.84 AU, just shy of the orbital radius of Earth, and in the process lose up to $\approx 50\%$ of its mass (Marigo et al., 2020). This mass loss will cause the planetary orbits to increase but the expanding Sun will almost certainly engulf the closer in planets; Mercury and Venus. It is still somewhat of an open question whether Earth will survive this phase of stellar evolution (Veras, 2016b), whilst the remaining planets are expected to remain intact and in orbit around the degenerate white dwarf. If the Earth is not engulfed during the RGB, it is likely the friction and loss of angular momentum during the mass loss may be sufficient to tidally disrupt the Earth into smaller rocky planetesimals (Schröder & Connon Smith, 2008). In this scenario it is possible that the planetesimals can be scattered into the white dwarf (Veras et al., 2017) or form a disk of dust or gas from which the white dwarf could steadily accrete. Such systems have been observed by the detection of gaseous and debris disks via numerous methods, such as; the transit method (e.g., WD1145+017; Gänsicke et al. 2016), doppler tomography (e.g., SDSS1228; Manser et al. 2020), and the detection of infrared excess consistent with scattering from a disk (e.g., Fig. 1.11 and Farihi et al. 2017).

The prevalence of metal pollution in white dwarf atmospheres is consistent with the mean occurence rate of planets around main-sequence stars. It was recently shown that on average every other main-sequence star hosts a planet (Cassan et al., 2012) and spectroscopic observations of polluted white dwarfs offer the only feasible way to measure the bulk composition of their interior (Zuckerman et al., 2007). This technique requires a detailed understanding of the journey of heavy metals once they reach the white dwarf envelope.

1.2.2 Accretion-diffusion

The first theoretical study of trace metals in white dwarf atmospheres was made by Schatzman (1945) who realised that, due to gravitational settling, metals would sink into deeper,

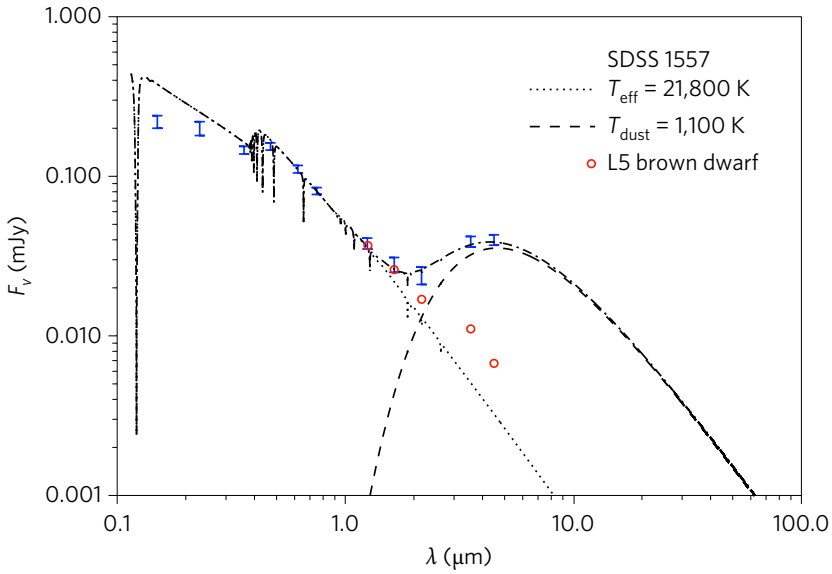

Figure 1.11: Spectral energy distribution. Multi-wavelength photometric data for SDSS 1557 are plotted as blue error bars, with the stellar flux from a pure hydrogen atmospheric model shown as a dotted line. Overlain as a dashed line is a 1,100 K blackbody fitted to the strong, infrared dust emission, and an L5-type brown dwarf is shown as red circles; any companion earlier than L3 is ruled out by the photometry below 2 μm. The measured 4.5 μm flux from the system is between five and six times brighter than any allowed companion, and hence must be due to circumbinary dust. Figure and caption reproduced from Farihi et al. (2017).

sub-photospheric layers on very short time scales. If this were the only process going on very few metal-polluted white dwarfs would have been discovered so the observations of metal pollution implied that one or more processes must conspire to oppose gravitational settling.

In the case of cool white dwarfs, the presence of a convection zone effectively opposes gravitational settling by homogenizing the surface layers. The gravitational settling is then governed by the diffusive physics at the base of the convection zone. This physics is non-trivial and developing a comprehensive model of the diffusion in these deeper layers took a considerable research effort.

A general formalism of the time-dependent diffusion of matter was given by Burgers (1969) with a partial differential equation describing the motion of a given field subjected to a *diffusion coefficient*. The first binary diffusion coefficients were presented by Chapman & Cowling (1970) who derived an analytic expression for the diffusion of a trace element through a pure background of some other element. Paquette et al. (1986a) found that the analytic formulae of Chapman & Cowling produced systematic errors in the regime of the dense plasmas typical of white dwarf envelopes and, improving upon this model, it was shown that Columb interactions and thermal diffusion were required to model the carbon dredge-up process in white dwarfs (Pelletier et al., 1986). In the same year (Paquette et al., 1986b) provided binary diffusion coefficients for C, N, O, Mg, Ca, and Fe, finding that, contrary to popular belief, the diffusion time scale possesses minimal dependence on the atomic mass.

Through these prolonged research efforts it became clear that the diffusion timescales in young white dwarfs were too short to maintain metals at the surface and that the presence of a convection zone could not reverse the gravitational sedimentation (e.g., Fontaine & Michaud 1979; Dupuis et al. 1992). The presence of metals thus necessitated ongoing accretion and led to the development of the *accretion-diffusion scenario* where a continuous or recurring accretion process replenishes metals in the surface layers as they sink. This model was first presented by Dupuis et al. (1992) and expanded later by Koester (2009) where they consider a continuously accreting white dwarf. In this scenario it is shown that after a few diffusion timescales the atmospheric abundance of a trace metal will reach a steady state such that

$$X(el) = \frac{\tau(el)\dot{M}(el)}{M_{\rm cvz}}\,, \tag{1.13}$$

where $X(el)$ is the abundance of a given element, τ is the diffusion timescale, $\dot{M}$ is the accretion rate and $M_{\rm cvz}$ is the mass of the convection zone. In Fig. 1.12 the diffusion timescales of Ca and Fe presented by Koester (2009) are shown at the base of the convective region for H- and He-dominated atmospheres. In the absence of a convection zone (for

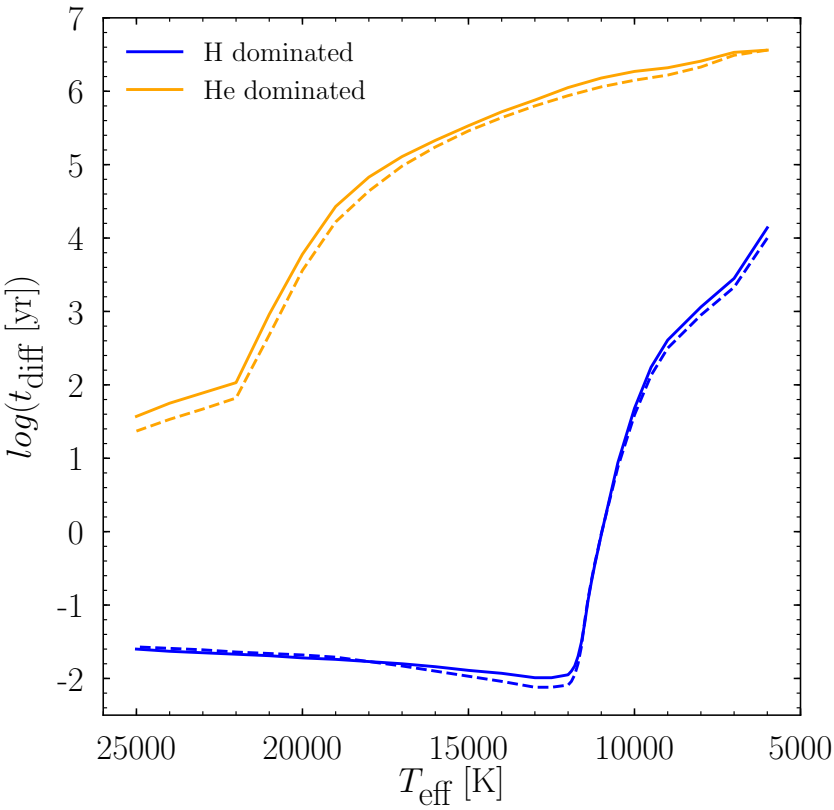

Figure 1.12: The diffusion timescales of Ca (solid) and Fe (dashed) as a function of effective temperature for DA (blue) and non-DA (orange) white dwarfs. Diffusion timescales are the results of calculations present in Koester (2009). Figure and caption adapted from Manser (2018).

the warmer white dwarfs) the uppermost diffusing layer is defined at an optical depth of $\tau = 5$. With knowledge of the diffusion timescale and mass of the convection zone, this model allows the inference of an accretion rate from the spectroscopic abundance. This has facilitated numerous studies on the accretion rates (and total accreted masses) onto white dwarfs (Bergfors et al., 2014; Farihi et al., 2016) and the bulk composition of evolved exoplanetary material (Xu et al., 2014, 2019; Farihi et al., 2016).

For white dwarfs with surface convection zones the accretion rates and total accreted masses are explicitly dependent on the size (or mass) of the convection zone. Typically this is derived using the approximate mixing length theory model of convection. Chemical abundances and atmospheric parameters (Teff, log g) are also often derived with these 1D models. One of the main aims of this thesis is to model convection using instead the physics of first principles with a multidimensional treatment and to assess the impact of these results, compared to the 1D models, on the accretion-diffusion scenario. This is

covered in considerable detail in Chapter 3 where the importance of a proper treatment of convection will be shown. Asides from convective regions there are additional processes against gravitational settling that one should also consider.

Additional processes opposing sinking

In younger white dwarfs with radiative atmospheres it was predicted that heavy elements, subjected to frequency-dependent radiation pressure, could be suspended at the surface (Vauclair et al., 1979; Fontaine & Michaud, 1979). Known as *radiative levitation*, this process was used to explain the unusual detection of atmospheric C, N and Si in EUV spectroscopy of young white dwarfs such as the hot (≈31,000 K) DA white dwarf Feige 24 (Vennes et al., 1989). With this as motivation, the radiative levitation model in white dwarfs was formalised by Chayer et al. (1995a,b). The authors calculated the interaction of radiative forces with many elements, namely: C, N, O, Ne, Na, Mg, Al, Si, S, Ar, Ca, and Fe, and since then many hot polluted white dwarfs have been discovered but in some cases photospheric abundances presented a disagreement with predicted values. A sample of 89 hot hydrogen dominated white dwarfs with temperatures between 16,000–77,000 K were analysed by Barstow et al. (2014). Although measured abundances of C, Si and P were in general systematically lower than those predicted by radiative levitation calculations, the study provided confirmation that radiative levitation remains the dominant process against gravitational settling in hot white dwarfs.

It has also been proposed that additional mixing processes may be relevant at the surface of a white dwarf triggered by the presence of a chemical gradient. A chemical gradient (∇_μ) can promote additional mixing instabilities, depending on the direction of the gradient, defined by the Ledoux criterion (Ledoux, 1947). If the chemical gradient follows the density gradient then *semi-convection* will occur. If the chemical gradient goes against the density gradient then *thermohaline mixing* may occur. The Schwarzschild and Ledoux criteria defining these mixing processes are depicted in Fig. 1.13. This process has been studied with 1D simulations in the context of polluted white dwarfs (Bauer & Bildsten, 2018, 2019). This thesis predominantly focuses on pure, convective atmospheres and those with only trace metals where one can take the limiting case as the chemical gradient tends to zero ($\nabla_\mu \rightarrow 0$). This is equivalent to considering only the $\nabla_\mu = 0$ line in Fig. 1.13 where it is not expected thermohaline mixing or semi-convection are likely to occur. We will now go to introduce the content of this thesis.

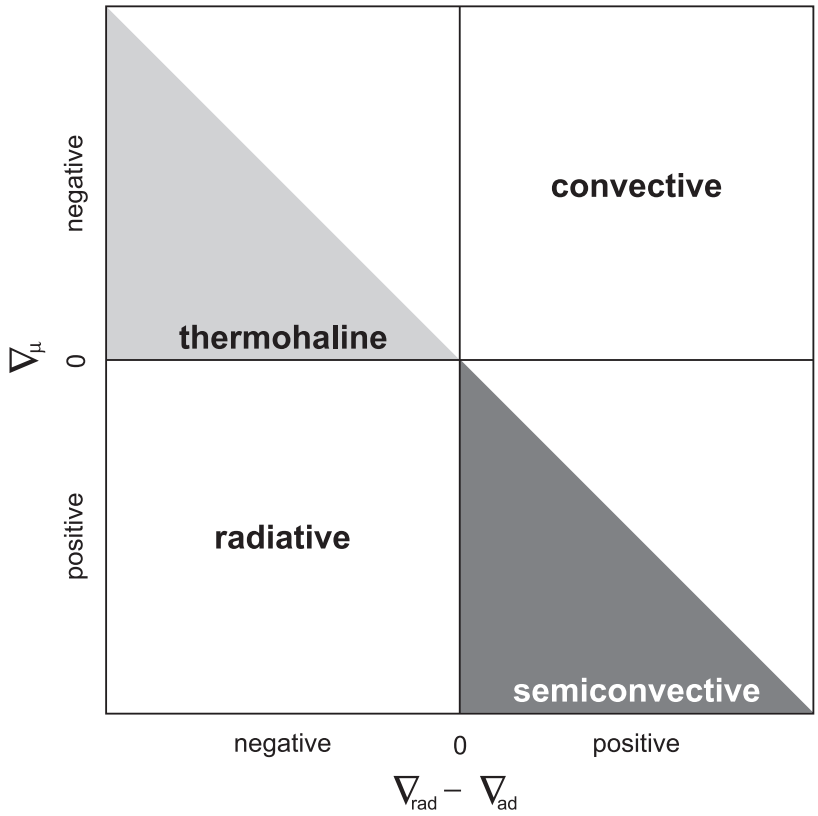

Figure 1.13: Sketch of the $\nabla_\mu - (\nabla_{rad} - \nabla_{ad})$ stability plane with different regimes labelled, where ∇_μ is the chemical gradient, ∇_{rad} is the radiative temperature gradient and ∇_{ad} is the adiabatic temperature gradient. The diagonal line dividing into half the top left and bottom right diagrams denotes ∇_L. Figure and caption reproduced from Salaris & Cassisi (2017).

1.3 Thesis Outline

This thesis comprises the research I have conducted on the surface convection zones of white dwarf stars. Chapter 2 introduces the field of stellar hydrodynamics and the CO5BOLD code used in this particular study. In Chapter 3 I present the characterisation of convective overshoot in pure-H atmosphere white dwarfs and consider the implications of these results on the field of metal-polluted white dwarfs and evolved planetary systems. Chapter 4 explores further the implications of these results by presenting new simulations of the horizontal mixing capabilities of convective white dwarfs, providing a constraint on possible surface inhomogeneities of metal-polluted white dwarfs. Chapter 5 is concerned with the spectral evolution of white dwarfs due to convective mixing where updates to previous studies are made possible with the novel characterisation of surface convection zones (presented in Chapter 3) and photometry from SDSS and *GALEX* and high-precision astrometry (and photometry) from the second data release of *Gaia*. In Chapter 6 I will contextualise the key results of the thesis with respect to the current state of the field. I will also detail future work to be carried out as a result of the findings in this thesis.

Chapter 2

Methodology

Fluid motions occur across a wide range of physical environments and this has led to the development of various numerical approaches to the problem of hydrodynamic flows. Computational methods for hydrodynamics can broadly be described as either Eulerian or Lagrangian. In the Eulerian formalism (e.g., Laney 1998; LeVeque 1998) fluid flow is characterised by physical parameters defined on a fixed grid, independent of the hydrodynamic motion. In the Lagrangian approach the flow becomes the frame of reference with the hydrodynamic properties defined by the forces acting on fluid parcels or particles. This can be achieved using a moving mesh which follows the flows or with a "mesh-free" or particle approach such as smoothed-particle hydrodynamics (SPH; Gingold & Monaghan 1977; Lucy 1977). Exploiting both numerical formalisms are the hybrid methods, such as the arbitrary Lagrangian-Eulerian (ALE; e.g., Amsden et al. 1980), which have a computational mesh that can move arbitrarily within a domain, and domain boundaries that can move with the material. All of these approaches have provided great utility in various astrophysical contexts, each with their benefits depending on the characteristics of the system being studied.

For instance, with the Lagrangian formalism it is more feasible to trace the history of specific fluid elements or particles (Anderson Jr, 1987) and significantly reduces the occurrence of numerical (unphysical) diffusion (LeVeque, 1998), which can impact the accuracy of a simulation, particularly regarding diffusive properties. On the other hand the Eulerian approach is advantageous in the modelling of turbulent flows with large vorticity; a phenomenon which can be particularly challenging for mesh-based Lagrangian codes. Although particle methods such as SPH can handle arbitrarily large turbulence, the shock-capturing methods and ability to define boundary conditions within the Eulerian approach are generally superior. It is for these reasons that the Eulerian formalism is most ubiquitous in the modelling of stellar atmospheres.

2.1 Stellar hydrodynamics

Stellar hydrodynamics is the study of fluid motions within stars and, enabled by recent advancements in computational resources, 2D and 3D stellar hydrodynamics has been used to probe the convective motions of stars throughout their main sequence and post-main sequence life (e.g., Nordlund & Dravins 1990; Asplund et al. 1999; Vögler et al. 2005; Gudiksen et al. 2011; Trampedach et al. 2013; Magic et al. 2015; Kupka & Muthsam 2017). In particular, the Eulerian approach to stellar hydrodynamics has proved to be a powerful tool for the characterisation of convective stellar atmospheres where it is necessary to include additional physics (e.g., magnetism and radiation) and boundary conditions. A stellar atmosphere can often be characterised by flows with a high Mach number (sub-sonic and

sonic), extremely high Reynold's number (low-viscosity) and, in the case of white dwarfs, short convective turnover timescale. Frequent turnover implies the existence of smaller convective cells, or *granules*, and this requires a high spatial resolution to be modelled accurately. In fact, the necessary resolution is often far too high to permit simulating the entire stellar surface but one can circumvent this issue by using the so-called *box-in-a-star* setup.

In this setup a grid is "placed" inside a star at a radius where convection is expected to occur and this approach is commonly used for the study of stellar atmospheres where the plane-parallel approximation can be exploited. The plane-parallel approximation is typically valid for surface convection zones where the convection zone depth is significantly less than the stellar radius. In this setup the convective motions can be studied more accurately than is possible with 1D models, but only if the boundary conditions are defined appropriately. Stars are not in thermal equilibrium with their surroundings, instead radiating their energy away via the emission of photons. Therefore an open top boundary is required, where the top layer has very small density and opacity, and mostly consists of outgoing radiative energy.

The lateral box boundaries (i.e., those quasi-parallel with the radial dimension) are typically periodic, meaning that the flow of mass and energy is not impeded in the horizontal directions. The lower boundary, i.e. that closest to the stellar core, specifies the inflowing stellar energy, either as convective flux, radiative flux, or both. The bottom boundary, along with local gravity, usually fully define the physical parameters of a simulation (e.g. $T_{\rm eff}$ and $\log(g)$).

For stars with long convective turnover timescales and thus large granules convection can be studied by simulating the entire star in the so-called *star-in-a-box* setup; for example in AGB stars (Freytag, 2017) and massive stars (Jiang et al., 2018). In this setup the boundary conditions are generally less significant to the numerical setup as the hydrodynamic flows are contained within the star. This assumption may not hold in the case of stars experiencing a rapid change in radius where a moving mesh or Lagrangian code may be more appropriate.

The hydrodynamic calculations performed in this thesis are all done with a 3-dimensional *box-in-a-star* setup utilising the CO^{5}BOLD code (Freytag et al., 2010a; Freytag, 2013); an Eulerian, grid-based code which uses finite volume methods to solve the fully compressible equations of radiation hydrodynamics (RHD) in the presence of a radiative flux and external gravity field. CO^{5}BOLD (and the studies leading up to its development) has been used in the modelling of such stellar environments as white dwarfs (Tremblay et al., 2013a), brown dwarfs (Freytag et al., 2010b), main sequence A/F/G/K/M-type stars (Freytag et al., 1996; Ludwig et al., 2009; Kučinskas et al., 2018), and helioseismology (Steiner et al., 2007). Employing the star-in-a-box setup CO^{5}BOLD has also been used to simulate AGB stars (Freytag & Höfner, 2008; Freytag et al., 2017) and red supergiants (Freytag et al., 2002;

Chiavassa et al., 2011). CO5BOLD is also capable of taking magnetic fields into account with magneto hydrodynamics (MHD, Schaffenberger et al. 2005, 2006) which has been used for main sequence models (Steiner et al., 2017) and white dwarfs (Tremblay et al., 2015c), though there are no MHD simulations presented in this thesis. Approximately 80% of white dwarfs have no evidence of magnetic fields (e.g., Landstreet & Bagnulo 2019) so this is a good approximation. In the following I will outline the theoretical framework of stellar hydrodynamics with CO5BOLD, the functionality of the code along with the particular numerical setup as it is employed in this thesis.

2.1.1 Compressible flows

Compressible flows are those where a fluid parcel will respond to a change of pressure or temperature by changing its density; as is typical of most fluids which exist in nature. If the density fluctuations which arise in response to the pressure and temperature changes are sufficiently small one can model the flow as being incompressible which has a computational advantage. This assumption is equivalent to demanding that the material derivative of the density, ρ, of a fluid parcel is zero, i.e.:

$$\frac{D\rho}{Dt} = 0 \tag{2.1}$$

The rule of thumb for whether compressible effects become important is when the maximum flow speed exceeds a Mach number of ≈ 0.3 (Anderson Jr, 2010), where the Mach number is the ratio of flow speed to fluid sound speed. For some of the white dwarf surface convection zones considered in this study the Mach number is expected to be higher than this threshold, necessitating a solution which treats the fluid as fully compressible. Previous hydrodynamic models of similar white dwarf surface convection zones have found depth-averaged Mach numbers as high as 0.8 (Tremblay et al., 2013b).

2.1.2 Equations

The framework of compressible hydrodynamics for inviscid flow are based on the *Euler equations* which account for the conservation of mass, and the balance of momentum and energy. In the presence of an external gravity field, $\vec{g}$, and a heating source from radiative

transfer, $Q_{\rm rad}$, these are

$$\frac{\partial \rho}{\partial t} = -\nabla \cdot (\rho \bar{\boldsymbol{v}}) \tag{2.2}$$

$$\frac{\partial (\rho \bar{\boldsymbol{v}})}{\partial t} = -\nabla \cdot (\rho \bar{\boldsymbol{v}} \bar{\boldsymbol{v}}) - \nabla P + \rho \bar{\boldsymbol{g}} \tag{2.3}$$

$$\frac{\partial (\rho e)}{\partial t} = -\nabla \cdot ([\rho e + P] \bar{\boldsymbol{v}}) + \rho \bar{\boldsymbol{v}} \cdot \bar{\boldsymbol{g}} + Q_{\rm rad} \tag{2.4}$$

where ρ is the gas density, $\bar{\boldsymbol{v}} = (v_x, v_y, v_z)$ is the 3-dimensional velocity field and e is the total internal and kinetic energy per unit mass. These five variables (ρ, v_x, v_y, v_z and e) are the only independent quantities solved for in the hydrodynamic calculations.

If the hydrodynamic flow is in a medium with high viscosity (low Reynold's number) then it would be necessary to include an explicit viscosity term, such as in the Navier-Stokes equations. Due to their low viscosity, flows in stellar atmospheres are well-known to have extremely large Reynold's numbers (Mihalas, 1978; Nordlund, 1974). In the case of white dwarf convective flows, the Reynold's number is typically in excess of $Re > 10^{10}$ (Tremblay et al., 2013a). Thus, it is not necessary to include an explicit viscosity term in the hydrodynamic equations. Instead the viscosity is generally determined by the numerical scheme and grid resolution, where the kinetic energy of the smallest turbulent features are dissipated at the grid-scale (Tremblay et al., 2013a). The numerical viscosity does not have significant impact on the physicality of the model as flows that occur at the sub-grid scale are generally too small to carry significant energy fluxes.

All of the simulations considered in this thesis are Cartesian, *box-in-a-star* models such that the external gravity field is given by

$$\bar{\boldsymbol{g}} = \begin{pmatrix} 0 \\ 0 \\ -g \end{pmatrix}, \tag{2.5}$$

where g is the acceleration due to gravity at the white dwarf surface ($g \sim 10^6\,\mathrm{m\,s^{-2}}$). In explicit component form the equations of hydrodynamics solved in this work are equivalently

written

$$\frac{\partial \rho}{\partial t} = -\left(\frac{\partial \rho v_x}{\partial x} + \frac{\partial \rho v_y}{\partial y} + \frac{\partial \rho v_z}{\partial z}\right) \tag{2.6}$$

$$\frac{\partial}{\partial t}\begin{pmatrix}\rho v_x\\ \rho v_y\\ \rho v_z\end{pmatrix} = -\frac{\partial}{\partial x}\begin{pmatrix}\rho v_x v_x + P\\ \rho v_y v_x\\ \rho v_z v_x\end{pmatrix} - \frac{\partial}{\partial y}\begin{pmatrix}\rho v_x v_y\\ \rho v_y v_y + P\\ \rho v_z v_y\end{pmatrix} - \frac{\partial}{\partial z}\begin{pmatrix}\rho v_x v_z\\ \rho v_y v_z\\ \rho v_z v_z + P\end{pmatrix} - \begin{pmatrix}0\\ 0\\ \rho g\end{pmatrix} \tag{2.7}$$

$$\frac{\partial \rho e}{\partial t} = -\frac{\partial (\rho e + P) v_x}{\partial x} - \frac{\partial (\rho e + P) v_y}{\partial y} - \frac{\partial (\rho e + P) v_z}{\partial z} - \rho g v_z + Q_{\mathrm{rad}} \tag{2.8}$$

The inclusion of the energy change due to radiation transport, Q_{rad}, is what brings this within the *radiation hydrodynamic* formalism and it is found by taking the divergence of the radiative flux

$$Q_{\mathrm{rad}} = -\left(\frac{\partial F_{\mathrm{x,rad}}}{\partial x} + \frac{\partial F_{\mathrm{y,rad}}}{\partial y} + \frac{\partial F_{\mathrm{z,rad}}}{\partial z}\right). \tag{2.9}$$

Calculating the radiative flux, F_{rad}, is the most intensive aspect of the computation as it's dependence on flow geometry and frequency are both taken into account (Ludwig & Steffen, 2013). The radiative flux across grid cells is given by integrating the frequency-independent total intensity, I, over the solid angle

$$F_{\mathrm{rad}} = \int_0^{2\pi}\int_0^{\pi} I \cos\theta \, \sin\theta \, d\theta \, d\phi \,, \tag{2.10}$$

where the total intensity can be found by integrating the frequency-dependent intensity, I_ν, over all frequencies; this quantity is found by solving the radiative transfer equation. Within CO^{5}BOLD the frequency integration is simplified by considering only a small number (either one, eight or thirteen) of frequency bins, a procedure which is described in Section 2.1.4.

Collectively, these equations encompass the analytic formulation of the fully compressible radiation hydrodynamics in the *box-in-a-star* setup used throughout this work for the simulations of white dwarf surface convection zones. The compressibility is accounted for by the presence of Equation (2.4) which, because the local fluid density is permitted to fluctuate, necessitates an equation of state (EOS) to relate density, pressure and temperature.

2.1.3 Equation of state

The pressure term in Equation (2.4) is typically found via the interpolation of an EOS table for a given density, ρ, and total internal energy, e, such that

$$P = P(\rho, e) \,. \tag{2.11}$$

A standard equation of state intended for use in low-density stellar envelopes was published by Hummer & Mihalas (1988) and was soon after incorporated into the Montreal white dwarf atmosphere code (Bergeron et al., 1991). In early studies of white dwarf atmospheres with 3D radiation hydrodynamics a more simple ideal equation of state was utilised in the study of the surface gravities of cool DA white dwarfs (Tremblay et al., 2011a). These simulations were improved by Tremblay et al. (2013a) with the inclusion of the Hummer & Mihalas non-ideal equation of state into the CO^{5}BOLD code. The authors found that the inclusion of the non-ideal effects into the equation of state did not significantly alter the predicted structures for white dwarfs with $T_{\rm eff} > 6000$ K and in layers with Rosseland mean optical depths of $\tau_R < 1{,}000$. Non-ideal effects are still important for modelling spectral lines, an output of CO^{5}BOLD simulations not considered in this thesis. However, we use the same (non-ideal) EOS for consistency with the literature.

2.1.4 Opacities

An opacity is required to calculate the conversion of radiative energy into thermal energy. The handling of opacities within CO^{5}BOLD and most radiation hydrodynamic codes is done using the Opacity Binning Method (OBM) (Nordlund, 1982; Ludwig et al., 1994). The OBM calculates an average opacity for a given frequency bin allowing an approximation of the heat transferred from frequency-dependent radiation. This requires frequency-dependent opacities, which vary as a function of temperature and pressure, that are stored in opacity tables. This method is particularly powerful and introduces only a small error when frequency-dependent opacities that have a similar strength and depth dependence are grouped together (Ludwig & Steffen, 2013).

Some of the earliest and most successful white dwarf atmospheric models were those of Bergeron et al. (1992) and Finley et al. (1997). Since then inclusion of more opacity sources has led to the development of increasingly sophisticated white dwarf atmospheric models. For instance; the improved treatment of Lyman quasi-molecular satellites (Allard et al., 2004), inclusion of Lyman-α red-wing opacity borne of H_2-H collisions (Kowalski & Saumon, 2006) and improvements in the Stark (pressure) broadening profiles (Tremblay & Bergeron, 2009). Calculating synthetic spectra from 3D simulations requires opacity bins numbering into the thousands, but running the radiative transfer at every time step with so many bins is computationally intractable. It has been shown that, using the OBM, CO^{5}BOLD can reproduce accurately the atmospheric structure using as few as only 8 frequency bins (Ludwig & Steffen, 2013). This would not produce accurate synthetic spectra, for which a more detailed radiative transfer calculation must be done, but it does produce a description of the heat transfer sufficient to evolve the hydrodynamic flows. Even with so few opcaity bins, the radiative transfer calculation takes approximately 98% of the computation

time for any given simulation. This is why the OBM is so crucial for running tractable calculations, but incorporating these detailed models into the 3D radiation-hydrodynamics required confirmation that the opacity binning method rendered an accurate approximation of the true opacity.

The LHD code (Caffau & Ludwig, 2007) is a Lagrangian 1D hydrostatic code which was developed to do just this; test the accuracy of the opacity binning method implemented in CO^{5}BOLD. The obvious difference to the RHD code is its 1D nature which prevents the use of full hydrodynamics (with convection being treated with the mixing-length theory instead) but it can operate with identical equation of state and opacities to CO^{5}BOLD. This was exploited in the specific case of cool DA white dwarfs by Tremblay et al. (2013a) to test if the same structure is recovered between the LHD code (8 frequency bins) and standard white dwarf model atmospheres (1813 frequency bins). Their results are shown in Fig. 2.1 which depicts a comparison of the atmospheric temperature yielded from a standard 1D white dwarf model (1813 frequency bins) and from the LHD code (8 bins). The authors here demonstrated that the 8 bin approach reproduces the temperature stratification of the white dwarf structure from the standard 1D white dwarf models. This important step ensures that the underlying 1D atmospheric structure of the 3D CO^{5}BOLD simulations is physically realistic and thus the properties drawn from the 3D hydrodynamics should reliably correspond to those predicted at a given effective temperature and surface gravity. It is this binned approach using the OBM which is used throughout this thesis when simulations are run with non-grey opacities. At the end of a simulation one can perform detailed 3D radiative transfer for a few selected time steps and as many frequencies as desired in order to predict the detailed emergent spectrum (e.g., line profiles). This procedure provides no direct feedback on a simulation and is omitted from this thesis as we do not predict new spectral models for DA white dwarfs which have already been calculated (Tremblay et al., 2013a).

2.1.5 Numerical schemes

Numerical methods have proved to be a powerful tool for solving by brute force equations for which analytic solutions cannot be reasonably found. But the discretization of the solution domain introduces discontinuities which can lead to artefacts and unphysical solutions, especially due to the presence of shocks. CO^{5}BOLD can deal with shocks using an artificial viscosity, but any grid-based (whether Eulerian or Lagrangian) hydrodynamic code still requires the numerical reconstruction of the quantities between grid points.

These schemes are also referred to as *flux limiters* or *slope limiters* because they reduce (or limit) the value of the derivative at discontinuities. Effectively this creates smooth continuous variables out of the grid-bound, implicitly discretized quantities allowing

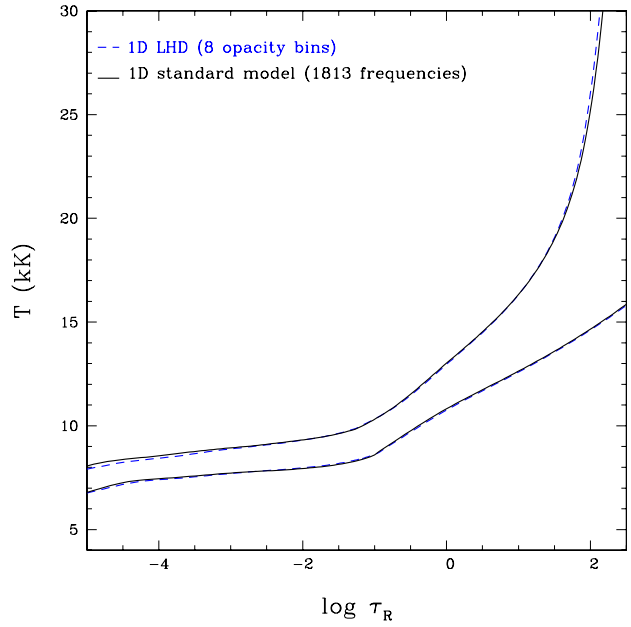

Figure 2.1: Atmospheric temperature as a function of the logarithm of the Rosseland optical depth for DA models with effective temperatures of 8000 (bottom) and 12 000 K (top). Shown are the standard 1D structures (solid black line) from Tremblay et al. (2011b), recomputed with a slightly higher numerical precision, and the improved 1D LHD structures (dashed blue line) described in the text. Figure and caption reproduced from Tremblay et al. (2013a).

physically reasonable solutions to be found throughout the solution domain. The choice of reconstruction scheme can have great implications for the results of the calculations and there are many varieties available in the literature.

Fig 2.2 shows the behaviour of six reconstruction schemes, five of which are implemented within CO^{5}BOLD, for a snapshot of arbitrary data points. The two simplest schemes shown are the zeroth-order (Constant) and first-order (MinMod, Roe 1986) reconstructions. Whilst the latter is slightly smoother, they are both prone to many discontinuities. Three of the second-order reconstructions implemented in CO^{5}BOLD are the van Leer (Van Leer, 1979), Piecewise Parabolic (Colella & Woodward, 1984) and the FRweno (Freytag, 2013). From the figure it can be seen that the second-order reconstruction schemes produce far fewer discontinuities between grid points than the zeroth- and first-order cases. The most simplistic of the second-order schemes is the Parabola (not implemented within CO^{5}BOLD) which has no enforced monotonicity between grid points and produces here significant overshoot and negative values. This is never ideal, but if the quantities being constructed are positive by definition (i.e., density, pressure) this can be catastrophic for the hydrodynamic solutions.

The choice of reconstruction scheme has further implications; in particular for numerical diffusion. In a study of shock-capturing schemes, Shu & Osher (1989) considered a set of four prominences, or spikes, designed to test the numerical diffusivity of a reconstruction scheme. These were simulated by Freytag (2013) for the numerical schemes implemented within CO^{5}BOLD and the results are reproduced in Fig. 2.3 for the linear advection of the *Shu & Osher spikes* over a fixed number of time steps. The ideal reconstruction scheme should have minimal numerical diffusivity to preserve small scale features in the hydrodynamic flows and it can be seen that the Constant, MinMod and van Leer schemes are rather susceptible to numerical diffusion. This means that, even in the absence of any physical diffusivity, the small scale features are "smeared" out. Whilst it exhibits minimal diffusivity, the simple Parabola method results again in negative values. It is only the PP and FRweno reconstructions which demonstrate the strict positivity and minimal diffusivity required for high-resolution hydrodynamics.

For the majority of calculations performed in this thesis the second-order FRweno scheme is used for the hydrodynamic flows which, despite some overshoot, is seen to model local extrema more smoothly than other schemes. Simultaneously, calculations involving a tracer density (introduced in the following chapter) are performed using the Piecewise Parabolic reconstruction. This scheme is the least prone to numerical diffusion (see Fig. 2.3) and thus preserves small scale features most precisely.

Regarding the time integrations, the 3-dimensional hydrodynamic time steps are performed as 1-dimensional sub steps using a Roe solver (Roe, 1981). A popular choice

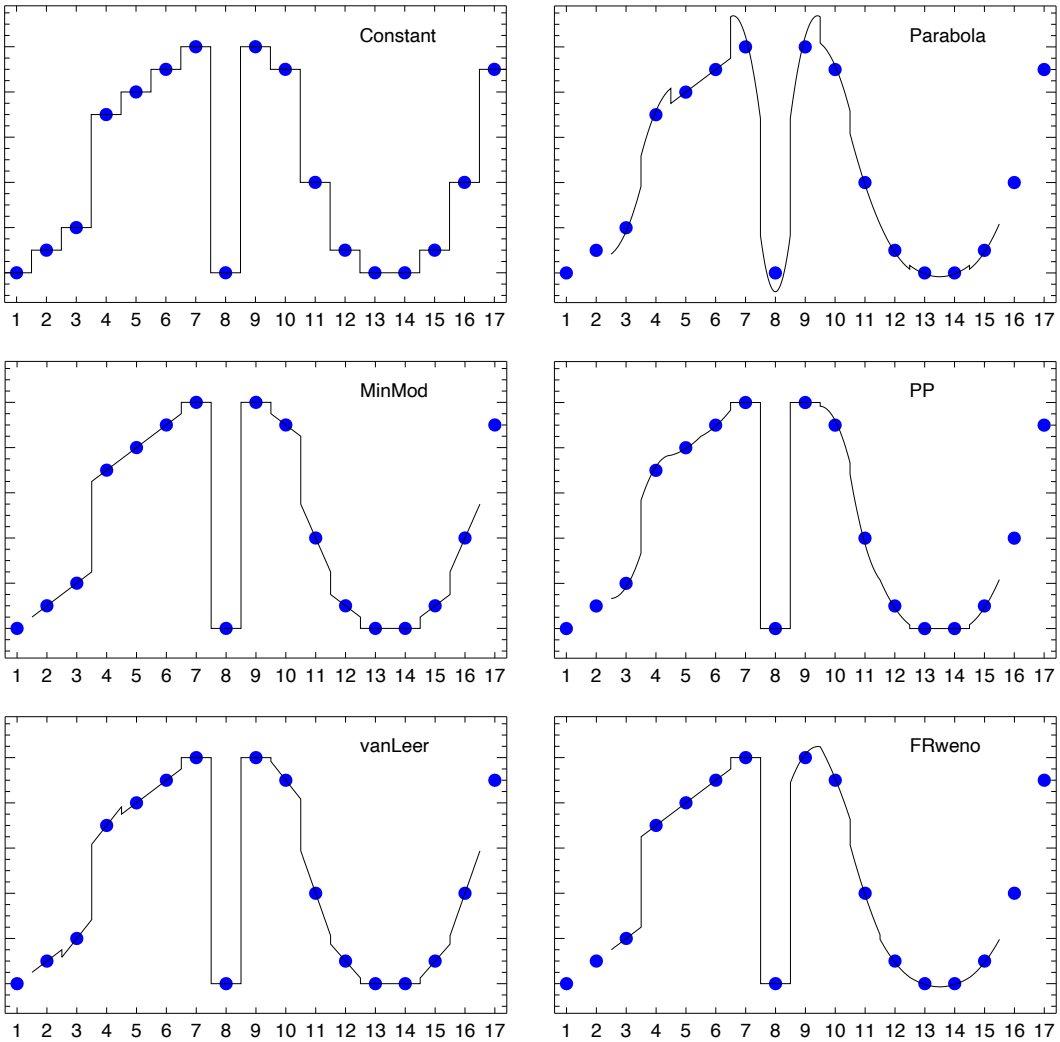

Figure 2.2: Various reconstruction schemes for a small vector of points (blue filled circles): 0.0, 0.1, 0.2, 0.7, 0.8, 0.9, 1.0, 0.0, 1.0, 0.9, 0.4, 0.1, 0.0, 0.0, 0.1, 0.4, 0.9. These points are an arbitrary collection of values distributed on an equidistant 1D grid. Here they have no physical meaning, but are chosen to demonstrate the behaviour of certain reconstruction schemes. The reconstruction schemes shown are zero- and first-order polynomials (left column) or second-order polynomials (right column). Note, that only the "parabola" and the "FRweno" scheme show some overshoot (e.g., in cells 9 and 10), in contrast to the other – monotonic – schemes. With the exception of the "parabola", all reconstruction schemes shown are implemented in CO^{5}BOLD. Figure and caption adapted from Fig. 1 of Freytag (2013).

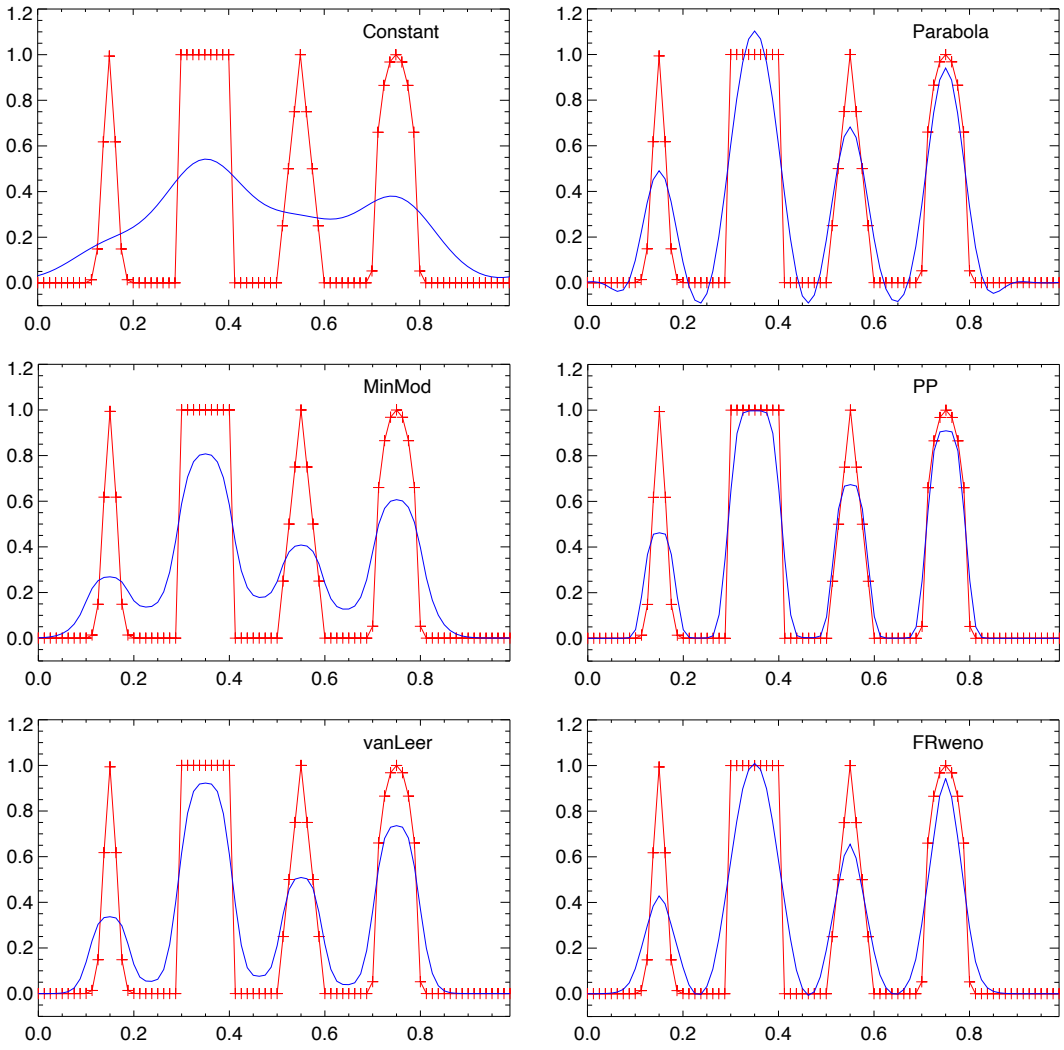

Figure 2.3: Linear advection of the Shu & Osher spikes (red curves with plusses) after one revolution (blue curves) using various reconstruction schemes (the same as in Fig. 2.2). As with Fig. 2.2 the y-value of each point is arbitrary, with the Shu & Osher spikes offering a collection of four shapes designed to test the diffusive behaviour of a given numerical scheme. The "Constant" scheme is highly diffusive and the "Parabola" scheme has lots of overshoot. The "MinMod" and "vanLeer" demonstrate relatively high diffusivity. The linear advection under the "PP" and "FRweno" schemes renders the least diffusion and overshoot and thus are considered the best behaved out of the schemes shown here. Figure and caption adapted from Fig. 2 of Freytag (2013).

in hydrodynamic codes, the Roe solver is an approximate solution to the Riemann problem which takes the reconstructed numerical data as input and computes an inter-cell flux via a linear calculation. The Riemann problem pertains specifically a conservation equation evaluated from initial, discrete data with a single discontinuity in the solution domain. This problem has led to many approximate solution methods which estimate the inter-cell flux between two adjacent cells in the solution domain. Within CO^{5}BOLD the Roe solver is suitable for pure hydrodynamics, i.e., in the absence of a magnetic field. Throughout this study I employ the time integration scheme ("single") that creates one single update of the quantities each time step, with higher-order terms in time being dealt with by the Roe solver according to whichever numerical reconstruction is chosen. For the amalgamation of the 1D sub steps into the full 3D hydrodynamics each time step uses the Corner-Transport Upwind (CTU) model (Colella, 1990) to compute the quantities for the next time step. This is a benchmark algorithm for temporal evolution of quantities within finite volume methods and was implemented in CO^{5}BOLD as an alternative to directional splitting (Freytag, 2013). The time required to run the simulations in this thesis vary from model to model depending on parameters such as the required resolution and the number of tracer density arrays. The majority (~98%) of the computation time is spent on the radiative transfer calculations, which is particularly important in the optically thin regime of the upper atmosphere. Typical CPU hours for each simulation ranges from 3000–10 000‘,h, normally run on 8 or 16 cores.

I have now introduced the equations and numerical methods that underpin the CO^{5}BOLD code. In the following chapter I will introduce the specific techniques utilised with CO^{5}BOLD in the study of convection in the surface layers of DA white dwarfs. The main omission here is in the exploitation of passive scalar particles and an in-built passive scalar density, but the methods and implementation will be described in detail in the next chapter.

Chapter 3

Convective overshoot in DA white dwarfs

3.1 Introduction

For decades, understanding the diffusion of heavy elements through stellar plasmas has been central to research in solar and stellar evolution (Michaud, 1970; Thoul et al., 1994), including the cooling of white dwarfs (Schatzman, 1945). In the latter case, large surface gravities ($7.0 \lesssim \log g \lesssim 9.0$) imply the rapid settling of the initial composition into a structure stratified according to atomic weight with an outer shell made of hydrogen and helium.

The related scenario of metal accretion onto white dwarfs has now matured into an extremely active field of research around evolved planetary systems (Veras, 2016a). For a small fraction of these systems it is possible to study the debris disk or gas around the white dwarf (Jura, 2003; Farihi et al., 2009; Manser et al., 2016; Xu et al., 2018) but in most cases the primary evidence is metal pollution from tidally disrupted asteroids in the stellar atmosphere (van Maanen, 1917; Zuckerman et al., 2003; Gänsicke et al., 2012; Vanderburg et al., 2015). To transform photospheric metal abundances into the parent body properties requires an accurate model describing the volume of the stellar envelope over which this abundance is prevalent. The accretion-diffusion model is usually employed, where microscopic diffusion removes the heavy elements out of the observable layers (Paquette et al., 1986a,b; Pelletier et al., 1986; Koester, 2009).

Constraining the mass and composition of the accreted material has wide-reaching implications for the chemical compositions of other rocky worlds and planetary evolutionary models (see, e.g., Zuckerman et al., 2007; Dufour et al., 2012; Farihi et al., 2013, 2016; Wilson et al., 2016; Xu et al., 2017; Melis & Dufour, 2017). Since the emergence of space-based UV spectroscopy the ability to detect metal pollution has significantly increased, putting the fraction of degenerate stars with evolved planetary systems at $\approx 50\%$ (Zuckerman et al., 2010; Koester et al., 2014). These advances have allowed to describe the frequency and properties of accretion events across white dwarf cooling age, mass, and spectral type, yet the possibly observed correlations are not fully understood (Farihi et al., 2012; Koester et al., 2014; Hollands et al., 2018a), and systematic model effects have been debated (Wachlin et al., 2017; Kupka et al., 2018; Bauer & Bildsten, 2018). This chapter is primarily focused on theoretical aspects of the accretion-diffusion scenario in the context of hydrogen-atmosphere DA white dwarfs.

Once DA white dwarfs have cooled sufficiently to develop a convection zone, small characteristic convective turnover timescales imply that metals become fully mixed within these turbulent layers, and that microscopic diffusion only takes place at the base of the convection zone. As this boundary layer is denser than the surface layers, this implies longer settling times of the metals of up to 10 000 yrs (Koester, 2009; Bauer & Bildsten, 2019).

Going back to the work of Prandtl & Tietjens (1925), convection has often been modelled using 1D mixing-length theory (MLT). This model requires that the Schwarzschild criterion for convective instability be satisfied and where it is not, the models show no convective motions (Böhm-Vitense, 1958; Tassoul et al., 1990). In the 1D MLT picture the base of the convection zone is at the Schwarzschild boundary. Beneath this, the dominant process for mass transport is that of microscopic diffusion. This microscopic diffusion comprises contributions from gravitational settling, thermal diffusion, radiative diffusion and diffusion driven by concentration gradients, unless the diffusion concerns tracer particles, in which case the latter term is neglected (Paquette et al., 1986b; Koester, 2009). From microscopic diffusion calculations, the characteristic elemental diffusion velocities near the Schwarzschild boundary are $v_{\rm diff} \sim 10^{-7}\,{\rm km\,s^{-1}}$ (Koester, 2009). This can be up to seven orders of magnitude less than the characteristic convective velocities of $\sim 1\,{\rm km\,s^{-1}}$ in the adjacent layer above.

The discontinuity between convective and non-convective layers in the 1D model is unphysical (Zahn, 1991; Spiegel, 1963) and multi-dimensional numerical simulations have also confirmed this for the case of white dwarfs (Freytag et al., 1996; Tremblay et al., 2015a; Kupka et al., 2018). Whilst the layers beneath the convectively unstable region are not able to accelerate material to greater depths, convective cells accelerated at the base of the unstable region can have sufficient momentum to penetrate the deeper layers before dissipating their kinetic energy. This process is known as convective overshoot and it has been shown from earlier 2D simulations to be capable of mixing material (Freytag et al., 1996). Constraining precisely the mass fraction of mixed material is crucial for our understanding of accretion onto white dwarfs.

This chapter presents the first direct tests of mixing due to convective overshoot using tracer particles and trace density in 3D radiation-hydrodynamics (RHD) CO^{5}BOLD simulations in the context of DA white dwarfs with shallow surface convection zones. Building upon the work of Freytag et al. (1996, 2012), we estimate macroscopic diffusion coefficients below the Schwarzschild unstable region from direct 3D experiments (Sections 3.2-3.3). We employ the dependence of macroscopic diffusion on mean convective velocities from these direct experiments to infer the increase in convectively mixed mass for a wide range of atmospheric parameters, using a grid of CO^{5}BOLD simulations covering $11\,400\,{\rm K} < T_{\rm eff} < 18\,000\,{\rm K}$ at $\log g = 8.0$ (Section 3.4). We discuss the implications on accretion rates and diffusion timescales (Section 3.5) and conclude in Section 3.6.

3.2 Numerical setup

The simulations presented in this work have been run using the 3D RHD code CO^{5}BOLD as described in Freytag et al. (2012) and the previous chapter. On a Cartesian grid, CO^{5}BOLD solves the coupled equations of compressible hydrodynamics and non-local radiation transport, implicitly respecting conservation laws of energy, mass and momentum. The vertical grid spacing is depth dependent, allowing for better resolution of radiative transfer in upper layers, whilst the grid spacing does not vary in the horizontal plane. For simulations presented throughout this study radiation is handled with opacity and EOS tables from Tremblay et al. (2013a,c), using both grey (Table 3.1) and non-grey schemes (Table 3.2). The upper (surface) boundary is open to mass flows and radiation (see Freytag 2017). The lower boundary is closed, requiring velocities to be zero, and with a fixed radiative flux for a given effective temperature. The four horizontal boundaries have periodic boundary conditions.

To increase stability around discontinuities a numerical reconstruction scheme is required by the hydrodynamics solver. For all simulations presented in this study the chosen scheme is designated as FRweno using a reconstruction by 2nd order polynomials (Freytag, 2013). For the handling of trace density arrays with CO^{5}BOLD, which will be discussed in detail in the following section, a piecewise-parabolic reconstruction scheme is used (Colella & Woodward, 1984).

The effective temperature is an input parameter for our simulations, as its value determines the radiative flux put into the simulation lower boundary. Following relaxation, the effective temperature is confirmed by the spatially and temporally averaged emergent radiative flux. For brevity the effective temperatures in Tables 3.1-3.2 will be referred to by rounding to the nearest 100 throughout this study, though any calculations involving the effective temperature will use the more precise values shown in the tables.

3.2.1 Diffusion coefficient experiments

Table 3.1 shows the numerical setups for the simulations analysed in the direct study of macroscopic diffusion in Section 3.3. All simulations have been built from previously relaxed 3D simulations and given sufficient time to relax after any parameter change.

Table 3.1: Numerical setup for grey opacity simulations analysed directly for macroscopic diffusion with methods of CO5BOLD tracer density and path integration. All simulations have a pure-hydrogen composition, closed bottom boundary and $\log g = 8.0$.

Sim. ID	$T_{\rm eff}$ [K]	z [km]	x,y [km]	$\log \tau_{\rm R,top}$	$\log \tau_{\rm R,bot}$	ΔH_p	$z_{\rm S,top}$ [km]	$H_{p,\rm S,bot}$ [km]	$v_{\rm z,S,bot}$ [kms^{-1}]	$[x, y, z]$	$t_{\rm diff\ exp}$ [s]	$N_{\rm tr\ dens}$
A1	11 992	4.7	7.5	−4.28	3.63	5.19	1.06	0.53	4.48	250, 250, 250	6.02	10
B1	13 000	4.5	7.5	−3.35	3.01	5.06	0.66	0.40		150, 150, 150	9.05	20
B2	12 999	4.5	7.5	−3.33	3.01	5.02	0.43	0.38	2.78	250, 250, 250	3.16	10
C1	13 498	3.6	7.5	−3.19	2.69	4.37	0.52	0.37		150, 150, 150	6.20	20
C2	13 498	3.6	7.5	−3.18	2.69	4.37	0.51	0.38		250, 250, 150	7.91	20
C3	13 498	3.6	7.5	−3.20	2.69	4.39	0.50	0.35	1.52	250, 250, 250	8.41	10
C1-2	13 499	3.6	15.0	−3.19	2.69	4.39	0.50	0.37		150, 150, 150	8.14	20

Notes: The vertical (horizontal) extent of the simulation box is indicated by z (x, y). The number of pressure scale heights from the horizontally averaged layer $\tau_{\rm R} = 1$ and the simulation base is given by ΔH_p. All simulations have been fully relaxed prior to the addition of tracer density at which point the diffusion experiment begins and its duration is denoted by $t_{\rm diff\ exp}$. The number of unique depths at which tracer densities are added is given by $N_{\rm tr\ dens}$. We also include the geometric position of the upper Schwarzschild boundary, $z_{\rm S,top}$, relative to the lower Schwarzschild boundary which is set to be at the origin of the depth axis, i.e., where $z = 0$ km. Denoted by $v_{\rm z,S,bot}$ is the time-averaged RMS vertical velocity at the lower Schwarzschild boundary. $T_{\rm eff}$ is derived from the time and spatially averaged outgoing radiative flux. $\tau_{\rm R,top}$ and $\tau_{\rm R,bot}$ are geometrical and time averages of the Rosseland optical depth at the boundary layers of the simulation box. Characteristic granule sizes for all simulations range from 1.0–1.2 km and data sampled from simulations with period $\Delta t = 0.01$ s.

3.2.2 Extended grid of closed 3D simulations

Diffusion experiments using the direct methods laid out in Section 3.3 are computationally expensive, in terms of both random-access memory during the simulation (Section 3.3.1) and data storage after the fact (Section 3.3.2). Furthermore, direct simulation of diffusion is hampered by numerical waves as we shall discuss in Section 3.4, and thus in this work we also infer indirectly about the macroscopic diffusion properties by using wave-filtered velocities as a proxy. Towards this goal we employ a newly computed grid of deep simulations across the effective temperature range 11 400 K $\leq T_{\rm eff} \leq$ 18 000 K. Numerical details are shown in Table 3.2. The simulations detailed with 12 009 K $\leq T_{\rm eff} \leq$ 17 004 K had nominal input effective temperatures to the nearest 500 K. The input effective temperatures for the two coolest (warmest) simulations were 11 400 K and 11 600 K (17 525 K and 18 025 K). As an indicator of the quality of relaxation of our simulations we find the maximum discrepancy between input effective temperatures and those determined at the surface to be 0.4%, whilst the majority of the grid ($T_{\rm eff} \geq$ 12 000 K) has a maximum difference of 0.1%.

These models are similar to the closed box simulations introduced in Tremblay et al. (2013c, 2015a) but were extended to deeper layers and are using a larger number of grid points. The new grid has a vertical and horizontal resolution of 30–50 m and 50–80 m, respectively. This is slightly less resolved than in the previous grid, which had resolutions ~20 m and 30–50 m in the vertical and horizontal, respectively; a necessary adaptation for probing deeper layers. Furthermore, the grid was extended to significantly cooler and hotter temperatures, with our coolest closed bottom simulation at $T_{\rm eff} \approx$ 11 400 K overlapping with an open lower boundary simulation in Tremblay et al. (2013c). All these simulations are sufficiently deep to contain the entirety of the convectively unstable layers and deeper overshoot layers, providing a unique opportunity to constrain convective velocities in layers deeper than previously done with CO^{5}BOLD, similarly to what has been performed in Kupka et al. (2018).

3.3 Simulating macroscopic diffusion

The motivation for this research is to characterise the macroscopic diffusion of trace metals in polluted white dwarfs for regions beneath the convection zone, where 1D models currently predict no such mixing. In particular, we aim at characterising the depth dependence of the efficiency of macroscopic mixing in these overshoot regions. We do this by implementing a statistical, ensemble averaged model for the mixing caused by overshoot in a finite region directly beneath the convectively unstable layers, which we outline in the following.

The concentration of a fluid, ϕ, can be described by the well known diffusion equation, or Fick's second law, in the absence of a source term and with a spatially dependent

Table 3.2: Extended grid of CO^{5}BOLD simulations with pure-H composition and $\log g = 8.0$. All simulations have 200^3 grid points, closed bottom boundaries and non-grey opacities (Tremblay et al., 2013a).

$T_{\rm eff}$ [K]	$\log \tau_{\rm R,top}$	$\log \tau_{\rm R,bot}$	ΔH_p	x,y [km]	z [km]
11445	−10.1	4.55	4.21	10.1	10.0
11651	−9.24	4.38	5.18	16.9	9.8
12009	−6.99	4.44	7.36	16.8	10.6
12514	−6.34	4.03	7.49	14.9	8.7
13005	−6.20	3.63	6.94	15.0	7.1
13503	−5.29	3.34	6.52	15.0	6.1
14000	−5.06	3.19	6.37	15.0	5.8
14498	−5.10	3.18	6.82	15.0	6.2
15000	−5.01	3.15	7.01	15.0	6.4
15501	−5.01	3.12	7.23	15.0	6.7
16002	−5.04	3.09	7.48	15.0	6.9
16503	−5.06	3.05	7.67	15.0	7.0
17004	−4.97	3.02	7.92	15.0	7.1
17524	−5.11	2.80	7.58	15.0	6.4
18022	−5.10	2.56	7.34	15.0	5.7

Notes: The number of pressure scale heights from $\tau_{\rm R} = 1$ and the simulation base is given by ΔH_p. $\tau_{\rm R,top}$ and $\tau_{\rm R,bot}$ are geometrical averages of the Rosseland optical depth at the boundary layers of the simulation box. Further details on the columns are given in the caption to Table 3.1.

diffusion coefficient as

$$\frac{\partial \phi(\mathbf{r}, t)}{\partial t} - \nabla(D(\mathbf{r})\nabla\phi(\mathbf{r}, t)) = 0 \,, \tag{3.1}$$

where D is the diffusion coefficient. We neglect any time dependence of the diffusion coefficient as we are working with a system in a statisically steady state - at least concerning transport properties in the vertical direction. Given the spherical symmetry of a white dwarf surface we exclude the possibility of horizontal dependence in the diffusion coefficient for the purposes of this chapter. This allows the horizontal information from our 3D simulations to be averaged, providing a robust statistical characterisation of trace element distributions and ultimately giving a one dimensional diffusion problem.

For a system undertaking a true diffusion process in one dimension the mean displacement, $\langle z \rangle$, of an ensemble of particles, representing the distance the concentration has travelled, is expected to evolve according to

$$\langle z^2 \rangle = 2Dt \tag{3.2}$$

where t is the time over which the system evolves. The objective of this study is to calculate the depth dependent diffusion coefficients associated with trace particles beneath the convectively unstable layers.

We use two methods to quantify the mean displacement of diffusing particles, both of which will be described in the following sections. Method I utilises a module built into CO^{5}BOLD, designed for the study of dust formation in stellar and solar environments, whilst Method II follows more closely the methodology of Freytag et al. (1996) using tracer particles and serves as an independent test of diffusion.

3.3.1 Method I: Tracer density arrays in CO^{5}BOLD

Utilising the dust module included in CO^{5}BOLD (Freytag et al., 2012) we can add extra passive scalar density arrays to relaxed simulations. These density fields have no mass, no opacity, and should thus only be advected by the local velocity fields. We note, however, that CO^{5}BOLD will adjust the time steps so that the additional density fields can be reconstructed adequately, indirectly influencing the overall numerical scheme. Microscopic diffusion velocity is orders of magnitude smaller than macroscopic velocity fields, hence it is ignored in these experiments. In any case we are only interested in the stellar layers above which microscopic diffusion takes over. Via this method we do not have actual tracer particles, but rather we store horizontally-averaged number density distributions, providing significant advantages for data storage and handling.

Additional and non-interacting density arrays are initially added to relaxed simulations. To provide the most localised estimation of the diffusion coefficient, a tracer density

is inserted as a delta function (or horizontal slab) in the z-direction such that

$$\rho_{\rm t}(z) = \begin{cases} 10^{5}\ {\rm cm}^{-3}, & \text{where } z = z_0. \\ 10^{-6}\ {\rm cm}^{-3}, & \text{where } z \neq z_0. \end{cases} \tag{3.3}$$

where $\rho_{\rm t}(z)$ is the tracer density. In our setup, Eq. (3.1) is linear in ϕ so a horizontal slab is ideal for probing vertical mixing. Since these density fields are massless the actual number density is only relevant for the precision of the numerical schemes and rounding errors. The large range between the peak and background tracer densities is chosen to minimise any signature of net downward mixing due to the atmospheric density gradient. Two of the initial distributions of tracer densities in simulation C3 are shown in the top panels of Fig. 3.1 where a vertical cross section of a relaxed simulation at $T_{\rm eff} = 13\,500$ K to which the massless tracer density (green) was added is shown.

Our initial experiments showed that standing waves appeared in the base layers of our simulations, driven by convection and trapped between the convectively unstable layer and bottom box boundary. We find that across all simulations the modes are either above or below the acoustic cut-off frequency, suggesting both p-modes, oscillations with pressure as the primary restoring force, and g-modes, oscillations with gravity as the primary restoring force, can be excited. In particular for the cooler models ($T_{\rm eff} \leq 12\,000$ K), in the region beneath the unstable layers, we favour the interpretation of g-modes (Freytag et al., 1996, 2010b). Similar wave effects have also been observed in deep white dwarf simulations by other groups (Kupka et al., 2018) where the authors found evidence to suggest the presence of both p- and g-modes. A comprehensive discussion on the treatment of these waves and extracting a conservative estimate of the diffusion coefficient in this region can be found in Section 3.4.2.

Preliminary results showed that the tracer densities were susceptible to enhanced mixing in the wave region. Multi-dimensional simulations of AGB stars have provided evidence that g-modes may be capable of mixing material (Freytag et al., 2010b). In order to ascertain whether the additional mixing is borne of waves or numerical diffusion a comprehensive study of the wave properties would be required, something beyond the scope of this thesis. Hence for the purposes of direct diffusion experiments we prioritise probing the region directly above the top of the wave region. The mixing timescale in the convectively unstable region, with convective velocities of ~ 1 km s^{-1}, is expected to be extremely short compared to timescales of accretion - effectively providing instantaneous mixing. As such, we prioritise probing the region beneath this, where $z < 0$ km. The convention used throughout this work is that our coordinate system is defined such that the lower Schwarzschild boundary lies at $z = 0$ km.

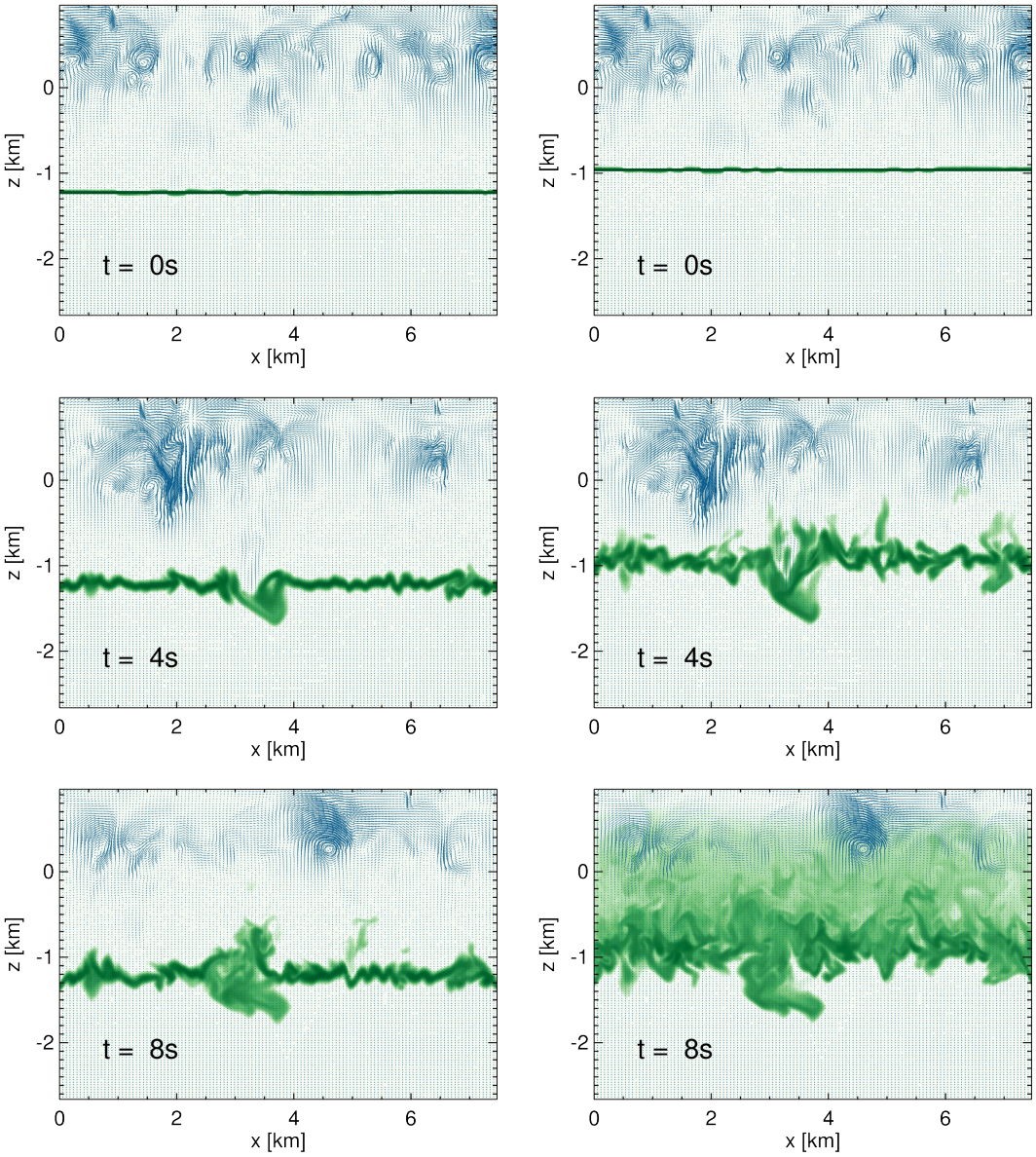

Figure 3.1: Demonstration of the tracer density implementation with CO^{5}BOLD for a simulation at $T_{\rm eff}$ = 13 500 K (Table 3.1, C3) with log g = 8.0 and box size 250^3. Snapshots of a 2D vertical slice through the simulation show the logarithmic tracer density (green) for two (left and right) of the multiple density arrays added to the simulation. The left and right columns are from exactly the same simulation, the only difference is the depth at which the shown tracer density (green) was added. Thus the convective velocities (blue) are identical between the left and right columns. For the tracer density, only values of $\rho_{\rm trace} \geq 1\,{\rm cm}^{-3}$ are shown. Convective velocities are shown in blue, where the magnitude is linear with line length. The depths on the y-axis have been adjusted such that the lower Schwarzschild boundary lies at $z = 0$ km. Animated versions of this figure are currently (at the time of publication) available at https://warwick.ac.uk/fac/sci/physics/research/astro/people/cunningham/movies/

We focus our attention on the seven simulations detailed in Table 3.1, all deep enough to fully enclose the convectively unstable layers and at least 4 pressure scale heights beneath the convectively unstable layers, defined by the region where the entropy gradient with respect to depth is negative, i.e., $z_{\mathrm{S,top}} > z > 0$ km. The tracer density method is implemented on all simulations in the table, from which diffusion coefficients are directly derived. Simulations A1, B2 & C3, corresponding to $T_{\mathrm{eff}} = 12\,000, 13\,000$ & $13\,500$ K, respectively, provide results for macroscopic diffusion across a range of temperatures with a fixed grid size (250^3). As an independent test of the results, these three simulations are analysed using the method of path integration, the methodology of which will be discussed in detail in Section 3.3.2.

Simulations C1 & C2, with $T_{\mathrm{eff}} = 13\,500$ K, are identical to C3, with the exception of grid resolution - and any numerical scheme adjustments, such as time steps, arising from this change in grid size. They are both analysed with the tracer density and path integration methods. The box sizes of 150^3 and $250^2 \times 150$, respectively, serve as a convergence test of the results with respect to spatial resolution. Simulations B1 & B2, with $T_{\mathrm{eff}} = 13\,000$ K and grid sizes 150^3 & 250^3, respectively, provide a similar test at a different effective temperature. Finally, simulation C1-2 is identical to C1, except for an extension in the x and y directions by a factor of two. This can provide a further convergence test and also inform us on the nature of the standing waves present in the bottom of the box.

Tracer density temporal evolution

A given tracer density array, inserted as a horizontal slab, is rapidly ($\sim \mu s$) smoothed by the velocity field, where the less deep and more vigorously convective layers promote this smearing to a greater extent. This is demonstrated in Fig. 3.1 for simulation C3 (see Table 3.1) at $T_{\mathrm{eff}} = 13\,500$ K. Here we show snapshots of a 2D vertical slice through 8 s of simulation time from the beginning of the diffusion experiment. Tracer densities (green) inserted 1.2 km (left) and 1.0 km (right) beneath the unstable layers can be seen to be advected by the convective flows (blue). The figure shows a range in tracer density of $1 \leq \rho_{\mathrm{trace}}/[\mathrm{cm}^{-3}] \leq 10^5$ with darker green corresponding to a higher tracer density. Clearly some of the distribution which began closer to the boundary of instability becomes incorporated into the unstable layers ($z \geq 0$ km) within $t \approx 8$ s, though as the tracer density is depicted logarithmically, the positional mean of the distribution remains near the initial position. We show the same evolution in Figs. 3.2 & 3.3 for simulations B1 and A1 (13 000 K and 12 000 K), respectively.

From the analytic solution of Eq. (3.1), in an ideal diffusion scenario an initially narrow distribution is expected to evolve in the form of a Gaussian for times $t > 0$. The spatial extent of the density fields in our simulations is quantified by the density-weighted

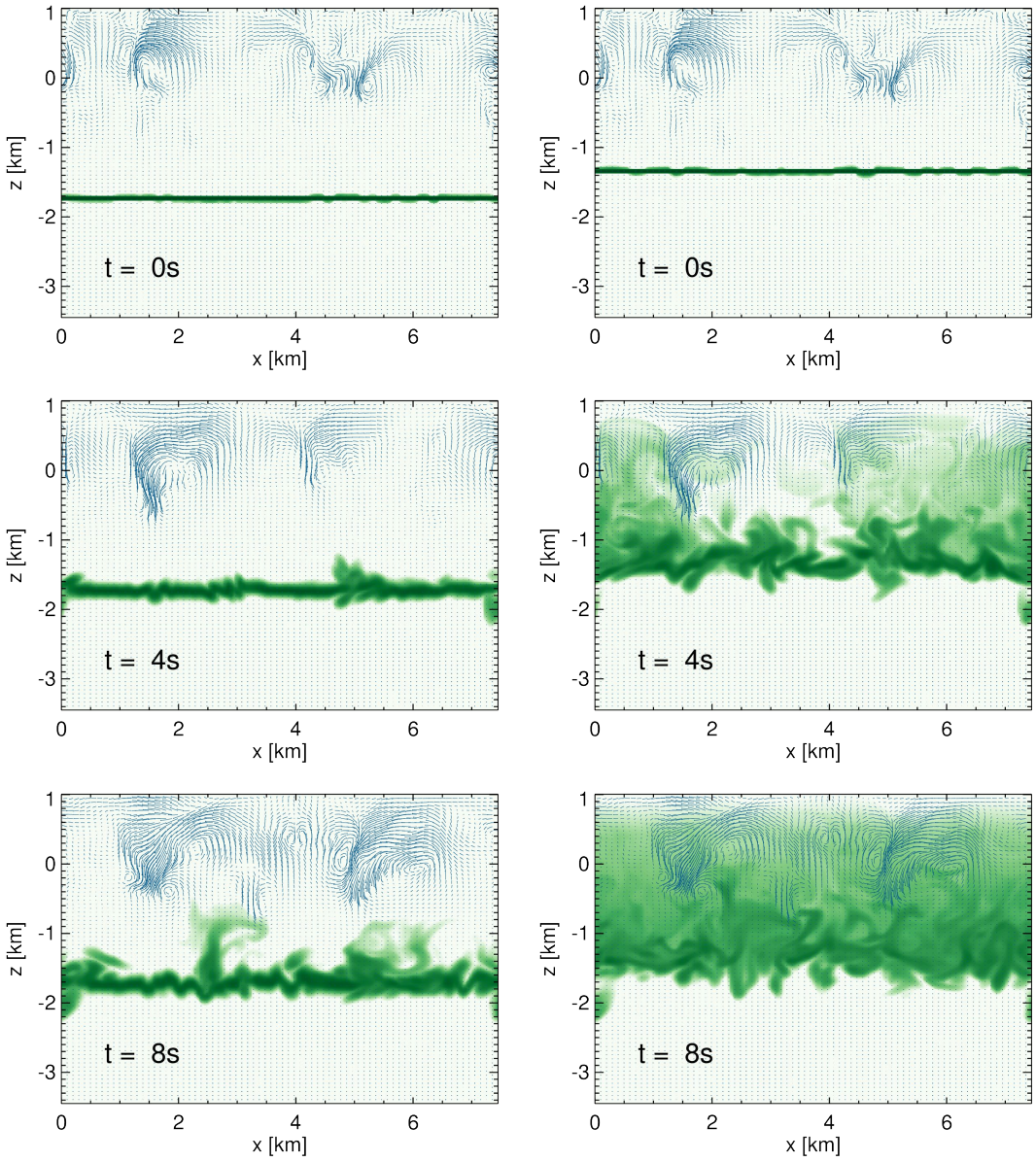

Figure 3.2: Similar to Fig. 3.1 for a simulation at $T_{\rm eff}$ = 13 000 K (Table 3.1, B1) with log g = 8.0 and box size 150^3.

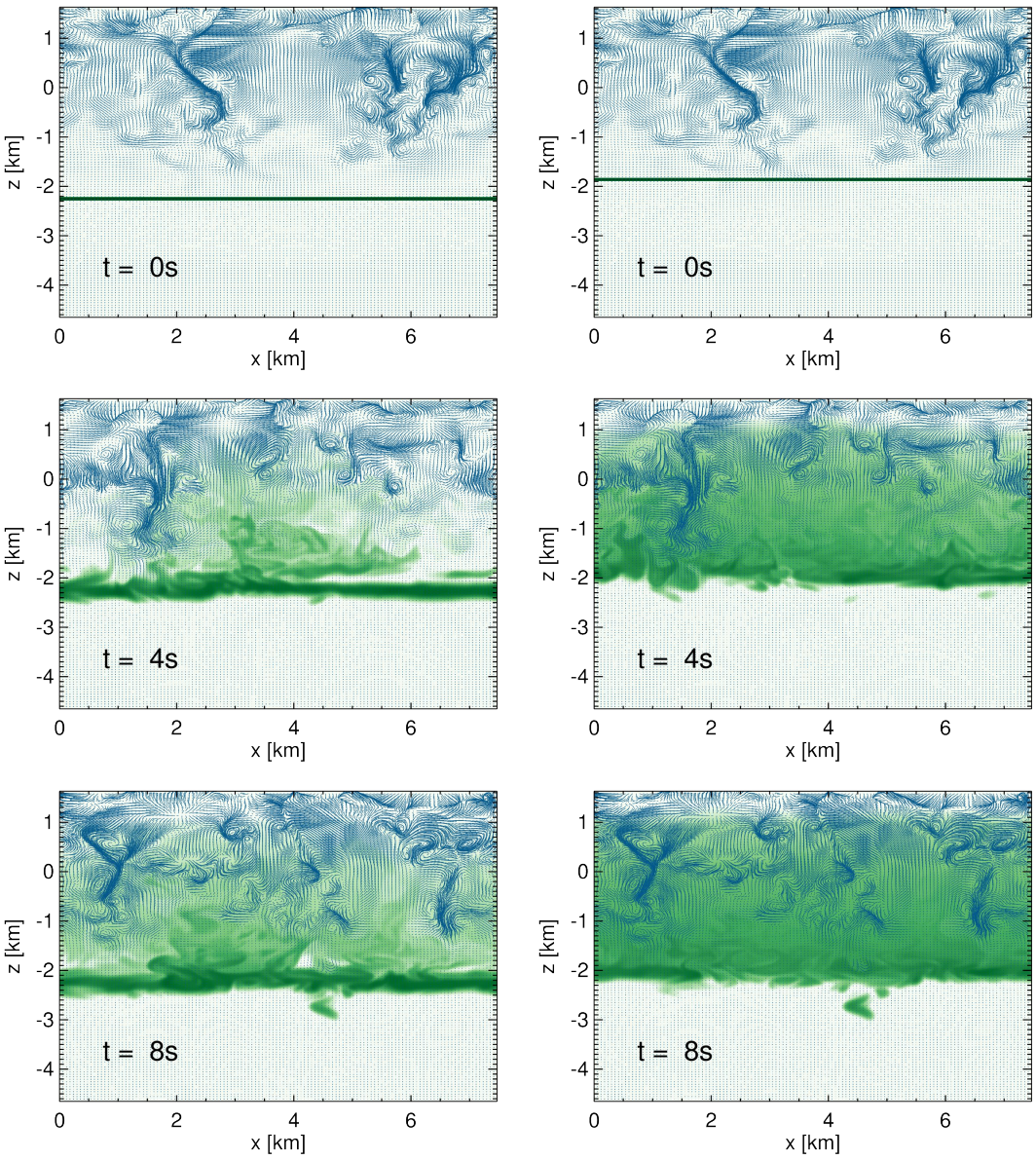

Figure 3.3: Similar to Fig. 3.1 for a simulation at $T_{\rm eff}$ = 12 000 K (Table 3.1, A1) with log g = 8.0 and box size 250^3.

standard deviation of the tracers, $z^*_{\rm rms}$, which is given by

$$z^*_{\rm rms} = \left(\frac{n_z}{n_z - 1} \sum_z \left(\rho_{\rm t}(z)(z - \langle z^* \rangle)^2 \right) \Big/ \sum_z \rho_{\rm t}(z) \right)^{1/2} \tag{3.4}$$

where $\rho_{\rm t}(z)$ is the horizontally-averaged, depth dependent tracer density, n_z is the number of cells in the vertical dimension and $\langle z^* \rangle$ is the density-weighted mean depth of the ensemble given by

$$\langle z^* \rangle = \left(\sum_z z \rho_{\rm t}(z) \right) \cdot \left(\sum_z \rho_{\rm t}(z) \right)^{-1} \tag{3.5}$$

To ascertain whether the ensemble of particles is evolving through a true diffusion process we plot the density-weighted standard deviation, $z^*_{\rm rms}$, as a function of time (see Fig. 3.4; middle panel). It is expected that for true diffusion, the square of the ensemble spread will evolve proportionally with time and we show the $\sqrt{t}$ fits made to the $z^*_{\rm rms}$ evolutions with dashed lines. The depth dependent diffusion coefficient, $D(z)$, is thus derived from Eq. (3.2) to be

$$2 \log_{10}(z^*_{\rm rms}(z,t)) = \log_{10}(t) + \log_{10}(2D(z)) \; . \tag{3.6}$$

The bottom panel of Fig. 3.4 shows the derived diffusion coefficients (circles) for the region extending 1.5 km beneath the lowest convectively unstable layer for simulation C3. Also shown are root mean square vertical velocity profiles - $v_{\rm z,rms}$ (dotted, orange) and $v^2_{\rm z,rms}$ (solid, blue) - time-averaged over the duration for which $\sqrt{t}$ fits are made (middle panel - dashed). It can be seen that the decline of the diffusion coefficient as a function of depth follows $D(z) = v_{\rm z,rms} \cdot 0.03$ km in the near-overshoot region, extending 0.8 km beneath the lower Schwarzschild boundary. For deeper layers, where $z < -0.8$ km, the diffusion coefficient is well described by $D(z) = v^2_{\rm z,rms} \cdot 0.23$ s.

Fig. 3.5 shows diffusion coefficients derived via this method for simulations B2 (left) at $T_{\rm eff} = 13\,000$ K and A1 (right) at $T_{\rm eff} = 12\,000$ K. We find that both of these simulations exhibit similar behaviour to the $T_{\rm eff} = 13\,500$ K simulation, with the depth dependence of the diffusion coefficient being described by $D(z) = v_{\rm z,rms} \cdot d_{\rm char}$ in the near-overshoot region and $D(z) = v^2_{\rm z,rms} \cdot t_{\rm char}$ in the deeper layers.

We find the transition from $v_{\rm z,rms}$ to $v^2_{\rm z,rms}$ behaviour occurs at $z = -0.8$, -1.2 and -1.6 km for simulations C3, B2, and A1 (with $T_{\rm eff} = 13\,500$, $13\,000$ and $12\,000$ K), respectively. The proportionality of transition depth with effective temperature is likely due to the inverse proportionality of convective velocity, or kinetic energy, and effective temperature in the range of these simulations. We find that the characteristic distance required to fit the near-overshoot region is relatively unchanging across the three temperatures, with

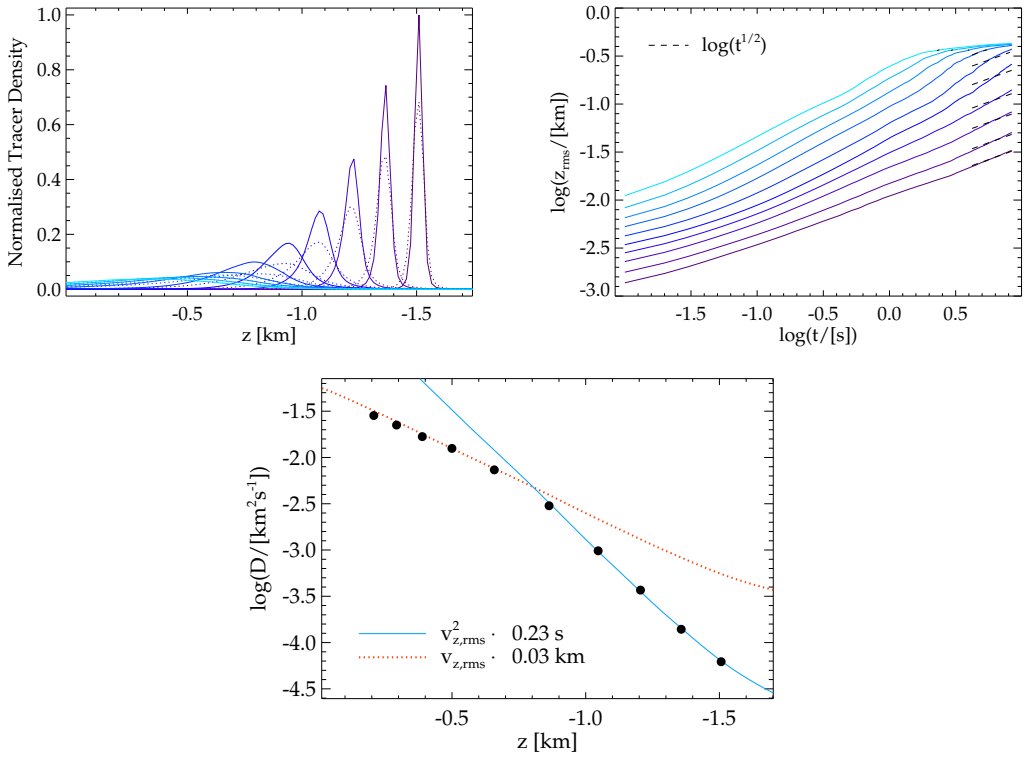

Figure 3.4: Analysis of massless density arrays implemented with the CO5BOLD tracer density for a simulation at $T_{\rm eff}$ = 13 500 K (Table 3.1; C3) with log g = 8.0 and box size 250^3. *Top-left:* Horizontally-averaged tracer number density profile at first (solid) and last (dashed) time step used in $\sqrt{t}$ fitting (see middle panel). Colours correspond to tracer densities added at different depths. *Top-right:* Evolution of the ensemble spread characterised by the tracer density-weighted standard deviation, $z^*_{\rm rms}$. Gaussian spread (solid) and a best fit of $\sqrt{t}$ (dashed). *Bottom:* Diffusion coefficients (circles) computed using Eq. 3.6. Vertical velocity profiles $v_{\rm z,rms}$ and $v^2_{\rm z,rms}$ are shown in orange (dashed) and blue (solid), respectively. The depths on the x-axis have been adjusted such that the lower Schwarzschild boundary lies at z = 0 km. We note that the full extent of the x-axis is considered convectively stable under the Schwarzschild criterion, yet considerable mixing is observed.

$d_{\rm char} \approx 0.03$ km, whilst the characteristic time required to fit the far-overshoot region varies between $0.06 \leq t_{\rm char}/[{\rm s}] \leq 0.28$.

Previous results have shown that this characteristic time could be estimated as $t_{\rm char} \sim H_p/v_{\rm z,rms}$ (i.e., Eq. (9) of Freytag et al. 1996) where the pressure scale height, H_p, and RMS vertical velocity are evaluated at the base of the convection zone. From an examination of Table 3.1, which provides these two quantities evaluated at the lower Schwarzschild boundary ($H_{p,{\rm S,bot}}$ and $v_{\rm z,S,bot}$), we find estimates of a characteristic timescales of $t_{\rm char} = 0.12$, 0.14 and 0.23 s for simulations A1, B2 and C3, respectively. These agree with the characteristic times which rendered the best fit to the $v^2_{\rm z,rms}$ lines to within a factor 0.5–2.0.

We find that all three simulations have sufficient motion from convective overshoot to mix material for at least 1.5 km beneath the lowest formally convective unstable layer, corresponding to at least 2.5 pressure scale heights. We observe in all cases two distinct behaviours of the overshoot diffusion coefficient. In the near-overshoot region, which extends 0.8–1.6 km beneath the unstable layers, the diffusive efficacy decays with $v_{\rm z,rms}{\cdot}d_{\rm char}$. In deeper layers the mixing efficacy decays more rapidly, following instead a $v^2_{\rm z,rms}{\cdot}t_{\rm char}$ profile.

The locations of the derived diffusion coefficients in Figs. 3.4 & 3.5 can be compared with the y-axis positions in Figs. 3.1–3.3 where snapshots show the evolution of tracer densities (green). For simulation C3 (13 500 K) the tracer densities were placed in the far-overshoot region (see Fig. 3.1) at $z \approx -1.0$ km and $z \approx -1.2$ km. It is evident that overshoot plumes are capable of penetrating this layer and mixing material in deeper layers ($z < -1.2$ km). These deeper layers correspond to the region which feels the effect of waves trapped in the base of our simulations. The tracer density method is susceptible to artificial diffusion driven by the increased velocities here, typically leading to an overestimation of the diffusion coefficients in this region. The increased velocities manifest as the upward inflexion visible at $z \approx -1.9$ km in the right panel of Fig. 3.5. This provides a lower limit on the depth at which a diffusion coefficient can be directly derived via the method of tracer density. In Section 3.4.2 we will discuss an approach which provides a conservative estimate of the decay of mixing efficacy toward the stellar interior and beyond the region directly simulated.

Effects of numerical resolution

The physical structures we wish to characterise include narrow overshoot plumes which require grid points to be spaced sufficiently close for these structures to be spatially resolved. Furthermore, numerical diffusion could adversely impact our results. We perform a convergence test on the dependence of our results on spatial resolution by using the tracer density to analyse simulations (C1, C2 & C3) at three different resolutions (150^3, $250^2 \times 150$ and 250^3) and $T_{\rm eff} = 13\,500$ K. We note that the time steps are changed accordingly to respect

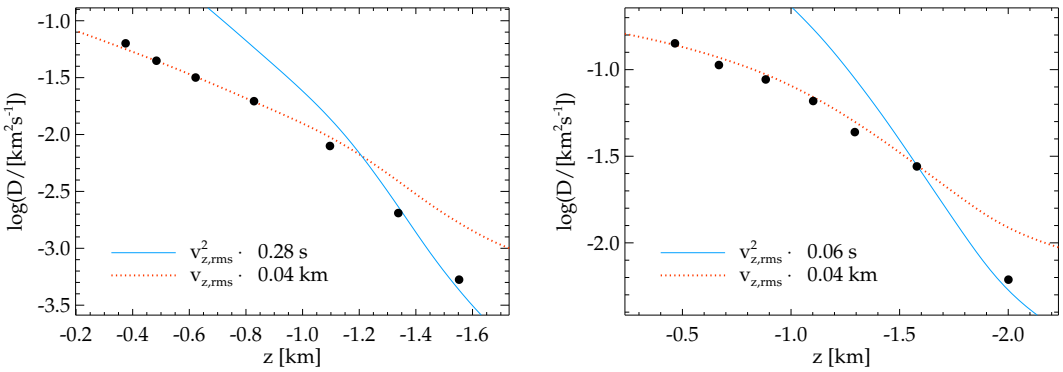

Figure 3.5: Similar to lower panel of Fig. 3.4 for simulations at $T_{\rm eff}$ = 13 000 K (left, Table 3.1, B2) and $T_{\rm eff}$ = 12 000 K (right, Table 3.1, A1), both with log g = 8.0.

the Courant condition (Freytag et al., 2012).

Fig. 3.6 shows diffusion coefficients derived for all three simulations and, qualitatively, we find that in the near-overshoot region the correlation of the diffusion coefficient with the vertical velocity profile, $v_{\rm z,rms}$, is insensitive to changes in spatial resolution for a fixed box geometry. We observe that in the far-overshoot region (i.e., $z < -0.8$ km) the diffusion coefficients tend to the $v^2_{\rm z,rms}$ profile as the horizontal resolution increases. No significant change is seen for an increase in the vertical resolution. We conclude that a resolution of $250^2 \times 150$ is sufficient to resolve the physical processes involved with macroscopic diffusion driven by convective overshoot for an atmosphere with $T_{\rm eff}$ = 13 500 K and log g = 8.

We now discuss a complimentary test to the above where the grid size is fixed at 150^3 and the box geometry is allowed to vary. The two simulations C1 and C1-2 from Table 3.1 have horizontal extents in the x and y direction of 7.5 and 15.0 km, respectively. This tests the spatial resolution in the horizontal plane and as the vertical extent is kept constant across both simulations this also serves as a test of varying aspect ratio. It can be seen from Fig. 3.7 that for layers deeper than 1 km beneath the unstable layers the diffusion coefficient exhibits similar behaviour, though decays less rapidly. Within 1 km of the unstable layers the diffusion coefficient behaviour is unchanged for an augmentation in the horizontal directions by a factor of two.

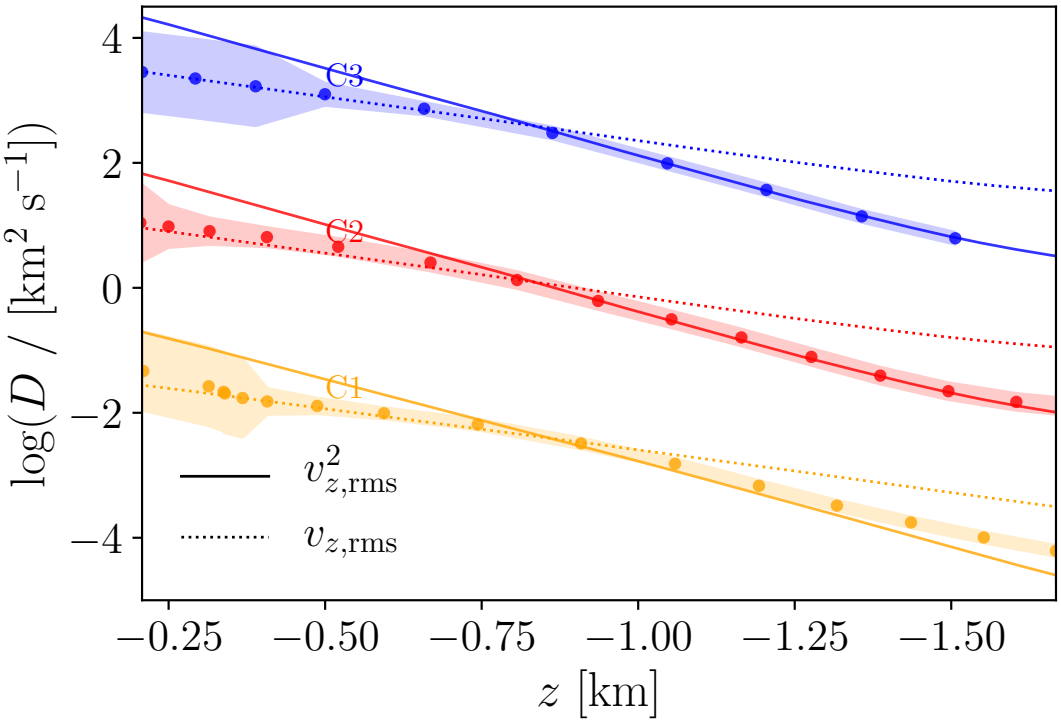

Figure 3.6: Spatial resolution sensitivity test using tracer density analysis for simulations C1, C2 and C3 and grid sizes 150^3 (orange), $250^2 \times 150$ (red) and 250^3 (blue), respectively, and $T_{\mathrm{eff}} = 13\,500$ K and $\log g = 8.0$. The time-averaged vertical velocity profiles $v_{\mathrm{z,rms}}$(dashed) and $v^2_{\mathrm{z,rms}}$(solid) are shown for each simulation with the diffusion coefficient extracted from each simulation (circles). The filled error bars represent the standard deviation of the $\sqrt{t}$ fits. Simulations C2 and C3 have been offset by $\log D = 2.5$ and 5 for clarity.

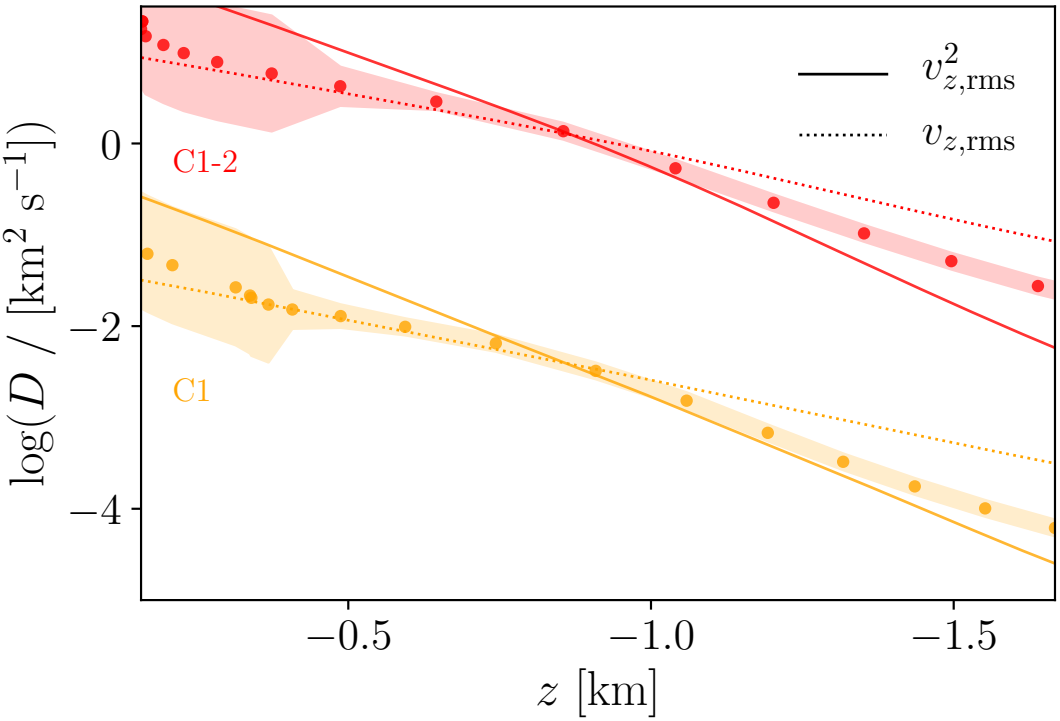

Figure 3.7: The derived diffusion coefficients for simulations C1 and C1-2 from Table 3.1 with $T_{\mathrm{eff}} = 13\,500$ K, $\log g = 8.0$ and grid size 150^3. The simulations differ only in horizontal size where, compared to simulation C1 (orange), the geometric extents in the x and y direction have been increased by a factor of two for simulation C1-2 (red). The time-averaged vertical velocity profiles $v_{\mathrm{z,rms}}$(dashed) and $v^2_{\mathrm{z,rms}}$(solid) are shown for each simulation with the diffusion coefficient extracted from each simulation (circles). The filled error bars represent the standard deviation of the $\sqrt{t}$ fits. Simulation C1-2 has been offset by $\log D = 2.5$ for clarity.

3.3.2 Method II: Path integration

We discuss in the following the derivation of diffusion coefficients using a method where the path of individual tracer particles is followed directly through the simulation. In principle, path integration should give the same results as the tracer density method presented in the previous section if we were to horizontally average tracers, with any difference caused by numerical schemes. Ostensibly, the way in which the diffusion coefficient is derived from either method, path integration or tracer density, is also much the same. We still look for a true diffusion process based on the spread evolving with the square root of time.

Without an implemented tracer particle module, the path integration is performed using the velocity field of pre-computed CO^{5}BOLD snapshots. This method is closer to the one presented in Freytag et al. (1996) and it allows a more direct comparison to their results.

To ensure that the path of the seeds is fully interacting with the physical processes within the simulation we are careful to sample velocity information sufficiently frequently. To account for temporal changes in the velocity field the sampling rate should be high enough that changes in the velocity field are small. Spatial changes in the velocity field, which dictate the path taken by the massless tracers, are handled by the integration time step being sufficiently small.

Fig. 3.8 shows the depth dependent maximum velocity in units of grid points per second for simulation C3, where the y-axis can be interpreted as the minimum sampling frequency for any given depth. Ideally data would be sampled such that massless particles are unlikely to travel much further than a few grid points in one sampling period. The figure shows that to capture fully the dynamical processes at every layer, velocity information would be required at intervals of $\Delta t \sim 10^{-3}$ s, though this is only necessary if we want to probe the most vigorous convective layers. It can be seen in Fig. 3.8 that an order of magnitude longer sampling period, $\Delta t \sim 10^{-2}$ s, is sufficient and this also represents the chosen integration period.

Fig. 3.9 illustrates the vertical displacement of seeds for the simulation C3 at $T_{\rm eff}$ = 13 500 K with grid size 250^3 over 8 seconds. At five depths beneath the unstable layers, 25×25 seeds were traced, at every tenth grid point. This lower number of particles helps to clearly demonstrate the depth dependence of the spread of particles, with those in deeper layers spreading less. For the path integration analysis proper, which we will discuss in the next section, we use at least two orders of magnitude more seeds at every depth.

For a given depth we place seeds at every grid point in a horizontal slice, which for the highest resolution simulations presented here (A1, B2 and C3) corresponds to 62500 seeds per depth. The three dimensional position, $r_{x,y,z}(t)$, of a tracer beginning at grid

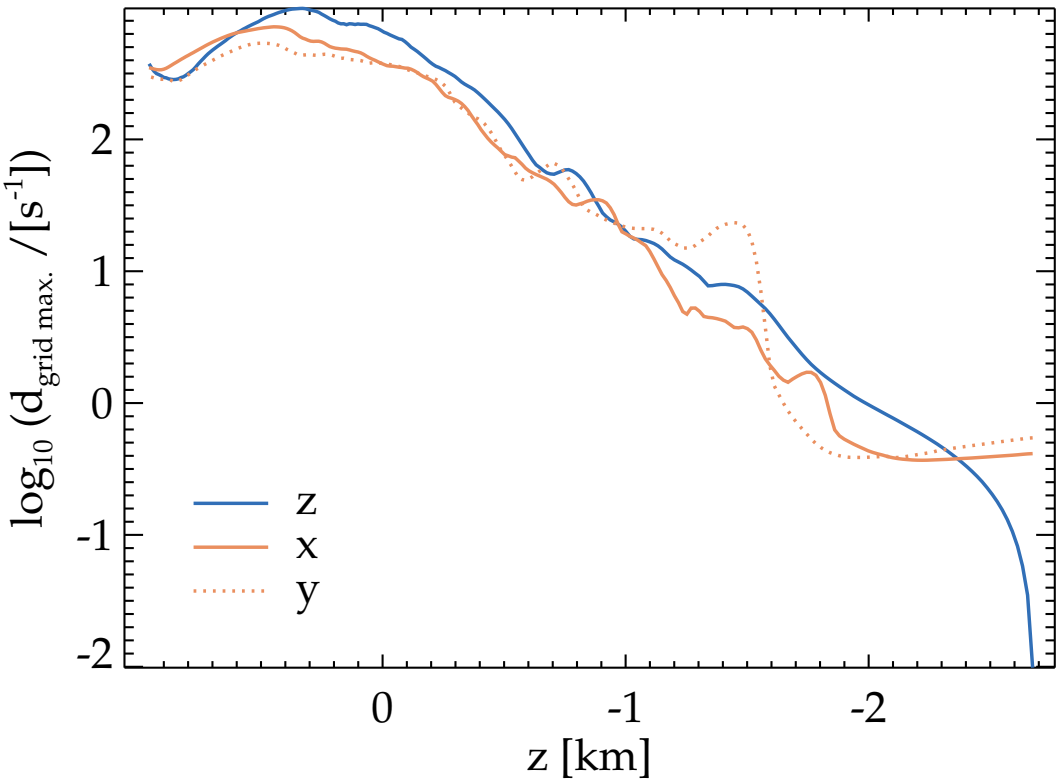

Figure 3.8: Depth dependence of maximum grid point displacement per second for simulation C3 from Table 3.1 with $T_{\rm eff}$ = 13 500 K and log g = 8.0. Vertical (blue) and horizontal (orange) displacements are shown independently. Displacements have been maximised over the final 25 ms of the diffusion experiment.

point $r = [x_0, y_0, z_0]$ is given by

$$r_{x,y,z}(t) = r_{x_0,y_0,z_0}(t_0) + \int v_{x,y,z}(t)\, dt\ , \tag{3.7}$$

where v_i represents the $i^{\rm th}$ component of the velocity. This integration is performed using a forward Euler method, where $dt = \Delta t_{\rm diff\ exp}$ is the time interval between consecutive snapshots of extracted velocity information (see Table 3.1). Although the quantity of interest is the depth dependence of diffusive efficacy it is necessary to track the three-dimensional position of each tracer so that all the physical processes present in our simulations have the opportunity to influence the trajectory of the particles.

For the high resolution simulations, Eq. (3.7) is solved 62500 times at each depth and time step such that we follow $\approx 10^7$ tracers per simulation. As our primary focus is the region beneath the unstable layers we present here tracers placed at every second vertical grid point for the region defined by $z < 0$ km, corresponding to $\approx 10^{6.5}$ tracer particles.

As discussed in Section 3.3.1, to derive a diffusion coefficient we need to quantify

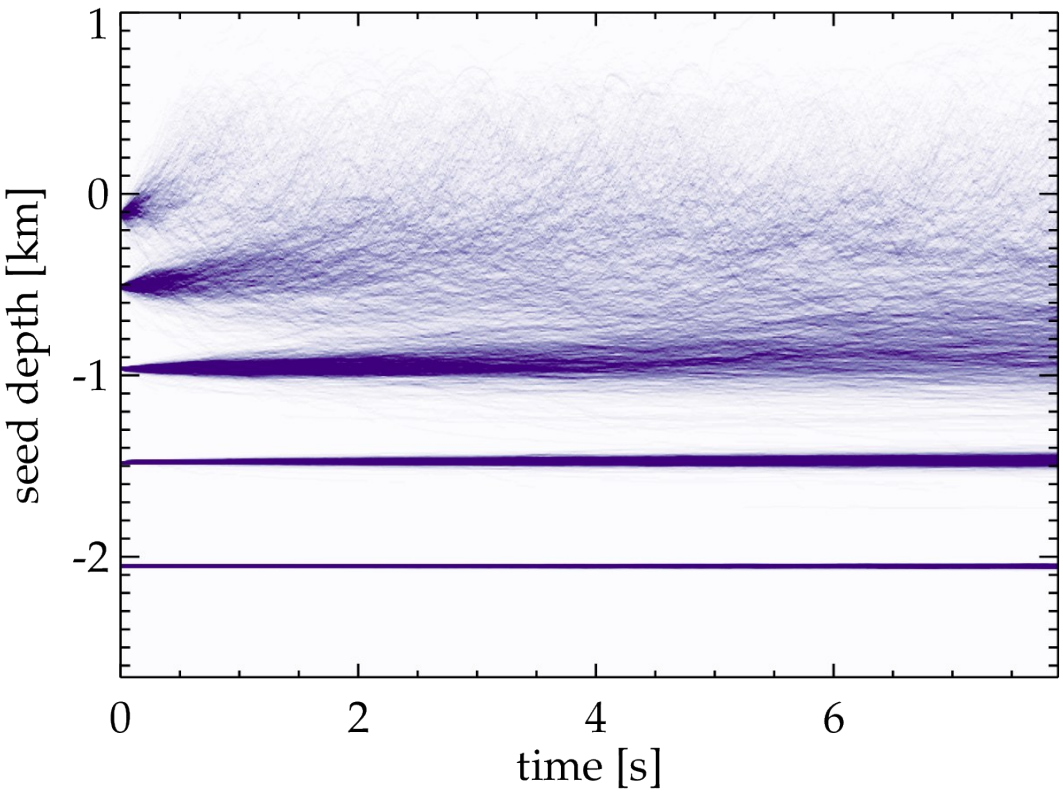

Figure 3.9: Tracer particle evolution for simulation C3 with $T_{\rm eff} = 13\,500\,\mathrm{K}$ and $\log g = 8.0$. Vertical displacement of 25×25 seeds (placed at every tenth horizontal grid point for clarity), each placed at five different atmospheric depths in the overshoot region. The colour intensity increases linearly with seed density.

and fit the ensemble spread. With the method of path integration we track the actual position of seeds and thus are able to access the mean square displacement, $z_{\rm rms}$, given by

$$z_{j,\rm rms}(t) = \left(\langle (z_j(t) - \langle z_j(t) \rangle_{x,y})^2 \rangle_{x,y} \right)^{1/2} , \tag{3.8}$$

where $z_j(t = 0)$ refers to the initial vertical position of a 'tray' of seeds placed at depth j and $\langle z_j \rangle_{x,y}$ to the mean vertical position of the seeds.

Eq. (3.8) is the standard deviation of the ensemble, making the retrieval of a meaningful spread computationally simple and statistically robust. We can then derive a diffusion coefficient from Eq. (3.2) as

$$2 \log_{10}(z_{\rm rms}(z,t)) = \log_{10}(t) + \log_{10}(2D(z)) . \tag{3.9}$$

The evolution of this quantity is shown in the top panel of Fig. 3.10 for simulation C3. The final half of the total evolution time is fitted with lines of $z_{\rm rms} \sim t^{1/2}$ (thick). All of the spread evolutions shown correspond to tracers which began beneath the unstable layers, with the distance beneath the lower Schwarzschild boundary indicated on the figure.

Characterising diffusion

Our experiments with path integration allow us to derive diffusion coefficients that can be compared to the method of density arrays (Section 3.3.1). We first discuss the results for simulation C3 with $T_{\rm eff} = 13\,500$ K and grid size 250^3 in Fig. 3.10. For the region within the convectively unstable layers ($0.5 > z/[\rm km] \geq 0.0$) it is expected that seeds are mixed rapidly (Freytag et al., 1996) with the spread increasing linearly with time. Just below the convectively unstable region ($z < 0.0$ km) seed ensembles are likely to couple with the convectively unstable layers over a short timescale, $t < 1$ s. This manifests in the top panel of Fig. 3.10 as a plateau in ensemble spread, $z_{\rm rms}$. Once the upper edge of a seed ensemble reaches the convectively unstable region, particles are carried in bulk by convective velocities and the statistical, enesmble averaged model of diffusion is no longer justified. Deriving a diffusion coefficient for the upper layers would require fitting the region in time before the seeds couple with the convectively unstable layer. There is significantly less data in this region and for this reason no diffusion coefficients are computed here for $z > -0.2$ km.

The smoothness of the $z_{\rm rms}$ evolution demonstrates that the resolution of this simulation provides a more than adequate sample of tracers from which robust statistics are drawn. The fits by $\sqrt{t}$ functions are excellent, implying that the average distribution of these tracers, whilst moved by convective overshoot, can unequivocally be described as a diffusion process. The diffusion coefficients computed from this evolution via Eq. (3.8) are shown in

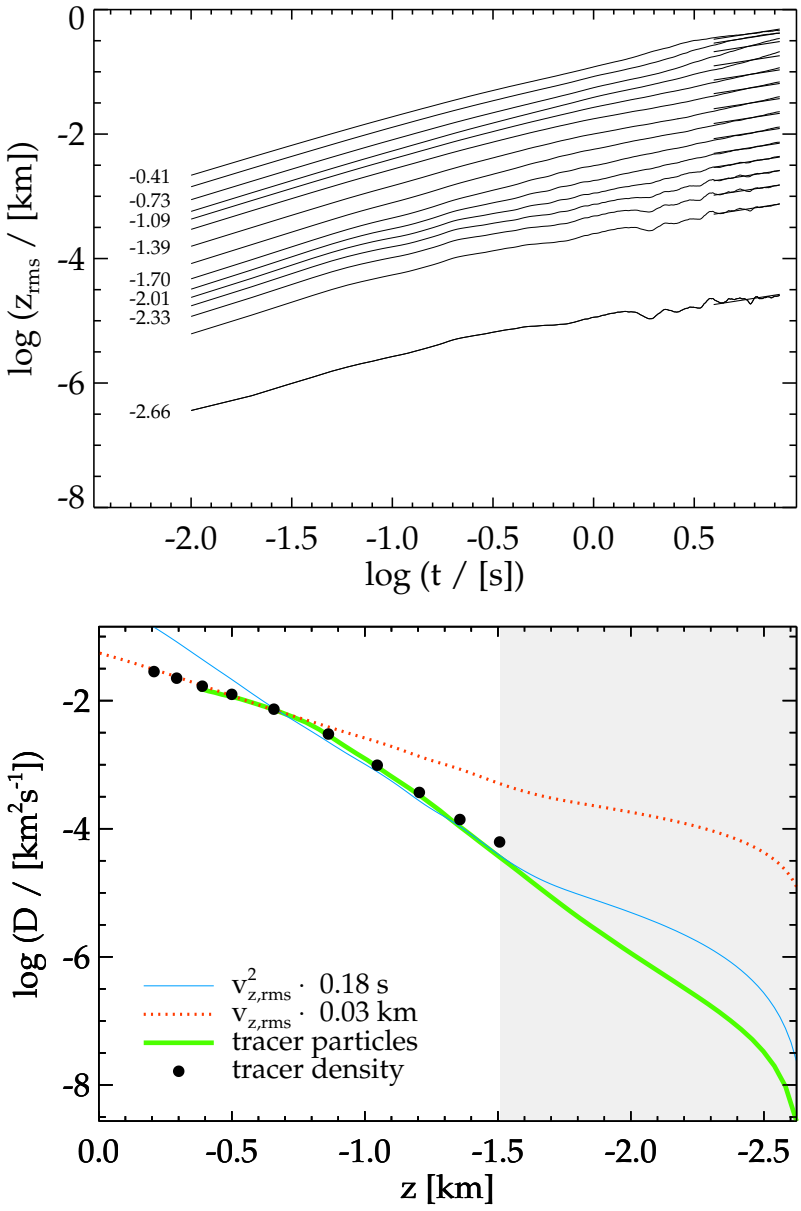

Figure 3.10: Path integration analysis of simulation C3 with $T_{\rm eff}$ = 13 500 K and grid size 250^3, with plots akin to the two lower panels of Fig. 3.4. *Top:* Standard deviation for 15 of the 62 unique depths at which seeds were placed. The $\sqrt{t}$ fits are shown in the thick, small segments on the right-hand-side. The mean initial depth of each set of 249 × 249 seeds is indicated, for every other distribution plotted. *Bottom:* Diffusion coefficients computed from the method of path integration (solid green) are shown with vertical velocity profiles ($v_{\rm z,rms}$, dotted-orange, and $v^2_{\rm z,rms}$, solid-blue). Also shown are the results from the tracer density experiment for the same simulation (black circles) from the bottom panel of Fig. 3.4. The layers impacted by waves (see Section 3.4.2) are indicated by the grey shaded region. No tracer density results are shown in this region due to the artificial enhancement of the diffusion coefficients (see Section 3.3.1).

the lower panel of Fig. 3.10 in green. This plot shows a strong correlation of the diffusion coefficient with $v_{\mathrm{z,rms}}$ in the region $-0.3 > z/[\mathrm{km}] > -0.8$, which is in agreement with the results from Method I (black circles) for the same simulation (Fig. 3.4; lower panel). The diffusion coefficients computed by the method of path integration are also in agreement in the far-overshoot region ($z < -0.8$ km) where a strong correlation with $v^2_{\mathrm{z,rms}}$ is evident. This is again in agreement to the prediction made by Freytag et al. (1996) where the authors used the method of path integration for a simulation at $T_{\mathrm{eff}} = 13\,400$ K.

Figs. 3.11 & 3.12 show the results for simulations B2 and A1, respectively, which have the same resolution as C3 and $T_{\mathrm{eff}} = 13\,000$ K and 12 000 K. It is again clear that the diffusion coefficients derived using the method of path integration are in good agreement with the tracer density method at all depths for which results are available. In the wave-dominated region (grey shaded), where tracer density results proved inaccessible, the method of path integration is able to separate diffusive action of the overshoot motions from the essentially reversible motions due to waves. This is evident from the flattening out of $v_{\mathrm{z,rms}}$ profile whilst the diffusion coefficient continues to follow an exponetial decay towards the core. This effect becomes more obvious as the effective temperature decreases, with simulation A1 at 12 000 K showing a sharp drop at the top of the wave region. In simulations A1 and B2 the diffusion coefficient flattens out at $z = -2.4$ and -2.5 km, respectively. This likely represents the limit of the path integration method to disentangle the two kinds of motion and further work would be required to ascertain the physical meaning of this behaviour.

Effects of numerical resolution

We present here a test of the diffusion coefficient's dependence on spatial resolution derived via the method of path integration. Fig. 3.13 shows the results for the two simulations C1 (top panel) and C2 (bottom panel) which were prepared with grid size 150^3 and $250^2 \times 150$, respectively, to compare to the 250^3 simulation shown in Fig. 3.10 with the same effective temperature. Qualitatively, both simulations retrieved similar behaviour in the diffusion coefficient compared to simulation C3 - with a diffusion coefficient scaling with $v_{\mathrm{z,rms}}$ for 0.8 km beneath the unstable layers and with $v^2_{\mathrm{z,rms}}$ for deeper layers with $z < -0.8$ km.

We observe a similar behaviour to the resolution test performed in Section 3.3.1 for the tracer density method with diffusion coefficient tending to $v^2_{\mathrm{z,rms}}$ in the far-overshoot region as the horizontal resolution increases. Qualitatively we also see no change as the vertical resolution increases and thus conclude the results are derived from sufficiently resolved simulations.

The three simulations are also in good agreement on the absolute value of the diffusion coefficient which is most readily seen by examining the characteristic distances and times required to fit the $v_{\mathrm{z,rms}}$ and $v^2_{\mathrm{z,rms}}$ profiles to the diffusion coefficients.

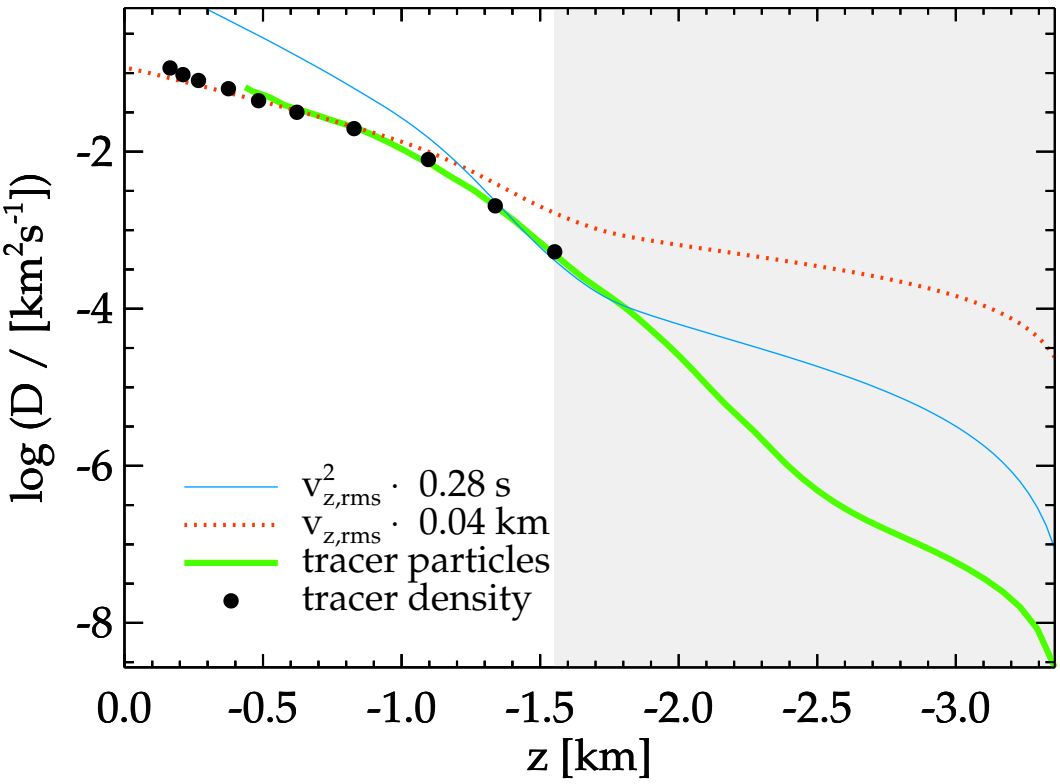

Figure 3.11: Results of path integration analysis of simulation B2 with $T_{\rm eff}$ = 13 000 K and grid size 250^3. Akin to lower panel of Fig. 3.10.

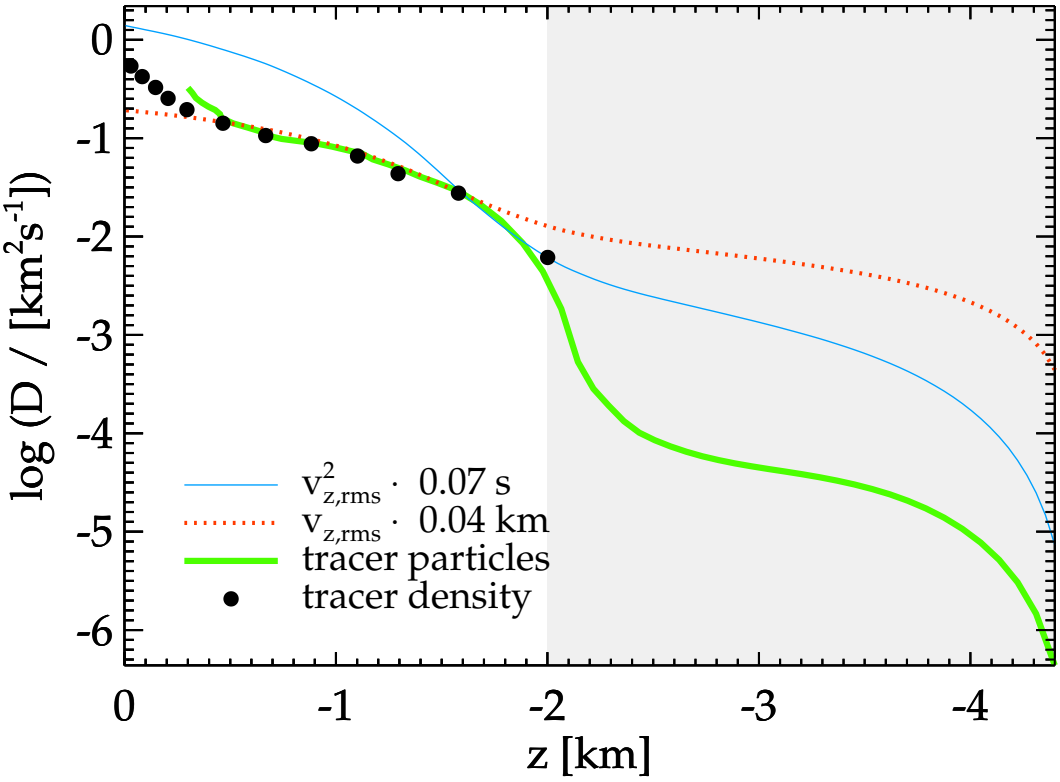

Figure 3.12: Results of path integration analysis of simulation B2 with $T_{\rm eff}$ = 12 000 K and grid size 250^3. Akin to lower panel of Fig. 3.10.

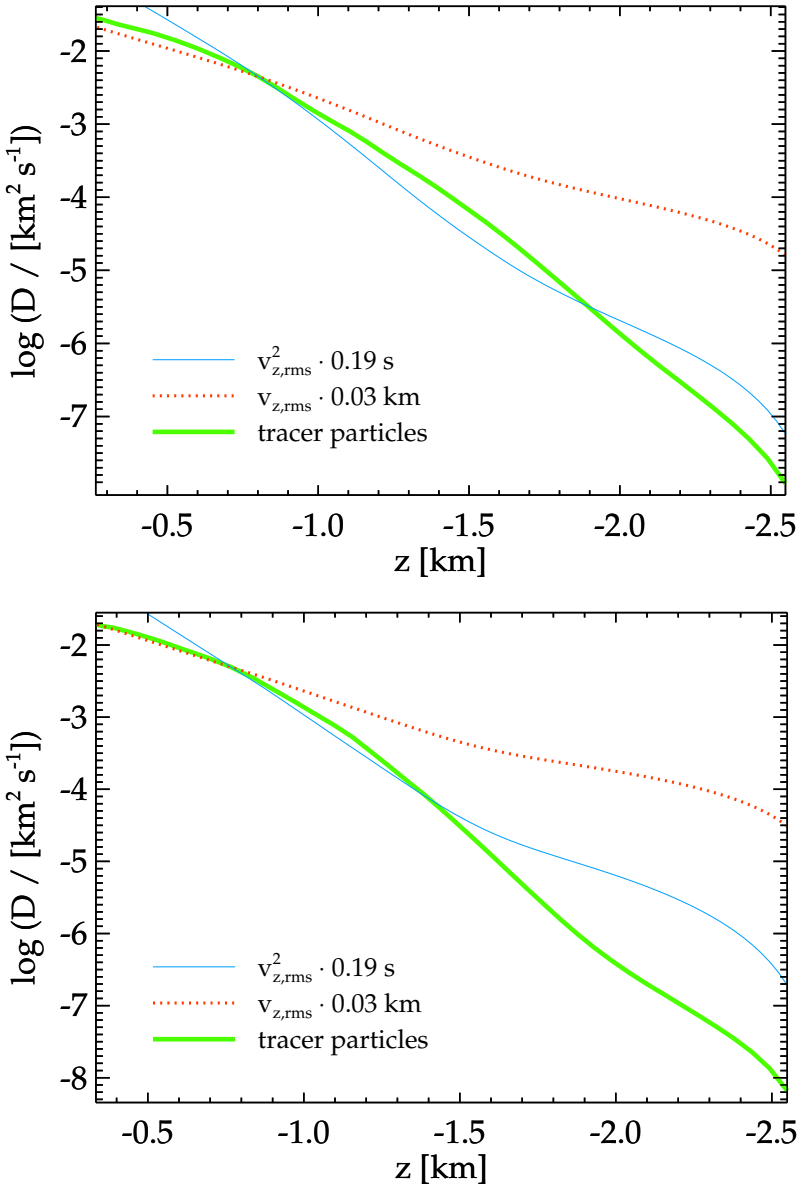

Figure 3.13: Similar to lower panel of Fig. 3.10 for simulations C1 (top) and C2 (bottom) from Table 3.1 with $T_{\rm eff}$ = 13 500 K with $\log g$ = 8.0 and resolutions 150^3 and $250^2 \times 150$, respectively.

What is evident from the analysis of the five simulations discussed throughout this section is that the vertical velocity profile is likely to be of great significance to the characterisation of diffusive efficacy beneath the convectively unstable layers, especially if one wishes to not perform a direct diffusion experiment at every temperature of interest. The scaling of the diffusion coefficient with $v_{\mathrm{z,rms}}$ immediately beneath the unstable layers and with $v^2_{\mathrm{z,rms}}$ in deeper layers found in both of tracer experiments is in good agreement with the dependence observed by Freytag et al. (1996). Both approaches agree in terms of the observable prediction, which is that trace elements are fully mixed in the overshoot region $\approx 2.5 - 3.5$ pressure scale heights immediately beneath the convection zone, with mixing timescales still orders of magnitudes shorter than those typical of microscopic diffusion. Furthermore, we emphasise that both methods are impacted by standing waves and do not currently allow to directly estimate the full extent of the mixed regions and the total mass of trace metals in a white dwarf, which is therefore the goal of Section 3.4.

3.4 Results

In Section 3.3 we detailed the two methodologies used in this study to probe the mixing efficiency of macroscopic diffusion due to convective overshoot, namely the inbuilt CO^{5}BOLD tracer density and path integration of seeds. While standing waves near the bottom of the simulations prevented us to simulate macroscopic diffusion over the full convective overshoot region, our results highlighted the possibility of using $v_{\mathrm{z,rms}}$ and $v^2_{\mathrm{z,rms}}$ as proxies for macroscopic diffusion. We therefore use the extended grid of CO^{5}BOLD simulations presented in Section 3.2.2 to study $v_{\mathrm{z,rms}}$ in detail for a wide range of depths and T_{eff} values. Then, in Section 3.4.2 we develop a framework to lessen the contribution of waves. We adopt this approach as fully quantifying the contribution of waves to mixing is beyond the scope of this work. Though there exists some evidence to suggest waves may contribute to the vertical mixing of material (Freytag et al., 2010b), our philosphy is that by removing their contribution we can provide a lower limit on the mixed mass.

3.4.1 Dynamical and thermal properties

We rely on the 15 deep and closed simulations presented in Table 3.2 and described in Section 3.2.2, covering the range $11\,400\,\mathrm{K} \leq T_{\mathrm{eff}} \leq 18\,000\,\mathrm{K}$. Selected mean quantities are shown in Figs. 3.14-3.15 for all simulations computed in the extended grid.

Radiative energy transport becomes fully dominant for DA white dwarf atmospheres above $T_{\mathrm{eff}} \approx 14\,000\,\mathrm{K}$ as illustrated by the bottom panel of Fig. 3.14. This warmer end of the grid is convectively unstable according to entropy profiles (Fig. 3.14, third panel from the top) but not convectively efficient i.e., negligible energy is transported in convective flows.

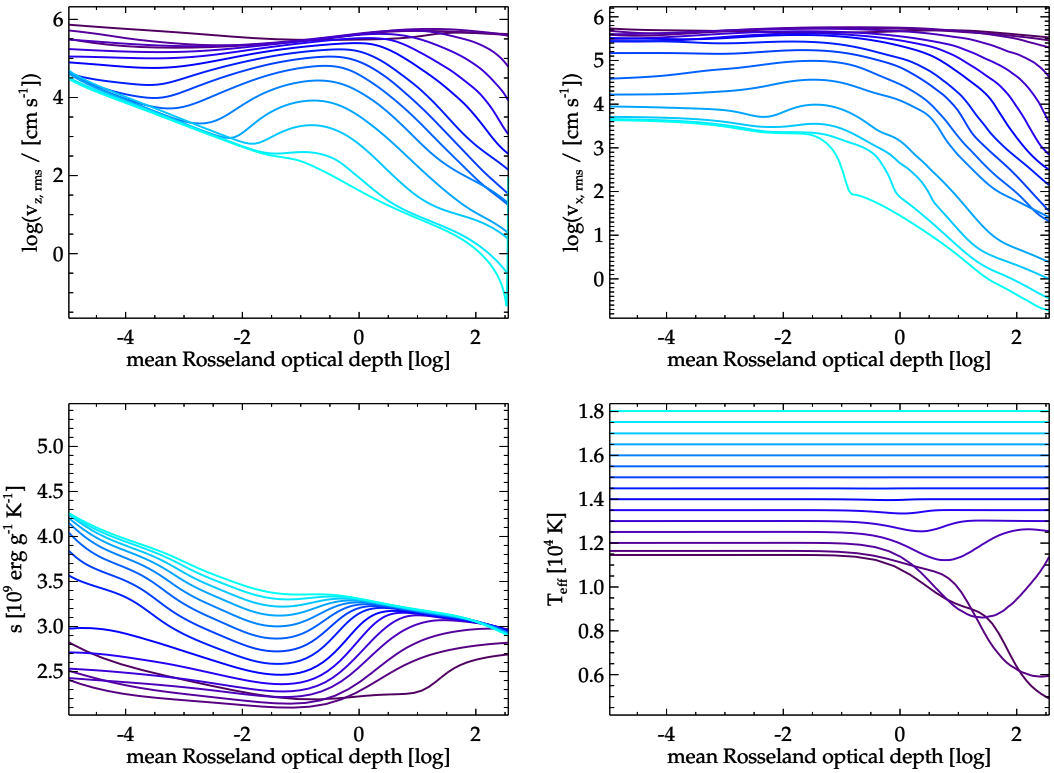

Figure 3.14: Dynamical and thermodynamic quantities extracted from the grid of deep 3D simulations (Table 3.2) as a function of average Rosseland optical depth. *Left to right, top to bottom:* Vertical component of convective velocities, horizontal component of convective velocities, entropy and effective temperature. Effective temperature is calculated as $T_{\rm eff} = \sqrt[4]{F_{\rm rad}/\sigma}$ where $F_{\rm rad}$ is the radiative flux and σ is the Stefan-Boltzmann constant. Line colours correspond to simulations at different effective temperatures and can be inferred by the intersection of each line with the y-axis in the bottom-right plot.

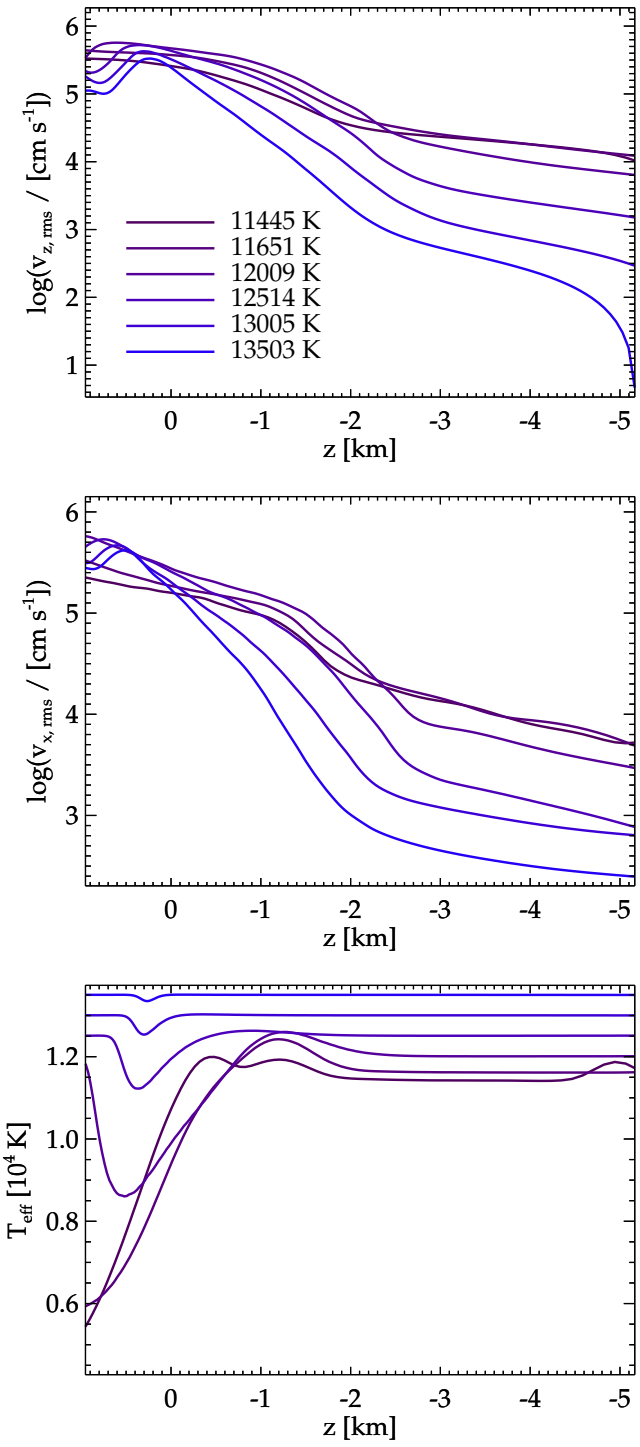

Figure 3.15: Similar to Fig. 3.14 but for models exhibiting sizable convection (11 400 $\geq T_{\rm eff}$ / [K] $\geq$ 13 500) and as a function of geometric depth.

In contrast, the three lowest effective temperature simulations ($T_{\rm eff}$ = 11 400, 11 600 and 12 000 K) can be seen in Fig. 3.15 to have deep wells in their radiative flux profiles which implies a large proportion of the energy carried in convective flows. Fig. 3.16 shows the time-averaged Péclet number, evaluated at $\tau_{\rm R} = 1$, as a function of $T_{\rm eff}$. The Péclet number is given by Tremblay et al. (2013b) as

$$\mathrm{Pe} = \frac{t_{\rm rad}}{t_{\rm adv}} = \frac{\langle\rho\rangle\langle c_p\rangle v_{\rm rms}\tau_{\rm e}}{16\sigma\langle T\rangle^3}\left(1+\frac{2}{\tau_{\rm e}^2}\right), \tag{3.10}$$

where $t_{\rm rad}$ is the radiative timescale and $t_{\rm adv}$ the advective, or convective turnover, timescale, c_p is the specific heat per gram, T the temperature, σ the Stefan-Boltzmann constant, and $\tau_e = \langle\kappa_{\rm R}\rangle\langle\rho\rangle H_p$ the characteristic optical thickness of a disturbance with size H_p, for $\kappa_{\rm R}$ the Rosseland mean opacity per gram. It represents the ratio of energy being carried by bulk movement of fluid and that being carried by radiation. For Pe $\ll$ 1, convection will not be responsible for carrying much of the energy. It can be seen from Fig. 3.16 that Pe < 1 for $T_{\rm eff} \geq$ 12 000 K and thus it describes the transition to inefficient convection at larger temperatures. We emphasise that it does not imply a change in the mixing properties of the atmosphere at that temperature. In fact, Tremblay et al. (2015a, see figure 13) have shown that $v_{\rm z,rms}$, and thus mixing capabilities, remain large for 3D simulations up to $T_{\rm eff}$ = 14 000 K, the hottest model in their grid at $\log g$ = 8.0. This behaviour is in agreement with the mixing-length theory, which predicts that thermally inefficient but dynamically active convective zones are found in DA white dwarfs up to 18 000 K, with the exact $T_{\rm eff}$ value strongly dependent on the assumed mixing-length parameter (ML2/α = 0.7 in Tremblay et al. 2015a). Furthermore, the 1D model can only suggest whether or not there is mixing and cannot provide realistic mixed masses due to its neglect of overshoot.

The entropy profiles of our extended grid of 3D simulations in Fig. 3.14 demonstrate that pure-hydrogen atmospheres become unstable to convection for $T_{\rm eff} \lessapprox$ 18 000 K. We attempted a $T_{\rm eff}$ = 18 250 K simulation, not shown on the panel, but it did not develop a convection zone. While this is similar to the 1D prediction of the onset of convection assuming a ML2/α = 0.7 parameterisation (Tremblay et al., 2015a), the 3D simulations provide a more robust threshold. Fig. 3.17 shows the maximum convective velocity in the convectively unstable region, time-averaged over the final 2.5 s, for all simulations in our deep grid (see Table 3.2) as well as Tremblay et al. (2015a). It can be seen that the grid presented in this work fully connects with the previous, shallower one. It is also observed that 1D MLT under-predicts convective velocities for lower temperatures ($T_{\rm eff}$ < 14 000 K) and over-predicts for higher temperatures ($T_{\rm eff}$ > 14 000 K), although this could be corrected by using a variable mixing-length parameter as a function of $T_{\rm eff}$. The first convective model at $T_{\rm eff}$ = 18 000 K is already showing large 1D velocities, illustrating the sharp and

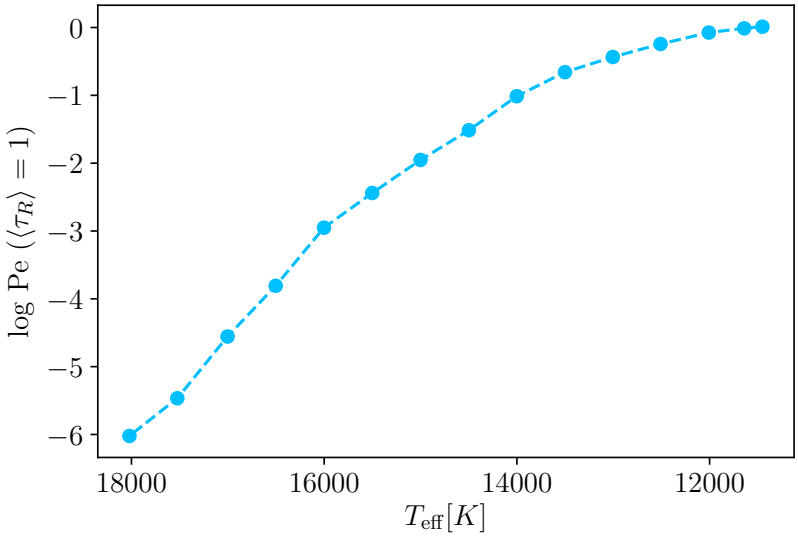

Figure 3.16: Péclet number evaluated at $\langle\tau_{\rm R}\rangle = 1$ as a function of effective temperature and averaged over the final 50 ms of the deep 3D grid presented in Table 3.2.

unphysical transition between convective and radiative atmospheres. In 3D, the warmer convective models have much lower velocities, in line with a smoother onset of convection in evolving DA white dwarfs. This effect may be enhanced by numerical viscosity which, in the regime where radiative energy transport is significantly more efficient than convection, may reduce the 3D convective velocities.

That the atmosphere is unstable is of critical importance for the capacity for DA white dwarfs in this temperature range to mix material, specifically accreted metals. Fig. 3.14 demonstrates that all simulations have large velocities, although with a contribution both from convection and waves. It therefore requires further investigation to fully characterise the mixing capabilities.

3.4.2 Mixed mass

The depth dependence of the diffusion coefficient just above the wave region is well described by the square of the RMS vertical velocity, $v^2_{\rm z,rms}$, (see Section 3.3) with the characteristic timescale $t_{\rm char} \approx 0.18$ s taken from the $T_{\rm eff} = 13\,500$ K simulation (see Fig. 3.10). Ideally our simulations would extend to sufficiently deep layers that convection driven velocities decay enough that microscopic diffusion takes over, bridging the discontinuity between macroscopic and microscopic diffusion highlighted by Tremblay et al. (2017a). This would be computationally intractable given the typical microscopic diffusion velocities of $v_{\rm diff} \sim 10^{-7}$ km s^{-1} and a significant hinderance to this approach is the presence of waves in the base of the simulation.

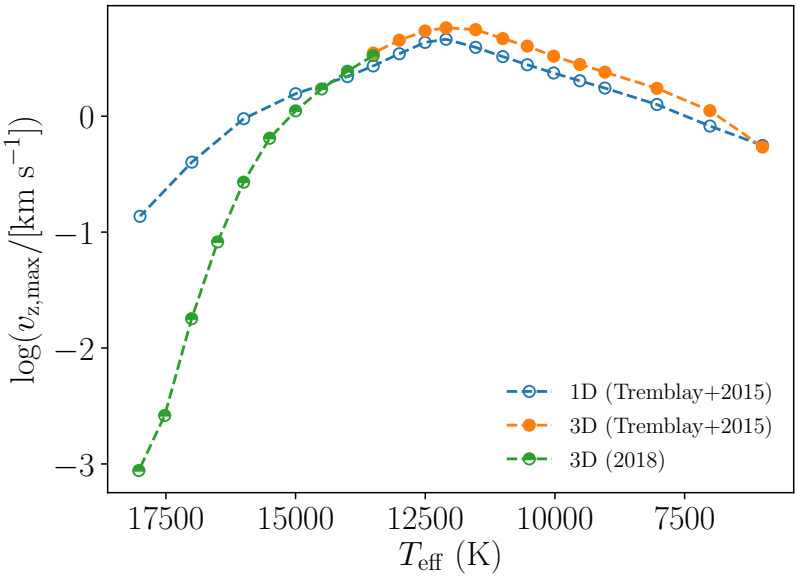

Figure 3.17: Maximum convective velocities, time-averaged over the final 2.5 s for simulations in Table 3.2 (green, half-filled) with 13 503 $\leq T_{\mathrm{eff}}$ / [K] $\leq$ 18 002. Also shown are previous 3D results (orange, filled) and 1D ML2/α = 0.7 mixing-length theory predictions (blue, open) from Tremblay et al. (2015a).

The upward inflexion in the velocity profile at the bottom of the overshoot region highlighted in earlier figures (see Figs. 3.10 & 3.12, and upper panel of Fig. 3.15) is due to these standing waves. Multi-dimensional simulations of brown dwarf atmospheres have provided evidence that waves may be capable of mixing material (Freytag et al., 2010b). However, using $v^2_{\mathrm{z,rms}}$ in the wave region as a proxy for macroscopic diffusion could lead to an overestimation as standing waves may be amplified by boundary conditions. Alternatively, extrapolating the diffusion coefficient from the top of the wave region, e.g. with an exponential decay as a function of the pressure scale height (Tremblay et al., 2015a), would lead to an extremely shallow decay of macroscopic mixing as a function of depth that may not be realistic (Kupka et al., 2018). This suggests that more investigation is needed to obtain sensible mixed masses.

Filtering

We employ a filtering technique to remove the waves from the velocity profile which has been implemented in convective studies of M-type, main-sequence and pre-main-sequence objects (Ludwig et al., 2006).

Fig. 3.18 shows the logarithmic vertical velocities at a layer within each of the three regions with distinct physical characteristics; the convectively unstable region (top), overshoot region (middle) and layer where plumes and waves overlap (bottom), for simulation

B1 from Table 3.1 with $T_{\rm eff} = 13\,000$ K, $\log g = 8.0$ and grid size 150^3. In the convectively unstable region the convective cells, with characteristic size $d_{\rm gran} \approx 1$ km, can be seen with upward (teal) and downward (bronze) velocities. Beneath this layer in the overshoot region one can identify on the order of twenty distinct overshoot plumes, which in the horizontal slice manifest as small circles with characteristic size ~ 100 m. These circles are surrounded by large scale patches of size ~ 5 km and relatively low velocity. These patches correspond to the standing waves. In the region below the deepest overshoot plume all that remains is the contribution from periodic oscillations.

The contrast in spatial extent of the overshoot plumes and standing waves is of great benefit as the two occupy different regions of the power spectrum in spatial frequency. This is depicted in Fig. 3.19 where the power as a function of horizontal wavenumber is shown for vertical velocities. The large scale wave features manifest as the blue peak at low wavenumber ($k < 4 \cdot 10^{-5}$), whilst the overshoot plumes correspond to the purple peak at higher wavenumbers. The masking of the blue region (low wavenumbers) allows the removal of the major contribution from waves in frequency space, while leaving the overshoot plumes ostensibly untouched.

Fig. 3.20 shows the diffusion coefficient computed from the $v^2_{\rm z,rms}$ profiles, time-averaged over the final 2 s, of the simulations from Table 3.2 with $T_{\rm eff} = 12\,000$ K and 13 500 K. The characteristic time required for the computation is taken from the results of simulation C3 (see Fig. 3.4). We note that the scaling of the diffusion coefficient with $v_{\rm z,rms}$ in the near-overshoot region is of little relevance for deriving the total mixed mass. The effect of removing increasingly small scale structures from the power spectrum is shown by the lines becoming bluer. There is a clear asymptotic behaviour which emerges below enclosed mass $\log M_{\rm above}/M_{\rm star} = -14$ in both cases. The simulations also show significant influence from the lower boundary condition which enforces zero mass flux. Clearly, filtering in k-space against low spatial frequencies removes a large contribution from waves yet results in little disturbance of the velocities within the convective zone or the upper overshoot region. Any increase in filtering beyond what is shown in Fig. 3.20 leads to a significant loss of velocities within the convection zone which is an unphysical scenario we seek to avoid.

In the study by Ludwig et al. (2006) the filtering technique was also implemented in the temporal domain, ultimately making a cut in k- and ω-space, where k is the horizontal wavenumber. In our white dwarf atmospheres the standing waves have typical periods of 0.1 s (see also Kupka et al., 2018), similar to the typical decay time of granulation within the convection zone (Tremblay et al., 2013c). Therefore, it is difficult to disentangle convection from waves in ω-space. Given the effectiveness of the k-space filtering technique discussed above, we simply neglect time filtering in the following.

We find that the asymptotic filtered $v^2_{\rm z,rms}$ is linear in $\log D$ - $\log M_{\rm above}/M_{\rm star}$ space,

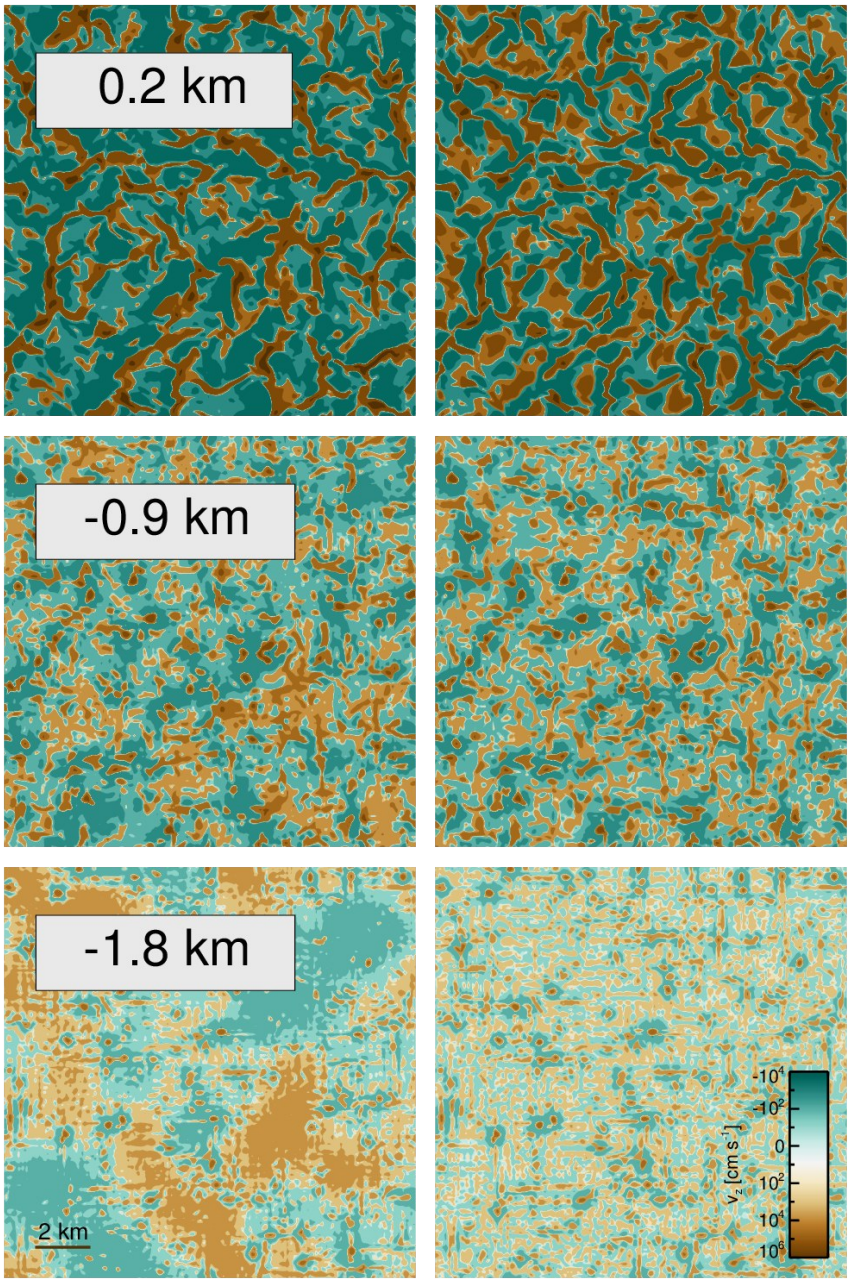

Figure 3.18: Logarithmically coloured vertical velocity snapshots with (right) and without (left) spatial frequency filtering for regions demonstrating: convective instabilities (top), overshoot plumes (middle) and transition from plumes to waves (bottom), for simulation B1 with $T_{\rm eff}$ = 13 000 K, $\log g$ = 8.0 from Table 3.1. The vertical distances from the lower Schwarzschild boundary are indicated in the panels.

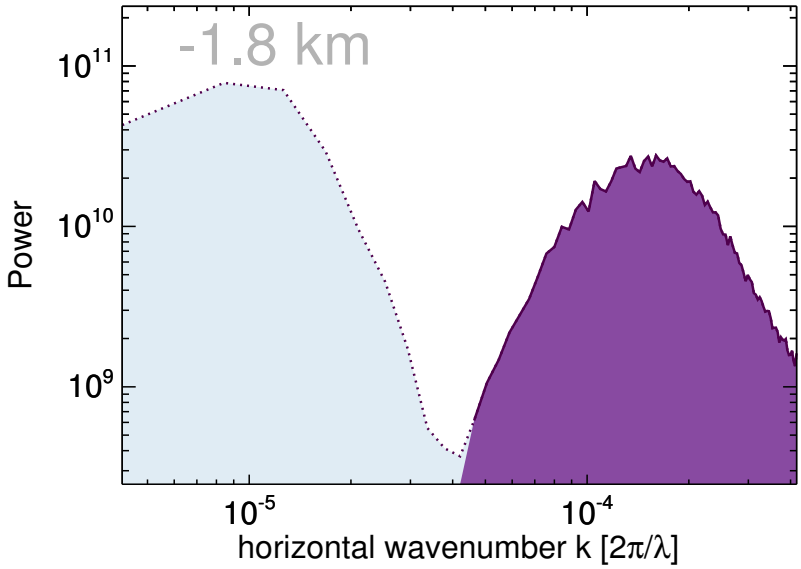

Figure 3.19: Power spectrum for spatial frequencies present in lower panel of Fig. 3.18. The unfiltered power spectrum (lower left panel of Fig. 3.18) can be interpreted as a combination of the blue and purple regions. The filtered power spectrum (lower right panel of Fig. 3.18) corresponds to the purple region only. The vertical distance from the lower Schwarzschild boundary is indicated in the panel and corresponds to the layer showing a transition from plumes to waves.

allowing us to perform a linear fit immediately beneath the start of the wave region. We can then extrapolate this behaviour to deeper layers that are out of reach with 3D simulations. Fig. 3.20 demonstrates that the decay of convective velocities in the wave region is much more rapid with depth than in the overshoot region above. Indeed the velocity scale height in the wave region (where overshoot structures still exist) is much less than the pressure scale height, reflecting similar behaviour which is observed in simulations of convection in brown dwarf atmospheres (Freytag et al., 2010b), but we cannot confirm whether this change in convective velocity profile is impacted by waves, e.g. with wave damping convective overshoot. For this reason and also our neglect of waves as a possible contributor to mixing, our estimate of the mixed mass is a lower limit.

We estimate the minimum amount of mixed mass in accreting white dwarfs by looking for the intersection of the asymptotic filtered macroscopic diffusion coefficient with 1D microscopic diffusion coefficients and in so doing should provide the most conservative estimate of mixed mass increase. In Fig. 3.20 we compare these to the representative cases of the magnesium, calcium and iron diffusion coefficients (dotted) from Koester (2009); using updated tables.[1] Here it is important to emphasise that 3D corrections to mixed

[1]http://www1.astrophysik.uni-kiel.de/~koester/astrophysics/astrophysics.html

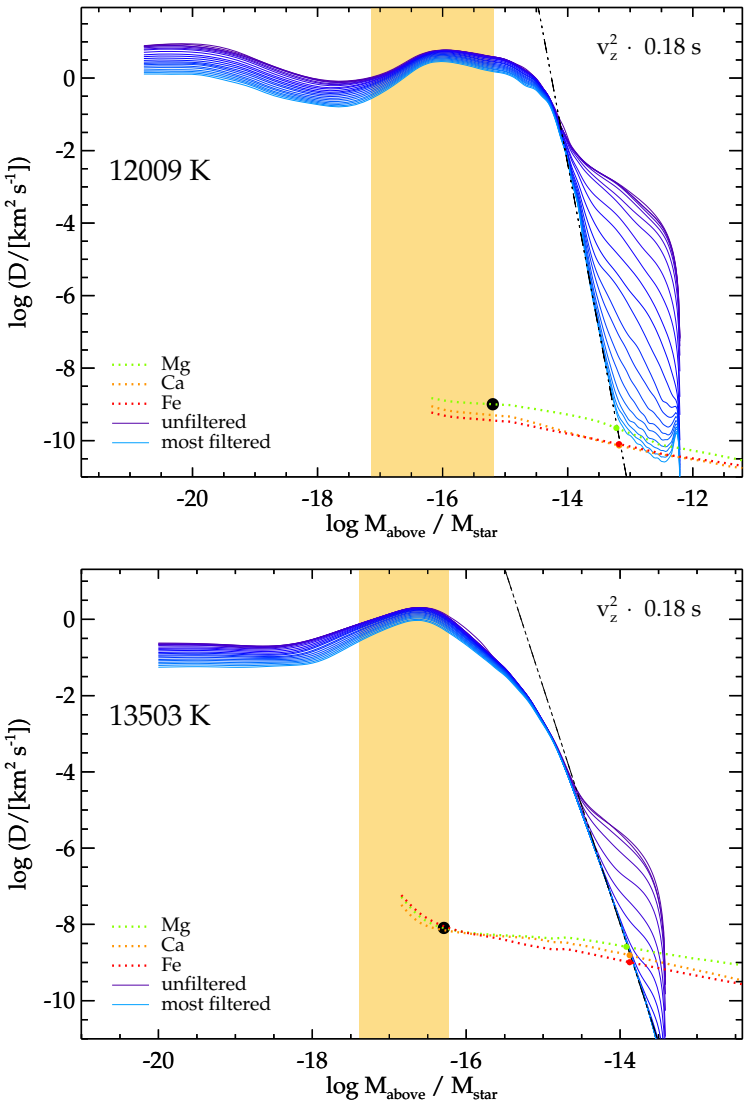

Figure 3.20: Diffusion coefficients as a function of enclosed stellar mass from deep simulations of Table 3.2 with $T_{\rm eff}$ = 12 000 K (left) and 13 500 K (right). The diffusion coefficients computed from the directly simulated $v^2_{\rm z,rms}$ profile are shown as a solid purple line. Those computed with an increasingly filtered $v^2_{\rm z,rms}$ profile (i.e., increasingly small structures removed) are shown in bluer colours, with adjacent lines increasing the filtering in Fourier space by $\Delta k = 1$ in box size units. The characteristic time scale of 0.18 s found in Section 3.3 is employed. The convectively unstable region defined by the Schwarzschild criterion is indicated by the orange shaded region. Also shown are the 1D diffusion coefficients for Mg, Ca and Fe from updated tables of Koester (2009, dotted lines), taken as characteristic elements. Our proposed extrapolation of diffusion coefficients is shown as a black dot-dashed line. Diffusion coefficients at the base of the mixed regions defined in 1D (black circle) and with our proposed parameterisation of convective overshoot for the three characteristic elements (coloured circles) are also presented.

masses can be read directly from Fig. 3.20. The crude 1D estimate is simply the intersection of the base of the convection zone with the diffusion coefficient (black circle), and the more robust 3D picture is based on the intersection of the asymptotic filtered macroscopic diffusion coefficient with the microscopic diffusion coefficients (coloured circles). The fact that convective velocities decay rapidly with depth in the wave region implies that while we extrapolate over a sizeable range in velocity space, it corresponds to a fairly modest additional amount in mixed mass. In other words, our direct simulations in Section 3.3 have robustly shown that a sizeable amount of mass is unambiguously mixed in the overshoot region, and the additional amount added by our extrapolation procedure is fairly moderate.

The convection zone mass after one includes the full extent of the convectively unstable and overshoot regions is shown in Fig. 3.21 with solid lines for Mg (blue), Ca (purple) and Fe (red) and described in Table 3.3. The figure also shows the mass at the base of the convection zone in 3D described from the Schwarzschild criterion for our deep grid of simulations (green line). Those are in fairly good agreement with the results of Tremblay et al. (2015a) (green triangles) and 1D structures (grey and orange points), and this corresponds to the mixed mass in the 1D picture, i.e. neglecting the contribution from overshoot. The lower limit on the 3D correction in mass is at least 1 dex but can reach ≈ 2 dex for the intermediate $T_{\rm eff}$ values in our grid. We will go on to consider the implications of this result for the accretion-diffusion picture.

Recently Kupka et al. (2018) also presented a prediction for the range of mixed mass for a simulation at $T_{\rm eff} = 11\,800$ K to be $-12.7 \gtrapprox \log q \gtrapprox -13.9$ based on the plume penetration depth and horizontal to vertical velocity ratios, respectively. An interpolation of Fig. 3.21 reveals this to be in good agreement with the predicted mixed mass from our 3D grid which estimates the mixed mass at $T_{\rm eff} = 11\,800$ K to be $\log q = -13.0$. We also find agreement with the predicted size of the convectively unstable zone that the authors found to be $\log q = -15.2$, which compares well with the green line in Fig. 3.21.

3.5 Discussion

Chemical abundances in polluted white dwarf atmospheres as well as characterisation of circumstellar dust and gas disks for a fraction of those are the main observational properties with which we can constrain evolved planetary systems. On the one hand, the chemical properties and time variability of circumstellar material is independent of the white dwarf convection model. These systems can be used to understand the variability of predicted accretion rates onto the white dwarfs (Wyatt et al., 2014). On the other hand, it is the accretion-diffusion scenario, currently under the 1D MLT assumption of no convective overshoot, that is used to predict parent body chemical compositions, the total accreted mass

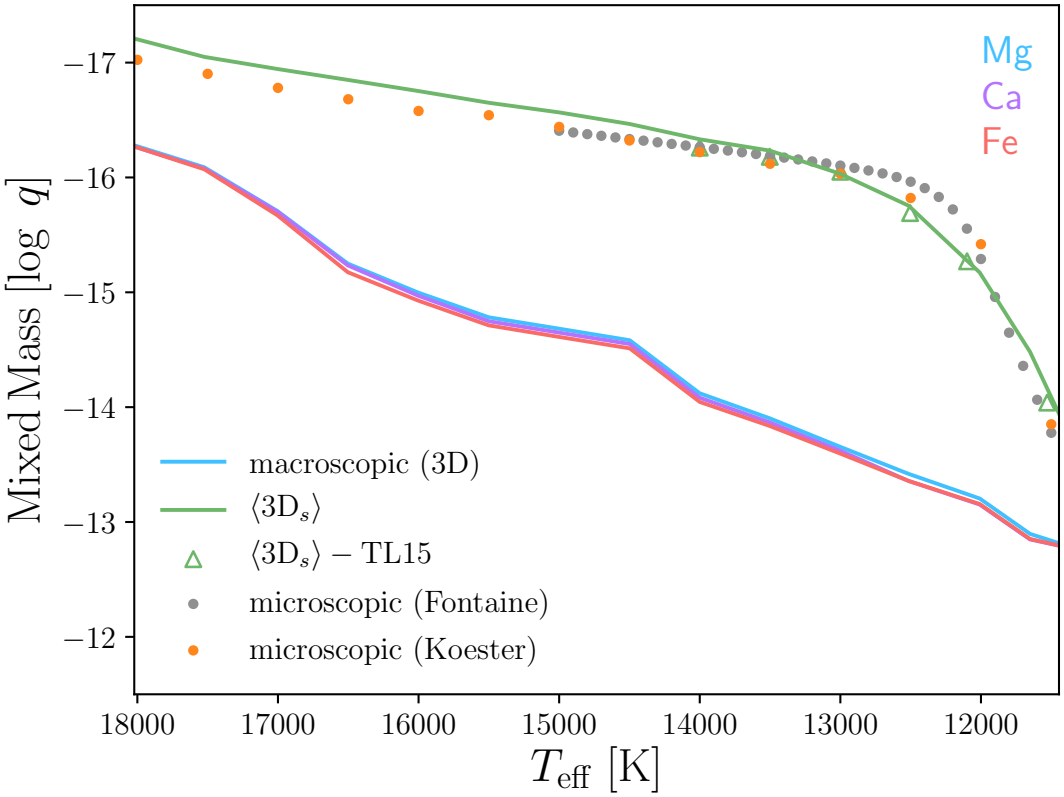

Figure 3.21: Mixed mass in units of enclosed mass, $\log q = \log M_{\rm above}/M_{\rm star}$, as a function of effective temperature. Mixed masses determined by the intersection of macroscopic and microscopic diffusion coefficients (see Fig. 3.20) for Mg (blue), Ca (magenta) and Fe (red) are shown in solid for all simulations detailed in Table 3.2. Also shown is the 3D definition of the unstable region from the grid presented in this study (green, solid) and selected models from the earlier lower resolution grid (green, triangles) from Tremblay et al. (2015a). This corresponds to the definition of mixed mass without overshoot. The two coolest models plotted from the latter grid are open bottom simulations, and show good agreement with the closed bottom simulations calculated in this work. In comparison, the orange and grey lines show the 1D mixed mass of the unstable layers according to 1D structures of Koester and Fontaine, respectively, using ML2/α = 0.8.

over the characteristic diffusion timescale, and in some cases, estimate the time elapsed since the last accretion event (Hollands et al., 2018a). In the case of the hydrogen abundance in helium-atmospheres, one can also infer about the full past history of accretion since hydrogen does not diffuse out of the convective layers (Gentile Fusillo et al., 2017a). Time variable abundances in the photosphere, although so far not observed (Farihi et al., 2018b; Debes & López-Morales, 2008), could also be used to understand the accretion process. All of those inferred quantities need to be re-evaluated in light of 3D convection. We have determined that the mixed mass, or the total accreted mass over a characteristic diffusion timescale, is 1–2.5 orders of magnitude larger than the crude 1D estimate and we dedicate this section to an overview of the other quantities derived from the accretion-diffusion model.

One starting point is the impact of convective overshoot on the settling times, $t_{\rm diff}$, of trace elements in polluted white dwarfs. Accretion calculations are usually performed under the assumption that a steady state has been reached between accretion at the white dwarf and diffusion out of the base of the convection zone, for at least a few diffusion timescales. This implies that the abundance in the mixed region is homogeneous and in this scenario the accretion rate is given by

$$\dot{M}_i = \frac{M_{\rm cvz} X_i}{t_{{\rm diff},i}} = 4\pi r^2 \rho v_{\rm diff} \tag{3.11}$$

where $M_{\rm cvz}$ is the mixed mass and, for an element i, $\dot{M}_i$ is the accretion rate, $t_{{\rm diff},i}$ the diffusion timescale, X_i the elemental atmospheric abundance, ρ the density at the base of the mixed region and r the stellar radius.

We use the 1D diffusion velocities presented in Koester (2009) to calculate the change in settling timescale when one redefines the base of the mixed region. Fig. 3.22 shows 3D corrections to diffusion timescales (top) and accretion rates (bottom). Convective overshoot implies that microscopic diffusion takes over as the dominant process of mass transport in deeper, denser layers where diffusion timescales are longer. For an inference of accretion rates we have two competing effects that partially cancel each other out as the base of the mixed layer goes deeper. The net result from this competition is an increase in accretion rate of up to an order of magnitude (see bottom panel of Fig. 3.22), which is not as large as the increase in mixed masses.

To demonstrate the impact of 3D corrections derived from our numerical study we recalculate accretion rates for a sample of 48 polluted DAZ white dwarfs (Bergfors et al., 2014). As a function of effective temperature the change in accretion rate is given by

$$\Delta\dot{M}(T_{\rm eff}) = \frac{1}{3} \sum_{\rm Mg,Ca,Fe} (\dot{M}_{el}^{\rm 3D} - \dot{M}_{el}^{\rm 1D}) \tag{3.12}$$

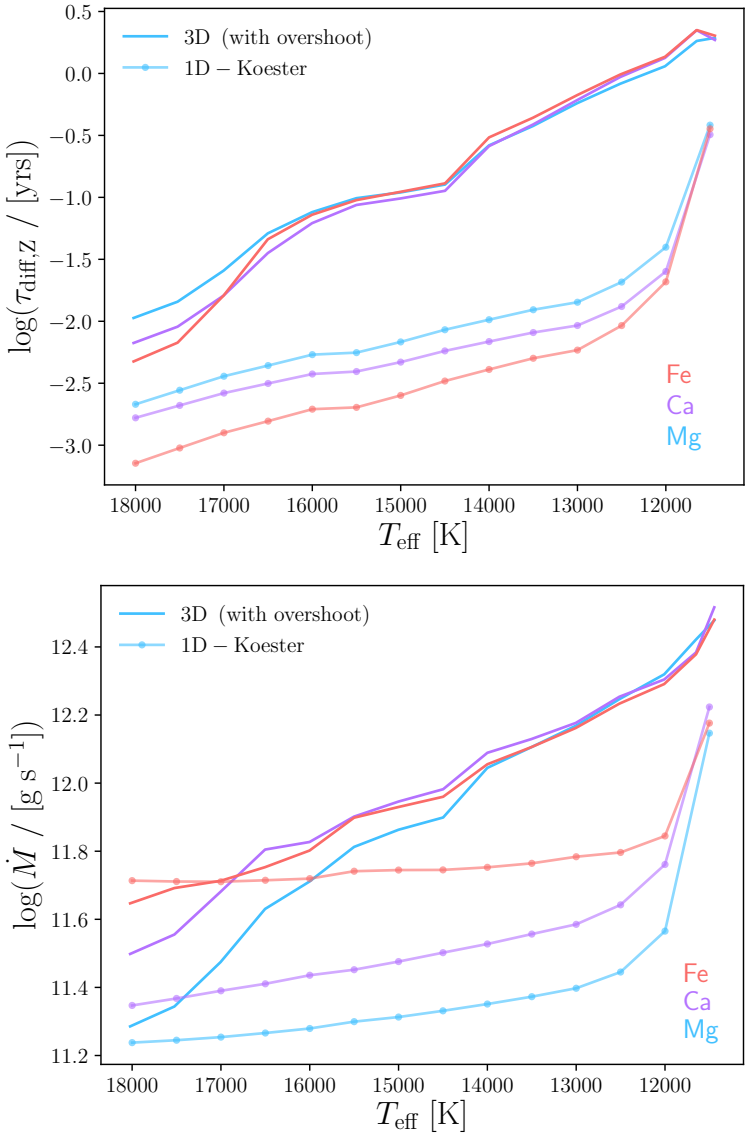

Figure 3.22: Diffusion timescale (top panel) and inferred accretion rates (lower panel) when using the mixed masses, shown in Fig. 3.21, borne from diffusion coefficients derived from our 3D grid using $v^2_{\mathrm{z,rms}}$ (solid). For simplicity the abundance, X_i, in Eq. (3.11) used to infer an accretion rate is assumed to be unity ($X_i = 1$). Also shown are 1D structures from Koester (solid-circles). All quantities are provided for Mg (blue), Ca (magenta) and Fe (red). The accretion rates are calculated using Eq. (3.11). The strong upward inflexion in the 1D accretion rates for models with $T_{\mathrm{eff}} < 12\,000$ K is a symptom of the strong downward inflexion seen in the mixed masses for the same models (see Fig. 3.21). The small predicted decrease in accretion rate for Fe in the warmest models ($> 17\,000$ K) is due to the fact that the increase in diffusion time scale (top panel) is greater than the increase in convectively mixed mass (Fig. 3.21) in that regime. It can be seen in Eq. (3.11) that this scenario produces a lower accretion rate.

Table 3.3: Input parameters for accretion-diffusion calculations derived for our full grid of deep 3D simulations (see Table 3.2). The mixed mass in units of enclosed mass, $M_{\rm cvz}$, diffusion velocity, $v_{\rm diff}$ and diffusion coefficient, D, are all evaluated at base of the 3D mixed region. Values are shown for mixed regions defined by diffusion coefficients with $D = v^2 \cdot t_{\rm char}$ (see Fig. 3.21). For brevity, all values are expressed as a mean across those computed for magnesium, calcium and iron.

$T_{\rm eff}$	$\log\langle M_{\rm cvz}\rangle$	$\log\langle v_{\rm diff}\rangle$	$\log\langle D\rangle$
11445	−12.82	−7.62	−10.28
11651	−12.89	−7.60	−9.97
12009	−13.19	−7.43	−9.90
12500	−13.41	−7.30	−9.64
13005	−13.64	−7.17	−8.88
13503	−13.89	−7.03	−8.76
14000	−14.09	−6.91	−8.68
14498	−14.58	−6.63	−8.51
15000	−14.49	−6.68	−8.52
15501	−14.60	−6.61	−8.47
16002	−15.01	−6.42	−8.39
16503	−15.24	−6.29	−8.31
17004	−15.73	−6.02	−8.19
17524	−16.12	−5.83	−8.11
18022	−16.33	−5.70	−8.04

where, for simplicity, the individual change in accretion rate from each element, el, considered - Mg, Ca and Fe - is weighted equally in the mean, corresponding to an equal abundance of all three elements which is reasonably close to solar abundance ratios.

Fig. 3.23 shows the DAZ and DBZ samples taken from Bergfors et al. (2014) (open circles and blue filled circles, respectively) along with the 3D corrected DAZ sample (black, filled circles). It can be seen that within the effective temperature range considered in this study (11 400 - 18 000 K), 3D corrections bring the mean accretion rates between the DAZ and DBZ samples into closer agreement, though additional physics is required to explain the observed difference. Furthermore, for the same region we find that the standard deviation of the corrected sample is contained within the standard deviation of the DBZ sample. This is shown in Fig. 3.24, where the mean (solid line) and one standard deviation (filled error regions) are plotted for the original sample from Bergfors et al. (2014) in the top panel and with the inclusion of macroscopic mixing due to overshoot shown in the lower panel. The lack of a correction below 11 000 K is due to the computational limitations of simulating lower temperatures (due to their deep convection zones) and above 18 000 K we predict no correction due to overshoot, owing to the non-convective, radiative atmospheres of these warmer objects. A small correction due to overshoot is expected for the DBZ sample, but to a lesser extent than for the DAZs at comparable temperatures.

3.6 Conclusions

Using the RHD code CO^{5}BOLD, we have presented the first macroscopic diffusion coefficients for DA white dwarfs in the range 12 000 K $\leq T_{\rm eff} \leq$ 13 500 K derived directly from 3D simulations. We have shown that the phenomenon of convective overshoot is capable of mixing material over a much greater extent than the MLT approximation, as suggested before (Freytag et al., 1996; Tremblay et al., 2015a; Kupka et al., 2018). These direct simulations have demonstrated that macroscopic diffusion decays with the vertical component of the velocities immediately beneath the unstable layers and with the same quantity squared for at least $\approx 2.5 - 3.5$ pressure scale heights beneath the unstable layers. For deeper layers, the 3D diffusion experiments were inconclusive because of the presence of waves amplified by boundary conditions, though the path integration method was less susceptible to artificial mixing in the wave-dominated regions.

We have developed an approach to acquire a lower limit on the mixed mass in the atmosphere which consists of using wave-filtered convective velocities as a proxy for macroscopic diffusion. We identify the points at which the diffusion coefficients derived from the filtered velocity squared profiles intersect the microscopic diffusion coefficients for magnesium, calcium and iron, providing a conservative and elemental dependent estimate

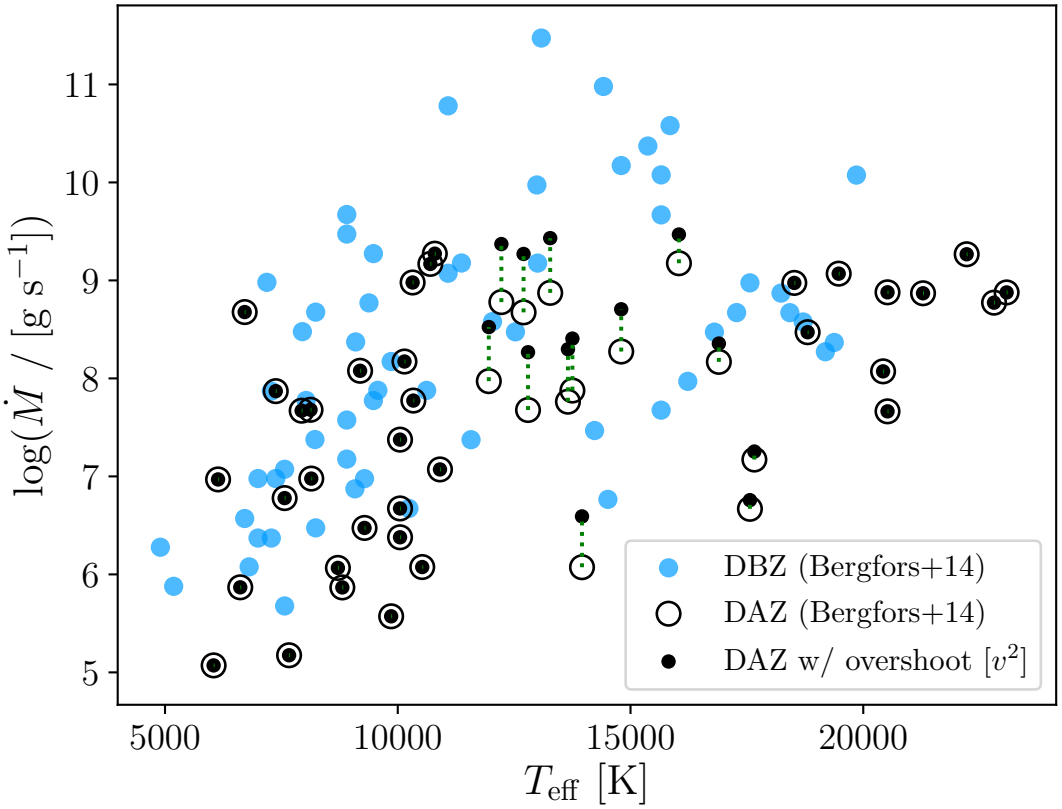

Figure 3.23: Sample of polluted white dwarfs comprising DAZs (black, open) and DBZs (blue) from Bergfors et al. (2014). The DAZ sample is also shown after the inclusion of convective overshoot (black, filled).

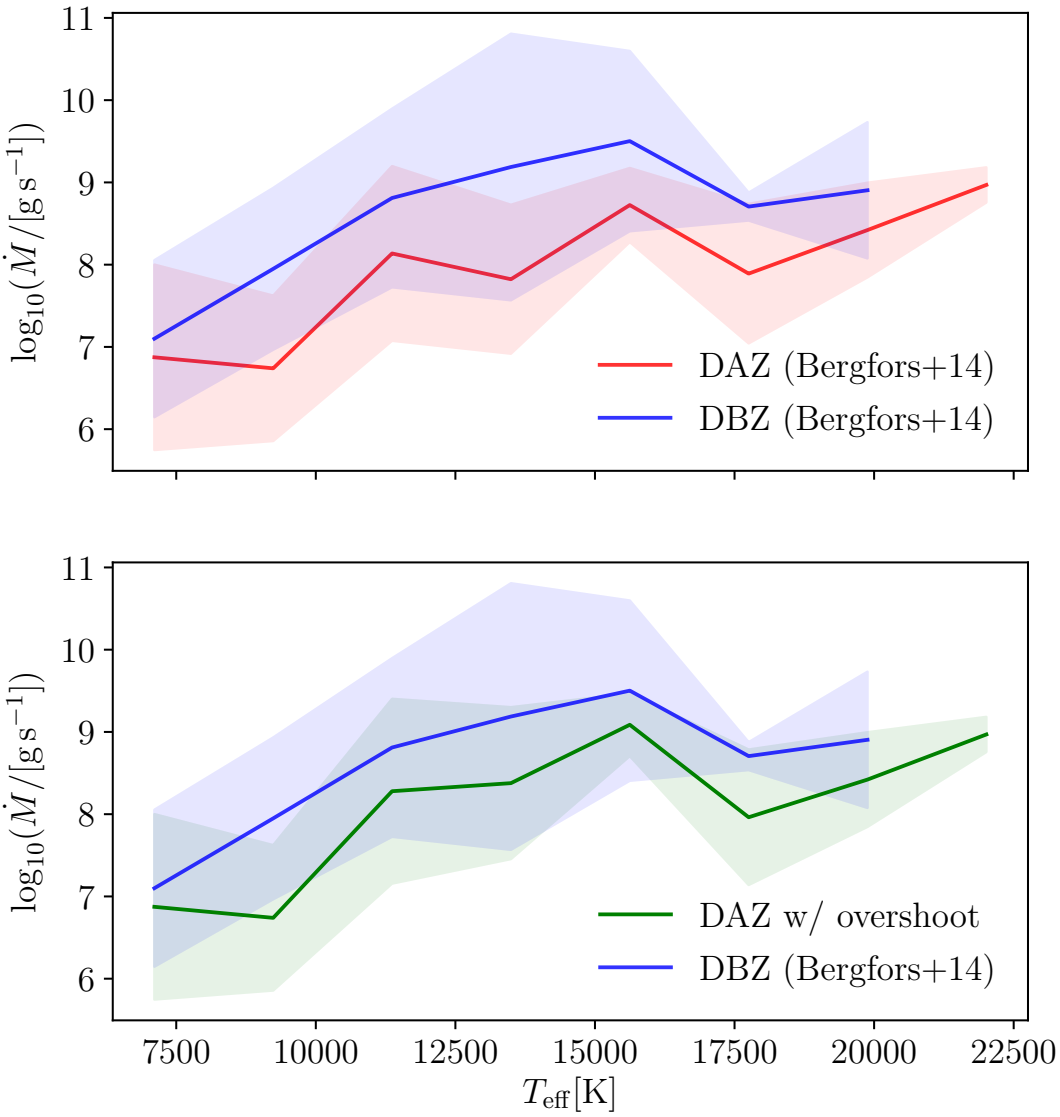

Figure 3.24: Accretion rates from Bergfors et al. (2014) and Fig. 3.23 mean-averaged within eight effective temperature bins. Shaded areas correspond to one standard deviation for the overshoot-corrected DAZ (green), original DAZ (red) and DBZ (blue) samples.

of the increase in mixed mass.

We have found evidence to suggest that settling times for pure-hydrogen atmosphere white dwarfs with $11\,400 \leq T_{\rm eff}/[{\rm K}] \leq 18\,000$ are likely to increase by 1.5 – 3 orders of magnitude (see Fig. 3.22; top). This has implications for predicting the period over which we are unlikely to observe pollution variability in white dwarfs, providing the possibility for constraining this model. The often discussed instantaneity of accretion at warm DAZ white dwarfs is still valid compared to the Myr timescales of accretion at DBZ white dwarfs (Wyatt et al., 2014), but we have presented evidence that it may be slower than typically thought. Despite this large increase in settling time, we predict that derived accretion rates may increase by only up to an order of magnitude.

Ultimately the intention behind this research is to provide robust constraints on accretion processes by improving the characterisation of the mass reservoir in white dwarf atmospheres, and should serve as an important step to better understand the evolution of planetesimals in old planetary systems.

In the modelling of debris-accreting white dwarfs one question which requires improved constraints is that of accretion geometry; i.e., whether material is accreted by direct impact of asteroids or disrupted into a disk and accreted more homogeneously (i.e., equatorially or spherically). In the following chapter we will exploit the simulations and techniques already outlined to derive the first coefficients describing the transport of material in the horizontal, or surface-plane, directions in a degenerate star. In so doing we aim to provide theoretical constraints on accretion geometry and white dwarf spectral variability. This will also serve as a test of the often-held assumption that metals in white dwarf convection zones are mixed homogeneously across the surface.

Chapter 4

Horizontal transport in debris-accreting white dwarfs

4.1 Introduction

The canonical model for the origin of metal-pollution in white dwarfs is that surviving planets gravitationally scatter asteroids and minor planets onto the central regions, where one or many tidally disrupted planetesimals form a disc of debris around the stellar remnant, constantly feeding metals and gaseous material onto the white dwarf surface (Jura, 2003; Debes et al., 2012; Wyatt et al., 2014; Manser et al., 2016). Other models suggest that direct impacts of asteroids on star-grazing orbits may provide a non-negligible source of this material (Bonsor & Veras, 2015; Brown et al., 2017). Modelling of these systems is typically dependent on the assumption that the material is homogeneously mixed throughout the surface layers, though there are only modest constraints on the validity of this approximation (Alcock et al., 1986). In the scenario that metals are inhomogeneously distributed across the surface it is possible that variations in the spectroscopic line strengths and equivalent widths may be detectable on the rotational period of the white dwarf.

A spectroscopic and photometric analysis of 27 pulsating ZZ Ceti white dwarfs allowed Hermes et al. (2017a) to constrain the rotation of single white dwarfs with masses between 0.51–0.73 $M_{\odot}$. They found that a mean period of 35 ± 28 hr could explain the rotational separation of pulsation frequencies.

Low level (few percent) photometric variations have been detected in non-pulsating white dwarfs and attributed to surface inhomogeneities that rotate in and out of view (Brinkworth et al., 2013; Kilic et al., 2015; Maoz et al., 2015; Hermes et al., 2017b). By combining Kepler photometry with Hubble Space Telescope (HST) UV spectroscopy for seven white dwarfs, Hallakoun et al. (2018) tested the hypothesis that low level variations in the photometry could be attributed to an accretion hot spot or inhomogeneous distribution of metals across the white dwarf surface. No such correlation could be claimed although their observations did not allow to rule out the hypothesis either. In contrast photometric variability has been linked to magnetic white dwarfs (Lawrie et al., 2013; Brinkworth et al., 2013; Reding et al., 2020). In those cases the light intensity is thought to be inhomogeneous across the stellar surface, e.g. due to an uneven temperature distribution from a yet unexplained physical mechanism related to stellar magnetism (Tremblay et al., 2015d). As a consequence, photometric variability cannot be uniquely linked to evolved planetary systems.

The metal-rich DA white dwarf GD 394 was observed to exhibit a 25 per cent modulation in its EUV flux on a period of 1.15 d (Dupuis et al., 2000). The hypothesis that this variability was due to an accretion spot was tested by Wilson et al. (2019) with time-resolved HST UV spectroscopy. They found no evidence for variations in flux, inferred accretion rate and radial velocity over the observed period.

The variability of accretion rates onto white dwarfs have also been studied. It was claimed that G29-38, at 17.54 pc the closest white dwarf with a debris disk, showed evidence of a variable accretion rate based on a variation in the calcium line strength (von Hippel & Thompson, 2007). However, by revisiting the observations Debes & López-Morales (2008) found no evidence for variation on timescales of days to years. Vanderbosch et al. (2019) have recently detected marginal calcium line variability at a white dwarf with transiting debris. However they conclude that the spectroscopic variability is likely related to circumstellar debris transiting along the line of sight rather than photospheric variations. All in all there is no robust evidence of surface metal inhomogeneities at white dwarfs. This is in contrast with magnetic chemically peculiar main sequence stars where inhomogeneities are routinely detected (see, e.g., Sikora et al., 2019).

Studies of debris disc variability at white dwarfs have also been performed (Swan et al., 2019; Rogers et al., 2020). This provides important information on disk evolution and replenishment (Jura et al., 2009; Rafikov, 2011; Metzger et al., 2012), although there is no confirmed causal connection between disc variability and accretion rate variability and geometry. For a sample of white dwarfs with dusty discs, Rogers et al. (2020) found no evidence of near-infrared K-band variability above the 10% level for 32 objects with optical magnitudes smaller than 18. The upper limit on variation from the disc was found to be 1.3% for objects brighter than magnitude 16. In contrast, Swan et al. (2019) used archival data from WISE at redder near-infrared wavelength to show that 69% of the 35 white dwarfs with an observable dust disc show infrared variations more significant than 3σ.

There have been significant theoretical efforts focused on accretion onto white dwarfs. Of particular importance, Wyatt et al. (2014) provided a theoretical constraint on the size of particles reaching the white dwarf surface. Metzger et al. (2012) provided a comprehensive discussion regarding models of discs, finding that magnetic fields as weak as 10 kG can affect the accreted material, potentially directing it toward the poles.

In the following we present a theoretical study which focuses on the horizontal (surface-plane) mixing capabilities of the white dwarf surface layers across the parameter space encompassing all convective white dwarfs. The motivation is to enhance our understanding of what happens to material once it lands on the surface. Whilst deviations from homogeneously distributed trace pollutants at the surface of white dwarfs have not yet been robustly observed, our aim is to address whether this outcome is consistent with detailed modeling of white dwarf convection zones. This could have a modest impact on inferred accretion rates and provide further constraints on the geometry of some of the accretion models detailed above. In Section 4.2 we describe our numerical approach to the problem. In Section 4.3 we present results from our 3D model atmosphere simulations. Section 4.4 focuses on the implications of our results on the white dwarf population and finally we

provide conclusions in Section 4.5.

4.2 Numerical setup

Our approach is to model the transport of trace metals across the white dwarf surface as an effective diffusion process. This requires the local diffusion coefficient describing mixing in the radial and angular directions. Because a white dwarf convection zone is very small in comparison to the stellar radius, we can simplify the problem to mixing in the radial and horizontal, or surface-plane, directions. In the next two sections we describe first the derivation of the diffusion coefficients and secondly the incorporation of these diffusion coefficients into a model describing the surface spreading.

4.2.1 Diffusion coefficients

We trace the effective diffusion in the surface layers of white dwarfs by adding a passive scalar to stable 3D simulations of surface convection zones. This is an extension to the method which was developed and explained in detail in Chapter 3. For the purposes of our model we adopt a plane-parallel assumption which has been shown to characterise sufficiently well the behaviour of surface convection zones in white dwarfs (Tremblay et al., 2013b).

Extending the method of Chapter 3 (and Cunningham et al. 2019) into the horizontal dimensions, the horizontal diffusion coefficient is calculated by adding slabs of tracer density into the $y-z$ plane. The spatial extent of these ensembles, if undergoing a diffusion process, should evolve proportionally to the square-root of time ($\sqrt{t}$), such that the diffusion coefficient in the x-dimension, D_x, can be calculated as

$$2\log_{10}(x^*_{\rm rms}(x,t)) = \log_{10}(t) + \log_{10}(2D_x)\ . \tag{4.1}$$

where $x^*_{\rm rms}$ is the density-weighted standard deviation of the tracers defined as

$$x^*_{\rm rms} = \left(\frac{n_x}{n_x - 1}\sum_x \left(\rho_{\rm t}(x)(x - \langle x^*\rangle)^2\right) \Big/ \sum_x \rho_{\rm t}(x)\right)^{1/2} \tag{4.2}$$

where n_x is the number of cells in the x dimension, $\rho_{\rm t}(x)$ is the tracer density mean-averaged across the y and z dimensions, and $\langle x^*\rangle$ is the density-weighted mean x-position of the tracer density given by

$$\langle x^*\rangle = \left(\sum_x x\rho_{\rm t}(x)\right) \cdot \left(\sum_x \rho_{\rm t}(x)\right)^{-1} \tag{4.3}$$

The initial condition for each independent slab of tracer density added at $x = x_i$ is defined as

$$\rho_{\rm t}(x) = \begin{cases} 10^5 \text{ cm}^{-3}, & \text{where } x = x_i. \\ 10^{-6} \text{ cm}^{-3}, & \text{where } x \neq x_i. \end{cases} \tag{4.4}$$

The tracer density, ρ_t, is a (massless) passive scalar and thus the magnitude of the number density bears no physical significance. The initial positions, x_i, are chosen to sample the full horizontal extent in the x-dimension. This procedure is repeated in the y-dimension such that an alternative component to the horizontal diffusion coefficient, D_y, is found by placing slabs of a passive scalar density in the $x - z$ plane. As it is not expected that the horizontal diffusion coefficient should vary across the x- and y-dimensions the final diffusion coefficient is computed as a mean across all slabs, such that

$$D_{\leftrightarrow} = \frac{1}{S_x + S_y} \left(\sum_{i=1}^{S_x} D_{x,i} + \sum_{j=1}^{S_y} D_{y,j} \right) \tag{4.5}$$

where S_x and S_y are the number of slabs added in the x- and y-dimensions, respectively, and $D_{\leftrightarrow}$ is the horizontal diffusion coefficient. The standard deviation around this mean quantity (Eq. (4.5)) is chosen to represent the error attributed to each horizontal diffusion coefficient. The results of these computations are considered in Section 4.3.1 and compared to the well-known 1D estimation of the diffusion coefficient.

In 1D mixing-length theory the local approximation of the diffusion coefficient is typically given (e.g., Zahn 1991; Ventura et al. 1998) as

$$D = \frac{1}{3} l_{\rm d} v_{\rm conv} \ , \tag{4.6}$$

where $l_{\rm d}$ is a characteristic convective length scale and $v_{\rm conv}$ is the mean convective velocity. Pressure scale height, H_P, has often been proposed to be a suitable choice of characteristic mixing length.

Here we explore the validity of this approximation by comparing this expression to results from direct tracer experiments in the convection zone of white dwarfs at nine effective temperatures spanning the full range of convective DA white dwarfs: 6000–18 000 K. The vertical diffusion coefficients for 11 400–18 000 K were presented in Chapter 3 and Cunningham et al. (2019). In Section 4.3 we present the results of these experiments, providing the first horizontal diffusion coefficients derived from multi-dimensional simulations in white dwarfs.

We rely on pre-computed CO^{5}BOLD simulations adapted from two previously published studies. A grid of deep, radiation-hydrodynamics (RHD) simulations for the surface

hydrogen convection zones of white dwarfs in the effective temperature range 11 400–18 000 K were presented in Chapter 3 (and Cunningham et al. 2019). Earlier, Tremblay et al. (2013a) developed a grid of RHD simulations for the surface convection zones of cooler DA white dwarfs with effective temperatures between 6000–13 500 K. Here we combine both grids such that the full parameter space of convective DA white dwarfs is probed: from when convective instabilities initially arise at 18 000 K down to when the convection zone is sufficiently deep that it couples with the degenerate core. For comparison, we show some key physical properties of both grids in Fig. 4.1. The model grid from Chapter 3 is shown in blue and the model grid from Tremblay et al. (2013a,c) is shown in orange.

4.2.2 Simulating surface transport

Here we introduce the method by which we model the global transport of metals across the surface of the white dwarf. We begin by taking the limiting case of a delta function accretion, both temporal and spatial. Physically, this effectively represents the collision of an asteroid with the surface of the white dwarf. Modelling the surface of the white dwarf as a ring allows us to exploit the well-known heat equation:

$$\dot{u}(r,t) = \nabla \left(D \nabla u(r,t) \right) . \tag{4.7}$$

Here, $u(r,t)$ is the local concentration of some scalar which, in our case, represents the accreted heavy elements. As a preliminary scenario we consider the situation that metals are not permitted to sink out of the observable layers. This assumption allows for a simple analytic form of position dependent abundance to be written down. We also assume throughout this study that the diffusion coefficient is independent of the position across the surface. In this case, with only surface (horizontal) transport and a delta function accretion the local concentration can be written as

$$\frac{\partial u}{\partial t} = (D_{\leftrightarrow}) \frac{\partial^2 u}{\partial x^2}, \tag{4.8}$$

where x corresponds to the position along the circumference of the white dwarf and $D_{\leftrightarrow}$ is the diffusion coefficient describing the effectiveness of material transport in the plane of the surface. This diffusion coefficient is assumed to have no depth dependence for the time being.

For spatial domain, x, contained in interval [-L,L] and with initial and boundary

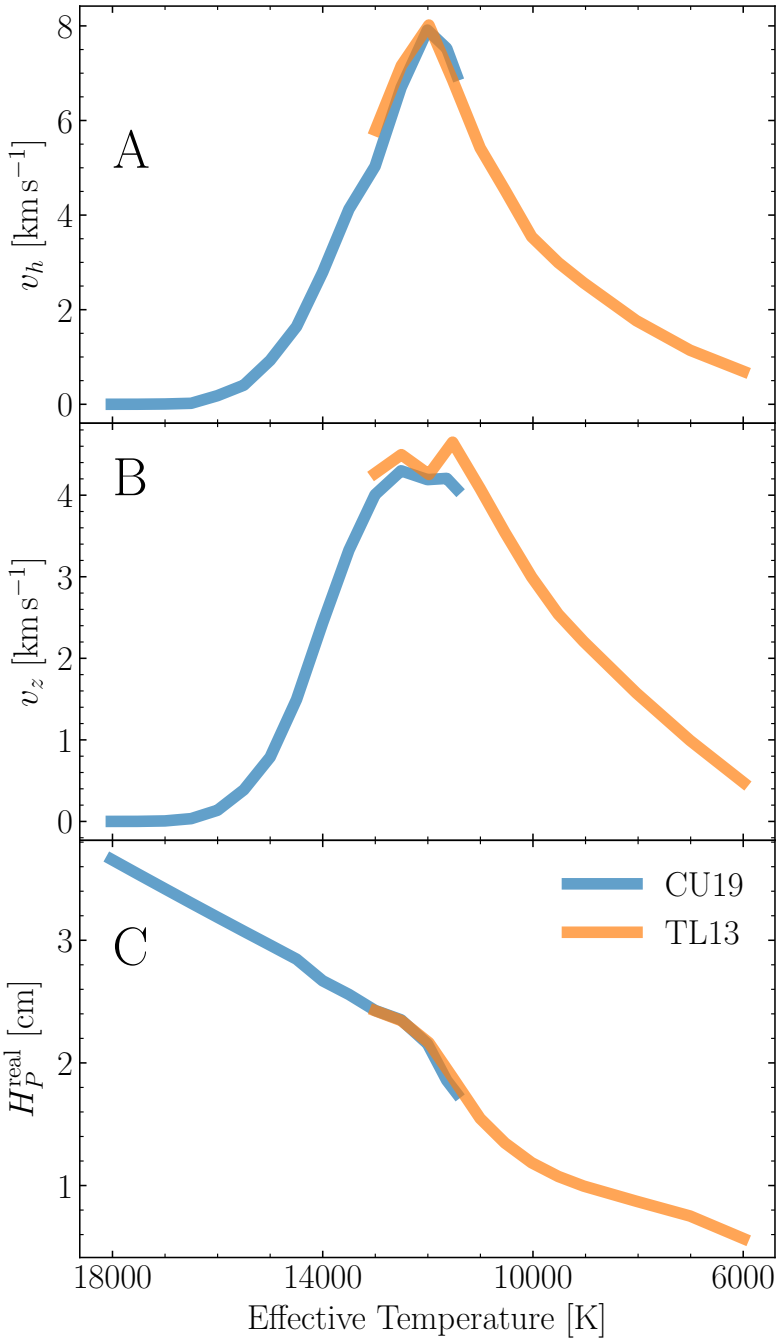

Figure 4.1: *Top to bottom:* A) Time-averaged horizontal velocity, $v_h = \sqrt{v_x^2 + v_y^2}$, at the photosphere (mean Rosseland optical depth $\langle \tau_{\rm R} \rangle = 1$, B) Time-averaged vertical velocity, v_z, at the photosphere. C) The actual pressure scale height that corresponds to the geometrical distance between the photosphere and the layer below where the pressure drops by a factor e. The labels CU19 and TL13 refer to results from Chapter 3 and Tremblay et al. (2013a), respectively, and are shown in blue and orange.

conditions

$$u(x,0) = \delta(x) \tag{4.9}$$

$$u(-L,t) = u(L,t) \tag{4.10}$$

$$u_x(-L,t) = u_x(L,t)\,, \tag{4.11}$$

where u_x denotes the derivative of u with respect to x, we can write the analytic solution to the heat equation as

$$u(x,t) = \frac{1}{2L} + \frac{1}{L}\sum_{n=1}^{\infty} cos\left(\frac{n\pi}{L}x\right) e^{-\left(\frac{n\pi}{L}\right)^2 Dt}\,. \tag{4.12}$$

This study is focused on deriving theoretical constraints on the timescales over which one may or may not expect to observe variability at a single spatially unresolved white dwarf. As a measure of the homogeneity at the white dwarf surface we define the contrast, Δ_Z, between the origin ($x = 0$) and an arbitrary point on the surface ($x = x_i$) to be

$$\Delta_Z(x_i,t) = \frac{u(x_i,t)}{u(0,t)}, \tag{4.13}$$

where u is the local concentration of the passive scalar defined in Eq. (4.8). The circumferential positions which will be used to illuminate the timescales of interest throughout this study will be the opposite side of the white dwarf ($x = \pi R_{\rm WD}$) and a quarter of a circumference ($x = \pi R_{\rm WD}/2$).

Fig. 4.2 shows the solution to Eq. (4.8) for the evolution of a delta function scalar around a circular ring of radius $R_{\rm WD}$. This serves as a demonstration of the simple global transport model we employ to estimate the spreading timescales.

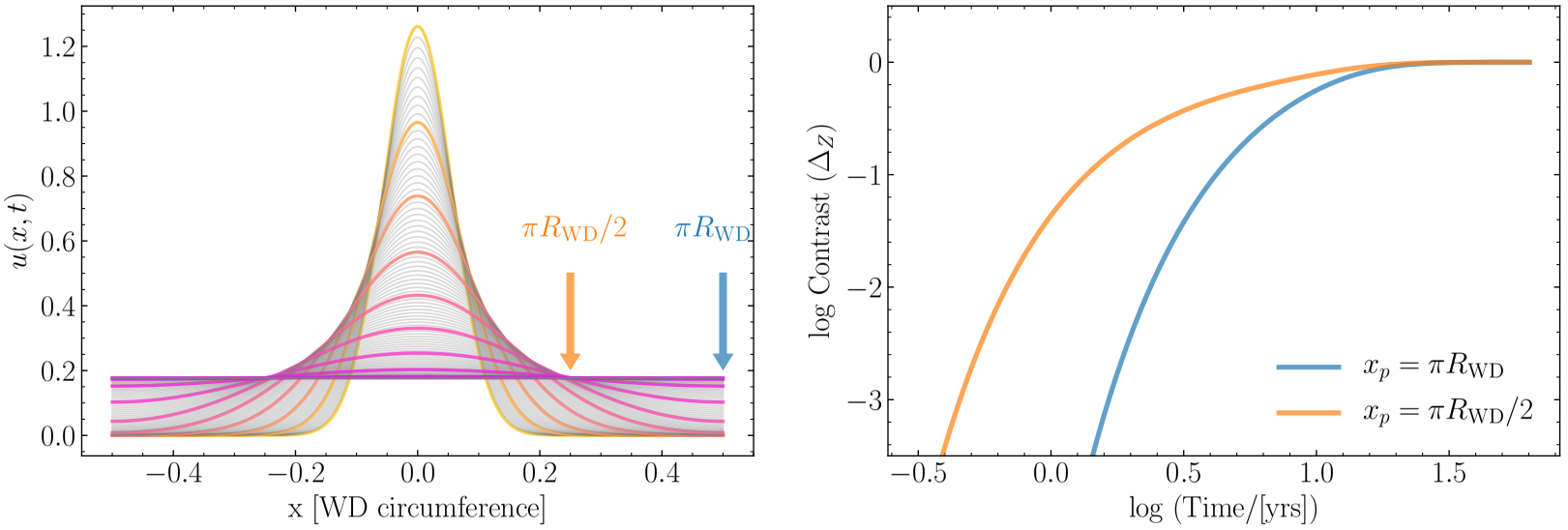

Figure 4.2: *Left:* Evolution of a passive scalar, u, according to Eq. 4.8 with a horizontal diffusion coefficient of $D_{\leftrightarrow} = 5 \times 10^9\,\mathrm{cm^2 s^{-1}}$ and a typical white dwarf radius of $R_{\rm WD} = 0.01288\,R_\odot$. To make clear the evolution, every tenth (logarithmic) time step is indicated with a colour; from yellow to purple. *Right:* Examination of the time-dependent contrast between points of interest along the white dwarf circumference. Here we define contrast (Δz) according to Eq. 4.13 and show the evolution of Δz at half and a quarter of the circumference.

We now go on to present the diffusion coefficients derived from our grid of 3D models. We then implement these diffusion coefficients into the simple model outlined previously for simulating surface transport. This is followed by a presentation of the results from a model which accounts for the sinking of material and depth dependence of the diffusion coefficient, though for narrative clarity we introduce that second model as part of the discussion in Section 4.3.2.

4.3 Results

4.3.1 Horizontal diffusion coefficients

The horizontal diffusion coefficient, $D\leftrightarrow$, derived from direct tracer experiments on nine simulations between 6000 and 18 000 K, are shown in Fig. 4.3. The tracer experiments were carried out with slabs of tracer density initially placed in the $y-z$ and $x-z$ planes, allowing to follow the diffusion process in the horizontal x and y directions, respectively. Each slab probes the entire vertical extent of the simulation box and does not allow for an explicit depth dependence of $D\leftrightarrow$, instead providing a vertically-averaged horizontal diffusion coefficient. The final horizontal diffusion coefficient (and associated error) is computed as the mean (and standard deviation) of the horizontal diffusion coefficient derived for each slab.

The pink points in Fig. 4.3 represent the mean horizontal diffusion coefficient throughout the entire box. For the closed bottom simulations ($\geq$ 12000 K) the mean horizontal diffusion coefficient includes a contribution from the non-mixing layers beneath the convective and overshoot region. We account for this contribution by limiting the maximum amplitude of the tracer density distributions (see Fig. 4.4), effectively removing the vertical layers with no or very little mixing. The purple circles in Fig. 4.3 show the horizontal diffusion coefficient when only accounting for the regions where the tracer density is 10 per cent or lower than the maximum initial value. The arbitrary value of 10 per cent is used to crudely separate the parts of the tracer slab in the deep, non-diffusing layers from those in the shallow, rapidly-diffusing layers. A more robust, but computationally-demanding, approach would be to follow the trajectories of individual tracer particles, preserving the depth dependence of the horizontal diffusion coefficient. A major limitation with this approach however is the large range of advective time scales spanned by a single simulation box, where the vertical diffusion coefficient was found in Chapter 3 (Cunningham et al., 2019) to vary by up seven orders of magnitude. This crude clipping procedure is thus adopted to disentangle the contributions of horizontal diffusion at different depths, without doing the detailed path integration. The distributions resulting from a clipping value of 10 percent are shown in purple in Figs. 4.4 & 4.5.

To investigate whether this clipping procedure negatively impacts our derived dif-

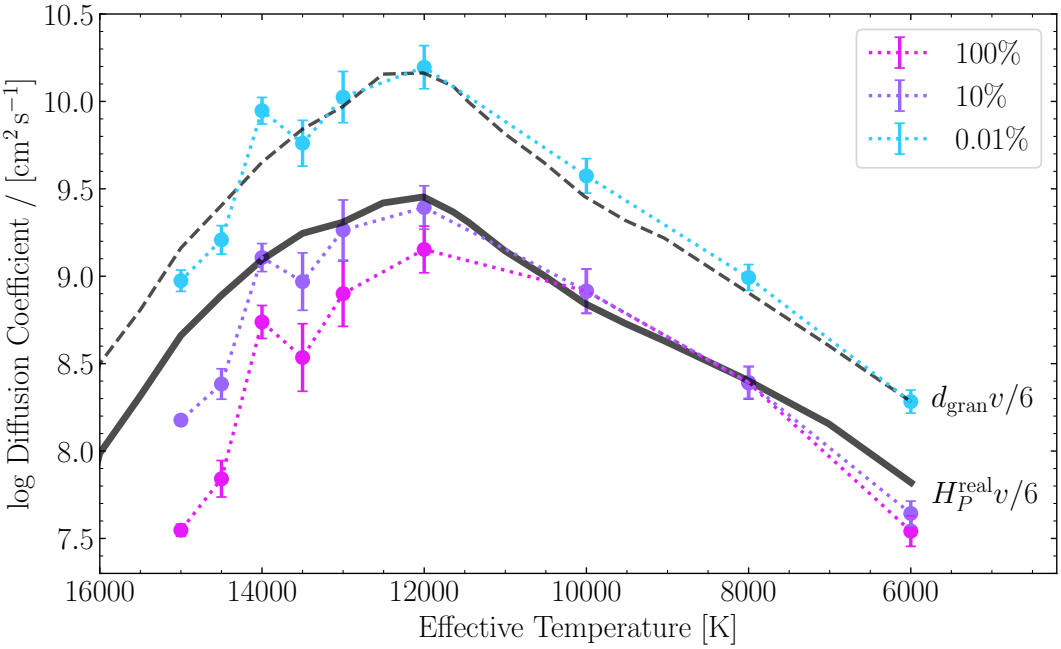

Figure 4.3: Effective horizontal diffusion coefficients derived from direct tracer experiments with nine CO5BOLD simulations (filled circles) between 6000 and 15 000 K at $\log g = 8.0$. The tracer distribution is averaged over all depths of a simulation. Models with $T_{\rm eff} \geqslant 12\,000$ K have closed bottom boundaries, as opposed to the cooler models with open bottom boundaries. For the closed bottom simulations, the trace density in the stable lower layers serves to reduce the effective diffusion coefficient by averaging over layers outside of the convectively mixed region. To mitigate this effect we employ a clipping procedure at <100, <10 and <0.01 per cent of the initial maximum tracer density in pink (i.e., no clipping), purple and cyan, respectively (see Fig. 4.4). A lower clipping value corresponds to probing increasingly fast and rare local diffusion events within the resolved simulation. The cyan line, representing the fastest diffusing layers or resolved diffusion events, can be considered a robust upper limit on the horizontal diffusion coefficient for passive scalars. The purple line corresponds to our best estimate of a mean diffusion coefficient across the accessible convectively mixed layers. The black solid line shows the analytic approximation of the local diffusion coefficient given by Eq. (4.15). The black dashed line shows an alternative analytic prescription for the diffusion coefficient where the length scale is chosen to be the characteristic granule size, rather than the pressure scale height.

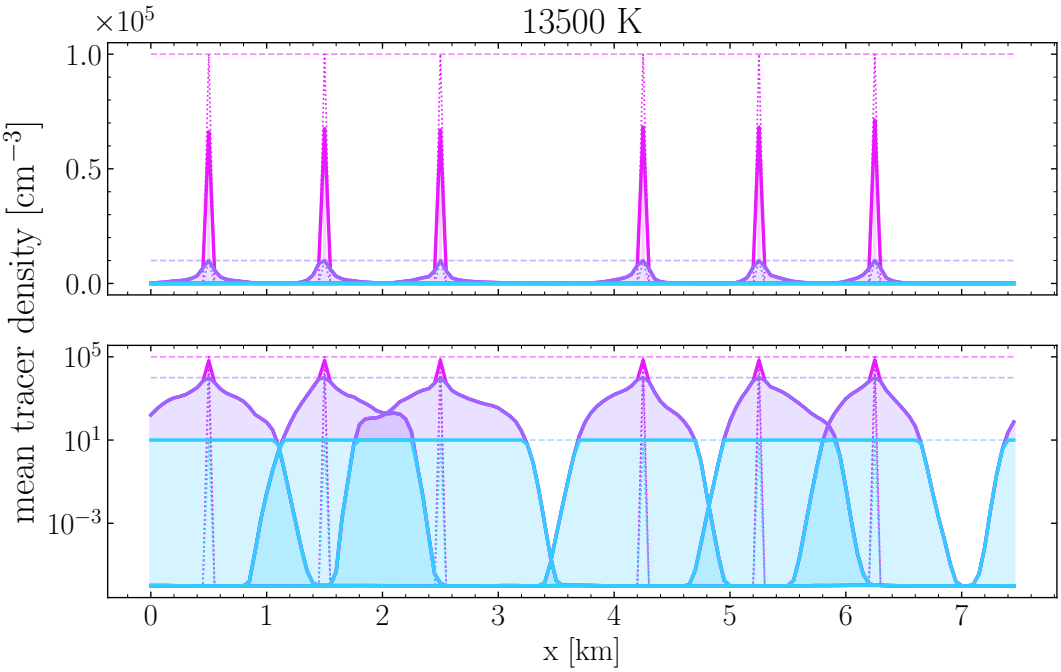

Figure 4.4: Mean tracer densities, $\rho_t(x)$, in the x dimension, averaged over the vertical (z) and other horizontal (y) dimension, for a simulation at 13 500 K and $\log g = 8.0$, and in the time interval $t = 0$ s (dotted) and $t = 0.1$ s (solid). The profiles are shown both linearly (top panel) and logarithmically (bottom panel) for clarity. To remove the contribution of the (non-diffusing) stable lower layers from the mean tracer densities, the distributions are clipped at <10% (purple) and <0.01% (cyan) of the initial maximum density as described in the text. These colours correspond to the lines shown in Fig. 4.3. The boundary conditions in the x-dimension are parallel such that the tracer density ($\rho_{\rm tr}$) satisfies $\rho_{\rm tr}(0) = \rho_{\rm tr}(x_{\rm b})$, for $x_{\rm b} = 7.5$ km.

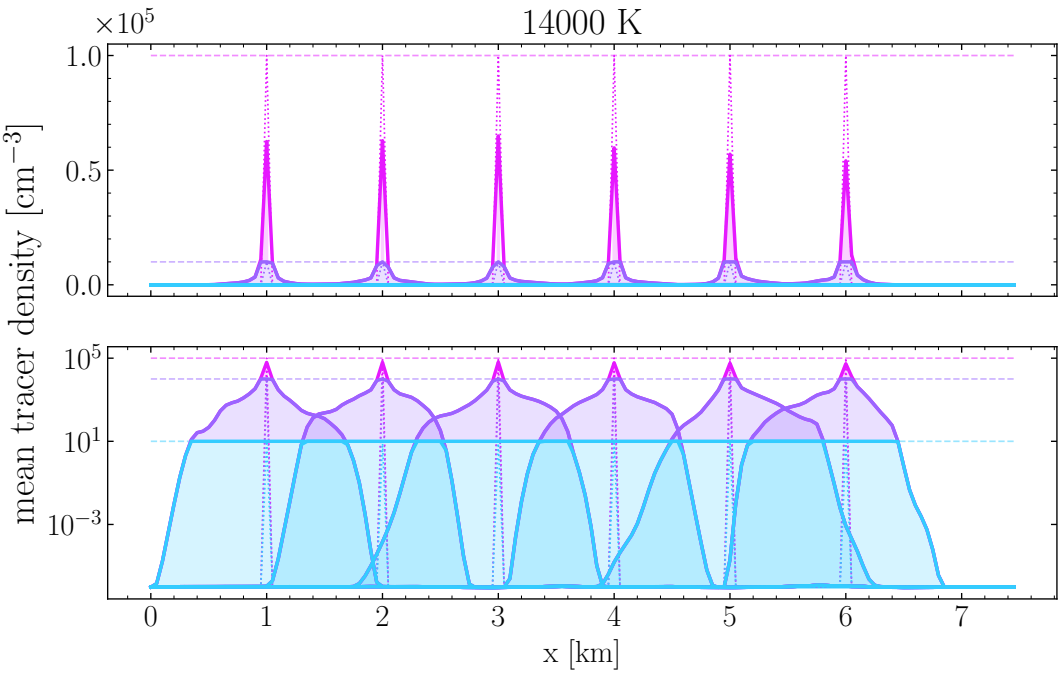

Figure 4.5: Similar to Fig. 4.4 for a simulation at 14,000 K.

fusion coefficients we consider its behaviour on the open-bottom and closed-bottom simulations, respectively. The clipping procedure should not alter the open-bottom simulations because the entire simulation domain is contained within the fast-moving photospheric layers. The closed-bottom simulations are those which possess the deep, slowly-diffusing layers, the contribution of which we seek to remove from the derived horizontal diffusion coefficients. We see in Fig. 4.3 that the open-bottom simulations ($T_{\rm eff} < 11\,000$ K) are barely affected by this clipping value of 10 per cent. On the contrary, the closed-bottom simulations ($T_{\rm eff} > 11\,000$ K) exhibit an increase in the diffusion coefficient of 0.2–0.5 dex.

By extending this approach it is possible to provide an upper limit on the horizontal diffusion coefficient. We probe the most rapidly diffusing layers by considering only the lowest 0.01 per cent of each tracer density distribution, corresponding to the wings of the tracer densities (see Fig. 4.4). Given that convective velocities peak just below the photosphere (Tremblay et al., 2015a), it is likely that these are the layers being described by this diffusion coefficient (cyan on Fig. 4.3). In fact, this case is well represented by

$$D_{\leftrightarrow} = \frac{1}{3}\frac{d_{\rm gran}}{2}\sqrt{v_x^2 + v_y^2}\,, \tag{4.14}$$

as shown by a dashed black curve in Fig. 4.3, where the characteristic length is half the characteristic granulation size, $d_{\rm gran}$, defined from the emergent intensity (Tremblay et al., 2013b). The granule size corresponds most directly to the characteristic size of convective

flows in the photosphere (Tremblay et al., 2013b), suggesting the equation characterises the mixing capabilities of the uppermost surface layers. We could not clearly establish the reason for the factor of $\frac{1}{2}$ to the granulation size compared to the 1D diffusion equation of Eq. (4.6), but this could be because granulation size is a 2D representation of a 3D process, or that in the definition of Tremblay et al. (2013b) a single granule is composed of both a downdraft and an updraft.

The photosphere only contains a small amount of mass compared to the full convection zone, hence Eq. (4.14) is unlikely to be a good representation of the overall horizontal mixing of accreted debris in the convection zone. As such to represent this process, we use instead, as describe above, the clipped estimate where the tracer density is 10 per cent or lower than the maximum initial value. By construction of our models (Tremblay et al., 2013a), this corresponds to mixing in surface layers above Rosseland optical depth $\tau_{\rm R} \lesssim 1000$. This case is best described by

$$D_{\leftrightarrow} = \frac{1}{3} \frac{H_P^{\rm real}}{2} \sqrt{v_x^2 + v_y^2}. \tag{4.15}$$

which is shown by a solid black curve in Fig. 4.3. The characteristic length $H_P^{\rm real}$ is the actual pressure scale height that corresponds to the geometrical distance between the photosphere ($\langle \tau_{\rm R} \rangle = 1$) and the layer below where the pressure drops by a factor e (Tremblay et al., 2013b). It is not clear whether the factor of $H_P^{\rm real}/2$ in Eq. (4.15), when compared to Eq. (4.6), has a fundamental physical justification, as here the diffusion process corresponds to an average over a range of convective layers.

For open bottom simulations with $T_{\rm eff} < 12\,000$ K, Eq. (4.15) may still represent an upper limit on the efficiency of the overall diffusion of accreted material across the stellar surface. The reason is that the lower portion of the convection zones, missing from our simulations, have lower convective velocities and are possibly less efficient to mix material. While this would not necessarily delay the process of achieving a fully homogeneous surface composition across the stellar disc, the actual absolute metal abundances could vary on longer timescales, as the bottom of the convective zone is still adjusting. A lower limit on horizontal diffusion could possibly rely on using the pressure scale height at the bottom of the convection zone in Eq. (4.6).

We provide the results of the direct tracer experiments in Table 4.1 where one can find the mean horizontal diffusion coefficient in the mixed layers (purple circles in Fig. 4.3) as $\log D_{\leftrightarrow}$. We also provide the upper limits (corresponding to the photosphere) on the diffusion coefficient at each effective temperature as $\log D_{\leftrightarrow}^{\rm max}$. Table 4.2 contains the diffusion coefficients derived analytically using Eqs. (4.14) and (4.15) from mean 3D properties for the grid of the warmer (> 11400 K) convective DAs at $\log g = 8.0$ presented

Table 4.1: Diffusion coefficients derived from direct diffusion experiments using nine simulations which were adapted from Chapter 3 (Cunningham et al., 2019) and Tremblay et al. (2013a) for DA white dwarfs at $\log g = 8.0$. The horizontal diffusion coefficient is given as $D_{\leftrightarrow}$ which represents the mean diffusion coefficient across the convectively mixed layers and is shown in explicitly in Eq. (4.5). The associated error is the standard error on the mean. The upper limits on the diffusion coefficient (corresponding to the photospheric layers) are also given.

$T_{\rm eff}$	$\log D_{\leftrightarrow}$	$\log D_{\leftrightarrow}^{\rm max}$
6000	7.64 ± 0.07	8.28 ± 0.07
8000	8.39 ± 0.09	8.99 ± 0.07
10000	8.92 ± 0.13	9.57 ± 0.10
12000	9.39 ± 0.12	10.20 ± 0.12
13000	9.26 ± 0.17	10.02 ± 0.15
13500	8.97 ± 0.16	9.76 ± 0.13
14000	9.11 ± 0.08	9.95 ± 0.08
14500	8.38 ± 0.09	9.21 ± 0.08
15000	8.18 ± 0.03	8.97 ± 0.06
16000	8.10 ± 0.04	8.85 ± 0.04
17000	8.12 ± 0.02	8.86 ± 0.03

in Chapter 3. These quantities correspond to the black solid and dashed line shown in Fig. 4.3. In Table 4.3 and Fig. 4.6 we show the same for the grid of cooler ($< 13\,000$ K) convective DAs from Tremblay et al. (2013a) for $\log g = 7.0$–9.0. The two grids have an overlap in effective temperature between 11 400–13 000 K and we present both grids in full for completeness. We find the diffusion coefficients where the grids overlap agree to within 0.06 dex, well within the estimated uncertainty of 0.1 dex. We also present the diffusion coefficients across the grid of DBs published by Cukanovaite et al. (2019b). These are given in Table 4.4.

4.3.2 Surface spreading

Instantaneous accretion

We begin by considering the evolution of a system whereby a large quantity of a passive scalar is instantaneously delivered either to a point on the white dwarf surface or equatorially, e.g. from an accretion disc.

In the first model, to account for the large range of timescales involved, we consider the spreading and sinking to be governed by two independent, one-dimensional equations. One governs the horizontal spreading of material and assumes all accreted metals are restricted to the convection zone. The other governs the sinking and assumes that the metals are homogeneously mixed across the surface. Clearly this problem setup is unphysical but

Table 4.2: Diffusion coefficients defined by Eq. (4.15) for DA white dwarfs with $\log g = 8.0$. Computed using mean 3D quantities from Cunningham et al. (2019) and Tremblay et al. (2013a) for models with effective temperatures $\geq$ 11 600 K and $\leq$ 11 500 K, respectively. We also show the upper limit on the diffusion coefficient (corresponding to the photospheric layers) defined by Eq. (4.14). The real effective temperature of a simulation can stabilise at a slightly different to the desired value. To represent this we include the quantity $\Delta(T)$ such that the true effective temperature is given by $T_{\rm eff} + \Delta(T)$. Equivalent quantities for DA white dwarfs at other surface gravities can be found in Table 4.3. An explicit error is not available for these results, but we note that typical errors from the direct diffusion experiments (Table 4.1) were on the order of $\sigma(\log D_{\leftrightarrow}) \approx 0.1$.

$T_{\rm eff}$	$\log g$	$\Delta(T)$	$D_{\leftrightarrow}$	$D_{\leftrightarrow}^{\rm max}$
6000	8.00	-3	7.82	8.28
7000	8.00	+11	8.16	8.60
8000	8.00	+34	8.41	8.91
9000	8.00	+36	8.63	9.22
9500	8.00	+18	8.73	9.32
10000	8.00	+25	8.85	9.46
10500	8.00	+32	9.01	9.65
11000	8.00	+5	9.15	9.81
11500	8.00	+29	9.33	10.02
11600	8.00	+41	9.37	10.09
12000	8.00	+8	9.45	10.16
12500	8.00	+9	9.42	10.16
13000	8.00	+4	9.31	9.97
13500	8.00	+1	9.25	9.84
14000	8.00	+1	9.09	9.65
14500	8.00	-2	8.89	9.41
15000	8.00	+0	8.66	9.16
15500	8.00	+1	8.32	8.81
16000	8.00	+2	7.99	8.50
16500	8.00	+3	7.06	7.54
17000	8.00	+3	6.55	7.44
17500	8.00	+24	5.78	7.02
18000	8.00	+21	5.35	6.61

Table 4.3: Similar to Table 4.2 but using the grid of cool DAs from Tremblay et al. (2013a).

$T_{\rm eff}$	$\log g$	$\Delta(T)$	$\log D_{\leftrightarrow}$	$\log D_{\leftrightarrow}^{\rm max}$
7000	7.00	+46	9.38	9.88
8000	7.00	+27	9.63	10.19
9000	7.00	+25	9.88	10.47
9500	7.00	+21	10.03	10.64
10000	7.00	+18	10.25	10.88
10500	7.00	+40	10.45	11.13
11000	7.00	+0	10.40	11.09
11500	7.00	+1	10.24	10.80
12000	7.00	+1	10.14	10.64
12500	7.00	+1	9.93	10.40
13000	7.00	+3	9.79	10.30
6000	7.50	+65	8.42	8.83
7000	7.50	+33	8.78	9.22
8000	7.50	+17	9.02	9.55
9000	7.50	+15	9.24	9.84
9500	7.50	+49	9.37	9.98
10000	7.50	+7	9.53	10.15
10500	7.50	+0	9.71	10.37
11000	7.50	-62	9.87	10.39
11500	7.50	-2	9.95	10.70
12000	7.50	-1	9.87	10.55
12500	7.50	+0	9.76	10.32
13000	7.50	+2	9.67	10.18
6000	8.50	+24	7.13	7.61
7000	8.50	-75	7.68	8.13
8000	8.50	+4	7.79	8.28
9000	8.50	+68	8.02	8.58
9500	8.50	+22	8.11	8.68
10000	8.50	-28	8.20	8.80
10500	8.50	-4	8.32	8.95
11000	8.50	-3	8.44	9.09
11500	8.50	-10	8.58	9.24
12000	8.50	-21	8.72	9.41
12500	8.50	-80	8.88	9.60
13000	8.50	-91	8.97	9.74
6000	9.00	+28	6.74	7.28
7000	9.00	-40	6.99	7.45
8000	9.00	+41	7.19	7.64
9000	9.00	-1	7.41	7.93
9500	9.00	+7	7.50	8.05
10000	9.00	-38	7.58	8.16
10500	9.00	-97	7.66	8.27
11000	9.00	-52	7.78	8.41
11500	9.00	-85	7.88	8.53
12000	9.00	-85	8.01	8.68
12500	9.00	-64	8.14	8.84
13000	9.00	-31	8.28	9.02

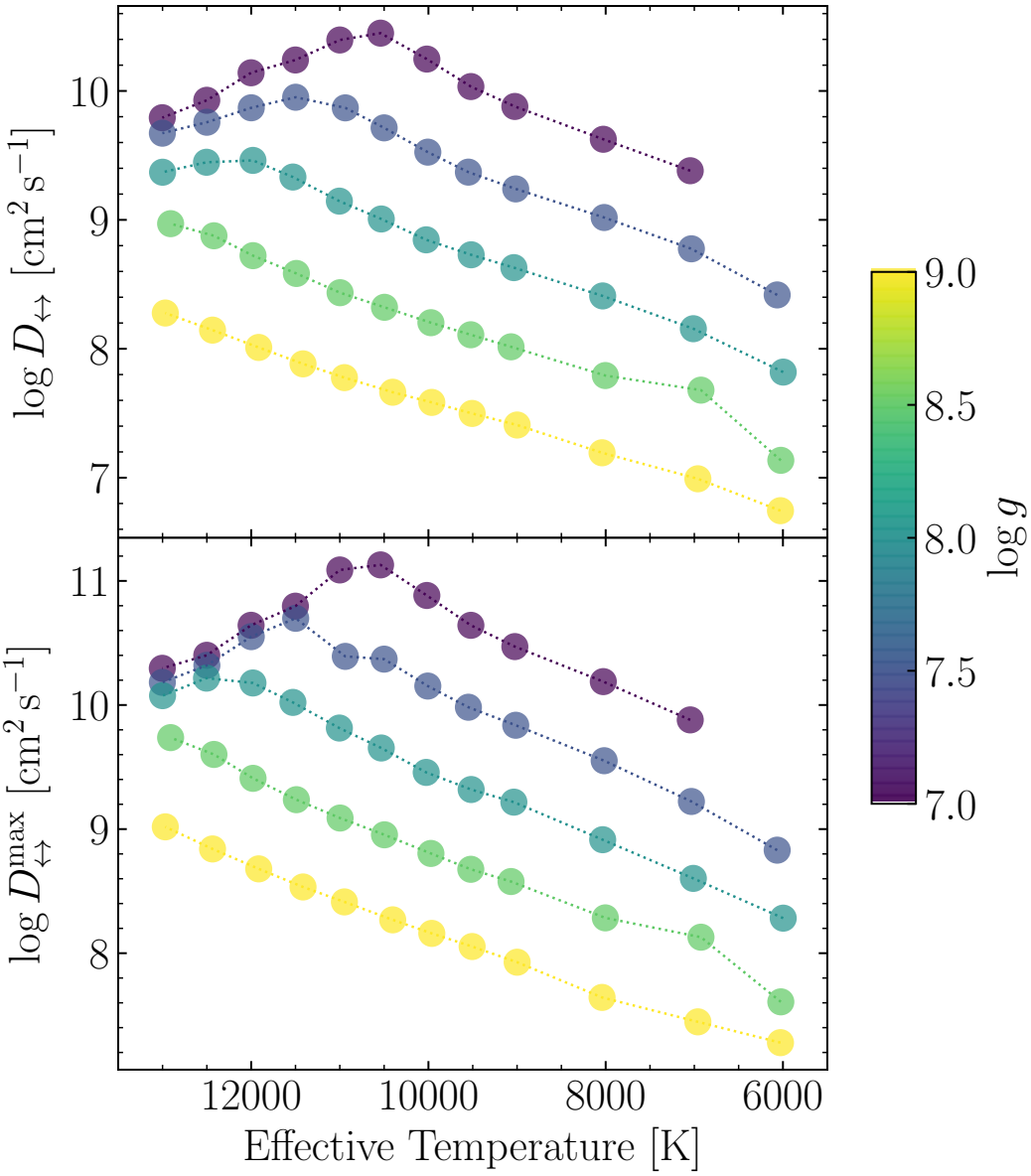

Figure 4.6: *Top*: Diffusion coefficients defined by Eq. (4.15) using mean 3D values derived from the grid of models presented in Tremblay et al. (2013a). *Bottom*: Similar to top panel except the diffusion coefficients were calculated for photospheric diffusion using Eq. (4.14). The mean error on the diffusion coefficients derived from direct diffusion experiments (Table 4.1) was found to be $\sigma(\log D_{\leftrightarrow}) = 0.1$ which we adopt as an estimate for the error on the points shown in this figure. All values shown here are displayed in Table 4.3.

Table 4.4: Similar to Table 4.2 for the grid of DB white dwarfs (log [H/He] = −10) from Cukanovaite et al. (2019b).

$T_{\rm eff}$	$\log g$	$\Delta(T)$	$\log D_{\leftrightarrow}$	$\log D_{\leftrightarrow}^{\rm max}$
14000	7.50	-5	8.59	9.20
16000	7.50	+63	8.81	9.38
18000	7.50	-37	9.15	9.75
20000	7.50	+42	9.55	10.43
22000	7.50	-56	9.66	10.83
23000	7.50	-75	9.71	10.87
26500	7.50	-29	9.77	10.88
28000	7.50	-7	9.70	10.76
30000	7.50	-18	9.63	10.63
32000	7.50	+9	9.45	10.44
12000	8.00	+44	7.74	8.29
14000	8.00	-47	7.97	8.55
16000	8.00	-17	8.19	8.78
18000	8.00	-39	8.46	9.08
20000	8.00	-97	8.84	9.49
22000	8.00	+26	9.10	10.20
24000	8.00	+6	9.18	10.33
25500	8.00	-167	9.22	10.30
28000	8.00	-32	9.30	10.40
30000	8.00	+13	9.29	10.37
32000	8.00	-3	9.24	10.26
34000	8.00	-11	9.12	10.09
12000	8.50	+13	7.12	7.63
14000	8.50	+13	7.37	7.90
16000	8.50	-6	7.58	8.15
18000	8.50	-4	7.80	8.38
20000	8.50	-38	8.11	8.73
22000	8.50	+44	8.53	9.38
24000	8.50	+25	8.61	9.68
26000	8.50	-31	8.65	9.77
27000	8.50	+179	8.72	9.81
30500	8.50	+35	8.84	9.93
32000	8.50	-148	8.85	9.94
34000	8.50	-70	8.87	9.92
12000	9.00	+25	6.50	6.99
14000	9.00	-14	6.75	7.27
16000	9.00	+1	6.97	7.52
18000	9.00	-19	7.18	7.76
20000	9.00	+38	7.45	8.07
22000	9.00	-77	7.78	8.47
24000	9.00	+31	8.03	8.88
26000	9.00	+31	8.10	9.18
28000	9.00	-20[111]	8.17	9.28
30000	9.00	-157	8.25	9.34
31000	9.00	+11	8.30	9.35
34000	9.00	-230	8.42	9.47

it allows for a simple analytic formulation of the problem. The analytic approach refers to the problem setup outlined in Section 4.2.2.

Fig. 4.7 shows the time required, $t_{\rm cover}$, for the metal abundance at the white dwarf surface to homogenize. From black to grey this is shown for increasing levels of homogeneity; namely contrasts of $\Delta_Z = 0.001, 0.1, 0.5, 0.99$. The vertical diffusion (sinking) times from Koester (2009) are shown in dotted purple for eight elements across the full effective temperature range. The mean sinking time arising from the model of convective overshoot presented in Chapter 3 is shown in thick green for effective temperatures between 11 400–18 000 K. It is expected that the convection zones of cooler white dwarfs will also exhibit convective overshoot, but simulating these deep convection zones, and the overshoot region underneath, is intractable with current computational methods. As an estimate of the enhanced mixing due to overshoot in these cooler stars (<11 400 K), we adopt an arbitrary overshoot correction of one pressure scale height (shown with the thin green line), motivated by the predicted overshoot correction for the coolest 3D model (11 400 K) in the overshoot grid (see Chapter 3). For comparison, our updated estimate of the disc lifetime (Girven et al., 2012) is shown in dashed blue, with the associated error (see Table 4.5). We find moderate dependence on whether the accretion is spot-like or equatorial from this model. The expected behaviour that equatorial accretion homogenizes faster is recovered, but the difference is no more than a factor of three.

We introduce in Fig. 4.8 the ratio of the spreading time, $t_{\rm cover}$, and the sinking time, $t_{\rm sink}$. This dimensionless quantity is a metric by which we will assess the capability of a white dwarf envelope to efficiently spread material. One can consider that when this ratio is below unity the surface layers are able to spread material out quicker than it sinks. In this figure we show the $t_{\rm cover}/t_{\rm sink}$ ratio for $t_{\rm cover}$ corresponding to $\Delta_Z = 0.1$, i.e., for chemical abundance variations of less than a factor 10.

Continuous Accretion

So far we have considered the scenario that the accreted metals arrive in a small region on the surface at one instant in time. This would correspond to a direct impact type scenario and is considered one of the least likely sources of accretion at white dwarfs (Wyatt et al., 2014). We have also required that the metals remain confined to the surface when modelling the spreading. We now relax these criteria and go on to consider the scenario in which a white dwarf accretes for a prolonged period with constant accretion rate. This would represent the stable accretion of material from a debris disc.

To model the behaviour of the metals at the surface of the white dwarf in such a system we adopt a two-zone model. In this model the horizontal diffusion coefficient, $D_{\leftrightarrow}$, is confined to some upper region and a lower adjacent region has a drift velocity, $v_{\rm drift}$. The

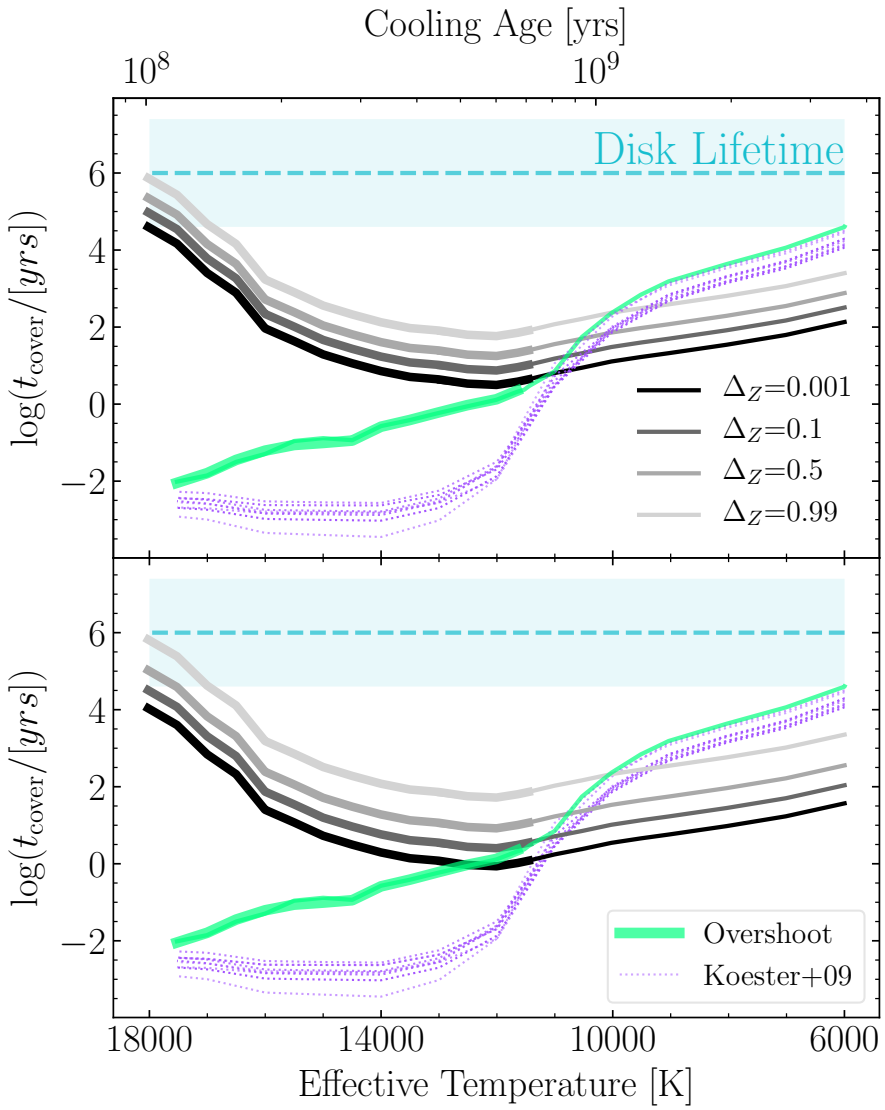

Figure 4.7: Estimates of the timescales corresponding to key physical processes in our model. From black to grey are the times required for the white dwarf surface to homogenize such that the variation of metal abundance with position, Δ_Z, is less than 0.001, 0.1, 0.5 and 0.99, respectively. The top panel depicts $t_{\rm cover}$ for instantaneous accretion onto a point whilst the bottom panel assumes instantaneous equatorial accretion. The diffusion calculations of Koester (2009) yield the vertical sinking times for C, O, Na, Mg, Al, Si, Ca and Fe which are all shown in pink dotted for clarity. Derived in Chapter 3, the modified sinking times inclusive of convective overshoot are shown in thick green for the range 18000–11400 K. The thin green line in the cooler effective temperature range (<11400 K) provides an estimate for the enhanced mixing due to overshoot of one pressure scale height beneath the lower Schwarzschild boundary. This arbitrary value for overshoot is motivated by the correction predicted at the coolest end of the 3D model grid (see Chapter 3). The dashed cyan line depicts an estimate of the mean disc lifetime and the expected uncertainty (see Table 4.5).

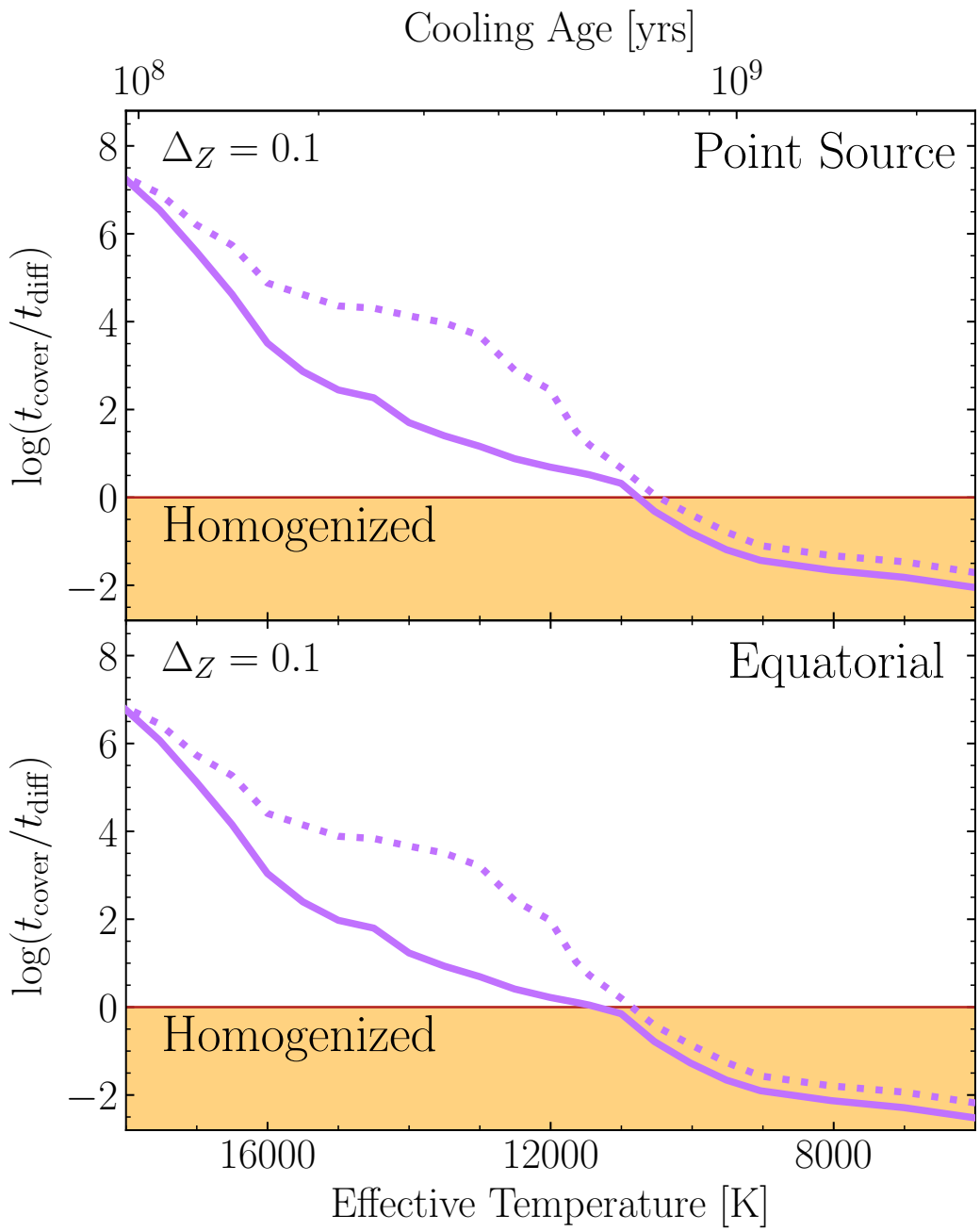

Figure 4.8: The ratio of the spreading and sinking timescales, $t_{\rm cover}$ and $t_{\rm diff}$, is shown here in black across the range of effective temperatures considered in this study. As with Fig. 4.7, the top and bottom panels correspond to accretion onto a spot and accretion onto the equator, respectively. The red line indicates where the timescales are equal. Accretion events which fall below this line are less likely to exhibit observable variability due to surface inhomogeneity of surface metal abundance. Dotted lines correspond to the 1D vertical diffusion times of Koester (2009) while thick solid lines are the results of Chapter 3 taking into account convective overshoot. The spreading timescale is defined for a maximum abundance contrast of $\Delta_Z = 0.1$.

equation describing the evolution of this scenario is as follows

$$\frac{\partial u}{\partial t} = (D_{\leftrightarrow})\Delta u - v_{\rm drift}\frac{\partial u}{\partial z}\,, \tag{4.16}$$

where $u = u(x, z, t)$ is the concentration of a passive scalar depending on depth, surface position and time. Once this system has reached a steady state, the equation reduces to

$$(D_{\leftrightarrow})\frac{\partial^2 u}{\partial x^2} = v_{\rm drift}\frac{\partial u}{\partial z}\,. \tag{4.17}$$

For a constant flux delivered to $x = 0$, this equation has the analytic solution of the form

$$u(x, z) \propto \exp\left(\frac{-x^2}{4z}\frac{v_{\rm drift}}{D_{\leftrightarrow}}\right)\,, \tag{4.18}$$

where z is the vertical extent of the surface zone, $v_{\rm drift}$ is the diffusion velocity at the base of the surface zone and x is the horizontal extent of the surface. We are interested in the global spreading properties which for a spot would require $x = \pi R_{\rm WD}$ and for an equatorial belt would require $x \approx \pi R_{\rm WD}/2$. Thus in the case of a white dwarf for convection to be efficient at spreading before material sinks requires

$$\frac{(\pi R_{\rm WD})^2}{4z_{\rm cvz}}\frac{v_{\rm drift}}{D_{\leftrightarrow}} \lesssim 1\,, \tag{4.19}$$

where $z_{\rm cvz}$ is the depth of the convection zone, $v_{\rm drift}$ represents a characteristic velocity for the settling of a trace amount of metal out of the convection zone. The drift velocity, $v_{\rm drift}$, could alternatively be expressed using the vertical diffusion coefficient, $D_{\downarrow}$, as $v_{\rm drift} = D_{\downarrow}/z_{\rm cvz}$ which allows the equation to be written with more explicit symmetry as

$$\frac{(\pi R_{\rm WD})^2}{4z_{\rm cvz}^2}\frac{D_{\downarrow}}{D_{\leftrightarrow}} \lesssim 1\,. \tag{4.20}$$

Throughout the rest of this chapter we adopt the explicit notation that $D_{\downarrow}$ refers to vertical diffusion coefficient. For the drift velocity in Eq. (4.19) we adopt the diffusion velocity at the base of the mixed region. Fig. 4.9 shows the diffusion velocity for O, Mg, Si, Ca and Fe computed at the lower Schwarzschild boundary (pink-dotted) and at the base of the overshoot region (purple-solid) taken from updated tables of Koester (2009) and Chapter 3, respectively. As was shown by the latter, convective instabilities arise at 18 000 K. In the radiative regime ($T_{\rm eff} > 18\,000$ K) diffusion velocities are given at an optical depth of $\tau_{\rm R} = 5$. We caution that none of these models include the effects of radiative levitation and thermohaline mixing which may become important in the radiative regime (Chayer et al., 1995a,b; Bauer & Bildsten, 2018).

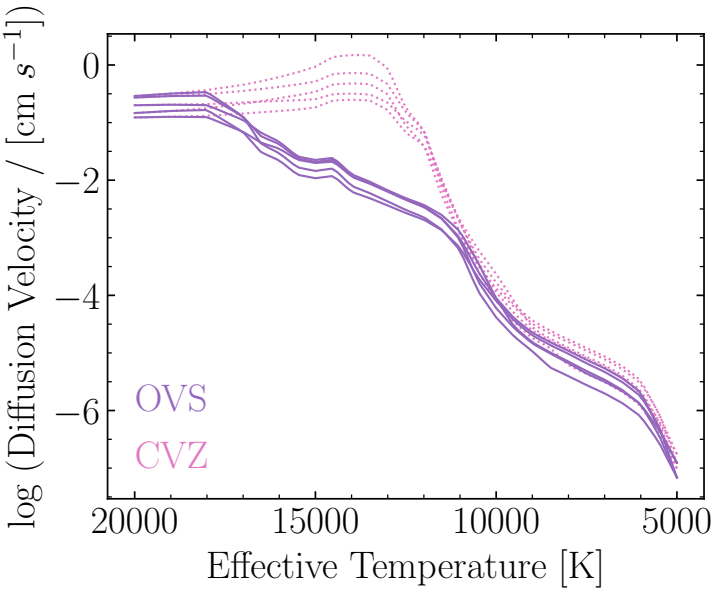

Figure 4.9: The two prescriptions for vertical diffusion velocities used throughout this study. Diffusion velocities at the lower Schwarzschild boundary taken from updated tables of Koester (2009) and are shown in pink (dotted). The diffusion velocities presented in Chapter 3 which account for significant convective overshoot regions between 14 000 and 18 000 K are shown in purple (solid). For lower effective temperatures (< 11400 K) the diffusion velocity is taken one pressure scale height beneath the lower Schwarzschild boundary as a minimum estimate of the contribution of convective overshoot. For higher effective temperatures with radiative atmospheres (> 18 000 K) the diffusion velocity is instead given at an optical depth of $\tau_R = 5$.

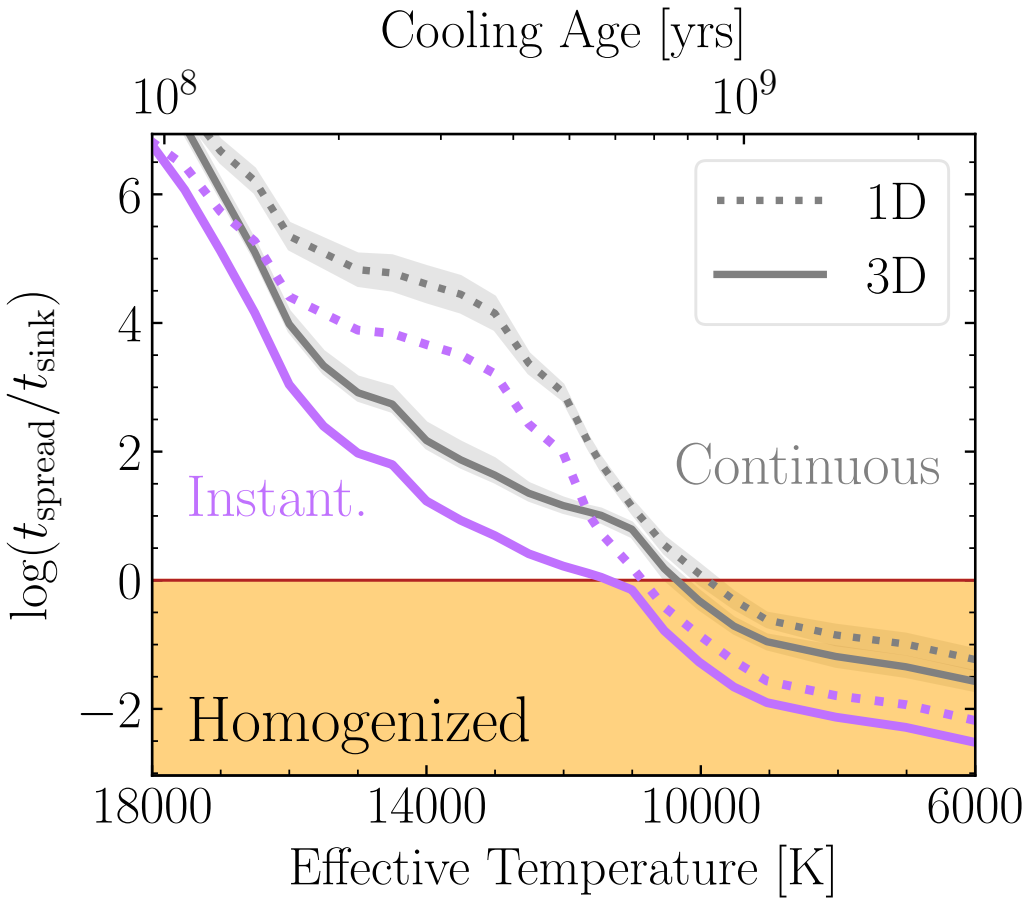

Figure 4.10: Comparison of two models, instantaneous accretion and continuous accretion, in the comparison of spreading and sinking timescales. The instantaneous accretion model, in purple, is shown where the vertical diffusion coefficient, $D_{\downarrow}$, is either given by the 1D mixing length theory results of Koester (2009) or from the 3D overshoot results of Chapter 3 in dotted or solid, respectively. The spreading timescale is defined for a maximum surface abundance contrast of $\Delta_Z = 0.1$ from equatorial accretion (reproduced from lower panel; Fig. 4.8). In grey, the latter model – continuous accretion – is expressed by the left-hand side of Eq. (4.19) as a mean across the elements O, Mg, Si, Ca and Fe, with the standard deviation shown as the filled error region.

We plot the left-hand side of Eq. (4.19) in Fig. 4.10 in grey and we include the results with (solid) and without (dotted) overshoot. We also reproduce the results for instantaneous accretion (see Fig. 4.8) in purple. We find that the continuous accretion is slightly less effective at homogenizing within a vertical diffusion time compared to the instantaneous case. The reason for this is that the origin of the accretion at the surface is constantly being replenished so this enhances the horizontal contrast. It should be noted that unlike the model of instantaneous accretion, the model of continuous accretion does not assume an explicit maximum surface abundance variation.

The models we have presented highlight the horizontal mixing capabilities across the full range of convective DA white dwarfs. In Fig. 4.6 and Table 4.3 we provide the horizontal diffusion coefficients for DA white dwarfs of different surface gravities, though for brevity we do not directly compare them here with vertical diffusion coefficients, as the results are similar to $\log g = 8.0$ but with a small shift in effective temperature. We now go on to consider the surface spreading behaviour in DB white dwarfs.

Surface spreading in DB white dwarfs

Approximately half of the known polluted white dwarfs are of DB spectral type (Farihi et al., 2016). In this section we repeat some of the procedures detailed in the previous sections to provide a picture of the mixing capabilities of DB white dwarfs as they cool. The left panel of Fig. 4.11 shows the horizontal diffusion coefficients for DA and DB white dwarfs at $\log g = 8.0$, derived in Section 4.3.1. The right panel of Fig. 4.11 shows, in pink, the ratio of the spreading and sinking times. This can be directly compared to the green line in the middle panel which shows the same quantity for the DAs. The correction for convective overshoot is not readily accessible for the DBs – requiring an overshoot study similar to Chapter 3 for the early convective DBs – and is outside the scope of this work. However, one can infer from the behaviour shown in the DAs (middle panel) that the 1D results for DBs represent a lower limit on the capability to spread material across the surface. Given that the majority of metal-polluted DBs have effective temperatures less than 25 000 K, this figure suggests that metal-polluted DBs are far more likely to be homogeneously mixed within a diffusion timescale.

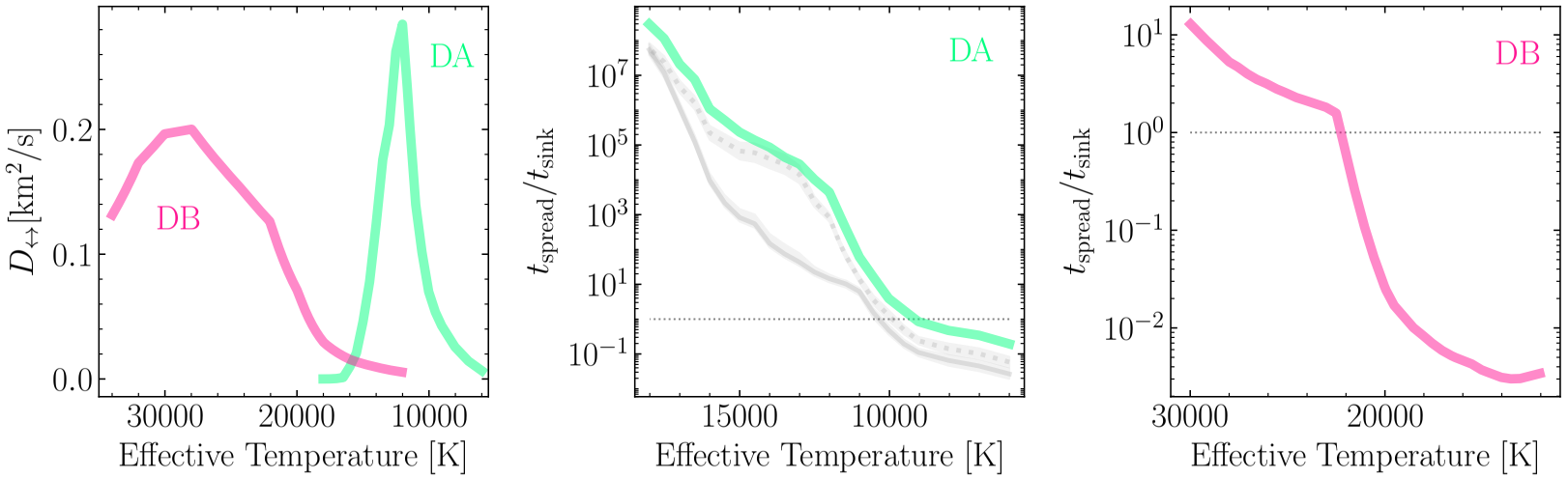

Figure 4.11: *Left:* Horizontal diffusion coefficients for DAs (green) and DBs (pink) derived from mean 3D parameters from Eq. (4.15) and the grids published in Cunningham et al. (2019); Tremblay et al. (2013a) and Cukanovaite et al. (2019b), respectively. *Center:* The ratio of the spreading time and sinking times for DA white dwarfs are shown in in green. The spreading time here is estimated as $t_{\rm spread} \approx (\pi R_{\rm WD})^2/D_{\leftrightarrow}$ and the sinking time is taken as the diffusion timescale from Table 4 of Koester 2009. Continuous accretion curves from Fig. 4.10 are also shown in grey for comparison. *Right:* Similar to the middle panel but for DB white dwarfs. The spreading time is based on the 3D horizontal diffusion coefficients and the sinking times are taken from the Montreal White Dwarf Database (Dufour et al., 2017). Further work would be required to add the grey curves for the DBs as this requires additional information, in particular $v_{\rm drift}$, at the base of the convection zone.

4.4 Discussion

For any white dwarf, the numerical solution of Eq. (4.16), using the horizontal diffusion coefficients presented in this chapter as well as vertical diffusion coefficients from the previous chapter or the literature, would yield a reasonable description of the distribution of metals across the white dwarf surface. This could provide the basis for the generation of synthetic spectra under different accretion conditions (geometries and time-dependence) and rotational periods. Such models are beyond the scope of this work where we instead favour a heuristic discussion of these systems across a wide-parameter space.

The results we have shown so far focus mostly on the competition between spreading and sinking. This led to a separation, based on atmospheric parameters, between metal-rich white dwarfs which are expected to have a homogeneous surface composition and those which are likely to show metals only close to the regions of accretion. When it comes to predict how likely it is to observe photometric or spectral variability in a white dwarf, we also need to consider the amplitude, periodicity and total duration of a predicted contrast, which depend on further physical variables. In addition to (1) the white dwarf atmospheric parameters (spreading and sinking times), we must also consider (2) the geometry of accretion, (3) the instantaneous accretion rate, (4) the duration of the event (e.g. the disc lifetime combined with the sinking time), and (5) the white dwarf rotation period and inclination with respect to the line of sight. Fortunately, some of these quantities are observationally or theoretically constrained and limiting cases are sometimes sufficient when considering the white dwarf population as a whole.

4.4.1 Variables

Accretion geometry

To predict white dwarf surface homogeneity, one should consider the initial distribution of metals onto the white dwarf surface, whether that be a spot or multiple spots as seen in the Shoemaker-Levy 9 disruption and accretion of an asteroid onto Jupiter (Brown et al., 2017), a stable accretion disc funneling material either to an equatorial belt or to the poles (Wyatt et al., 2014; Farihi et al., 2018a), or a near-homogeneous (spherical) deposition. We emphasise that we obtain a trivial result if accretion is fully spherical, in which case the surface is homogeneous and diffusion is only of relevance in the radial direction, where 3D convective effects nevertheless still play a role.

The geometry of accretion is not well constrained but equatorial accretion is generally favoured in low-magnetic field cases (Farihi et al., 2016), in analogy to the more widely studied accretion processes in cataclysmic variables which have accretion rates many orders of magnitude larger (Patterson & Raymond, 1985; Piro & Bildsten, 2004). We discuss the

particular case of magnetic white dwarfs in Section 4.4.4, where accretion is more likely proceed to the poles (Metzger et al., 2012).

Accretion rates and timescales

Another dimension in the problem is that of the time-dependence of the accretion. This includes the total duration of a particular event, the accretion rate in mass per time unit and its variability.

Accretion can take an instantaneous form (say with the chance impact of an asteroid), a continuous form which could be the steady accretion of material from a disc (i.e., as is proposed for G29-38, Xu et al. 2014) or episodic accretion where the accretion rate of material from the disc has a non-zero time derivative. All these scenarios are explicitly covered by our surface spreading model of Section 4.3. We have demonstrated that continuous accretion can lead to a slightly less homogeneous distribution of metals across the surface compared to instantaneous accretion due to constant replenishment of the high-abundance regions. Episodic accretion is bounded by instantaneous and continuous accretion.

The instantaneous accretion rate directly sets the absolute density of tracers in Eq. (4.16), hence the detectability of metal lines. In most cases this can be constrained from observed spectroscopic surface abundances, from which one can infer about the average accretion rate over a sinking timescale (see, e.g., Fig. 4.12, bottom panel).

The total duration of the event, i.e. the actual duration of accretion followed by the decay phase over the sinking timescale, impacts the chances of variability being observed. This is especially the case for white dwarfs with short sinking times, where a direct impact may lead to an event of very short total duration compared to continuous accretion over a disc lifetime (see next section). For white dwarfs with long sinking timescales, this effect is mitigated as the long decay phase can also be observed.

Disc lifetimes

Girven et al. (2012) provided an estimate for the lifetime of a disc of disrupted planetesimals around a white dwarf. They based their calculation on the mean inferred accretion rate at warm polluted DAZ stars, where the short sinking timescales suggest a nearly instantaneous rate. This was compared to the mass of metals enclosed in DBZ white dwarf convection zones. The latter is a lower estimate of the total accreted mass considering that some of the material has already sunk or is still within the disc. Given the long sinking times in DBZ stars, of the same order as the disk lifetime, the mass within the convection zone still provides a good estimate of the disk mass. The inclusion of convective overshoot impacts these measured quantities and therefore we take this opportunity to update the estimate for

Table 4.5: Disc lifetimes based on a re-analysis of the polluted white dwarfs from Farihi et al. (2016). We also show the results presented by Girven et al. (2012) for comparison.

	$\log t_{\rm disc}$ [yr]	$\langle \log \dot{M}^*_{\rm DAZ} \rangle$ [g s^{-1}]	$\langle \log M^*_{\rm DBZ} \rangle$ [g]	Overshoot?	$N_{\rm DAZ}$	$N_{\rm DBZ}$
Girven et al. (2012)	5.6 ± 1.1	8.8 ± 0.4	21.9 ± 1.1	×	13	8
This work	6.3 ± 1.4	8.6 ± 0.5	22.4 ± 1.4	×	19	11
	6.0 ± 1.4	8.8 ± 0.5	22.4 ± 1.4	✓	19	11

the lifetime of a disc from

$$t_{\rm disc} \sim \frac{\langle M^*_{\rm DBZ} \rangle}{\langle \dot{M}^*_{\rm DAZ} \rangle}\,, \tag{4.21}$$

where the asterisk denotes polluted white dwarfs with a confirmed IR excess, i.e. with a debris disc. Girven et al. (2012) found $\log(t_{\rm disc}) = 5.6 \pm 1.1$ [yr] to be their best estimate with $\langle \log \dot{M}^*_{\rm DAZ} \rangle \geqslant 8.8$ [g s^{-1}] and $\langle \log M^*_{\rm DBZ} \rangle = 21.9$ [g].

We repeated the same analysis with the now slightly larger sample of metal-polluted white dwarfs which exhibit IR excess from Farihi et al. (2016), using a model both with and without overshoot, the latter being directly comparable to the original result. Fig. 4.12 shows the accreted masses and accretion rates for a sample of 19 DAZ and 11 DBZ white dwarfs which exhibit IR excess. These disc lifetime estimates are presented in Table 4.5. We note that these calculations assume that Ca makes up 1.6 per cent of the accreted material. This value corresponds to the bulk-Earth abundance of Ca (Morgan & Anders, 1980) and is typically used to convert Ca abundances in evolved planetary systems into a total accreted mass (Girven et al., 2012; Bergfors et al., 2014; Farihi, 2016).

We find that the new observed sample with the updated sinking times from Koester et al. (2014) supports a longer disc lifetime (Myr) than the earlier estimate of Girven et al. (2012). Without overshoot the disc lifetime estimate has increased by almost an order of magnitude, though the two results are still consistent within error bars. This is because the sample is now larger than in the previous study and the mean total accreted mass in the DBZ/DZ white dwarfs has increased (see Table 4.5). The inclusion of convective overshoot in the analysis yields a disc lifetime which is 0.3 dex shorter than its non-overshoot counterpart, a correction that is well within observational uncertainties. This relatively small 3D correction is in part because a third of the DAZ stars in the sample have effective temperatures above 18 000 K for which there is no overshoot correction. For white dwarfs with $T_{\rm eff} < 11\,400$ K we use the correction applied to the coolest end of the overshoot grid. We therefore propose an updated disc lifetime estimate of $\log(t_{\rm disc}) = 6.0 \pm 1.4$ [yr]. We note that this update does not include an overshoot correction to the DB models, as constraining the overshoot mixing in these helium-rich white dwarfs is beyond the scope of

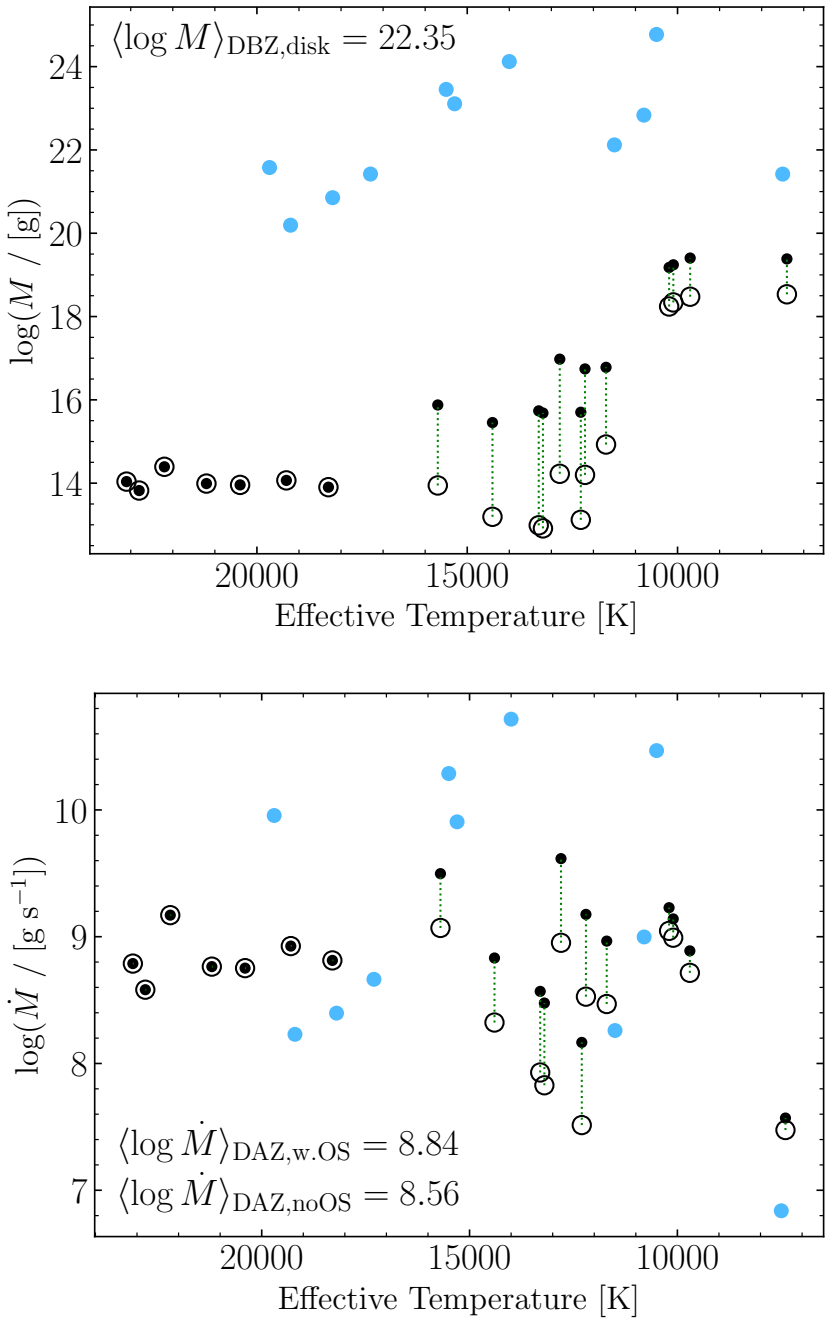

Figure 4.12: Accretion rates (bottom panel) and lower limit on the accreted mass (top panel) for a sample of 19 DAZ (black) and 11 DBZ (blue) white dwarfs with a detected IR excess from Farihi et al. (2016).

this work.

4.4.2 Predicting variability

Given the number of independent variables, we split our discussion based on white dwarf temperature and spectral type, which are readily available observational quantities.

Cool DA white dwarfs

Below 10 000 K, DA white dwarfs have relatively large convection zones and long sinking timescales. For instance metals will stay visible for at least 10 000 yrs at 7000 K, but it could be several times longer when considering the disk lifetime and decay phase. Fig. 4.10 shows that convection is efficient at spreading metals across the surface in this regime, under any accretion geometry or whether it is instaneous or continuous. Homogenizing the surface such that global variations are less than 50% takes only $\sim$ 1000 yrs. Thus surface variations could only be observed during the initial, non-steady phase of accretion, which is less than 0.1 percent of the disk lifetime. Thus the probability of finding an inhomogeneous surface is low, but dynamically active planetary systems in an early phase of disruption may still show atmospheric abundance variabilities (Vanderburg et al., 2015; Vanderbosch et al., 2019).

Warm DA white dwarfs

Above 14 000 K, a DA white dwarf will have a relatively small convection zone in radius and mass ($\log M_{\rm convective}/M_{\rm tot} \lesssim -14$) with maximum convective velocities on the order of 1 km s^{-1}. Fig. 4.10 shows that such an object is unable to effectively homogenize its surface, regardless of whether accretion is instantaneous or continuous over a disk lifetime. The reason for this behaviour is that any metals accreted do not have enough time to travel across the stellar surface before they diffuse out of the convection zone.

For temperatures above 18 000 K, no convective instabilities are expected to develop in DA white dwarf atmospheres. Thus our improved convective model is not directly relevant. In this regime thermohaline instabilities may be the dominant form of horizontal mixing (Bauer & Bildsten, 2018). These instabilities have similar sizes and timescales compared to convection, hence we expect spreading times in warm radiative white dwarfs to be similar to those of warm convective objects. As a consequence, it is unlikely that thermohaline mixing can lead to significantly more homogeneous stellar surfaces than predicted in this work.

If the accretion rate is variable in time, additional variations are expected over the sinking time, which is of the order of days to months. Radiative levitation must also be considered when predicting such temporal abundance variations.

Overall, we predict that all DAZ white dwarfs above 14 000 K are expected to show surface inhomogeneity. The only know physical mechanism that would be able to prevent this outcome is near-spherical accretion geometry.

DA white dwarfs at intermediate temperatures

We see in Fig. 4.10 that the inclusion of convective overshoot makes a considerable impact to the homogenizing efficacy of the surface layers. Because overshoot has no impact on the horizontal diffusion coefficient one can explain this as a direct consequence of the longer sinking times that result from including overshoot in the modelling (because the base of the mixed region is in deeper, slower moving layers). This changes the onset of surface homogeneity by about 500 K. Figs. 4.8 and 4.10 also demonstrate that the time dependence and geometry of accretion can also change the onset of surface homogeneity by about 1000 K. Furthermore, solving Eq. (4.16) for continuous accretion should in principle include the depth dependence of the horizontal diffusion coefficient (Fig. 4.6), which is likely to result in a relatively complex surface abundance profile with extended low abundance tails corresponding to the faster photosphere spreading. Therefore, it is difficult to predict a firm outcome for DA white dwarfs in the range 10 000-14 000 K.

We note that this temperature range corresponds to the quickest spreading time, with variations expected to smear out within 100 yrs (see Fig. 4.7). This is a direct consequence of the diffusion coefficient experiencing a maximum at this temperature (i.e., the $\log g = 8.0$ track of Fig. 4.6), which is directly tied to this being the peak in convective velocities. However, this is somewhat balanced out by the relatively short sinking timescales on the order of 1–100 years.

Helium-rich atmospheres

The convective instabilities in white dwarf atmospheres are driven by the opacity. For DAs the hydrogen opacity is maximal around 12 000 K, whereas for DBs the helium opacity peaks around 28 000 K. One might thus expect a similarity between the two evolutionary tracks, offset by $\approx$ 16 000 K. An examination of Fig. 4.11 reveals such behaviour. We see that DB white dwarfs with effective temperatures cooler than $\approx$ 24 000 K are very efficient at moving accreted metals across the surface and that they are likely to be fully mixed within one diffusion timescale, similarly to cool DA white dwarfs below 10 000 K as discussed above. Since very few DBZ white dwarfs are known to have temperatures above $\approx$ 24 000 K (Kepler et al., 2019a), this scenario applies for the vast majority of DBZ and DZ white dwarfs.

4.4.3 Previous studies

In Montgomery et al. (2008), the authors have derived a horizontal diffusion coefficient of $1.5 \times 10^{10}\,\mathrm{cm}^2\ \mathrm{s}^{-1}$ appropriate for G29-38 (11 360 K and $\log g = 8.02$; Gentile Fusillo et al. 2019b). We can compare that to the diffusion coefficients shown in Fig. 4.6 and see that it is in close agreement with our predicted maximum value $D_{\leftrightarrow}^{\mathrm{max}}$ corresponding to the photosphere. However, it is about an order of magnitude larger than our adopted coefficient considering mixing over the entire convection zone.

4.4.4 Magnetic white dwarfs

Magnetic white dwarfs have to be treated differently to what was discussed so far. Magnetic fields larger than 10-100 kG in DAZ and DBZ white dwarfs, and larger than 0.1-1 MG in DZ stars, will inhibit convective energy transfer in the atmosphere (Tremblay et al., 2015d; Gentile Fusillo et al., 2018). As a consequence both surface spreading and sinking of metals are likely to have different timescales. We emphasise that the lack of significant convective energy transfer does not necessarily imply that mixing is inhibited. In fact, Tremblay et al. (2015d) demonstrated that for a DA white dwarf at 10 000 K with an average field of 5 kG, convective velocities were of similar amplitude to the non-magnetic case even though convective energy transfer was largely suppressed. Furthermore, magnetic waves and magnetic levitation perpendicular to field lines may contribute to additional mixing processes. In many of the limiting cases we have discussed so far, changing the diffusion coefficients by one or two orders of magnitude would not necessarily have major observational consequences. Magnetic fields are also likely to influence debris disc formation and geometry of accretion, for which a full discussion is outside of the scope of this work.

4.4.5 Observational constraints

There are three main observational methods to detect surface abundance inhomogeneities in white dwarfs: time-domain photometry (Maoz et al., 2015; Hallakoun et al., 2018), time-domain spectroscopy (Wilson et al., 2019) and detailed spectral analysis of metal line profiles. None of these methods have yet demonstrated any convincing case of surface inhomogeneities, and therefore in this section we describe how these non-detections can constrain our model.

The photometric method can be applied to large samples but gives weak constraints on surface homogeneity. This is because small metal lines have a near-negligible effect on broadband photometric fluxes. This method is therefore only sensitive to variations from strong metal lines, or hypothetical surface heating near an accretion spot.

Time-domain spectroscopy is in principle much more robust to detect metal line variability, especially if the rotation period is known and accretion is on a well defined spot. However, if accretion is equatorial the averaging effect across the visible disk implies that variations may be small or even negligible over the rotation period. This leaves us with the detailed spectral analysis of metal line profiles as the best method to provide direct constraints on surface spreading.

For any white dwarf with inhomogeneous surface metal abundances, the spectral intensity must be calculated at each point of the surface and then integrated over the stellar disk taking into account center-to-limb variations. All regions without metals will contribute nothing to the equivalent width of a given metal line. Therefore, the maximum depth of a metal line with respect to the continuum flux is roughly proportional to the fraction of the surface covered by metals. In other words, if metals only cover 10% of the surface, the flux decrement in any metal line can not be much larger than 10%, with the exact maximum value depending on the region of accretion, inclination and center-to-limb coefficient. Therefore the presence of saturated photospheric metal lines in any white dwarf spectrum should be sufficient to rule out any significant surface inhomogeneities.

On the one hand, saturated metal lines are routinely observed in cool DZ white dwarfs (Hollands et al., 2018a; Coutu et al., 2019), which is consistent with our model predicting surface homogeneity for these objects. On the other hand, strong metal lines are rarely detected in optical observations of warm DA white dwarfs. However, the main reason for that behaviour is the strong hydrogen opacity and weak metal opacities rather than a fundamental difference in surface metal coverage. In fact, saturated metal lines have been detected in UV observations of some of the strongest metal polluted DAZ white dwarfs (see, e.g., Figure 1 of Gänsicke et al., 2012) at $T_{\rm eff} \approx 20\,000$ K. While it is possible that some of the observed absorption is from circumstellar or interstellar material, the consistent abundance ratios and gravitational redshift between different lines strongly suggest photospheric line saturation. This implies a near homogeneous spreading of metals across the surface.

These observational constraints are in direct contradiction with our models of Section 4.3 for surface spreading from equatorial accretion from a disk or accretion on a spot, which predict strong surface inhomogeneities for warm DAZ white dwarfs. While it is tempting to conclude that accretion must take place near-spherically in these objects, we can not rule that we are missing another physical ingredient, e.g. another source of mixing in addition to convection and thermohaline instabilities.

Constraining accretion

In the equatorial accretion belt scenario, material is slowed down from Keplerian velocities in the inner disc to the rotation velocity of the white dwarf. Since the free-fall velocity

for a white dwarf is $\sim 1000\,\mathrm{km\,s^{-1}}$, compared to rotational velocities of the order of 1–$10\,\mathrm{km\,s^{-1}}$, that must involve significant shear, turbulence, shocks and mixing above the white dwarf atmosphere (Patterson & Raymond, 1985; Piro & Bildsten, 2004). This has so far received little attention in the context of the low accretion rates of metal polluted white dwarfs. For white dwarfs in cataclysmic variables where the accretion rates are up to ten orders of magnitude larger, the mixing region was however found to be relatively small and restricted to less than one degree of the equator (Piro & Bildsten, 2004). Further work is therefore necessary to understand if the accretion process itself can be a source of mixing. Nevertheless, large enough accretion rates may lead to observational signatures such as X-ray fluxes, which is a promising method to test the accretion geometry in white dwarfs.

In Chapter 3 we demonstrated that the inclusion of convective overshoot in the modelling of debris accretion increases the inferred accretion rate by up to an order of magnitude. A similar hypothesis was also made by Bauer & Bildsten (2018) who claimed that the inclusion of thermohaline mixing could increase the accretion rates. We show in Fig. 4.13 the predicted X-ray fluxes to the Earth from a selection of polluted DAZ white dwarfs with IR excesses from debris discs. Among them G29-38 has garnered much attention over the last few decades because of its proximity and clearly detectable debris disc (Jura et al., 2009; Xu et al., 2014). With the current and future X-ray detecting facilities, accretion rates at G29-38 and a handful of the other polluted objects may be measured. This is a branch of study in its infancy with XMM-Newton observations having been made but yielding no statistically significant X-ray detections (Jura et al., 2009; Farihi et al., 2018a). The X-ray emission from accreting white dwarfs would serve as a powerful constraint on the geometry and time dependence of accretion as well as convective overshoot effects at these objects.

4.5 Conclusions

We have presented the first diffusion coefficients of stellar surface-plane transport derived from 3D tracer experiments. We have utilised 3D RHD simulations for DA and DB white dwarfs, which collectively span most of the parameter space of convective atmospheres, to examine the journey of trace metals once they are accreted to the white dwarf surface. We find a strong temperature dependence in the ability of a white dwarf to homogenize its surface composition, a finding that somewhat challenges the often employed assumption that white dwarf surface layers can be assumed to be homogeneous in chemical composition. This assumption is verified only for cooler white dwarfs, a consequence of the increasing sinking time. In DA stars we find that surface homogeneity is verified below $10\,250 \pm 500$ K where the stated uncertainty takes into account the accretion geometry and time dependence.

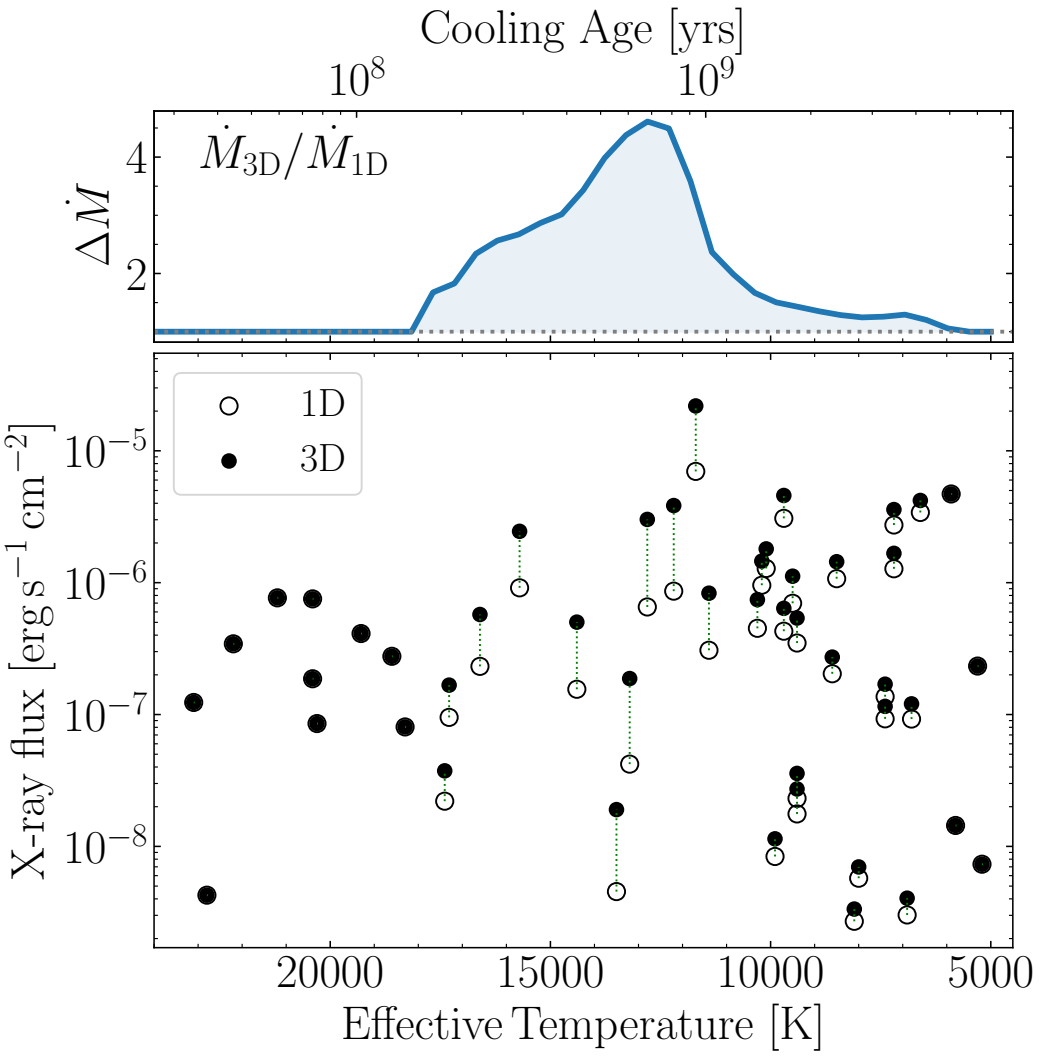

Figure 4.13: *Bottom*: Predicted X-ray flux (between 0.3–10 eV) reaching the Earth from 48 polluted H-atmosphere white dwarfs with published accretion rates inferred from spectroscopic observations (Farihi et al., 2016). The fluxes were calculated from the inferred accretion rate using the luminosity from Eq. (1) of Jura et al. (2009) and the parallax from *Gaia*. The fluxes computed using either the 1D or 3D model atmospheres (Chapter 3) and are shown in open or filled circles, respectively. The green dashed lines indicate the impact of using either of the contending models for each object with a convective atmosphere ($T_{\rm eff} < 18\,000$ K). *Top*: Change in accretion rate between the 1D and 3D overshoot models. The y-axis values are $\Delta\dot{M} = \dot{M}_{\rm overshoot}/\dot{M}_{\rm 1D}$ such that no overshoot correction corresponds to $\Delta\dot{M} = 1$ (dotted line).

For DB white dwarfs the surface becomes homogeneous below about 24 000 K.

We have demonstrated that DAZ white dwarfs above 14 000 K are predicted to show metal lines only in the regions of the stellar surface close to that of accretion. In contrast, UV observations of warm DA white dwarfs where strong and nearly saturated metal lines are observed suggest rather homogeneous metal coverage at the surface. This discrepancy can only be explained by a near-spherical geometry of accretion or a yet unknown surface mixing process that would be several orders of magnitude faster than convection or thermohaline mixing. We have also updated the estimate of disc lifetimes around white dwarfs based on 3D RHD stellar atmosphere models.

Chapter 5

Spectral evolution and convective mixing in white dwarfs

5.1 Introduction

From models of stellar evolution it is generally considered that white dwarfs are born with canonical masses of hydrogen and helium, $M_{\rm H}/M_{\odot} \approx 10^{-4}$ and $M_{\rm He}/M_{\odot} \approx 10^{-2}$ (Schoenberner & Weidemann, 1983; Iben & Renzini, 1983; D'Antona & Mazzitelli, 1990), with more recent estimates providing a parameterisation as a function of stellar mass (Althaus et al., 2015; Romero et al., 2017). These values are determined based on nuclear burning rates following the main sequence lifetime of the progenitor to the white dwarf. Over some decades, however, analyses of pulsating white dwarfs and stars evolving through and beyond the AGB (Werner & Herwig, 2006; De Gerónimo et al., 2018), as well as population studies of cool white dwarfs (Tremblay & Bergeron, 2008; Rolland et al., 2018; Blouin et al., 2019), have led to the understanding that this is in all likelihood an upper limit on the mass of hydrogen. There has been much interest in constraining the mass of light elements in white dwarfs over the last few decades to understand their formation and evolution.

Pulsating DA stars (DAV or ZZ Cetis) provide the opportunity to probe the chemical structure of white dwarfs as they cool between $\approx 12\,500$ K and 10 500 K (Tremblay et al., 2015b). It is generally accepted that all (non-magnetic) DA stars will exhibit variability from non-radial g-mode pulsations as they move through this temperature range during their evolution (Brickhill, 1983, 1991; Bradley, 1996; Fontaine & Brassard, 2008). One of the great benefits of studying this population of white dwarfs is that models of asteroseismology describing the oscillatory behaviour are most sensitive to, among other parameters, the mass of the hydrogen layer (Fontaine & Brassard, 2008). Predicted pulsation periods typically decrease when the hydrogen layer mass is increased, with the mean period spacing also decreasing slightly (Bradley, 1996). Recent asteroseismological studies often require significantly smaller hydrogen masses than the canonical value ($\log M_{\rm H}/M_{\rm WD} \ll -4$) to allow matching observed and predicted g-mode pulsations (Giammichele et al., 2016; Romero et al., 2017).

The small hydrogen masses that are invoked to model observed pulsations in some ZZ Cetis are thought to be explained by late hydrogen burning during the AGB and post-AGB (D'Antona & Mazzitelli, 1990; Herwig et al., 1999; Werner & Herwig, 2006; Althaus et al., 2010b). Numerical simulations and theoretical calculations have shown that thermal pulses during and shortly after the AGB phase are able to burn up almost all of the remaining hydrogen (Straniero et al., 2003).

The radii of DA white dwarfs derived using evolutionary models with thin hydrogen layers are smaller than those with thick layers for a given mass (Wood, 1990; Tremblay et al., 2017b). Overestimating the hydrogen layer thickness can also lead to ages that are up to $\approx$1 Gyr too old for the coolest known white dwarfs (Fontaine et al., 2001). The field

of Galactic archaeology has found white dwarfs to be useful chronometers in studies of the solar neighbourhood (Tremblay et al., 2014) and in determinations of the age of the Galactic disk (Winget et al., 1987; Fontaine et al., 2001; Wood, 1990; Leggett et al., 1998; Chen & Hansen, 2012) or the Galactic halo (Kalirai, 2012; Kilic et al., 2019). Providing an independent constraint on the occurrence of different hydrogen layer masses could help to improve the accuracy of these models.

As white dwarfs cool, the total amount of hydrogen and helium present, either primordial or accreted, can influence their subsequent evolution, and in particular their spectral appearance. The study of the spectral evolution of white dwarfs (Sion, 1984; Fontaine & Wesemael, 1987; Bergeron et al., 2001; Tremblay & Bergeron, 2008) thus provides a method to learn about their past history and internal structure. In this work we focus on the hydrogen content, although we note that the study of hot hydrogen-deficient PG1159 stars (Werner & Herwig, 2006; Miller Bertolami, 2016), carbon dredge-up in helium-rich atmosphere DQ white dwarfs (Pelletier et al., 1986; Coutu et al., 2019; Koester & Kepler, 2019), as well as asteroseismology can also help to constrain the mass of helium.

After gravitational separation has occurred (Schatzman, 1945), it is thought that hot white dwarfs will either cool as helium-rich DO atmospheres with He II lines, or hydrogen-atmosphere DA white dwarfs with Balmer lines if there is enough hydrogen to float at the surface. In both cases, radiative levitation can still keep trace metal species for ≈100 Myr, long after gravitational settling is complete (Chayer, 2014; Koester et al., 2014; Werner et al., 2018). Both types of white dwarfs can also develop convective instabilities in their atmospheres or envelopes as they grow older, allowing for further changes in spectral types.

If a white dwarf has a thick enough hydrogen envelope ($\log M_{\rm H}/M_{\rm WD} \gtrapprox -14$; Rolland et al. 2018; Genest-Beaulieu & Bergeron 2019b) the convection zone will initially be confined to the hydrogen atmosphere. The numerical simulations of Chapter 3 have constrained the onset of convection in DA white dwarfs to arise at 18 000–18 250 K (Cunningham et al., 2019) which sets an upper limit on the temperature range over which convection can impact the evolution of these objects. As the convection zone grows with decreasing surface temperature, if the hydrogen layer is sufficiently small ($\log M_{\rm H}/M_{\rm WD} \lessapprox -6$), eventually the convection zone will reach the deeper helium layer (Fontaine et al., 2001). At this point the significantly larger reservoir of helium ($\log M_{\rm He}/M_{\rm WD} \approx -2$) is expected to be immediately mixed into the surface convection zone in a runaway process resulting in a larger helium-dominated convection zone, a process named *convective mixing* (Strittmatter & Wickramasinghe, 1971; Shipman, 1972; Baglin & Vauclair, 1973; Koester, 1976). With convective velocities reaching $v \approx 1$ km s^{-1} the chemical profile will almost instantaneously become homogeneously mixed (Cukanovaite et al., 2018; Cunningham et al., 2019). The result will appear to be a helium-rich atmosphere white dwarf (DB spectral type with He

I lines or DC type with no lines) that may have detectable hydrogen (DBA or DA spectral types; Rolland et al., 2018).

If a white dwarf has a thin enough total hydrogen mass (log $M_{\rm H}/M_{\rm WD} \lessapprox -14$), a different evolutionary path is expected. Either the full evolution is in the form of a hydrogen-deficient PG1159, DO, DB, and then DC atmosphere (Genest-Beaulieu & Bergeron, 2019b), or alternatively when the DO white dwarf reaches $T_{\rm eff} \approx 45\,000$ K it transforms into a DA with a very thin hydrogen atmosphere. Such a hydrogen layer is sufficiently small that the underlying helium layer is expected to become unstable to convection in the range $30\,000 \gtrapprox T_{\rm eff}/[{\rm K}] \gtrapprox 18\,000$ (MacDonald & Vennes, 1991; Rolland et al., 2018; Genest-Beaulieu & Bergeron, 2019b). Convective overshoot is then expected to rapidly mix the top hydrogen layer with the underlying small helium convection zone (Cunningham et al., 2019; Cukanovaite et al., 2019a), resulting in the so-called *convective dilution* process. The result is a DB or DBA white dwarf like in the convective mixing process described above, albeit with a different range of possible hydrogen abundances (Genest-Beaulieu & Bergeron, 2019b).

In principle the hydrogen abundances in DBA stars could be used to reconstruct their past evolution, but this is not accounting for the fact that accretion of planetary debris can significantly impact their hydrogen content. In fact, several DBA white dwarfs have orders of magnitude more hydrogen than would be possible by the convective dilution or convective mixing scenarios, and it is thought that the accretion of water-rich asteroids is the most likely explanation for the hydrogen abundance in these objects (Farihi et al., 2011; Raddi et al., 2015; Gentile Fusillo et al., 2017b). The study of spectral evolution is clearly complex and involves many competing models that need to be constrained with well defined samples of the local white dwarf population.

Observational statistical studies on the number ratio of H- to He-atmospheres as a function of temperature have mainly been carried out using spectroscopically identified samples with a magnitude limit (Bergeron et al., 1997, 2001; Tremblay & Bergeron, 2008; Blouin et al., 2019; Ourique et al., 2019; Genest-Beaulieu & Bergeron, 2019b) with the exception of Limoges et al. (2015) who relied on the volume-limited 40 pc sample. In particular, we note that studying spectral evolution with the Sloan Digital Sky Survey spectroscopic sample, the largest known such sample for white dwarfs (Kepler et al., 2019b), involves complex completeness corrections that are still not fully understood (Gentile Fusillo et al., 2015). Photometrically selected or volume-complete samples have a strong advantage because the selection effects are better understood, especially in light of the recent *Gaia* Data Release 2 (Gaia Collaboration et al., 2016, 2018a).

In this work we make use of *Gaia* and a new robust photometric technique to study spectral evolution for volume-complete white dwarf samples. We utilise a catalogue of ≈

260 000 high probability white dwarf candidates from *Gaia* (Gentile Fusillo et al., 2019a) to select among them those with *ugriz* photometry from the Sloan Digital Sky Survey (SDSS; Blanton et al. 2017). The SDSS $u - g$ colour is sensitive to the Balmer jump in the range $20\,000 \gtrapprox T_{\rm eff}/[{\rm K}] \gtrapprox 9000$, allowing us to separate white dwarfs with hydrogen atmospheres (H-rich) from those with helium atmospheres (He-rich) without using the much more incomplete SDSS spectroscopic sample. Coupling photometric data from *Gaia*, SDSS, and *GALEX* with the grid of 3D radiation-hydrodynamic simulations of convective DA white dwarf atmospheres presented in Chapter 3 (and Tremblay et al. 2013c; Cunningham et al. 2019), we study the scenario of convective mixing which is expected to happen within that temperature range. We investigate the mass distribution of hydrogen layers in white dwarfs with the highest precision to date, albeit within a limited mass range of $-14 \lessapprox \log M_{\rm H}/M_{\rm WD} \lessapprox -10$ given the $T_{\rm eff}$ range allowed to be studied with our technique.

We first describe our observed sample selection in Section 5.2. Section 5.3 discusses the atmospheric models used to fit the photometric and astrometric data for the determination of effective temperature and stellar mass. Section 5.4 highlights the key results from the investigation and Section 5.5 contextualises the implications of our study.

5.2 Photometric Sample

For this investigation we chose a volume limited sample of high-confidence white dwarfs using the *Gaia* DR2 catalogue built by Gentile Fusillo et al. (2019a). The selection criteria used were; a quality cut ($P_{\rm WD} \geq 0.75$) which returned 262 480 objects, a parallax cut (parallax ≥ 7.5 mas) returning 35 056 objects, an effective temperature range determined by fits to the *Gaia* parallax and photometry ($20000 \geq T_{\rm eff}/[{\rm K}] \geq 9000$) returning 6512 objects and a cross-match with the Sloan Digital Sky Survey (SDSS) photometry which returned a final sample size of 2207 objects. We emphasise that a large fraction of these objects do not have SDSS spectra. The cut in effective temperature is not essential at this stage, but included to indicate the size of the working sample. In Section 5.4 the parallax cut is also relaxed to explore the results at greater distances and diagnose whether small number statistics can impact our results. All significant results, however, are borne from the sample with cuts detailed in the aforementioned.

In order to separate the hydrogen- and helium-dominated atmosphere white dwarfs from photometry alone we exploit the Balmer jump discontinuity which can be observed in spectra from sources with $T_{\rm eff} \approx 8\,000$ – $20\,000$ K. This discontinuity occurs at $\lambda \approx 364.4$ – 380.0 nm, depending on the stellar mass and strength of non-ideal effects (Hummer & Mihalas, 1988), making the SDSS u and g filters (central wavelengths of 354.3 and 477.0 nm, respectively) ideally suited to detect this feature. This can be seen in Fig. 5.1

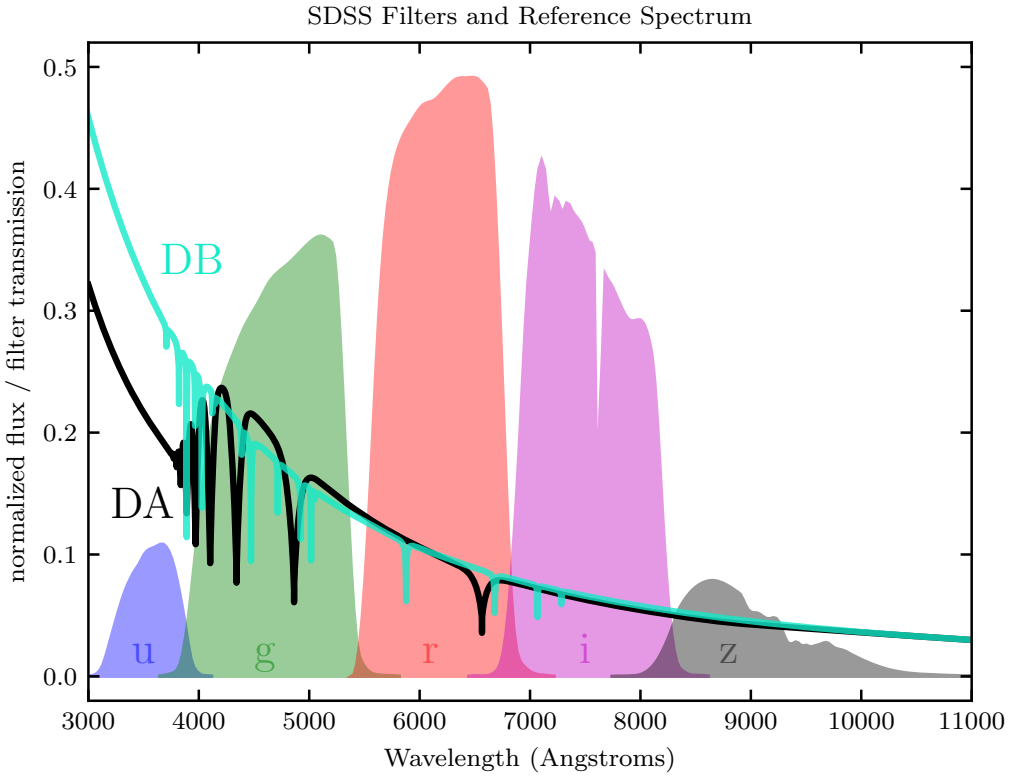

Figure 5.1: The pass-bands for the five filters (u, g, r, i and z) of SDSS. Also shown are synthetic spectra for a DA and DB white dwarf at 14,000 K. The SDSS pass-bands were plotted using the `python` package `astroML` written by Vanderplas et al. (2012).

which shows synthetic spectra for a DA (black) and DB (green) white dwarf at 14 000 K along with the five SDSS pass-bands. As a comparison colour we use $g - r$ with the central wavelength of r at 623.1 nm. As an illustration, Fig. 5.2 shows the sub-sample of 690 objects with SDSS spectra in a $u - g$, $g - r$ colour-colour plot where spectroscopically classified DAs are shown with pink circles and non-DAs are shown with green squares. The convention used throughout is that DAs include magnetic (DAH) and metal-rich (DAZ) objects, whilst non-DAs comprise DB, DBA, DAB, DC, DQ and all magnetic (H) and polluted (Z) variations therein.

Fig. 5.3 shows the full sample from the photometric *Gaia* - SDSS cross-match in an analogous plot where objects with a spectral classification are shown in pink (DA, DAH, DAZ) and green (non-DA), while objects with blue points have no spectroscopic classification.

Obtaining an immaculate separation of spectrally classified DA and non-DA objects is not feasible, with some DA objects (pink) occupying the same colour space as the strip of non-DA objects (green). An inspection of their spectra reveals that predominantly the DA type objects in the He-rich region of the colour plot are He-rich DA or DAZ (Zuckerman et al., 2007; Tremblay et al., 2011c; Gentile Fusillo et al., 2017b; Rolland et al., 2018). Whilst it may appear a contradiction in terms, the existence of these objects is permitted; i.e., when the effective temperature is too low to observed He lines. In these instances - where there is sufficient helium to suppress the Balmer jump - these objects are correctly positioned photometrically, despite being classified as DA. That these objects sit in the photometric He-rich region is apposite for our analysis of the H- to He-rich atmosphere ratio. However there exists an area between the photometric clusters sparsely populated by objects which have an ambiguous atmospheric composition. To improve the separation we employ additional photometry from *GALEX* which we discuss in the following.

5.2.1 *GALEX*

The all-sky survey *GALEX* (Morrissey et al., 2007) provides photometry in the near- and far-ultraviolet for a large number of objects in our sample. We find that the separation between the spectrally classified sources (Fig. 5.4) is increased when the colour $g - r$ (see Fig. 5.3) is replaced by $nuv - g$. The large majority of DA stars found in the He-rich cluster in colour-space are He-rich DA white dwarfs, with only a handful of true contaminants (see Section 5.4). Approximately 400 objects in the sample were found to have unreliable or missing near-UV photometric data in *GALEX*, reducing the final working sample to 1781 high-confidence white dwarfs. Of those, 604 have SDSS spectral classifications as either DA[H,Z] (423) or non-DA (181).

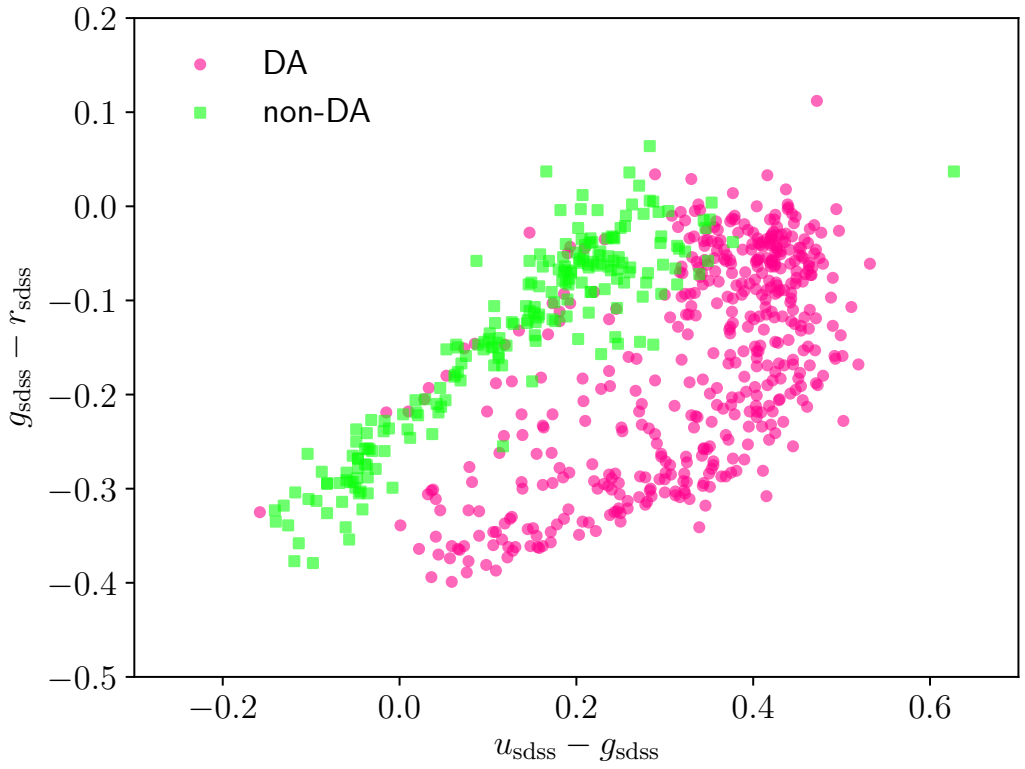

Figure 5.2: Colour-colour diagram showing 690 objects from the volume limited white dwarf sample (parallax $\geq$ 7.5 mas) with a SDSS spectral classification (Gentile Fusillo et al., 2019a). Of those shown, 479 are spectrally classified as DA (including DAH or DAZ) and 211 are classified as non-DA (including DB, DC, DQ, DBA, DAB and all magnetic and polluted variants of the aforementioned) with pink (circles) and green (squares), respectively.

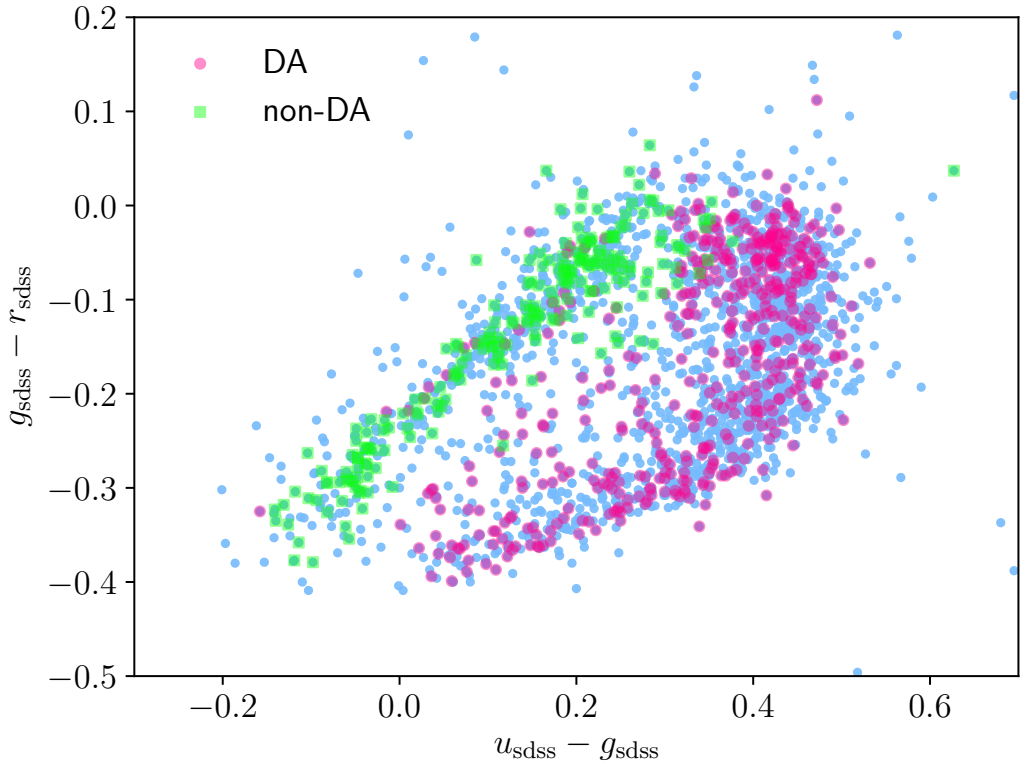

Figure 5.3: Colour-colour diagram showing 2207 objects (blue) from the volume limited *Gaia*-SDSS photometric sample (parallax ≥ 7.5 mas). Of those shown, 479 are spectrally classified as DA (including DAH or DAZ) and 211 are classified as non-DA (including DB, DC, DQ, DBA, DAB and all magnetic and polluted variants of the aforementioned) in pink (circles) and green (squares), respectively. 74 objects from the full sample populate a region of colour space outside the axis range shown. A manual inspection of the SDSS catalogue revealed that ≈65% of those objects had been marked with a CLEAN=0 flag. This SDSS flag indicates whether the target has "clean" photometry, which is assessed with respect to *r*-band deblending issues, interpolation problems, suspicious detections and edge issues (for full details see Blanton et al. 2017 or https://www.sdss.org/dr16/algorithms/photo_flags_recommend). However, simply removing targets with a CLEAN=0 flag is not a suitable or complete way to ensure all photometry is reliable. Upon inspection we found that the vast majority of all outliers are close to a bright star. And we therefore remove these 74 objects from our sample as they occupy a colour space outside of the physically reasonable range, in most cases due to the presence of nearby bright stars.

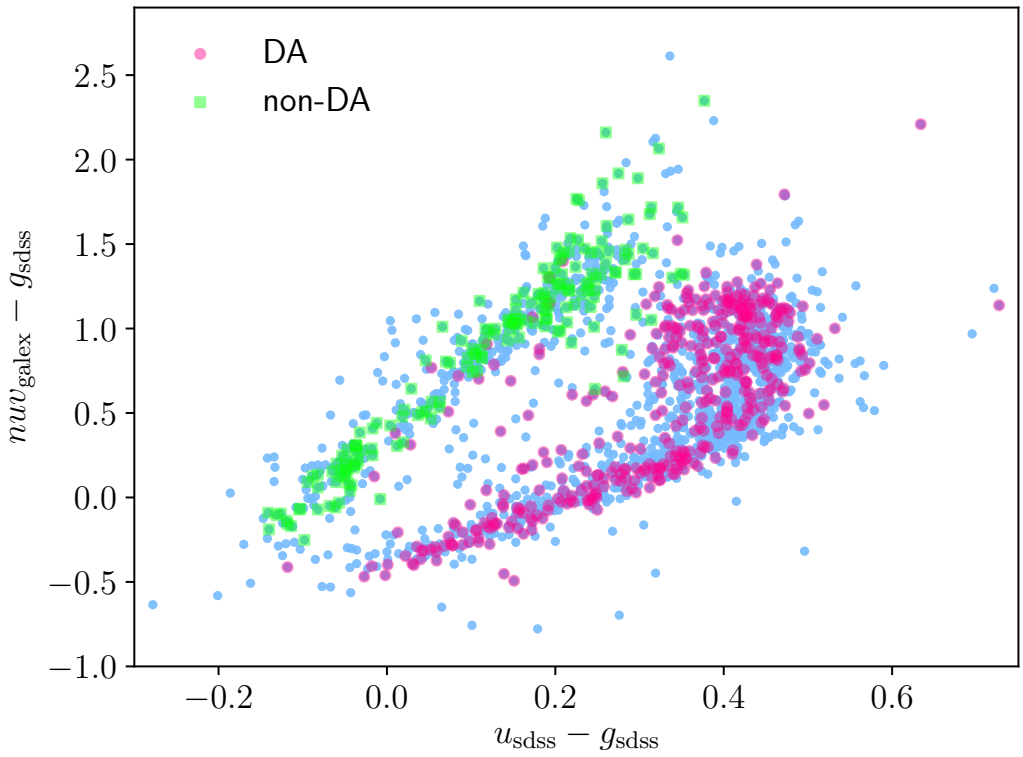

Figure 5.4: Similar to Fig. 5.3 but utilising NUV from *GALEX*, which reduces the sample to 1781 objects (blue). Of those, 423 are spectrally classified as DA (pink circles) and 183 are classified as non-DA (green squares).

5.2.2 Completeness

We have shown that it is possible to calculate the fraction of H- and He-rich atmosphere white dwarfs relying solely on *Gaia*, SDSS and *GALEX* photometry for a limited $T_{\rm eff}$ range but it is also important to understand the completeness of this sample. A discussion on the completeness of the *Gaia*-SDSS photometric sample is in section 6 of Gentile Fusillo et al. (2019a) and summarised below. We emphasise that these authors also derive a *Gaia*-SDSS spectroscopic sample (their section 5), which is separate and not as complete since SDSS used complex surveying strategies to follow-up their photometric sources (see, e.g., Eisenstein et al., 2006). In Figs. 5.2-5.3 and Section 5.4 we use this spectroscopic sample as a guide and comparison to our main photometric results. However, it is outside of the scope of this work to review the completeness of the spectroscopic *Gaia*-SDSS sample, which is known to vary considerably within colour-colour space, hence with $T_{\rm eff}$ and spectral type (Gentile Fusillo et al., 2015, 2019a), and very likely impacting DA to non-DA ratios. Most earlier studies on spectral evolution have used such spectroscopic samples, although not as complete as with the selection defined in Gentile Fusillo et al. (2019a). As a consequence we do not attempt to quantify the differences between these earlier studies and our method until spectroscopic completeness is better understood. Volume-complete spectroscopic samples, e.g. within 40 pc (Limoges et al., 2015), still suffer from low number statistics in the $T_{\rm eff}$ range we are interested in.

In Gentile Fusillo et al. (2019a) the authors estimated the completeness of the *Gaia*-SDSS photometric cross-match based on the number of objects from the SDSS that were successfully retrieved by *Gaia*. They found that for white dwarfs with $G \leq 20$ and $T_{\rm eff} \geq 7\,000$ K, *Gaia* catalogued 60–85% of the objects in the fairly complete SDSS footprint (sky images). However this includes white dwarfs at faint magnitudes and large distances that are too far to have a detectable parallax in *Gaia*. Given that our sample only includes objects within 133 pc we expect the completeness of the cross-match to be much higher than this estimate. In fact Hollands et al. (2018b) find that the Gaia completeness is near 99% for white dwarfs at 20 pc, and Gentile Fusillo et al. (2019a) argue that there is no reason for this completeness to drop significantly within ≈ 100 pc and for $G < 20$ mag. Most importantly, Gentile Fusillo et al. (2019a) also quantified the completeness with respect to $u - g$ colour using the SDSS filters and found it to be colour independent (see their figure 18). This is a key parameter that makes our photometric method potentially more robust than earlier spectroscopic studies.

The SDSS footprint covers approximately one third of the sky meaning our sample is volume-limited only over the SDSS footprint. Within the distance set by the parallax cut our sample should be representative of the whole sky. The SDSS has a bright magnitude limit, with most white dwarfs brighter than $G \approx 15$ missing from the cross-match. Our sample

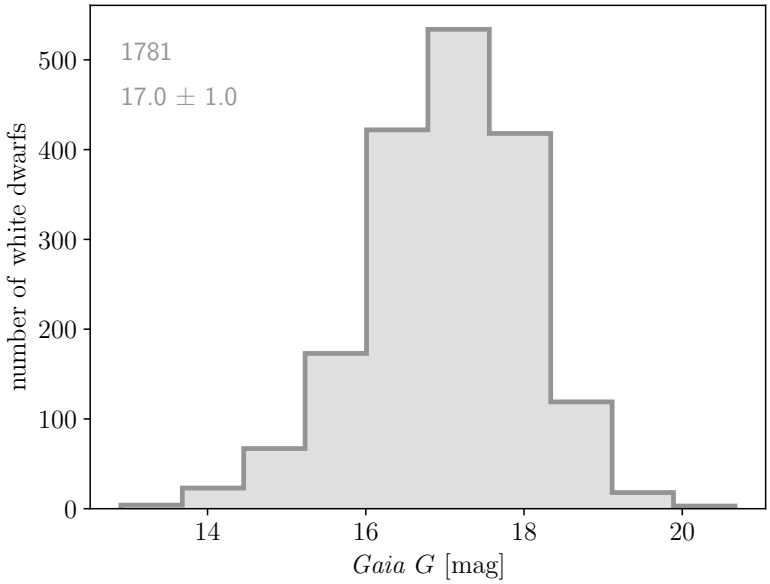

Figure 5.5: Distribution of *Gaia G* magnitudes for the 1781 objects included in our working sample after a cross-match with SDSS and *GALEX*. The mean magnitude is 17.0 with a standard deviation of 1.0.

is therefore not truly volume-limited. Our final magnitude distribution peaks at $G = 17.0$ with a standard deviation of 1.0 (Fig. 5.5) and, with 70 of the 1781 objects having $G < 15$, we infer that we are likely missing no more than $\approx 4\%$ of all objects which is not expected to introduce a significant DA versus non-DA bias (see Section 5.2.3).

In Fig. 5.6 we show the cumulative distribution of the distances to each member of the cross-matched *Gaia*-SDSS photometric sample used in this study. A volume complete sample with small radius is expected to scale linearly with volume, a relation that breaks down for larger volumes where the finite thickness of the Galactic disk may become important. Taking into account the finite thickness of the Galactic disk, we assume the space density of white dwarfs to follow $\rho = \rho_0 \exp(-|z|/h)$ where z is the vertical Galactic coordinate, h is the scale height and ρ_0 is the local space density. We adopt a scale height of $h = 230$ pc which has been found to be appropriate for white dwarfs within ~100 pc (Gentile Fusillo et al., 2019a). The local space density for the 20 pc sample (Hollands et al., 2018a) was found to be $\rho_0 = (4.49 \pm 0.38) \times 10^{-3}$ pc^{-3} but, given that our sample considers a relatively small range of effective temperatures, we instead leave this as a free parameter. Using a least squares fit we find a local space density of $\rho_0 = 0.282 \times 10^{-3}$ pc^{-3} for white dwarfs between 20 000–9 000 K. The theoretical cumulative distribution of distances reproduces very closely the observations, providing clear evidence that the sample considered here is volume complete.

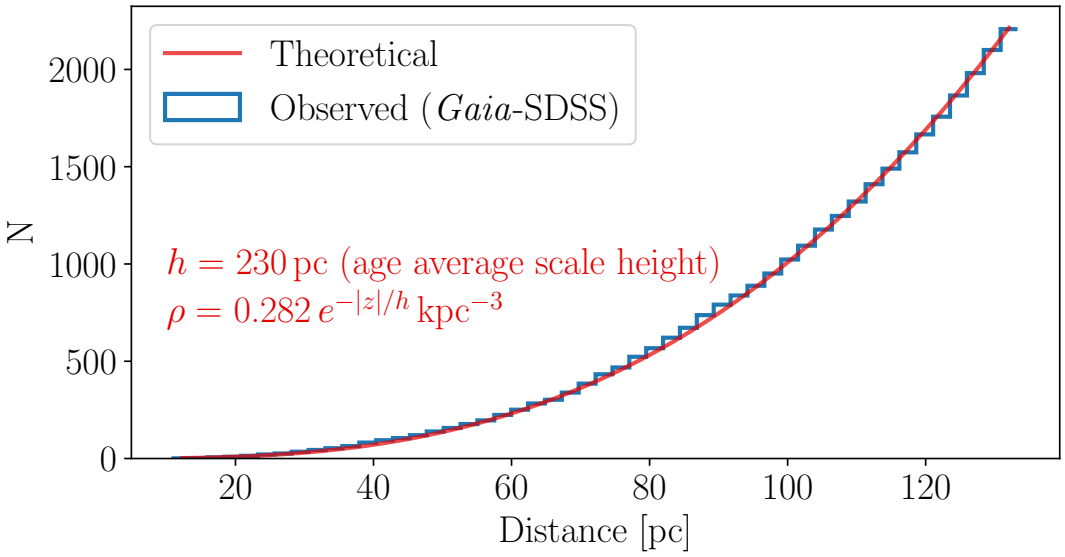

Figure 5.6: Cumulative distribution of distance for the *Gaia*-SDSS sample of 2,207 objects (blue). The red line shows the theoretical cumulative distribution for a volume complete sample. This model takes into account the finite thickness of the Galactic disk, where the density profile is assumed to be of the form $\rho = \rho_0 \exp(-|z|/h)$. The scale height is taken from Gentile Fusillo et al. (2019a) who found best-fit scale height to be $h = 230\,\mathrm{pc}$. The only free-parameter used to fit the data was central density, ρ_0, which was found to be $\rho_0 = 0.282\,10^{-3}\,\mathrm{pc}^{-3}$.

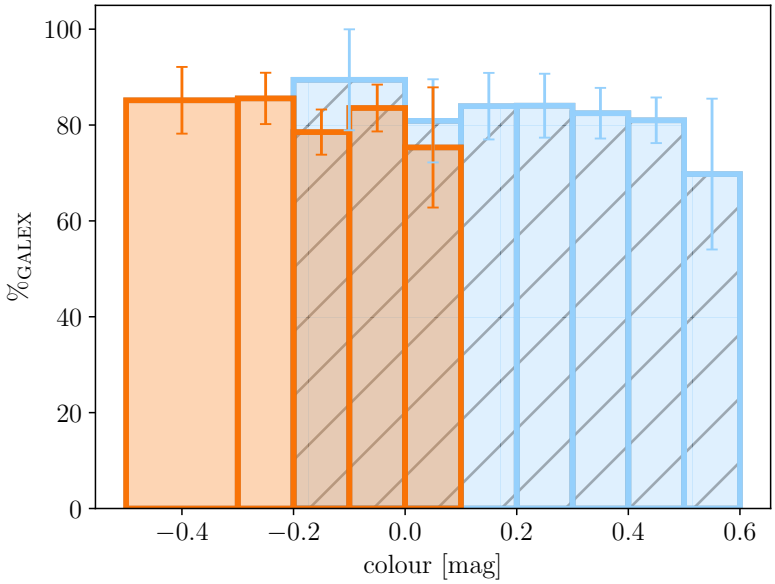

Figure 5.7: Colour distributions of percentage of SDSS objects (Fig. 5.3) recovered during the GALEX cross-match. In blue is the $u-g$ distribution for objects with colours from −0.2 to 0.6 mag. In orange we show the $g-r$ distribution for objects with colours from −0.5 to 0.1 mag. The colour ranges encompass the full extent of the locus of points in Fig. 5.3.

The final sample uses a further cross-match with *GALEX*, and as such the completeness of *GALEX* is also important. To assess whether the inclusion of *GALEX* photometry introduces any bias within our sample we consider the colour distributions for the percentage of objects in the original SDSS sample which were also retrieved during the *GALEX* cross-match. Fig. 5.7 shows the distributions for $u-g$ (blue, hatched) and $g-r$ (orange, solid) colours for the final working sample. We find no significant colour dependence for objects found in the *GALEX* cross-match, where all bins are consistent with an $\approx 80\%$ retrieval rate to within 1σ. In other words, $\approx 20\%$ of objects were lost following the SDSS-*GALEX* cross-match, and this loss showed no dependence on distance.

We also show the distribution of objects recovered in the *GALEX*-SDSS cross-match as a function of distance (Fig. 5.8) to investigate whether any spatial bias could have been introduced. The distance is inferred using the *Gaia* parallax and we find the recovery rate of objects in *GALEX* shows no dependence on this parameter. As with the colour distributions we find all bins are consistent with a retrieval rate of 80% to within 1σ. We conclude that the volume completeness of the final, working sample is likely to be 80% that of the original SDSS sample and that no bias has been introduced as a result of including *GALEX* photometry. Given the SDSS bright magnitude limit and our $T_{\rm eff}$ range, our *GALEX* sources do not suffer significantly from non-linearity problems (Camarota & Holberg, 2014; Wall

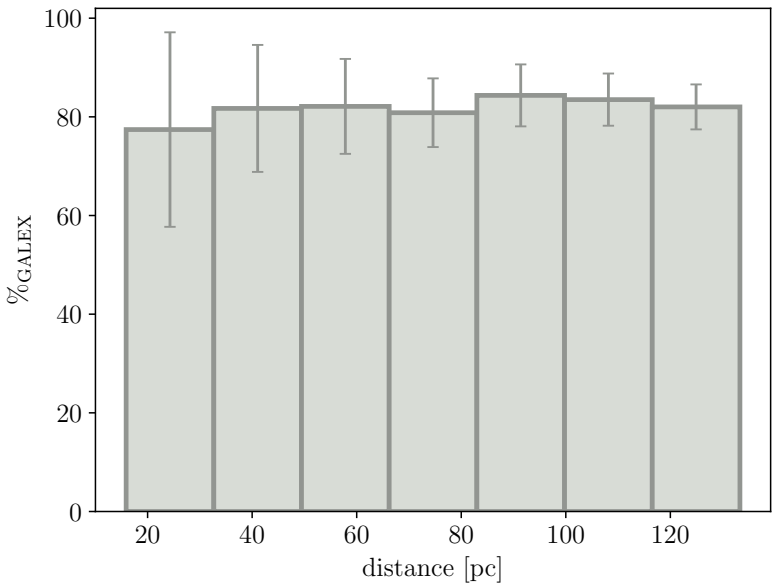

Figure 5.8: Distance distribution, inferred from *Gaia* parallax, of the percentage of the SDSS sample (Fig. 5.3) recovered during the *GALEX* cross-match.

et al., 2019).

Finally we note that given our lower temperature limit of 9000 K and the lower magnitude limits of *Gaia*, SDSS and *GALEX*, our distance limit of 133 pc ensures that a negligible number of white dwarfs are removed for being too faint in any of the surveys. At 9000 K *Gaia* is the limiting survey and Fig. 5.5 illustrates that our distribution peaks well above the lower magnitude limit of $G \approx 20$.

5.2.3 Absolute magnitudes and cooling rates

The use of a volume-limited sample largely removes possible selection biases due to absolute magnitude differences between spectral types but this concern still applies because of the bright magnitude limit of the SDSS. In addition a difference in the cooling rates of DA and DB stars could influence the ratio of spectral types as a function of temperature. To understand these biases we have simulated *Gaia* samples using the methods outlined in Tremblay et al. (2016a) and Gentile Fusillo et al. (2019a). These simulations assume a stellar formation rate (Tremblay et al., 2014), the Salpeter initial mass function, the Cummings et al. (2016) initial-to-final mass relation and the white dwarf evolution models of Fontaine et al. (2001). Most importantly, 28% of the white dwarfs are born with He-atmospheres (all with thin hydrogen layers), and 72% with hydrogen atmospheres (where among those 14% have thin hydrogen layers). In the subsequent evolution no spectral change is allowed.

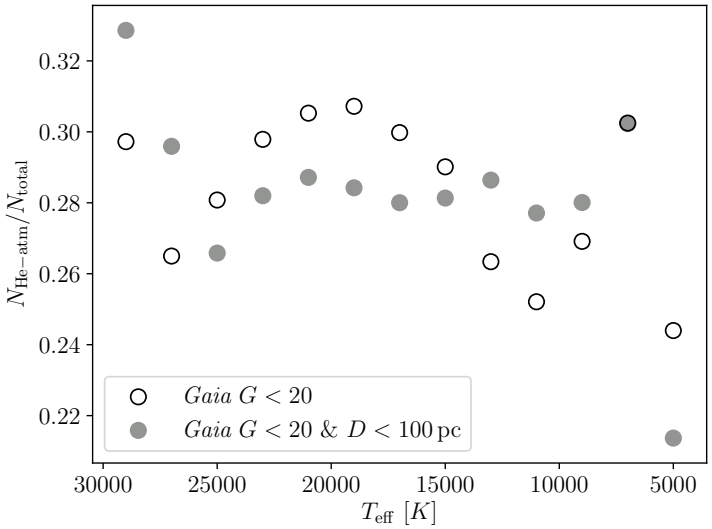

Figure 5.9: Simulated temperature dependence of the helium dominated white dwarf fraction for volume (open circles) and magnitude limited samples (filled circles) assuming no spectral evolution at any time during the evolution. Input at birth included 72% H-rich and 28% He-rich atmospheres. The coolest bin is affected by the age of the Galactic disk and collision-induced opacities and should be interpreted with caution (Blouin et al., 2019).

This provides an indication of the H-to-He ratio if convective mixing does not occur. To eliminate random noise the white dwarf space density was artificially enhanced. Fig. 5.9 demonstrates that for a volume limited sample, differences in cooling rates lead to small few percent-level changes of spectral type ratio over time. For reference, Fig. 5.9 also shows the evolution for a magnitude-limited sample, where differences in absolute magnitude between DA and DB also play a role in the observed ratio. Once again, the effect from these biases is fairly minor, as outlined in Tremblay & Bergeron (2008). We conclude that any significant change ($> 2\%$) in the observed $N_{\rm He}/N_{\rm Tot}$ ratio, in the range $20\,000 \gtrapprox T_{\rm eff}/[{\rm K}] \gtrapprox 9000$ and for a volume-limited sample, must be caused by additional physical processes that happen during white dwarf evolution and that are not included in our simulations, such as convective mixing or accretion.

5.3 Atmospheric Composition

Using *Gaia* photometry and astrometry, most high-probability white dwarfs in the DR2 catalogue of Gentile Fusillo et al. (2019a) have a derived effective temperature from a dereddening procedure and model atmosphere calculation under the assumption of either a pure hydrogen or a pure helium atmosphere. The catalogue also makes use of the mass-radius

relation of Fontaine et al. (2001) to derive a mass for each object.

The authors showed that, for a sample of 4778 bright DA stars, the $T_{\rm eff}$ determinations using *Gaia* photometry were in agreement with those derived independently utilising photometry from SDSS and Pan-STARRS.

Tremblay et al. (2019a) and Genest-Beaulieu & Bergeron (2019a) also made a comparison of photometric and spectroscopic effective temperatures derived from the SDSS. Individual objects were in agreement to within 1–2σ, but spectroscopic temperatures were systematically higher than those derived from *Gaia* photometry. It was concluded that this was most likely due to residual issues with the spectroscopic temperature scale.

Bergeron et al. (2019) have shown that using pure-He models in the photometric technique for objects below $T_{\rm eff} \approx 11\,000$ K results in a systematic effective temperature and mass offset compared to mixed H/He models (see their figures 10 & 11). In the following section, the ratio of He- and H-rich objects - calculated from the SDSS-*GALEX*-*Gaia* photometric sample and empirical cuts described below - is computed using $T_{\rm eff}$ bins of 1000 K. Hence the systematic offset in $T_{\rm eff}$ and mass is not a significant concern for this analysis.

The cuts in $u-g$, $g-r$ and $u-g$, $nuv-g$ space employed to optimise the separation between the spectrally classified objects in Figs. 5.2-5.4 are given, respectively, by the following equations:

$$(g-r) = 0.8 \times (u-g) - 0.3 \tag{5.1}$$

$$(nuv-g) = 3.9 \times (u-g) - 0.1 \tag{5.2}$$

These empirical cuts are then used to estimate the ratio of H- to He-dominated atmospheres, below and above those lines, respectively. We then employ the *Gaia* photometric effective temperatures as described in Gentile Fusillo et al. (2019a) to transform this ratio into the context of white dwarf spectral evolution. White dwarf cooling takes place over a Gyr timescale (D'Antona & Mazzitelli, 1990) and employing evolutionary models would allow the study of spectral evolution as a function of age. For simplicity, effective temperatures are used as a proxy for age in this study. We use the pure-H and pure-He solutions for the H-rich and He-rich sides of our colours cuts, respectively. We note that the differences between H- and He-rich effective temperature using *Gaia* photometry are sufficiently small compared to the size of our bins that even if pure-H effective temperatures were used for all objects similar results would be obtained.

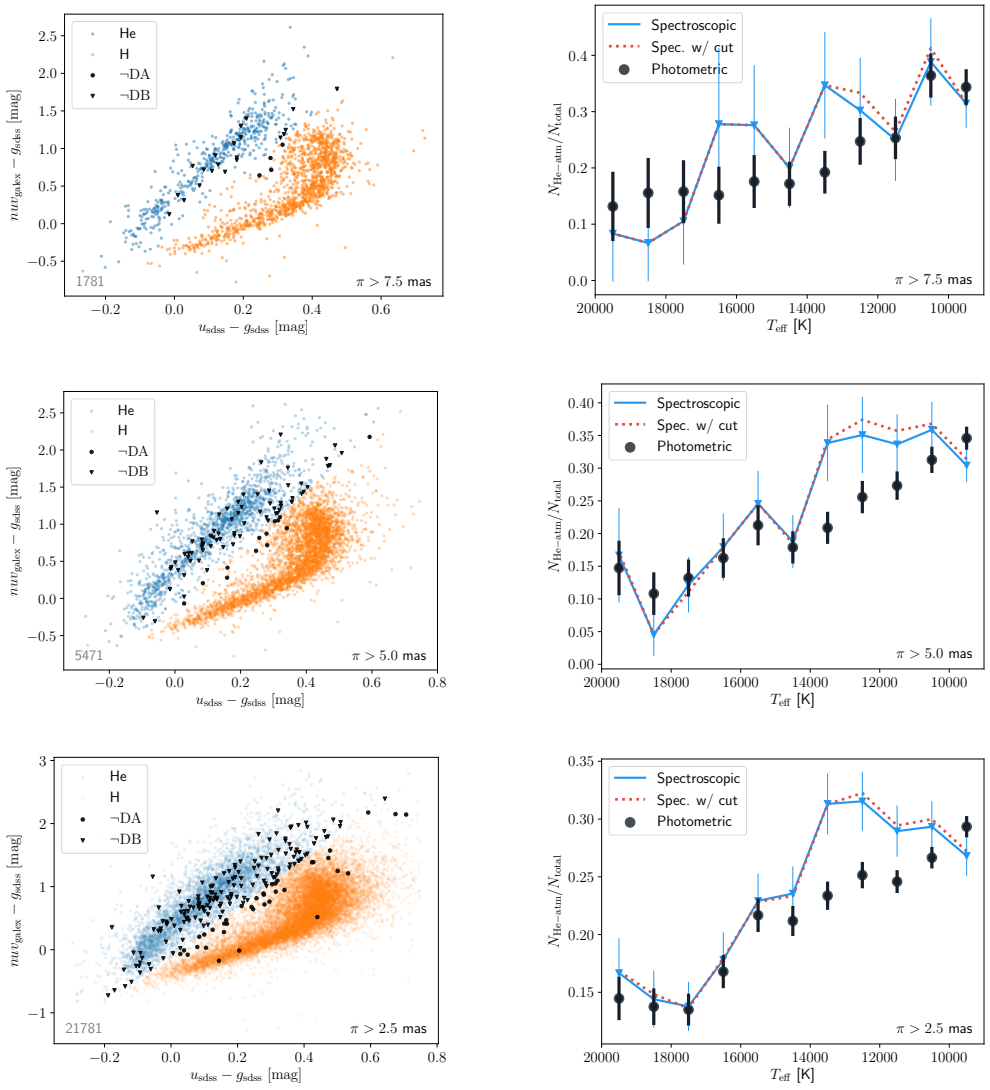

Figure 5.10: *Top-to-bottom*: Same analysis shown for samples limited by increasing volume with the parallax (bottom right) and sample size (bottom left) indicated in the panels. *Left*: Photometric sample with separation of colour space for hydrogen dominated (orange) and helium dominated atmospheres (blue) according to Fig. 5.4 and Eq. (5.2). Spectrally classified objects are a small subsample of the photometric sample. Any objects with a spectral classification which apparently disagrees with its photometric assessment are shown in black for DAs with photometry predicting He-dominance (triangles) and non-DAs with photometry indicating H-dominance (circles). *Right*: Ratio of helium dominated objects to total as a function of effective temperature based on the photometric cuts (black circles). We also show the spectroscopic ratio in the same bins with (red, dotted) and without (blue, solid) respect for the photometric cut. Error bars result from the propagation of Poisson errors (see Eq. (5.3)).

5.4 Results

For our derivation of the number of H- and He-atmospheres ($N_{\mathrm{H-atm}}$ and $N_{\mathrm{He-atm}}$) we devote our attention to the colour cut defined by Eq. (5.2) utilising the near-ultraviolet from *GALEX*, which creates a cleaner separation than Eq. (5.1). The top-left panel of Fig. 5.10 shows the effect of the photometric cut, with objects on the hydrogen side coloured orange and those on the helium side coloured blue. This includes objects with spectral classification. Shown in black are the spectrally classified objects which apparently fall on the *wrong* side of the photometric cut with DA-type objects on the helium side (triangles) and non-DAs on the hydrogen side (circles). Of the 604 spectrally classified objects we find 26 to be on the incorrect side of the cut. However, we point out that our goal is to separate H- and He-rich objects, rather than DA and non-DA.

We note the misidentification is skewed toward DA-type objects with 5.2% (22/423) of these objects on the He-rich side of the cut, compared to 2.2% (4/183) for the non-DA types. An inspection of the spectra for the DA-type objects in the He-rich region finds the majority (16/22) are either He-rich DAs or DA+DC binaries (Rolland et al., 2018; Kepler et al., 2019b), suggesting those objects may sit correctly in the photometric analysis. A further 5 objects on both sides show evidence of metal pollution or strong magnetic fields. Calcium lines in the former case can reduce the *u*-band flux (Hollands et al., 2017), emulating the Balmer jump, and strong magnetic fields can significantly disrupt the Balmer jump. The remaining 5 objects have $T_{\mathrm{eff}} \approx 9000$ K and higher-than-average surface gravities, where we expect the strength of the Balmer jump to be marginal. We conclude that H- and He-rich atmospheres separate relatively well under the photometric colour cut chosen, with 96–98% of objects being assigned the correct composition.

The spectroscopic identifications were provided in the *Gaia* DR2 white dwarf catalogue of Gentile Fusillo et al. (2019a). This included all the spectroscopically confirmed white dwarfs in SDSS DR10 (Gentile Fusillo et al., 2015) that were retrieved in *Gaia* DR2. These spectroscopic classifications serve as an indication of the photometric regions corresponding to hydrogen and helium dominance. Given a large enough and unbiased sample of spectra one could study the atmospheric composition of each object in turn and model the spectral evolution in that fashion. With the small size or biases present in the current spectroscopic samples this is not a well-justified approach, which is why we focus our analysis on the photometric sample.

The top-right panel of the figure shows the photometric fraction, $N_{\mathrm{He-atm}}/N_{\mathrm{total}}$, as a function of effective temperature in bins of 1000 K. As a comparison the red dotted line shows the same quantity but only including objects with SDSS spectra, i.e. following the photometric cuts without regard to the actual spectral type. In this case we also rely

on the photometric temperatures since some spectral types, e.g., DC, DZ, and DQ white dwarfs, have uncertain spectroscopic temperatures. Finally, this can be compared to the spectroscopic non-DA to total ratio in the same bins with the blue solid line. It demonstrates that the combined presence, as discussed above, of a few He-rich DA, strongly magnetic DAH, and DZ white dwarfs, only have a minor impact on our results.

The same analysis was carried out for increasing distance with a parallax cut of $\pi > 7.5$ (upper), 5.0 (middle) and 2.5 mas (lower) also shown in the figure. As photometric precision and volume completeness decrease with distance, we expect that our colour cut of Eq. (5.2) becomes less reliable to select atmospheric composition, and as such we favour the smaller volume photometric results. In contrast, larger distances may be able to overcome low number statistics for spectroscopic ratios, without necessarily adding more contaminants. The largest volume results in an approach that is closer to those of Genest-Beaulieu & Bergeron (2019b) and Ourique et al. (2019). In the former, a sample of 11 000 DA and DB white dwarfs with spectroscopic observations in SDSS DR7, DR10 & DR12, and a S/N>10, was used to determined the DA-to-DB ratio for white dwarfs within $D < 1$ kpc. They found that the DB fraction increases by 18% between 20 000–12 500 K. Their Figure 23 shows that between 20 000 K and 12 500 K, the DB fraction goes from $N_{\rm DB}/N_{\rm tot} = 0.07$ to 0.25. In the 15 000–12 500 K range this result is consistent within error bars with the non-DA fraction shown in the lower-right panel of Fig. 5.10, for our largest sample defined out to $D < 400$ pc. In the range 20 000–17 500 K, the DB fraction (0.07 ± 0.01) derived by Genest-Beaulieu & Bergeron (2019b) is smaller than that found in our largest volume sample (0.14 ± 0.04). The values agree at the 2-sigma level, however, the two works are not expected to produce the same results as the largest volume considered in this work ($D < 400$ pc) is only 6.4% the volume of that in Genest-Beaulieu & Bergeron (2019b). The scale height of the Galactic disk has been derived to be around 230 pc (Gentile Fusillo et al., 2019a) or 300 pc (Kepler et al., 2017), and thus the remaining volume (defined by $300 < D < 1000$ pc) is expected to lack completeness. Ourique et al. (2019) employed a sample of nearly 13 000 DAs and 3 000 non-DA stars with SDSS DR12 spectroscopy to probe the DA-to-non-DA fraction. In their full, magnitude-limited sample they found the non-DA fraction to increase from 0.15 to 0.32 between 21 000–12 500 K. Although their sample contained white dwarfs with distances up to $D < 1.1$ kpc, this result is in reasonable agreement with the spectroscopic ratio derived from our largest sample.

The errors associated with the photometric and spectroscopic ratios are derived from propagated Poisson errors by the expression

$$\alpha = \left(\left(\frac{n_{\rm He} + \alpha_{\rm He}}{n_{\rm tot}} - \frac{n_{\rm He}}{n_{\rm tot}} \right)^2 + \left(\frac{n_{\rm He}}{n_{\rm tot} + \alpha_{\rm tot}} - \frac{n_{\rm He}}{n_{\rm tot}} \right)^2 \right)^{1/2} \tag{5.3}$$

where $n_{\rm tot}$ and $n_{\rm He}$ are respectively the total number of objects and inferred numbers of helium dominated atmosphere white dwarfs from the photometry or spectroscopy and $\alpha_{\rm X} = \sqrt{n_{\rm X}}$ represents the counting (Poisson) error on both quantities.

Biases in the SDSS spectroscopic follow-up selection function, which depends on the SDSS colours (Gentile Fusillo et al., 2015), implies that the spectroscopic ratio may be less reliable. However a comparison of the photometric and spectroscopic ratios for $\pi > 7.5$ mas finds them to be in agreement to within 1σ throughout the effective temperature range studied, with the exception of the bin centered at $T_{\rm eff} = 13\,500$ K. At larger distances we observe a more prominent disagreement in the same temperature range.

The Poisson errors derived do not take into account the error on the effective temperature. We investigate the validity of the expressed error margin by calculating the sum of normal distributions in effective temperature for all objects in the top, left panel of Fig. 5.10. The normal distribution for species X (=H or He), $P_X(T_i)$, assigned to data point, i, obeys

$$P_X(T_i) = \frac{1}{\sqrt{2\pi}\sigma_i} \exp\left(\frac{(T - T_i)^2}{2\sigma_i^2}\right) \tag{5.4}$$

where T_i and σ_i represent the modelled effective temperature and associated error. An expression of the continuous ratio of He-rich to total objects would then be computed as

$$\frac{N_{\rm He-atm}}{N_{\rm total}} = \sum_{i=1} \frac{P_{\rm He}(T_i)}{P_{\rm H}(T_i) + P_{\rm He}(T_i)} \tag{5.5}$$

We find that all error bars from the original histogram bins are intersected by this function, with the exception of the bin centered at $T_{\rm eff} = 10\,500$ K. We conclude that the errors attributed to the histogram bins from number statistics are a reasonable reflection of the uncertainty on the estimated photometric ratio.

5.4.1 Fitting the spectral evolution

One of the aims of this research is to model the observed spectral evolution. In order to do this we wish to express the fractional change of He-rich objects as a function of effective temperature. One could employ the values attributed to the histogram bins shown in Fig. 5.10 (top-left panel), where the local gradient is the quantity of interest. However, the local gradient of the He-rich fraction versus effective temperature in the histogram picture has some dependence on the choice of histogram bins. This is not conducive to a robust result and so we instead seek a continuous function of effective temperature.

Logistic regression is a well established technique used in statistics and machine learning that estimates the likelihood of a function to describe a set of data, and it is

increasingly being utilised in problems of an astrophysical nature (Hollands et al., 2018b; Chromey, 2019). We assume that at a given effective temperature, $T_{\rm eff}$, the probability of a white dwarf being He-rich is given by $S(\boldsymbol{\theta}, T_{\rm eff})$, where θ is the vector of parameters that describe the form of function S - whose shape we would like to find. Given that our data is categorical - objects are either deemed to be H-rich or He-rich - logistic regression is an apposite choice for finding this function. We summarise the methodology in the following.

We define S in terms of the logistic curve

$$S(\boldsymbol{\theta}, T_{\rm eff}) = \frac{1}{1 + \exp(-f(\boldsymbol{\theta}, T_{\rm eff}))} \quad , \tag{5.6}$$

where the function f is defined as second-order polynomial in the natural logarithm of effective temperature such that

$$f(\boldsymbol{\theta}, T_{\rm eff}) = \theta_0 \log\left(\frac{T_{\rm eff}}{[K]}\right)^2 + \theta_1 \log\left(\frac{T_{\rm eff}}{[K]}\right) + \theta_2 \quad . \tag{5.7}$$

Defining S in this fashion ensures that the probability of an object being He-rich is confined to the interval [0,1]. This function differs from that used by Hollands et al. (2018b) with the addition of the second-order term in the polynomial. Adopting this term gives the model the freedom not to tend to zero, which is important as we expect the He-rich fraction to be non-zero for all temperatures.

Now that we have a functional form with the freedom necessary to describe the likely shape of the probability of a white dwarf being He-rich, we invoke an optimization routine. The quantity we wish to maximize is the likelihood of the function S with parameters $\boldsymbol{\theta}$ being the the best description of the data. Under the assumption that our data is independently Bernoulli distributed - that data has either the value 1, or 0 - the likelihood of a given $\boldsymbol{\theta}$ describing the data is expressed as

$$L(\boldsymbol{\theta}|T_{\rm eff}) = \prod_{i=1}^{N} S_i^{y_i} (1 - S_i)^{(1-y_i)} \tag{5.8}$$

where N is the sample size and $S_i = S(\boldsymbol{\theta}, T_{\rm eff,i})$. The observation of whether an object is He-rich or H-rich is encapsulated with $y_i = 1$ for He-rich objects or $y_i = 0$ for H-rich objects. The optimization is made more straightforward by maximizing the natural logarithm of this quantity

$$\log L(\boldsymbol{\theta}|T_{\rm eff}) = \sum_{i=1}^{N} \log(S_i) + \sum_{i=1}^{N} \log(1 - S_i) \tag{5.9}$$

Equivalently, one can minimize the negative log likelihood to find the best fit parameters. The optimization was performed using the Nelder-Mead algorithm built into the *minimize*

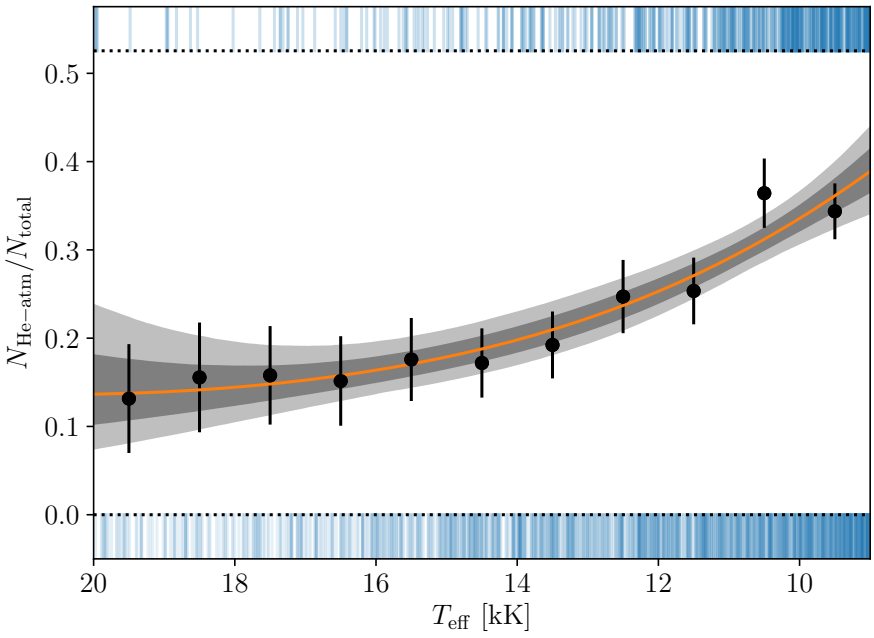

Figure 5.11: Observed fraction of helium atmosphere white dwarfs derived by the method of logistic regression using Eq. (5.6) and our $\pi > 7.5$ mas *Gaia*-SDSS-*GALEX* photometric sample. Filled error regions correspond to the 1σ and 2σ confidence intervals. Blue vertical lines indicate the effective temperature of a white dwarf with either a He-rich or H-rich atmosphere on the top and bottom, respectively. Photometric ratio derived using the binning method (see Fig. 5.10; top right) are also shown in black circles.

function of SCIPY which uses a simplex to find the minimum gradient in the parameter space (Jones et al., 2001).

The best fit parameters for θ_0, θ_1 and θ_2 were 0.010 ± 0.007, -0.43 ± 0.20 and 2.57 ± 1.26, respectively. The logistic curve with these parameters is shown in Fig. 5.11 with the 1σ and 2σ confidence intervals shown in grey. The detections of He-rich or H-rich white dwarfs are shown in blue on the top and bottom axes, respectively. For comparison we show again the values from the histogram bin method presented earlier (Fig. 5.10) in black circles. We remind the reader that the logistic curve is not a fit to the black points, but derived independently as discussed via the method of logistic regression. On the statistical significance of the increase of the He-fraction, an inspection of the best-fit logistic function at 17 000 and 9 500 K finds that the increasing He-fraction across this temperature range can be considered a 5σ result.

Looking only at the histogram points, we find that for $20\,000 \geqslant T_{\mathrm{eff}}/[\mathrm{K}] \geqslant 14\,000$ the percentage of helium dominated atmospheres lies between 10–20%, with the general trend increasing by approximately 5% toward the low temperature end of this interval, although

we note that this is only a 1σ result given the size of the error bars from Poisson errors. At lower effective temperatures, $13\,000 \geqslant T_{\rm eff}/[{\rm K}] \geqslant 10\,000$, we find a more significant increase, resulting in a final percentage of helium dominated atmospheres of 35–40%.

5.4.2 Mass distribution of thin hydrogen shells

The hypothesis being tested is whether the inverse proportionality between effective temperature and the relative number of helium-atmosphere white dwarfs is due to convective mixing or convective dilution.

Convective mixing, also referred to as dredge-up, is the process by which deeper material is dragged up by convective motions near the base of the (in this case hydrogen) convection zone. If the hydrogen convection zone is sufficiently close to the chemical boundary between the hydrogen and helium layers the material dragged up will be helium, and thus the two elements will mix.

Convective dilution describes the interaction of the top of the helium convection zone with a thin hydrogen shell located above. As the upper boundary of the convection zone reaches the hydrogen layer the hydrogen will be steadily incorporated into the helium convection zone.

Our first hypothesis is that the observed change in He-rich fraction is caused by convective mixing alone. As the helium envelope is typically orders of magnitude more massive (Iben & Renzini, 1983; Romero et al., 2019), the prediction is that this runaway process quickly leaves a trace amount of hydrogen in a predominantly helium atmosphere (Rolland et al., 2018). Furthermore, convective motions in He-rich envelopes are many orders of magnitude faster (Fontaine & van Horn, 1976) than any microscopic diffusion process that could separate helium and hydrogen (Koester, 2009), hence we assume this transition to be permanent. In this picture we predict that the objects which change to appear helium dominated are white dwarfs with a total mass of hydrogen equal to the size of the convectively mixed region (i.e. convection zone size for chemical mixing) for a DA white dwarf at that temperature. Across the temperature range this allows us to predict the total hydrogen mass for a percentage of the total white dwarf population within 133 pc. For DA stars that do not mix, we can only estimate the minimum mass of hydrogen.

To parameterize the convectively mixed region as a function of effective temperature we turn to the results from 3D radiation-hydrodynamic simulations presented in Chapter 3 (Cunningham et al., 2019). Fig. 5.12 shows the predicted mass of hydrogen being mixed convectively. Results from 3D numerical simulations for white dwarfs in the temperature range $11\,400 \leqslant T_{\rm eff}/[{\rm K}] \leqslant 18\,000$ are shown in solid blue where the multi-dimensional treatment allows for the inclusion of convective overshoot without employing free-parameters. Mixing-length theory mixed masses taken from Koester (2009), with updated tables, are

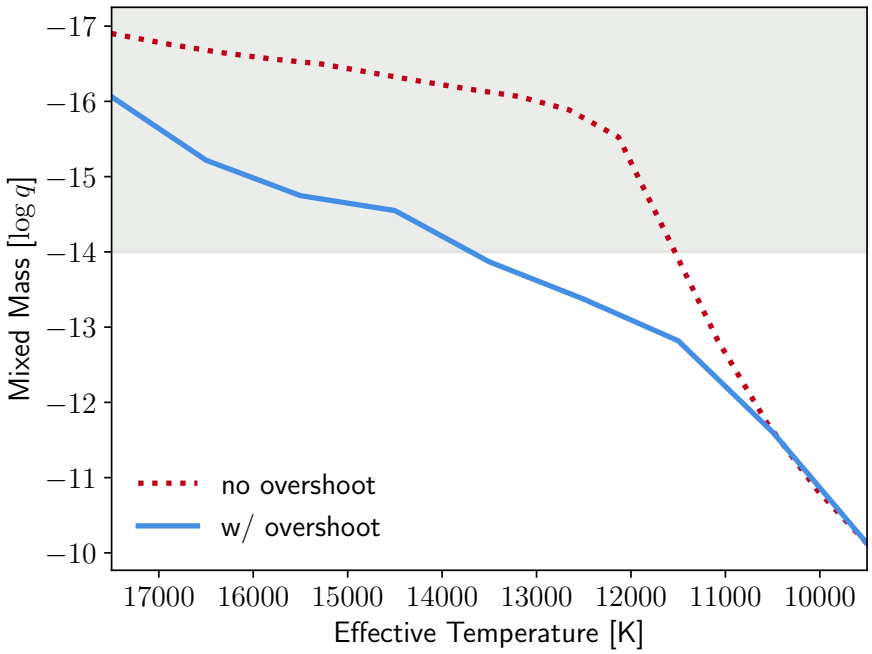

Figure 5.12: Temperature dependence of the fractional mass ($q = M_{\rm H}/M_{\rm WD}$) of the convectively mixed region in a DA white dwarf. Results are shown for mixed masses derived from 3D simulations (Chapter 3, blue solid) and 1D MLT (ML2/α = 0.8) with the convection zone defined by the Schwarzschild criterion (Koester 2009, red dotted). In this work we assume that when convective mixing occurs with the underlying helium layer, the mixed mass of hydrogen is equal to the total hydrogen mass in the star. The region in grey corresponds to hydrogen shell masses where convective dilution is expected to proceed (Genest-Beaulieu & Bergeron, 2019b).

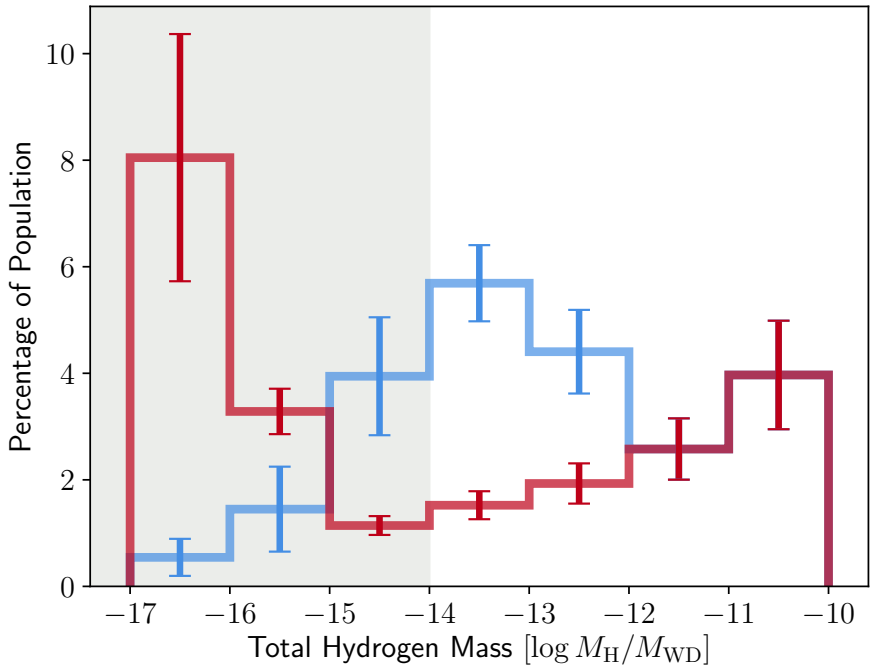

Figure 5.13: Percentage of white dwarfs with a given total hydrogen mass inferred from the percentage change of He-dominated white dwarfs (see Fig. 5.11). Results are shown for the two mixed mass prescriptions described in Fig. 5.12 with 3D and 1D results in blue and red, respectively. The sum is less than 100% because we do not include white dwarfs with lower or upper limits on the total hydrogen masses (see Section 5.5). The region in grey corresponds to hydrogen shell masses that are *forbidden* for DA white dwarfs in our studied $T_{\rm eff}$ range according to convective dilution studies (Genest-Beaulieu & Bergeron, 2019b). Under that scenario these objects would evolve as He-rich white dwarfs and show no spectral change in our studied $T_{\rm eff}$ range.

shown in dotted red. The results presented in Chapter 3 suggested that the mixed mass can be increased by 2.5 dex when convective overshoot is accounted for in these hydrogen atmosphere white dwarfs.

We show our derived total mass of hydrogen for white dwarfs within 133 pc in Fig. 5.13 as a percentage of the total sample. Similarly to Fig. 5.12, results are given for the convectively mixed mass with (blue) and without (red) the inclusion of convective overshoot. To derive the histogram values we sampled the parameter space of the function given in Eq. (5.6) using normally distributed parameters with means and standard deviations equal to the best-fit parameters and their associated errors, respectively. The histogram values presented are the mean of the 10 000 histograms calculated and the error is the standard deviation around that mean.

We find that including the larger mixed masses borne from the convective overshoot

results increases the inferred total mass of hydrogen for ≈ 15% of the population by 2 dex. An increase in mixed mass due to convective overshoot is expected for $T_{\rm eff} < 11\,400$ K but is currently not accessible directly from 3D numerical simulations. As such no difference is accounted for in the current model for total hydrogen masses above $M_{\rm H}/M_{\rm WD} \approx 10^{-12}$ because of the convergence of 3D and 1D results at lower temperatures (see Fig. 5.12).

The second hypothesis includes the possibility of convective dilution occurring. We use results from Genest-Beaulieu & Bergeron (2019b) which predict that convective dilution will occur in white dwarfs with a thin hydrogen shell of mass of $\log M_{\rm H}/M_{\rm WD} < -14.0$ when they cool to $T_{\rm eff} \approx 25\,000$ K. The inference is that these thinnest hydrogen shells are unlikely to exist by the time the white dwarf reaches $T_{\rm eff} < 20\,000$ K. More massive hydrogen layers are predicted to suppress convection in the underlying helium layer, preventing convective dilution, and allowing the hydrogen and helium shells to remain stratified down to lower effective temperatures or until convective mixing happens. In this scenario convective mixing can therefore only occur in white dwarfs with total hydrogen masses $\log M_{\rm H}/M_{\rm WD} > -14$. Fig. 5.12 shows the region where convective dilution would have already happened in grey. In other words, convective mixing is only permitted for white dwarfs with $T_{\rm eff} < 13\,750$ K in the 3D picture or $T_{\rm eff} < 11\,500$ K in the 1D picture.

In Fig. 5.11 the temperature dependence of the helium-rich percentage appears to follow a steeper gradient for $T_{\rm eff} \lessapprox 14\,000$ K, while a zero gradient could be used to fit the behaviour of the percentage for $T_{\rm eff} > 14\,000$ K. This interpretation supports the hypothesis that convective dilution has already occurred in objects with $\log M_{\rm H}/M_{\rm WD} < -14.0$ by $T_{\rm eff} = 20\,000$ K and the next available mechanism for spectral evolution is the onset of convective mixing at $T_{\rm eff} \approx 14\,000$ K.

Fig. 5.13 also includes the region of stratified hydrogen masses *forbidden* by convective dilution in grey. It shows that, in this scenario, approximately half of the thin hydrogen shell masses predicted using 1D models of convection would be ruled out as nonphysical at the $T_{\rm eff}$ values of interest. So too would a quarter of the inferred hydrogen shell masses in the 3D picture. The fewer non-physical predictions of the latter model suggests the 3D overshoot picture provides a more robust description of convection in these objects. Furthermore, for the 3D results we find that the two bins associated with the smallest total hydrogen mass are consistent with zero within 2σ. This provides evidence that the 3D overshoot model is in better agreement with the convective dilution model than a simple 1D treatment of convection alone. We note that the predictions of the convective dilution scenario are borne from a 1D mixing length treatment of convection. However, it was previously inferred that once the top of the helium layer becomes convectively unstable, a mechanism, that we suggest here is likely to be 3D convective overshoot, is able to dilute the top hydrogen layer into the helium convection zone (Rolland et al., 2018). As such 3D effects are already accounted

implicitly in this scenario, although hydrodynamical simulations may give a more detailed picture of the onset of convective dilution, which is outside the scope of this work.

We will now go on to discuss the implications of these results for the evolution of white dwarfs and time-dependent accretion.

5.5 Discussion

We have presented a statistical analysis of a sample of 1781 white dwarfs to extract the most accurate characterisation of the fraction of He-rich white dwarfs as a function of temperature or cooling age. There is a highly statistically significant trend that the fraction of objects to have He-dominated atmospheres increases with cooling age. We find that this fraction increases from 10–20% to 35–40% between 20 000 and 9000 K, corresponding to cooling ages ranging from 60 to 800 Myr. The implementation of a rigorous optimization method allowed to constrain this increase continuously across the temperature range. When combined with our convective mixing model, this provided a mass distribution of thin hydrogen shells (total hydrogen mass in the star) as a percentage of the total white dwarf population. We now consider some of the implications of these results outside of the white dwarf sample directly considered in this study.

The He-rich fractions observed at 20 000 K and 9000 K, respectively, allow for a mass distribution to be inferred across the full range of physically reasonable hydrogen shell masses. Fig. 5.14 shows this distribution for three bins. The central bin in orange comprises all objects observed to change from H- to He-rich in this study, where we use 3D convection for the hydrogen mass determination. The blue bins comprise all objects inferred to remain unchanged across the temperature range considered. We find that 61% of white dwarfs must have a total hydrogen mass greater than $\log M_{\rm H}/M_{\rm WD} = -10$, and canonically it is considered that white dwarfs must have no more than $\log M_{\rm H}/M_{\rm WD} \approx -4$ (Romero et al., 2019).

At the other extreme of masses we find that ∼15% of white dwarfs must have a total hydrogen mass less than $\log M_{\rm H}/M_{\rm WD} = -14$. We note that this mass is dictated by the mass limit found in the convective dilution studies of Rolland et al. (2018) and Genest-Beaulieu & Bergeron (2019b). These objects may have been DA stars at temperatures higher than 20 000 K. Our study can not derive the total number of white dwarfs that spend their full evolution as He-rich atmospheres. For this result, spectral evolution must be studied directly at hotter and cooler temperatures.

Table 5.1: Fraction of helium-rich atmosphere white dwarfs ($N_{\rm He-atm}/N_{\rm tot}$) in the temperature range 8000–7000 K presented in previous studies, collated by Blouin et al. (2019).

Study	$N_{\rm He-atm}/N_{\rm tot}$
Bergeron et al. (1997)	0.33 ± 0.12
Leggett et al. (1998)	0.45 ± 0.23
Bergeron et al. (2001)	0.37 ± 0.09
Tremblay & Bergeron (2008)	0.31 ± 0.06
Limoges et al. (2015)	0.23 ± 0.05
Blouin et al. (2019)	0.14 ± 0.03

5.5.1 Connecting with previous studies

The temperature range considered throughout this study was defined by the region where the Balmer lines have the greatest prominence. For cooler temperatures this technique does not satisfactorily distinguish between H-rich and He-rich atmosphere white dwarfs. There have been recent efforts to quantify the ratio of DA to non-DA white dwarfs for cooler temperatures (Blouin et al., 2019).

We expect the contribution of convective mixing to the spectral evolution of white dwarfs to be less significant below 9000 K as the size of the convection zone becomes less sensitive to effective temperature. This was evidenced in Blouin et al. (2019) where they observed a small change in He-rich fraction for white dwarfs with effective temperatures 8000–4000 K. Therefore we would expect the He-rich fraction at the cooler end of our study to be somewhat comparable to the warmer end of the sample in their study. In Table 5.1 we show the fraction of He-rich white dwarfs between 8000 and 7000 K from literature values derived via various methods. To draw a comparison we consider the results obtained for the objects with effective temperature in the range 10 000–9000 K. The histogram method returned a He-rich fraction of 0.34 ± 0.03, whilst the logistic regression method found a He-rich fraction of 0.36 ± 0.02 at 9500 K, i.e. in the centre of that temperature bin. We find our results to be in agreement within 1σ with four earlier studies (Bergeron et al., 1997; Leggett et al., 1998; Bergeron et al., 2001; Tremblay & Bergeron, 2008). In contrast Limoges et al. (2015) and Blouin et al. (2019) find lower He-fractions. These differences could be investigated in the future with volume-complete spectroscopic follow-ups of local *Gaia* white dwarfs.

5.5.2 Hydrogen abundance in DBA white dwarfs

The origin of hydrogen in DB(A) white dwarfs above 9000 K (Rolland et al., 2018) can be reviewed in light of our improved description of the scenario of convective mixing. In Fig. 5.15 we plot in black circles the observed surface hydrogen abundance in a sample of

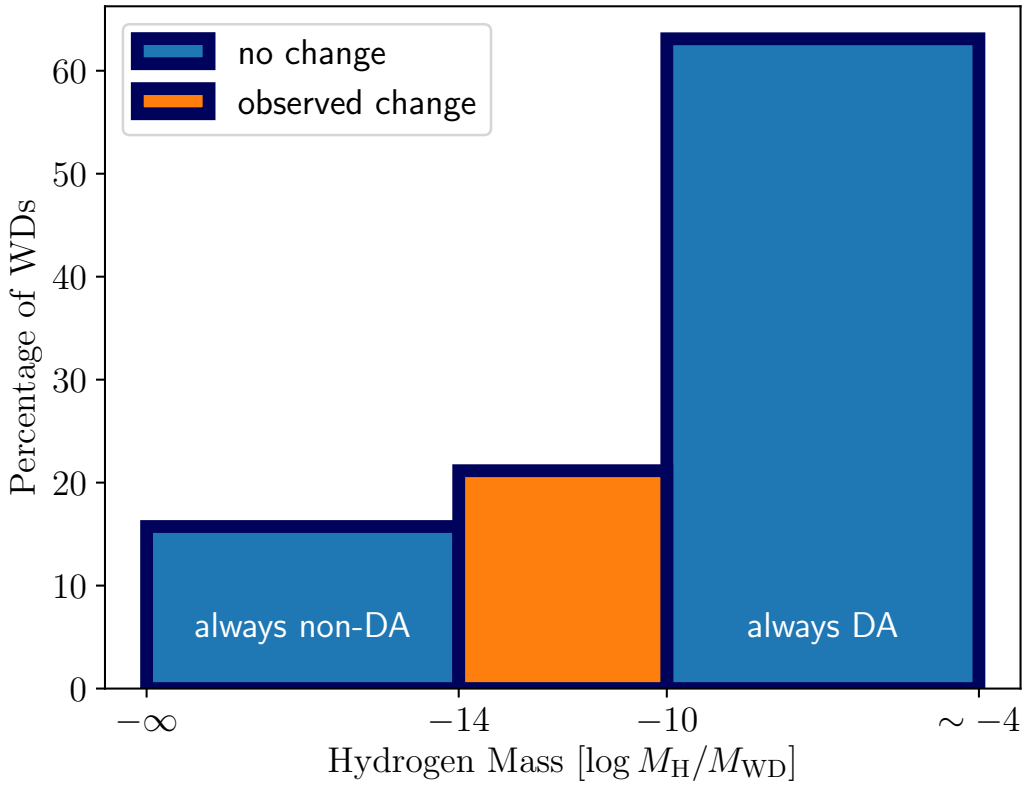

Figure 5.14: Percentage of white dwarfs with a given total hydrogen mass. The percentage observed to undergo a spectral change from DA to non-DA within the range $20\,000 \geqslant T_{\mathrm{eff}}/[\mathrm{K}] \geqslant 9000$ are shown in orange. Those for which no change was observed within that range are shown in blue. Spectral evolution may be possible for temperatures outside of that range.

79 He-rich white dwarfs from Rolland et al. (2018). Open circles correspond to upper limits inferred from a non-detection of hydrogen.

For each effective temperature, the convective mixing scenario predicts a mass of hydrogen that gets mixed with the underlying helium layer. Since this mass increases with decreasing $T_{\rm eff}$, at any given temperature, the maximum amount of hydrogen possible in a DB(A) white dwarf is for an object that has just experienced mixing. Lower hydrogen abundances are possible for DB(A) stars that have mixed at higher temperatures. We restrict our discussion to this upper limit of hydrogen in DB(A) stars.

For the mass of the helium convection zone we use the results of a grid of 3D simulations of DBA white dwarfs (Cukanovaite et al., 2019a). These simulations do not include a parameterisation for (helium) convective overshoot since DB(A) stars in that temperature range have deep convection zones for which a direct simulation is not yet possible. Including overshoot would result in larger helium convection zones, and therefore smaller upper limits on the surface abundance of hydrogen. This grid is interpolated iteratively so that the final surface hydrogen abundance is taken into account for the size of the convection zone.

The red, dashed line in Fig. 5.15 shows the predicted abundance of hydrogen in a He-rich white dwarf after convective mixing has occurred assuming a 1D mixed mass. The blue line shows the same quantity with the inclusion of the larger mixed mass from convective overshoot presented in Chapter 3. In both cases the calculation assumes that the hydrogen is homogeneously mixed into a larger He-rich convection zone.

The shaded regions beneath these upper limits can be considered the region in which all observations should lie if explained only by convective mixing. We note that the scenario of convective dilution predicts even smaller hydrogen abundances (Genest-Beaulieu & Bergeron, 2019b). The entire observed sample of Rolland et al. (2018) lies well outside of these regions, with hydrogen abundances being $\approx$ 3–5 dex higher than the upper limit derived from 3D overshoot results. It seems clear that another mechanism must be invoked to explain these hydrogen abundances. 3D effects are clearly not able to provide a better fit to the observed hydrogen abundances. We favour the accretion of planetesimals as the most likely source of the observed hydrogen.

In principle, hydrogen accretion could cause a reverse change from He- to H-dominated atmospheres. However, recent studies on the spectral evolution of helium atmosphere white dwarfs and their accretion of hydrogen have suggested that this is an extremely rare scenario (Gentile Fusillo et al., 2017b; Rolland et al., 2018). As such our assumption that the relative number of helium-atmosphere white dwarfs should increase monotonically with cooling age is likely a robust one.

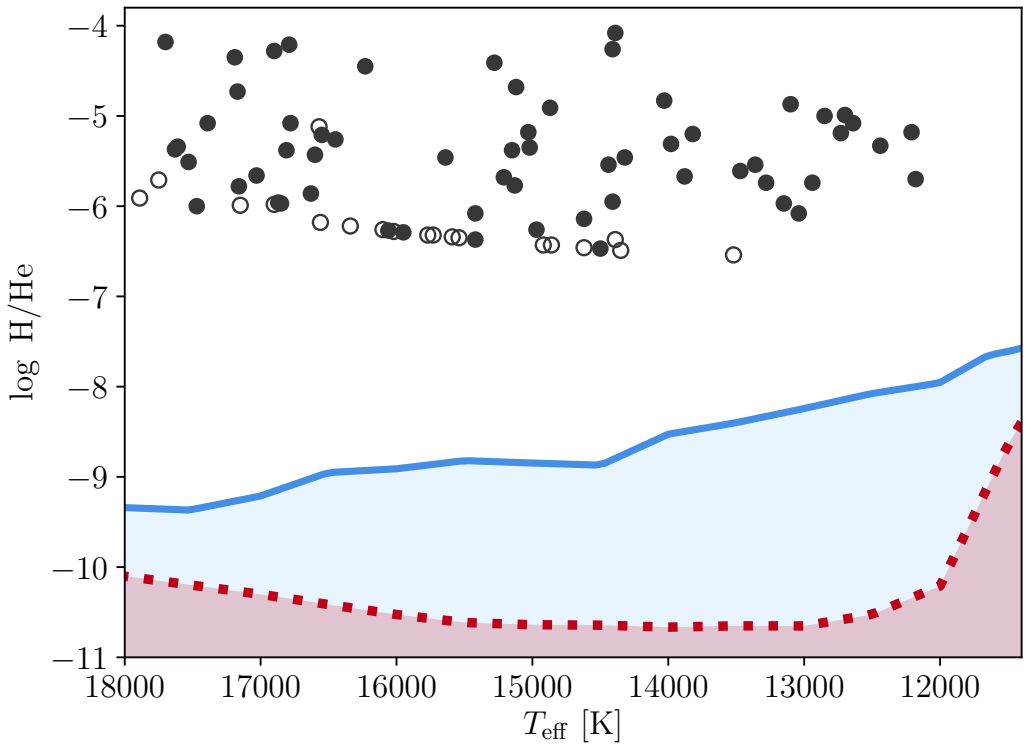

Figure 5.15: Observed hydrogen abundances in DB(A) white dwarfs drawn from the spectroscopic observations of Rolland et al. (2018). Filled circles show detections while open circles designate upper limits based on a non-detection of hydrogen lines. Theoretical upper limits calculated using the overshoot model of Chapter 3 shown in blue, and limits using 1D convection (Koester, 2009) are shown in red dashed. Shaded regions correspond to H abundances that could be explained by convective mixing in either the 3D overshoot (blue) or no overshoot (red) models. All observed H-abundances are well outside the range predicted by these models.

5.6 Conclusions

We have presented a statistically significant (>5σ) detection of white dwarfs undergoing a transition from hydrogen-dominated to helium-dominated atmospheres as they cool across the effective temperature range 20 000–9000 K. This was done using the largest volume limited sample (133 pc) of white dwarfs for any previous study of this kind, with the precise determinations of effective temperature utilising *Gaia* photometry. We have characterised the temperature dependence of the rate of spectral evolution and used the most current grid of convection zone sizes for DA white dwarfs to determine the distribution of total hydrogen masses in white dwarfs. We find that the observed distribution of hydrogen shells in the white dwarf population peaks in the range of $\log M_{\rm H}/M_{\rm WD}$ from -10 to -4, with 60% of all objects found within that range. Another 25% of white dwarfs have thin hydrogen masses in the range $-14 < \log M_{\rm H}/M_{\rm WD} < -10$, and finally 15% have even thinner hydrogen masses ($\log M_{\rm H}/M_{\rm WD} < -14$).

These results have implications for models of pulsations in white dwarfs, stellar evolution - in particular during the AGB - and the accretion of material after the formation of white dwarfs. In the future, volume-complete spectroscopic samples will be able to increase the range in mass for which we can constrain the total amount of hydrogen in a white dwarf.

Chapter 6

Conclusions and future directions

6.1 Conclusions

In this thesis I have used the high-resolution radiation hydrodynamics of CO^{5}BOLD to provide precise characterisations of the surface convection zones and overshoot region of DA white dwarfs. These results have been applied to samples of metal-polluted and isolated white dwarfs in the Solar neighbourhood to provide constraints on models of accretion, surface variability, debris disc lifetimes and stellar evolution. The major implications of this work are outlined below.

Firstly, this thesis presented a theoretical description of macroscopic diffusion caused by convective overshoot in pure-hydrogen DA white dwarfs using three-dimensional (3D), closed-bottom, radiation hydrodynamics CO^{5}BOLD simulations. This result depended on a new grid of deep 3D white dwarf models in the temperature range 11 400 K $\leq T_{\rm eff} \leq$ 18 000 K where tracer particles and a tracer density were used to derive macroscopic diffusion coefficients in the vertical (or radial) direction, driven by convective overshoot. Comparing these to microscopic diffusion coefficients revealed that the mass of the fully mixed region at the white dwarf surface is likely to increase by up to two and a half orders of magnitude. Inferred accretion rates are predicted to increase by a more moderate order of magnitude. An increase in settling time of up to three orders of magnitude is also to be expected which is of significance for time-variability studies of polluted white dwarfs. The new grid of white dwarf surface convection zones also provides the most robust constraint on the onset of convective instabilities in DA white dwarfs to be in the effective temperature range from 18 000 to 18 250 K.

Furthermore, using the CO^{5}BOLD code I presented the first transport coefficients in degenerate star atmospheres which describe the advection-diffusion of a passive scalar across the surface-plane. Combining these horizontal diffusion coefficients with the vertical

diffusion coefficients due to convective overshoot, I provided theoretical constraints on the surface spreading of metals in white dwarfs. The grid of simulations used in this study probed the vast majority of the parameter space of convective white dwarfs, with pure-hydrogen atmospheres (DA) in the effective temperature range 6000–18 000 K and pure-helium atmospheres (DB) in the range 12 000–30 000 K. I found that warm DA white dwarfs ($\gtrsim$ 14 000 K) are unable to efficiently spread the accreted metals across their surface, regardless of the time dependence of accretion. This is at odds with the current non-detection of surface abundance variations at white dwarfs with debris discs and challenges the often-held assumption that metals in white dwarf surface layers are homogeneously mixed. For cooler DAs, and DBs with temperatures below about 22 000 K, I found evidence which supports a homogeneous distribution of metals across the surface except for the early transient phase of accretion, typically lasting less than 0.1 % of the lifetime of the disc. These results have relevance for studies of the bulk-composition of evolved planetary systems and models of accretion disc physics.

Finally, I combined these theoretical results with observational data to constrain the mass of hydrogen in the local white dwarf population. I examined the hypothesis that white dwarfs undergo a spectral change from hydrogen- to helium-dominated atmospheres using a volume-limited photometric sample drawn from the *Gaia* DR2 catalogue, the Sloan Digital Sky Survey (SDSS) and the *Galaxy Evolution Explorer* (*GALEX*). This technique exploited the Balmer jump in hydrogen-atmosphere (DA) white dwarfs to separate them from those with a helium-atmosphere (DB). I found that 22% of white dwarfs will undergo a spectral change from hydrogen to helium in the temperature range 20 000 K to 9000 K, with no spectral evolution ruled out at 5σ. The increase in He-rich objects can be explained by convective mixing in DA stars, in which helium is dredged up when the base of the hydrogen convection zone reaches the underlying helium layer. The previous characterisation of the convection zone mass with convective overshoot was combined with the fractional increase in He-rich objects to derive a distribution of total hydrogen mass in white dwarfs. I found that 60% of white dwarfs must have a hydrogen mass larger than $M_{\rm H}/M_{\rm WD} = 10^{-10}$, another 25% have masses in the range $M_{\rm H}/M_{\rm WD} = 10^{-14} - 10^{-10}$, and 15% have less hydrogen than $M_{\rm H}/M_{\rm WD} = 10^{-14}$. These results have implications for white dwarf asteroseismology, stellar evolution through the asymptotic giant branch (AGB) and accretion of planetesimals onto white dwarfs. In particular, the hydrogen shell mass is an input parameter to models of pulsations in white dwarfs and an output of stellar evolution calculations.

6.2 Future directions

6.2.1 Further advances in computational convection

The research findings presented in this thesis have advanced our understanding of the overshoot region underneath the convection zones in the surface layers of DA white dwarfs and it has shown that a multi-dimensional treatment of convection predicts significantly larger mixed masses in these surface layers. The immediate implications of this, such as constraining hydrogen layer masses in white dwarfs and recalculating the accretion rates of metal-polluted white dwarfs, have already been considered within this work, but there is still great potential for further scientific advancements.

Cooler models

The temperature range (18 000–11 400 K) used in this thesis for the study of convective overshoot in DA white dwarfs was constrained at the cool end by the maximum convection zone size which is feasible to simulate with current computational resources. Convective overshoot remains important for cooler white dwarfs, but the large convection zones make 3D RHD simulations of the overshoot region in this regime computationally expensive or even intractable. This will be a necessary challenge to overcome to extend the direct macroscopic diffusion results presented in this work to cooler models. One promising step in this direction is the recent effort to parallelise CO^{5}BOLD using Message Passing Interface (MPI).

Analytic convective overshoot

The overshoot region has been defined throughout by comparing the convective velocities from detailed 3D RHD calculations with those of microscopic diffusion from 1D structures. The results of this empirical approach could be used to develop an analytic or semi-analytic description of the diffusion coefficient as a function of white dwarf structural parameters (such as Rosseland mean optical depth, temperature or pressure). This would facilitate the incorporation of the convection zone structure revealed by 3D RHD simulations into stellar evolution tools, e.g., MESA (Paxton et al., 2015), that currently rely on the 1D mixing length theory interpretation of convection. Replacing this with the 3D RHD prescription could greatly improve the accuracy of models involving white dwarfs. In order to constrain such a model, extending the grid of deep CO^{5}BOLD simulations to cooler ($< 11\,400$ K) temperatures is again necessitated.

Convective overshoot has been shown to be an important consideration in predicting the evolution (Stancliffe et al., 2015; Claret & Torres, 2017; Costa et al., 2019) and g-mode

pulsations (Pedersen et al., 2018) of main sequence stars. This presents the possibility that, if generalised into other star types, a well-constrained analytic model of convective overshoot may provide insight. High-resolution 3D RHD simulations will play a vital role in constraining such a model. A vast array of different stellar and sub-stellar bodies have now been modelled using multi-dimensional simulations, e.g. just within CO^{5}BOLD the list includes: brown dwarfs (Freytag et al., 2010b), main sequence A–M-type stars (Freytag et al., 1996; Ludwig et al., 2009; Kučinskas et al., 2018), AGB stars (Freytag & Höfner, 2008; Freytag et al., 2017) and red supergiants (Freytag et al., 2002; Chiavassa et al., 2011). This highlights the possibility for a much wider study of convective overshoot in different stellar environments.

An additional extension to the work presented here is to make a more detailed study of the boundary between convective overshoot and microscopic diffusion. One approach would be to implement physical tracers with a mass and charge, rather than passive scalars, and to model both convective motions and microscopic diffusion processes in the same calculation. This would provide the opportunity to investigate the role of other instabilities which may arise, e.g. from the presence of a chemical gradient. It would also allow to study in more detail how the inclusion of convective overshoot impacts metal abundance ratios in polluted white dwarfs, with implications for the bulk composition of evolved planetary systems. This would require simulation times orders of magnitude longer than those presented here in order to model the convective flows ($\sim$ km s^{-1}) and the microscopic diffusive motions ($\sim$ mm s^{-1}) simultaneously, and is well out of reach with current computational resources. Alternatively one could attempt to find a novel method whereby the overshoot region can be modelled without resolving the rapid turnover inside the convection zone proper. However, this is not possible within CO^{5}BOLD and developing such a method would require significant research effort.

Magnetic fields

Magnetic fields in excess of a given threshold will inhibit the convective energy transfer in the atmosphere of white dwarfs (Tremblay et al., 2015d; Gentile Fusillo et al., 2018). Whilst this does not imply that convective velocities need be reduced, for DAZ and DBZ white dwarfs this threshold is 10-100 kG and in DZ white dwarfs this is 0.1-1 MG. Approximately 20% of the local white dwarf population have evidence of magnetic fields, though mostly weaker than 1 MG (Landstreet & Bagnulo, 2019). The parameter space covered in this study could thus be meaningfully expanded to magnetic white dwarfs with the MHD module of CO^{5}BOLD.

6.2.2 Observations

Multi-object spectroscopic surveys

With first light scheduled for 2020–21, in the next half decade it is expected that ≈ 200 000 white dwarfs will be observed spectroscopically with the multi-object spectroscopic (MOS) surveys DESI (Aghamousa et al., 2016a,b), 4MOST (De Jong et al., 2016), WEAVE (Dalton et al., 2012, 2016), and SDSS-V (Kollmeier et al., 2017). This represents an order of magnitude increase when compared with current samples. Detailed abundance determinations will be made on hundreds of metal-polluted white dwarfs, bringing the opportunity to carry out robust statistical analyses on the accreted mass and accretion rates at these objects. This will allow testing of the overshoot model presented in this thesis, and investigation of the correlations between metal abundances with properties of the main sequence progenitors to white dwarf stars.

X-rays

A conclusive detection of X-rays at debris-accreting white dwarfs has yet to be made. The non-detection of X-rays at G29-38 in recent observations with XMM-Newton (Jura et al., 2009; Farihi et al., 2018b) were consistent with the predicted accretion rate from 1D models, but inconsistent with the predictions from the convective overshoot model presented in this thesis. Detecting X-rays from nearby metal-accreting white dwarfs could provide an independent constraint on the accretion rate and much needed confirmation of current and novel models. The *Chandra X-ray Observatory* (Weisskopf et al., 2000) may provide the best available opportunity to study X-rays at G29-38. If X-ray facilities develop towards higher sensitivity and better spatial resolution then it may be possible to extend this observational study to the several white dwarfs with X-ray fluxes at Earth predicted to be an order of magnitude lower than that of G29-38.

Bibliography

Abrikosov A. A., Gor'kov L. P., 1960, Zhur. Eksptl'. i Teoret. Fiz., 39

Adams W. S., 1914, Publications of the Astronomical Society of the Pacific, 26, 198

Adams F. C., Laughlin G., 1997, Reviews of Modern Physics, 69, 337

Aerts C., 2019, arXiv e-prints, p. arXiv:1912.12300

Aghamousa A., et al., 2016a, arXiv preprint arXiv:1611.00036

Aghamousa A., et al., 2016b, arXiv preprint arXiv:1611.00037

Alcock C., Fristrom C. C., Siegelman R., 1986, ApJ, 302, 462

Allard N. F., Kielkopf J. F., Loeillet B., 2004, A&A, 424, 347

Althaus L. G., et al., 2005, A&A, 435, 631

Althaus L. G., Córsico A. H., Isern J., García-Berro E., 2010a, A&ARv, 18, 471

Althaus L. G., et al., 2010b, ApJ, 717, 897

Althaus L. G., et al., 2015, A&A, 576, A9

Amsden A., Ruppel H., Hirt C., 1980, Technical report, SALE: A simplified ALE computer program for fluid flow at all speeds. Los Alamos Scientific Lab., NM (USA)

Anderson W., 1929, Zeitschrift fur Physik, 56, 851

Anderson Jr C. E., 1987, International journal of impact engineering, 5, 33

Anderson Jr J. D., 2010, Fundamentals of aerodynamics. Tata McGraw-Hill Education

Anguiano B., et al., 2017, Monthly Notices of the Royal Astronomical Society, 469, 2102

Asplund M., Nordlund Å., Trampedach R., Stein R. F., 1999, A&A, 346, L17

Baglin A., Vauclair G., 1973, A&A, 27, 307

Barstow M. A., et al., 2014, MNRAS, 440, 1607

Bauer E. B., Bildsten L., 2018, ApJ, 859, L19

Bauer E. B., Bildsten L., 2019, ApJ, 872, 96

Benvenuto O. G., De Vito M. A., 2005, MNRAS, 362, 891

Bergeron P., Wesemael F., Fontaine G., 1991, ApJ, 367, 253

Bergeron P., Saffer R. A., Liebert J., 1992, ApJ, 394, 228

Bergeron P., Ruiz M. T., Leggett S. K., 1997, ApJS, 108, 339

Bergeron P., Leggett S. K., Ruiz M. T., 2001, ApJS, 133, 413

Bergeron P., et al., 2011, ApJ, 737, 28

Bergeron P., et al., 2019, ApJ, 876, 67

Bergfors C., Farihi J., Dufour P., Rocchetto M., 2014, MNRAS, 444, 2147

Bessel F. W., 1844, MNRAS, 6, 136

Blanton M. R., et al., 2017, AJ, 154, 28

Blouin S., Dufour P., Thibeault C., Allard N. F., 2019, ApJ, 878, 63

Böhm-Vitense E., 1958, Z. Astrophys., 46, 108

Böhm-Vitense E., 1992, Introduction to stellar astrophysics. Volume 3. Stellar structure and evolution.. Vol. 3

Bond H. E., Bergeron P., Bédard A., 2017, ApJ, 848, 16

Bonsor A., Veras D., 2015, MNRAS, 454, 53

Bradley P. A., 1996, ApJ, 468, 350

Brickhill A. J., 1983, MNRAS, 204, 537

Brickhill A. J., 1991, MNRAS, 251, 673

Brinkworth C. S., et al., 2013, ApJ, 773, 47

Brown J. C., Veras D., Gänsicke B. T., 2017, MNRAS, 468, 1575

Burgers J. M., 1969, Flow Equations for Composite Gases

Caffau E., Ludwig H. G., 2007, A&A, 467, L11

Camarota L., Holberg J. B., 2014, MNRAS, 438, 3111

Camisassa M. E., et al., 2019, A&A, 625, A87

Carroll B. W., Ostlie D. A., 2006, An introduction to modern astrophysics and cosmology

Carson T. R., Mayers D. F., Stibbs D. W. N., 1968, MNRAS, 140, 483

Cassan A., et al., 2012, Nature, 481, 167

Castanheira B. G., et al., 2010, MNRAS, 405, 2561

Chabrier G., 2003, PASP, 115, 763

Chandrasekhar S., 1935, MNRAS, 95, 207

Chapman S., Cowling T. G., 1970, The mathematical theory of non-uniform gases. an account of the kinetic theory of viscosity, thermal conduction and diffusion in gases

Chayer P., 2014, MNRAS, 437, L95

Chayer P., Fontaine G., Wesemael F., 1995a, ApJS, 99, 189

Chayer P., et al., 1995b, ApJ, 454, 429

Chen E. Y., Hansen B. M. S., 2012, ApJ, 753, L16

Chiavassa A., Freytag B., Masseron T., Plez B., 2011, A&A, 535, A22

Chin C.-W., Chiu H.-Y., Stothers R., 1966, Annals of Physics, 39, 280

Chromey A., 2019, arXiv e-prints, p. arXiv:1908.05352

Claret A., Torres G., 2017, ApJ, 849, 18

Colella P., 1990, Journal of Computational Physics, 87, 171

Colella P., Woodward P. R., 1984, Journal of Computational Physics, 54, 174

Costa G., et al., 2019, in Kerschbaum F., Groenewegen M., Olofsson H., eds, IAU Symposium Vol. 343, IAU Symposium. pp 375–376, doi:10.1017/S1743921318006208

Coutu S., et al., 2019, ApJ, 885, 74

Cukanovaite E., et al., 2018, MNRAS, 481, 1522

Cukanovaite E., et al., 2019a, arXiv e-prints, p. arXiv:1909.10532

Cukanovaite E., et al., 2019b, MNRAS, 490, 1010

Cummings J. D., et al., 2016, ApJ, 820, L18

Cummings J. D., et al., 2018, ApJ, 866, 21

Cunningham T., et al., 2019, MNRAS, 488, 2503

Cunningham T., et al., 2020, MNRAS, 492, 3540

D'Antona F., Mazzitelli I., 1978, A&A, 66, 453

D'Antona F., Mazzitelli I., 1989, ApJ, 347, 934

D'Antona F., Mazzitelli I., 1990, ARA&A, 28, 139

Dalton G., et al., 2012, in Ground-based and Airborne Instrumentation for Astronomy IV. p. 84460P

Dalton G., et al., 2016, in Ground-based and Airborne Instrumentation for Astronomy VI. p. 99081G

De Gerónimo F. C., et al., 2018, A&A, 613, A46

De Jong R. S., et al., 2016, in Ground-based and Airborne Instrumentation for Astronomy VI. p. 99081O

Deardorff J. W., 1961, Journal of Atmospheric Sciences, 18, 540

Deardorff J. W., 1966, Journal of Atmospheric Sciences, 23, 503

Debes J. H., López-Morales M., 2008, ApJ, 677, L43

Debes J. H., Walsh K. J., Stark C., 2012, ApJ, 747, 148

Dirac P. A. M., 1926, Proceedings of the Royal Society of London Series A, 112, 661

Dufour P., et al., 2007, ApJ, 663, 1291

Dufour P., et al., 2012, ApJ, 749, 6

Dufour P., et al., 2017, in Tremblay P. E., Gaensicke B., Marsh T., eds, Astronomical Society of the Pacific Conference Series Vol. 509, 20th European White Dwarf Workshop. p. 3 (arXiv:1610.00986)

Dupuis J., Fontaine G., Pelletier C., Wesemael F., 1992, ApJS, 82, 505

Dupuis J., et al., 2000, ApJ, 537, 977

Eddington A. S., 1926, The Internal Constitution of the Stars

Eddington A. S., 1927, Stars and atoms

Eisenstein D. J., et al., 2006, ApJS, 167, 40

Farihi J., 2016, New Astronomy Reviews, 71, 9

Farihi J., Jura M., Zuckerman B., 2009, ApJ, 694, 805

Farihi J., et al., 2011, ApJ, 728, L8

Farihi J., et al., 2012, MNRAS, 424, 464

Farihi J., Gänsicke B. T., Koester D., 2013, Science, 342, 218

Farihi J., et al., 2016, MNRAS, 463, 3186

Farihi J., Parsons S. G., Gänsicke B. T., 2017, Nature Astronomy, 1, 0032

Farihi J., et al., 2018a, MNRAS, 474, 947

Farihi J., et al., 2018b, Monthly Notices of the Royal Astronomical Society, 481, 2601

Fermi E., 1926, Zeitschrift fur Physik, 36, 902

Ferrini F., Penco U., Palla F., 1990, A&A, 231, 391

Finley D. S., Koester D., Basri G., 1997, ApJ, 488, 375

Flammarion C., 1877, Astronomical register, 15, 186

Fontaine G., Brassard P., 2008, PASP, 120, 1043

Fontaine G., Michaud G., 1979, ApJ, 231, 826

Fontaine G., Wesemael F., 1987, in Philip A. G. D., Hayes D. S., Liebert J. W., eds, IAU Colloq. 95: Second Conference on Faint Blue Stars. pp 319–326

Fontaine G., van Horn H. M., 1976, ApJS, 31, 467

Fontaine G., Brassard P., Bergeron P., 2001, PASP, 113, 409

Fontaine G., et al., 2013, in European Physical Journal Web of Conferences. p. 05001, doi:10.1051/epjconf/20134305001

Fowler R. H., 1926, MNRAS, 87, 114

Freytag B., 2013, Memorie della Societa Astronomica Italiana Supplementi, 24, 26

Freytag B., 2017, Mem. Soc. Astron. Italiana, 88, 12

Freytag B., Höfner S., 2008, A&A, 483, 571

Freytag B., Ludwig H.-G., Steffen M., 1996, A&A, 313, 497

Freytag B., Steffen M., Dorch B., 2002, Astronomische Nachrichten, 323, 213

Freytag B., et al., 2010a, CO5BOLD: COnservative COde for the COmputation of COmpressible COnvection in a BOx of L Dimensions with l=2,3 (ascl:1011.014)

Freytag B., et al., 2010b, A&A, 513, A19

Freytag B., et al., 2012, Journal of Computational Physics, 231, 919

Freytag B., Liljegren S., Höfner S., 2017, A&A, 600, A137

Gaia Collaboration et al., 2016, A&A, 595, A1

Gaia Collaboration et al., 2018a, A&A, 616, A1

Gaia Collaboration et al., 2018b, A&A, 616, A10

Gänsicke B. T., et al., 2012, MNRAS, 424, 333

Gänsicke B. T., et al., 2016, ApJ, 818, L7

Genest-Beaulieu C., Bergeron P., 2019a, ApJ, 871, 169

Genest-Beaulieu C., Bergeron P., 2019b, ApJ, 882, 106

Gentile Fusillo N. P., Gänsicke B. T., Greiss S., 2015, MNRAS, 448, 2260

Gentile Fusillo N. P., et al., 2017a, MNRAS, 468, 971

Gentile Fusillo N. P., et al., 2017b, MNRAS, 468, 971

Gentile Fusillo N. P., et al., 2018, MNRAS, 473, 3693

Gentile Fusillo N. P., et al., 2019a, MNRAS, 482, 4570

Gentile Fusillo N. P., et al., 2019b, MNRAS, 482, 4570

Giammichele N., Fontaine G., Brassard P., Charpinet S., 2016, ApJS, 223, 10

Gianninas A., Bergeron P., Ruiz M. T., 2011, ApJ, 743, 138

Gingold R. A., Monaghan J. J., 1977, Monthly notices of the royal astronomical society, 181, 375

Girven J., et al., 2012, ApJ, 749, 154

Gudiksen B. V., et al., 2011, A&A, 531, A154

Hallakoun N., et al., 2018, MNRAS, 476, 933

Hansen C. J., Kawaler S. D., 1994, Stellar Interiors. Physical Principles, Structure, and Evolution., doi:10.1007/978-1-4419-9110-2.

Hansen B. M. S., et al., 2015, ApJ, 809, 141

Harwit M., 1988, Journal of the British Astronomical Association, 98, 374

Hermes J. J., et al., 2013, ApJ, 771, L2

Hermes J. J., et al., 2017a, ApJS, 232, 23

Hermes J. J., et al., 2017b, MNRAS, 468, 1946

Herschel W., 1785, Philosophical Transactions of the Royal Society of London Series I, 75, 40

Herwig F., Blöcker T., Langer N., Driebe T., 1999, A&A, 349, L5

Hollands M. A., et al., 2017, MNRAS, 467, 4970

Hollands M. A., Gänsicke B. T., Koester D., 2018a, MNRAS, 477, 93

Hollands M. A., et al., 2018b, MNRAS, 480, 3942

Hügelmeyer S. D., et al., 2007, in Napiwotzki R., Burleigh M. R., eds, Astronomical Society of the Pacific Conference Series Vol. 372, 15th European Workshop on White Dwarfs. p. 249 (arXiv:astro-ph/0610746)

Hummer D. G., Mihalas D., 1988, ApJ, 331, 794

Iben I. J., Renzini A., 1983, ARA&A, 21, 271

Iben Icko J., Ritossa C., García-Berro E., 1997, ApJ, 489, 772

Jeans J. H., 1902, Philosophical Transactions of the Royal Society of London Series A, 199, 1

Jiang Y.-F., et al., 2018, Nature, 561, 498

Jones E., Oliphant T., Peterson P., others 2001, SciPy: Open source scientific tools for Python, http://www.scipy.org/

Jura M., 2003, ApJ, 584, L91

Jura M., Muno M. P., Farihi J., Zuckerman B., 2009, ApJ, 699, 1473

Kalirai J. S., 2012, Nature, 486, 90

Kepler S. O., et al., 2015, MNRAS, 446, 4078

Kepler S. O., et al., 2016, MNRAS, 455, 3413

Kepler S. O., et al., 2017, in Tremblay P. E., Gaensicke B., Marsh T., eds, Astronomical Society of the Pacific Conference Series Vol. 509, 20th European White Dwarf Workshop. p. 421 (arXiv:1610.00371)

Kepler S. O., et al., 2019a, MNRAS, 486, 2169

Kepler S. O., et al., 2019b, MNRAS, 486, 2169

Kilic M., et al., 2015, ApJ, 814, L31

Kilic M., et al., 2019, MNRAS, 482, 965

Kilic M., et al., 2020, arXiv e-prints, p. arXiv:2006.00323

Kippenhahn R., Weigert A., 1990, Stellar Structure and Evolution

Kirzhnitz D., 1960, JETP, 11, 365

Kleinman S. J., et al., 2013a, ApJS, 204, 5

Kleinman S. J., et al., 2013b, ApJS, 204, 5

Koester D., 1976, A&A, 52, 415

Koester D., 2009, A&A, 498, 517

Koester D., Kepler S. O., 2015, A&A, 583, A86

Koester D., Kepler S. O., 2019, arXiv e-prints, p. arXiv:1905.11174

Koester D., Gänsicke B. T., Farihi J., 2014, A&A, 566, A34

Kollmeier J. A., et al., 2017, arXiv preprint arXiv:1711.03234

Kovetz A., Yaron O., Prialnik D., 2009, MNRAS, 395, 1857

Kowalski P. M., Saumon D., 2006, ApJ, 651, L137

Kroupa P., 2001, MNRAS, 322, 231

Kupka F., Muthsam H. J., 2017, Living Reviews in Computational Astrophysics, 3, 1

Kupka F., Zaussinger F., Montgomery M. H., 2018, MNRAS, 474, 4660

Kučinskas A., et al., 2018, A&A, 613, A24

Landstreet J. D., Bagnulo S., 2019, A&A, 628, A1

Laney C. B., 1998, Computational gasdynamics. Cambridge university press

Lattimer J. M., Prakash M., 2001, ApJ, 550, 426

Lawrie K. A., Burleigh M. R., Dufour P., Hodgkin S. T., 2013, MNRAS, 433, 1599

LeVeque R. J., 1998, in , Computational methods for astrophysical fluid flow. Springer, pp 1–159

Lecoanet D., et al., 2016, ApJ, 832, 71

Ledoux P., 1947, ApJ, 105, 305

Leggett S. K., Ruiz M. T., Bergeron P., 1998, ApJ, 497, 294

Limoges M. M., Bergeron P., Lépine S., 2015, ApJS, 219, 19

Livio M., Truran J. W., 1994, ApJ, 425, 797

Lucy L. B., 1977, AJ, 82, 1013

Ludwig H. G., Steffen M., 2013, Memorie della Societa Astronomica Italiana Supplementi, 24, 53

Ludwig H. G., Jordan S., Steffen M., 1994, A&A, 284, 105

Ludwig H.-G., Allard F., Hauschildt P. H., 2006, A&A, 459, 599

Ludwig H. G., et al., 2009, Mem. Soc. Astron. Italiana, 80, 711

Luyten W. J., 1922, PASP, 34, 54

MacDonald J., Vennes S., 1991, ApJ, 371, 719

Magic Z., Chiavassa A., Collet R., Asplund M., 2015, A&A, 573, A90

Manser C. J., 2018, PhD thesis, University of Warwick, University of Warwick

Manser C. J., et al., 2016, MNRAS, 455, 4467

Manser C. J., et al., 2020, MNRAS, 493, 2127

Maoz D., Mazeh T., McQuillan A., 2015, MNRAS, 447, 1749

Marigo P., et al., 2020, Nature Astronomy,

Maschberger T., 2013, MNRAS, 429, 1725

McCook G. P., Sion E. M., 1999, ApJS, 121, 1

Melis C., Dufour P., 2017, ApJ, 834, 1

Mestel L., 1952, MNRAS, 112, 583

Metzger B. D., Rafikov R. R., Bochkarev K. V., 2012, MNRAS, 423, 505

Michaud G., 1970, ApJ, 160, 641

Mihalas D., 1978, Stellar atmospheres /2nd edition/

Miller G. E., Scalo J. M., 1979, ApJS, 41, 513

Miller Bertolami M. M., 2016, A&A, 588, A25

Mollá M., Cavichia O., Gavilán M., Gibson B. K., 2015, MNRAS, 451, 3693

Montgomery M. H., Thompson S. E., von Hippel T., 2008, The Astrophysical Journal, 685, L133

Morgan J. W., Anders E., 1980, Proceedings of the National Academy of Science, 77, 6973

Morrissey P., et al., 2007, ApJS, 173, 682

Nelemans G., Tauris T. M., 1998, A&A, 335, L85

Nordlund A., 1974, A&A, 32, 407

Nordlund A., 1982, A&A, 107, 1

Nordlund Å., Dravins D., 1990, Astronomy and Astrophysics, 228, 155

Öpik E., 1916, ApJ, 44, 292

Ourique G., et al., 2019, MNRAS, 482, 649

Paquette C., Pelletier C., Fontaine G., Michaud G., 1986a, ApJS, 61, 177

Paquette C., Pelletier C., Fontaine G., Michaud G., 1986b, ApJS, 61, 197

Patterson J., Raymond J. C., 1985, ApJ, 292, 535

Pauli W., 1925, Zeitschrift fur Physik, 31, 765

Pauli E.-M., et al., 2006, Astronomy & Astrophysics, 447, 173

Paxton B., et al., 2015, ApJS, 220, 15

Pedersen M. G., Aerts C., Pápics P. I., Rogers T. M., 2018, A&A, 614, A128

Pelletier C., et al., 1986, ApJ, 307, 242

Piro A. L., Bildsten L., 2004, ApJ, 610, 977

Pols O. R., et al., 1998, Monthly Notices of the Royal Astronomical Society, 298, 525

Prandtl L., Tietjens O., 1925, Naturwissenschaften, 13, 1050

Priestley C. H. B., Swinbank W. C., 1947, Proceedings of the Royal Society of London Series A, 189, 543

Raddi R., et al., 2015, MNRAS, 450, 2083

Rafikov R. R., 2011, ApJ, 732, L3

Raithel C. A., Özel F., Psaltis D., 2016, ApJ, 831, 44

Reding J. S., et al., 2020, ApJ, 894, 19

Roe P., 1981, Journal of Computational Physics, 43, 357

Roe P. L., 1986, Annual Review of Fluid Mechanics, 18, 337

Rogers L. K., et al., 2020, arXiv e-prints, p. arXiv:2003.13711

Rolland B., Bergeron P., Fontaine G., 2018, ApJ, 857, 56

Romero A. D., et al., 2017, ApJ, 851, 60

Romero A. D., et al., 2019, MNRAS, 484, 2711

Roxburgh I. W., 1978, A&A, 65, 281

Russell H. N., 1944, AJ, 51, 13

Salaris M., Cassisi S., 2005, Evolution of Stars and Stellar Populations

Salaris M., Cassisi S., 2017, Royal Society Open Science, 4, 170192

Salaris M., et al., 1997, ApJ, 486, 413

Salpeter E. E., 1955, ApJ, 121, 161

Salpeter E. E., 1961, ApJ, 134, 669

Savedoff M. P., van Horn H. M., Vila S. C., 1969, ApJ, 155, 221

Schaeberle J. M., 1896, AJ, 17, 37

Schaffenberger W., Wedemeyer-Böhm S., Steiner O., Freytag B., 2005, in Innes D. E., Lagg A., Solanki S. A., eds, ESA Special Publication Vol. 596, Chromospheric and Coronal Magnetic Fields. p. 65.1

Schaffenberger W., Wedemeyer-Böhm S., Steiner O., Freytag B., 2006, in Leibacher J., Stein R. F., Uitenbroek H., eds, Astronomical Society of the Pacific Conference Series Vol. 354, Solar MHD Theory and Observations: A High Spatial Resolution Perspective. p. 345

Schatzman E., 1945, Annales d'Astrophysique, 8, 143

Schoenberner D., Weidemann V., 1983, in Aller L. H., ed., IAU Symposium Vol. 103, Planetary Nebulae. pp 359–371

Schröder K.-P., Connon Smith R., 2008, Monthly Notices of the Royal Astronomical Society, 386, 155

Schwarzschild K., 1906, Nachrichten von der Königlichen Gesellschaft der Wissenschaften zu Göttingen. Math.-phys. Klasse, 195, 41

Shipman H. L., 1972, ApJ, 177, 723

Shu C.-W., Osher S., 1989, Journal of Computational Physics, 83, 32

Siess L., 2006, A&A, 448, 717

Sikora J., et al., 2019, MNRAS, 487, 4695

Sion E. M., 1984, ApJ, 282, 612

Spiegel E. A., 1963, ApJ, 138, 216

Stancliffe R. J., Fossati L., Passy J. C., Schneider F. R. N., 2015, A&A, 575, A117

Stein R. F., Nordlund Å., 1998, ApJ, 499, 914

Steiner O., et al., 2007, Astronomische Nachrichten, 328, 323

Steiner O., Calvo F., Salhab R., Vigeesh G., 2017, Mem. Soc. Astron. Italiana, 88, 37

Stoner E., 1930, The London, 9, 944

Straniero O., Domínguez I., Imbriani G., Piersanti L., 2003, ApJ, 583, 878

Strittmatter P. A., Wickramasinghe D. T., 1971, MNRAS, 152, 47

Swan A., Farihi J., Wilson T. G., 2019, MNRAS, 484, L109

Tassoul M., Fontaine G., Winget D. E., 1990, ApJS, 72, 335

Tayler R. J., 1994, The Stars, Their Structure and Evolution

Thoul A. A., Bahcall J. N., Loeb A., 1994, ApJ, 421, 828

Timmes F. X., Woosley S. E., Taam R. E., 1994, ApJ, 420, 348

Trampedach R., et al., 2013, ApJ, 769, 18

Tremblay P.-E., Bergeron P., 2008, ApJ, 672, 1144

Tremblay P. E., Bergeron P., 2009, ApJ, 696, 1755

Tremblay P. E., et al., 2011a, A&A, 531, L19

Tremblay P. E., Bergeron P., Gianninas A., 2011b, ApJ, 730, 128

Tremblay P. E., Bergeron P., Gianninas A., 2011c, ApJ, 730, 128

Tremblay P.-E., Ludwig H.-G., Steffen M., Freytag B., 2013a, A&A, 552, A13

Tremblay P.-E., et al., 2013b, A&A, 557, A7

Tremblay P.-E., Ludwig H.-G., Steffen M., Freytag B., 2013c, A&A, 559, A104

Tremblay P.-E., et al., 2014, ApJ, 791, 92

Tremblay P.-E., et al., 2015a, ApJ, 799, 142

Tremblay P. E., et al., 2015b, ApJ, 809, 148

Tremblay P. E., et al., 2015c, ApJ, 812, 19

Tremblay P. E., et al., 2015d, ApJ, 812, 19

Tremblay P.-E., et al., 2016a, MNRAS, 461, 2100

Tremblay P. E., et al., 2016b, MNRAS, 461, 2100

Tremblay P.-E., et al., 2017a, Mem. Soc. Astron. Italiana, 88, 104

Tremblay P. E., et al., 2017b, MNRAS, 465, 2849

Tremblay P.-E., et al., 2019a, MNRAS, 482, 5222

Tremblay P.-E., et al., 2019b, Nature, 565, 202

Unglaub K., Bues I., 2000, A&A, 359, 1042

Van Leer B., 1979, Journal of computational Physics, 32, 101

Vanderbosch Z., et al., 2019, arXiv e-prints, p. arXiv:1908.09839

Vanderburg A., et al., 2015, Nature, 526, 546

Vanderplas J., Connolly A., Ivezić Ž., Gray A., 2012, in Conference on Intelligent Data Understanding (CIDU). pp 47 –54, doi:10.1109/CIDU.2012.6382200

Vauclair G., Vauclair S., Greenstein J. L., 1979, A&A, 80, 79

Vennes S., Chayer P., Fontaine G., Wesemael F., 1989, ApJ, 336, L25

Ventura P., Zeppieri A., Mazzitelli I., D'Antona F., 1998, A&A, 334, 953

Veras D., 2016a, Royal Society Open Science, 3, 150571

Veras D., 2016b, MNRAS, 463, 2958

Veras D., Carter P. J., Leinhardt Z. M., Gänsicke B. T., 2017, MNRAS, 465, 1008

Vögler A., et al., 2005, A&A, 429, 335

Wachlin F. C., Vauclair G., Vauclair S., Althaus L. G., 2017, A&A, 601, A13

Wall R. E., et al., 2019, arXiv e-prints, p. arXiv:1909.02617

Weidemann V., 2003, in NATO ASIB Proc. 105: White Dwarfs. p. 3

Weisskopf M. C., Tananbaum H. D., Van Speybroeck L. P., O'Dell S. L., 2000, in X-Ray Optics, Instruments, and Missions III. pp 2–16

Werner K., Herwig F., 2006, PASP, 118, 183

Werner K., Rauch T., Kruk J. W., 2018, A&A, 609, A107

Wilson D. J., 2017, PhD thesis, University of Warwick, University of Warwick

Wilson D. J., Gänsicke B. T., Farihi J., Koester D., 2016, MNRAS, 459, 3282

Wilson D. J., et al., 2019, MNRAS, 483, 2941

Winget D. E., et al., 1987, ApJ, 315, L77

Winget D. E., et al., 2004, ApJ, 602, L109

Wood M. A., 1990, J. R. Astron. Soc. Canada, 84, 150

Wood P. R., Olivier E. A., Kawaler S. D., 2004, The Astrophysical Journal, 604, 800

Wyatt M. C., Farihi J., Pringle J. E., Bonsor A., 2014, MNRAS, 439, 3371

Xu S., et al., 2014, ApJ, 783, 79

Xu S., et al., 2017, ApJ, 836, L7

Xu S., et al., 2018, MNRAS, 474, 4795

Xu S., et al., 2019, AJ, 158, 242

Zahn J.-P., 1991, A&A, 252, 179

Zuckerman B., Koester D., Reid I. N., Hünsch M., 2003, ApJ, 596, 477

Zuckerman B., et al., 2007, ApJ, 671, 872

Zuckerman B., et al., 2010, ApJ, 722, 725

van Horn H. M., 1968, ApJ, 151, 227

van Horn H. M., 1970, ApJ, 160, L53

van Maanen A., 1917, PASP, 29, 258

von Hippel T., Thompson S. E., 2007, ApJ, 661, 477